

## Durham E-Theses

---

*Carbon dioxide emissions from the oxidative  
weathering of sedimentary rocks in highly erosive  
settings*

ROYLANDS, TOBIAS

### How to cite:

---

ROYLANDS, TOBIAS (2022) *Carbon dioxide emissions from the oxidative weathering of sedimentary rocks in highly erosive settings*, Durham theses, Durham University. Available at Durham E-Theses  
Online: <http://etheses.dur.ac.uk/14490/>

### Use policy

---

The full-text may be used and/or reproduced, and given to third parties in any format or medium, without prior permission or charge, for personal research or study, educational, or not-for-profit purposes provided that:

- a full bibliographic reference is made to the original source
- a [link](#) is made to the metadata record in Durham E-Theses
- the full-text is not changed in any way

The full-text must not be sold in any format or medium without the formal permission of the copyright holders.

Please consult the [full Durham E-Theses policy](#) for further details.

*Carbon dioxide emissions from the oxidative  
weathering of sedimentary rocks in highly  
erosive settings*

Tobias Roylands

A thesis submitted for the  
Degree of Doctor of Philosophy in Geography and Earth Sciences

Department of Geography, Durham University

2022



*You must never think of the whole street at once, understand? You must only concentrate on the next step, the next breath, the next stroke of the broom, and the next, and the next. Nothing else. That way you enjoy your work, [...]*

*And all at once, before you know it, you find you've swept the whole street clean, bit by bit. What's more, you aren't out of breath.*

Beppo Road sweeper in *Momo* by **Michael Ende**<sup>1</sup>

<sup>1</sup> 1984, translated by J. M. Brownjohn, Penguin Books Ltd, United Kingdom.

## Abstract

Chemical weathering of sedimentary rocks is an important control on the composition of Earth's surface system and climate over geological timescales, via two main pathways: i) the oxidation of petrogenic organic carbon ( $OC_{\text{petro}}$ ); and ii) the oxidation of sulfide minerals coupled to the dissolution of carbonate minerals. Both processes are characterized by the release of carbon dioxide ( $CO_2$ ) and consumption of oxygen ( $O_2$ ). However, the corresponding present-day weathering fluxes and their environmental controls are only partly constrained due to a lack of *in situ* measurements. This research presents direct measurements of  $CO_2$  release that were performed in steep, rapidly eroding terrains of the Waiapu catchment, North Island, New Zealand, and two neighbouring catchments in the French southern Alps that are part of the Draix-Bléone observatory. For this, the tools for studying the gaseous exchange of  $CO_2$  and  $O_2$  during oxidative weathering are refined. It is shown that direct measurements using drilled gas accumulation chambers are feasible during short-term ( $\geq 1$  week) field campaigns in remote areas. In addition, the gaseous movement of  $CO_2$  and  $O_2$  in shallow weathering zones can be quantified, which supports upscaling local findings to the wider landscape. Following this approach, high  $CO_2$  emissions are reported that identify steep terrains as hotspots of oxidative weathering in the geological carbon cycle. Furthermore, the contributions to the bulk weathering fluxes from  $OC_{\text{petro}}$  oxidation and sulfide oxidation coupled to carbonate dissolution are assessed with radiocarbon and stable carbon isotope analyses. For this, a microbial impact on the oxidation of  $OC_{\text{petro}}$  is discussed. Based on repeated fieldtrips across multiple seasons, important environmental controls on the size and source of *in situ*  $CO_2$  emissions are identified, including temperature, precipitation and the chemical composition of the bedrock. Overall, the oxidative weathering fluxes and their environmental controls presented here provide a basis for future models of Earth's geochemical and climatic history. It is highlighted that these now need to consider a positive climate feedback by the response of oxidative weathering fluxes to warming.

# Contents

<b>Abstract</b> .....	<b>i</b>
<b>Contents</b> .....	<b>ii</b>
<b>List of Figures</b> .....	<b>vi</b>
<b>List of Tables</b> .....	<b>viii</b>
<b>Declaration</b> .....	<b>ix</b>
<b>Statement of Copyright</b> .....	<b>x</b>
<b>Acknowledgements</b> .....	<b>xi</b>
<b>1 Introduction</b> .....	<b>1</b>
1.1 Thesis aim .....	2
1.2 The geological carbon cycle .....	2
1.3 Oxidative weathering of sedimentary rocks .....	5
1.3.1 OC <sub>petro</sub> oxidation .....	5
1.3.1.1 Tracing OC <sub>petro</sub> oxidation .....	5
1.3.1.2 Controls on OC <sub>petro</sub> oxidation .....	8
1.3.2 Sulfide oxidation and carbonate dissolution .....	10
1.4 Studying the critical zone .....	11
1.4.1 The concept of critical zone observatories .....	11
1.4.2 The Draix-Bléone observatory .....	13
1.5 Research aim and questions .....	15
1.6 Thesis synopsis .....	16
<b>2 Capturing the short-term variability of carbon dioxide emissions from sedimentary rock weathering in a remote mountainous catchment, New Zealand</b> .....	<b>18</b>
2.1 Abstract .....	20
2.2 Introduction .....	21
2.3 Material and methods .....	23
2.3.1 Study site .....	23
2.3.2 CO <sub>2</sub> measurements .....	26
2.3.2.1 <i>In situ</i> weathering chambers .....	26
2.3.2.2 Rock pCO <sub>2</sub> measurements .....	27
2.3.2.3 CO <sub>2</sub> flux measurements .....	27
2.3.2.4 CO <sub>2</sub> sampling and isotopic analyses .....	28
2.3.3 Bulk geochemistry .....	28
2.4 Results .....	29

2.4.1	Bulk geochemistry .....	29
2.4.2	Environmental variables.....	29
2.4.3	CO <sub>2</sub> fluxes .....	31
2.4.4	Rock chamber <i>p</i> CO <sub>2</sub> .....	34
2.4.5	Carbon isotope composition of CO <sub>2</sub> .....	34
2.5	Discussion .....	37
2.5.1	Source of rock-derived CO <sub>2</sub> .....	37
2.5.1.1	Geothermal contributions of CO <sub>2</sub> and CH <sub>4</sub> oxidation.....	38
2.5.1.2	Microbial impact on OC <sub>petro</sub> oxidation and carbon isotope fractionation.....	39
2.5.2	Rock-derived CO <sub>2</sub> fluxes and their environmental controls .....	40
2.5.2.1	Local topographic position and moisture .....	40
2.5.2.2	Temperature .....	41
2.5.3	Wider implications for understanding Earth's carbon cycle .....	43
2.5.3.1	Feasibility of short-term investigations to reveal environmental controls on rock-derived CO <sub>2</sub> fluxes .....	44
2.5.3.2	Rock <i>p</i> CO <sub>2</sub> and silicate weathering .....	45
2.6	Conclusions.....	47
2.7	Acknowledgements .....	47
<b>3</b>	<b>Probing the exchange of CO<sub>2</sub> and O<sub>2</sub> in the shallow critical zone during weathering of marl and black shale .....</b>	<b>48</b>
3.1	Abstract .....	50
3.2	Introduction.....	51
3.3	Material and methods .....	53
3.3.1	Study area.....	53
3.3.2	Drilled gas accumulation chambers .....	55
3.3.3	Rock temperature and humidity .....	57
3.3.4	Partial pressure of rock CO <sub>2</sub> .....	59
3.3.5	CO <sub>2</sub> flux measurements.....	59
3.3.6	CO <sub>2</sub> sampling .....	60
3.3.7	Measuring <i>p</i> O <sub>2</sub> and O <sub>2</sub> fluxes.....	61
3.4	Results .....	62
3.4.1	Chamber temperature and meteorological conditions.....	62
3.4.2	<i>p</i> CO <sub>2</sub> measurements and CO <sub>2</sub> collection .....	64
3.4.3	<i>p</i> O <sub>2</sub> measurements.....	66
3.5	Discussion .....	66
3.5.1	Probing the gas exchange of the shallow critical zone.....	67

3.5.1.1	Explaining the patterns of CO <sub>2</sub> accumulation during a single flux measurement.....	67
3.5.1.2	Assessing the diffusivity of the shallow weathering zone .....	69
3.5.2	Assessing the contributing rock pore volume .....	75
3.5.2.1	Quantification of the contributing rock pore volume.....	75
3.5.2.2	Environmental controls on the contributing rock pore volume .....	77
3.5.2.3	Upscaling chamber-based CO <sub>2</sub> fluxes.....	79
3.5.3	Implications for CO <sub>2</sub> flux measurements.....	83
3.5.3.1	Accuracy and precision of CO <sub>2</sub> flux measurements .....	83
3.5.3.2	Reporting CO <sub>2</sub> flux as a function of temperature .....	85
3.5.4	Linking CO <sub>2</sub> and O <sub>2</sub> fluxes .....	87
3.6	Conclusions.....	91
3.7	Acknowledgements .....	92
3.8	Supplementary .....	93
3.8.1	Details of the fitting model for chamber temperatures.....	93
3.8.2	Linear regression of $p\text{CO}_{2\text{Rock}}$ and CO <sub>2</sub> accumulation rates.....	93
3.8.3	Linear regression of diffusivity measures.....	94
3.8.4	Different diffusion pathways of a closed versus manipulated chamber.....	94
<b>4</b>	<b>Carbon dioxide emissions during sedimentary rock weathering scale with organic matter content and temperature.....</b>	<b>95</b>
4.1	Abstract .....	97
4.2	Introduction.....	98
4.3	Material and methods .....	100
4.3.1	Study area.....	100
4.3.2	Rock bulk chemistry .....	101
4.3.3	CO <sub>2</sub> fluxes .....	101
4.3.3.1	Total CO <sub>2</sub> fluxes.....	101
4.3.3.2	C <sub>CO2</sub> isotope measurements and source partitioning .....	103
4.3.3.3	Temperature sensitivity of CO <sub>2</sub> fluxes.....	104
4.4	Results .....	105
4.4.1	Carbon isotope composition of rock-derived CO <sub>2</sub> and source partitioning .....	105
4.4.2	Source-specific CO <sub>2</sub> fluxes and their response to temperature .....	106
4.4.3	Relation of the lithological composition and source-specific CO <sub>2</sub> fluxes .....	109
4.5	Discussion .....	110
4.5.1	OC <sub>petro</sub> content in shallow weathering rocks scales CO <sub>2</sub> emission .....	111
4.5.1.1	OC <sub>petro</sub> -derived CO <sub>2</sub> .....	111
4.5.1.2	Carbonate-sourced CO <sub>2</sub> .....	112

4.5.2	Fate of OC <sub>petro</sub> during oxidative weathering.....	114
4.5.3	Highly erosive sedimentary rocks as hotspots of oxidative weathering .....	115
4.6	Conclusions.....	117
4.7	Acknowledgements .....	118
4.8	Supplementary .....	119
4.8.1	Carbon isotope data of rock-derived and atmospheric CO <sub>2</sub> samples.....	119
<b>5</b>	<b>Conclusions .....</b>	<b>120</b>
5.1	Main research findings .....	121
5.1.1	RQ1: Is it possible to quantify the gas exchange of CO <sub>2</sub> and O <sub>2</sub> during weathering of sedimentary rocks in steep terrains by direct <i>in situ</i> measurements?.....	121
5.1.2	RQ2: On what timescale do significant changes of CO <sub>2</sub> release from oxidative weathering of organic matter and of sulfides in highly erosive settings occur, and how are they linked to environmental changes? .....	123
5.1.3	RQ3: How do differences in the chemical composition of sedimentary rocks undergoing oxidative weathering influence the weathering processes? .....	125
5.2	Future research directions.....	126
5.2.1	The role of microorganisms during oxidative weathering of sedimentary rocks in highly erosive terrains.....	126
5.2.2	Alteration of OC <sub>petro</sub> during oxidative weathering and the geological O <sub>2</sub> cycle.....	128
5.2.3	Sedimentary rock weathering in terrains with moderate to low erosion rates.....	130
5.2.4	Spatial and temporal upscaling of <i>in situ</i> constraints on chemical weathering processes	131
	<b>References .....</b>	<b>133</b>

## List of Figures

Figure 1-1. Earth’s geological carbon cycle.....	3
Figure 1-2. Weathering of OC <sub>petro</sub> -rich sedimentary rocks.....	6
Figure 1-3. Novel technique for directly measuring CO <sub>2</sub> fluxes from weathering in the field. ....	8
Figure 1-4. Link of physical erosion and OC <sub>petro</sub> oxidation on the catchment-scale. ....	9
Figure 1-5. Link of physical erosion and carbonate weathering by sulfuric acid on the catchment-scale. ....	11
Figure 1-6. Illustration of Earth’s critical zone. ....	12
Figure 1-7. Imagery of the Draix-Bléone observatory in the French southern Alps. ....	14
Figure 2-1. Map and imagery of the study area. ....	25
Figure 2-2. Time series of carbon dioxide fluxes and partial pressures alongside environmental variables. ....	30
Figure 2-3. Time series of air temperatures and chamber temperatures. ....	31
Figure 2-4. Carbon dioxide flux from weathering chambers versus their elevation above the riverbed.....	32
Figure 2-5. Carbon dioxide flux versus temperature. ....	33
Figure 2-6. Carbon dioxide flux versus partial pressure of carbon dioxide in the weathering zone. ....	34
Figure 2-7. Stable carbon isotope measurement of CO <sub>2</sub> from weathering chambers versus sampling efficiency. ....	36
Figure 3-1. Location of the French Draix-Bléone observatory and of the study sites for CO <sub>2</sub> and O <sub>2</sub> monitoring.....	55
Figure 3-2. The study sites in the Brusquet catchment and in the Moulin catchment. ....	57
Figure 3-3. Overview of modeled chamber temperatures. ....	58
Figure 3-4. Environmental variables for weathering chambers in 2018 and 2019.....	63
Figure 3-5. Two examples of monitoring the CO <sub>2</sub> concentration in a chamber during a flux measurement.....	65
Figure 3-6. Examples of CO <sub>2</sub> flux measurements consisting of several repeated accumulation rate measurements. ....	69
Figure 3-7. Comparisons of diffusivity, CO <sub>2</sub> partial pressures and accumulation rates, and chamber temperatures. ....	74
Figure 3-8. Catchment-specific summary of measured volumes of rock pores. ....	76
Figure 3-9. Chamber-specific summary of measured volumes of rock pores. ....	77

Figure 3-10. Comparisons of $V_{\text{Rock pores}}$ , diffusivity, $\text{CO}_2$ accumulation rates, and chamber temperatures. ....	78
Figure 3-11. Comparison of $\text{CO}_2$ fluxes determined by using the average of repeated accumulation rates and by an exponential fitting model. ....	85
Figure 3-12. Comparison of $\text{CO}_2$ fluxes with different normalizations and chamber temperature. ....	87
Figure 3-13. Comparison of $\text{O}_2$ partial pressure and $\text{O}_2$ flux with temperature. ....	88
Figure 4-1. The source of chamber-derived $\text{CO}_2$ inferred from carbon isotope compositions.	106
Figure 4-2. Response of $\text{OC}_{\text{petro}}$ -derived $\text{CO}_2$ release to changes in chamber temperature. ....	110
Figure 4-3. Dual control of $\text{OC}_{\text{petro}}$ content and temperature in shallow, aerated weathering zones on $\text{OC}_{\text{petro}}$ -derived $\text{CO}_2$ release. ....	112
Figure 5-1. Generalized diagram for the response of $\text{CO}_2$ emissions from oxidative weathering of sedimentary rocks to environmental changes in highly erosive terrains. ....	124

## List of Tables

Table 2-1. Properties of gas accumulation chambers drilled into weathering sedimentary rocks in the Waiapu catchment, New Zealand.....	27
Table 2-2. Summary table of CO <sub>2</sub> fluxes. ....	31
Table 2-3. Carbon isotope composition of sampled CO <sub>2</sub> . ....	37
Table 3-1. Properties of gas accumulation chambers drilled into weathering sedimentary rocks in the Brusquet catchment and in the Moulin catchment. ....	56
Table 3-2. Overview of the variability of air temperature, chamber temperature and rock surface temperature.....	62
Table 3-3. Chamber-specific overview of CO <sub>2</sub> partial pressures in the shallow weathering zone. ....	64
Table 3-4. Overview of the chamber-specific sampling ratio. ....	66
Table 3-5. Chamber-specific overview of CO <sub>2</sub> Excess, V <sub>Rock pores</sub> and CO <sub>2</sub> accumulation rate (q <sub>Plateau</sub> ). ....	82
Table 4-1. Overview of the total rock-derived CO <sub>2</sub> fluxes from marly limestones and black shales and their temperature sensitivity in comparison with the contribution from OC <sub>petro</sub> oxidation. ....	108

## Declaration

I confirm that no part of the material presented in this thesis has previously been submitted by me or any other person for a degree in this or any other university. In all cases, where is relevant, material from the work of others has been acknowledged.

**Tobias Roylands**

## Statement of Copyright

The copyright of this thesis rests with the author. No quotation from it should be published without the author's prior written consent and information derived from it should be acknowledged.

## Acknowledgements

Throughout the research presented here, I have been supported by numerous people, with some named here:

I am especially thankful to Bob Hilton and Erin McClymont for the supervision over the last 4 years. Their knowledge, enthusiasm and support were essential for this thesis to thrive.

This research was funded by the European Research Council via a Starting Grant to Bob Hilton, and I am very thankful for this support. Furthermore, I gratefully acknowledge the support of a Radiocarbon Grant from the Natural Environment Research Council. Also, many thanks go to Durham University for extending the funding of my doctoral studentship.

For all the shared research experiences, I would like to thank the ROC-CO<sub>2</sub> team led by Bob Hilton: Guillaume Soulet, Mateja Ogrič, Mathieu Dellinger, Eleanor Georgiadis, Jesse Zondervan, Katie Grant and Thomas Croissant. Especially, I enjoyed our reading groups.

I have benefitted from the laboratory teams in the Department of Geography and in the Department of Earth Sciences, and would like to thank especially Joanne Peterkin, Darren Gröcke, Eleanor Ross, Frank Davies, Amanda Hayton, Martin West and Mervyn Brown. I am also thankful for the administrative support at Durham University, especially, from Kathy Wood.

Many thanks go to my further research collaborators, most importantly, Mark Garnett and Josephine-Anne Newton from the NEIF Radiocarbon Laboratory, and Sébastien Klotz and Caroline Le Bouteiller who manage the Draix-Bléone observatory. I also would like to thank Peter Hancock, Harriet Roil and Christiaan Delpont from the Gisborne District Council. Furthermore, I am thankful for the help from Mathis Degler and Felipe Napoleoni in the field.

Finally, I am deeply grateful for the support from my family and friends – this thesis is for you!

# 1 Introduction



*Sedimentary rocks exposed in the Draix-Bléone observatory, France. May 2018.*

## 1.1 Thesis aim

The ultimate aim of this thesis is to better understand the drivers of carbon dioxide (CO<sub>2</sub>) release to the atmosphere that occurs during the oxidative weathering of sedimentary rocks. This is a key process in Earth's carbon cycle and essential to the long-term geochemical and climatic evolution of the planet.

The rationale for the thesis aim is provided in this chapter, which summarizes the main themes in which the research is placed. First, an overview of the global carbon cycle and its operation over geological timescales is presented. In addition, the framework of the "critical zone" is discussed, providing the opportunity to study complex environmental processes such as chemical weathering in a holistic manner. From this grounding, the main research questions and objectives required to deliver the thesis aim are introduced. The introduction ends with a summary of the following chapters of the thesis.

## 1.2 The geological carbon cycle

The carbon cycle is essential to the maintenance of life, to the composition of the atmosphere and oceans and to global climate (Berner, 2004; Sundquist and Visser, 2003). It describes the exchange of carbon between the following reservoirs on Earth: oceans, lakes and rivers, biota, soils, rocks and atmosphere (Battin et al., 2009; Berner, 1999), with atmospheric CO<sub>2</sub> acting as the most climate-relevant greenhouse gas (Arrhenius, 1896; Lacis et al., 2010; Rohling et al., 2012). On timescales of decades to thousands of years, the net balance of carbon fluxes associated with primary production and respiration, alongside the gas exchange between hydrosphere and atmosphere can control the carbon cycle and the concentrations of CO<sub>2</sub> in the atmosphere (Berner and Berner, 2012; Hilton and West, 2020). However, on geological timescales (i.e., greater than hundreds of thousands of years), the carbon cycle can ultimately be viewed as the transfer of carbon between the atmosphere and the lithosphere (Figure 1-1) (Hilton and West, 2020).

In this view, sinks of atmospheric carbon are represented by the formation of carbon inventories in rocks. The continental weathering of silicate minerals results in the drawdown of atmospheric CO<sub>2</sub>, subsequent riverine export of bicarbonate and dissolved cations and eventually in the precipitation of carbonate minerals in the oceans (Berner, 1999; Chamberlin, 1899; Walker et al., 1981), with modern fluxes of ~ 90 MtC yr<sup>-1</sup> – 140 MtC yr<sup>-1</sup> (Gaillardet et al., 1999; Moon et al., 2014). The analogue uptake of inorganic carbon during the reaction of seawater with marine sediments, oceanic crust and mantle is less constrained, but may exceed 20 MtC yr<sup>-1</sup> (Alt and Teagle, 1999; Berner, 2009; Kelemen et al., 2011; Sun and Turchyn, 2014;

Torres et al., 2020; Wallmann et al., 2008). Another major sink of atmospheric carbon is the burial of organic carbon (OC) from the marine and continental biosphere in sediments (Berner, 1982; Blair and Aller, 2012; France-Lanord and Derry, 1997; Galy et al., 2015; Hilton, 2017), with a modern flux of  $\sim 170 \text{ MtC yr}^{-1}$  (Hedges and Keil, 1995; Smith et al., 2015), which results in the long-term formation of petrogenic organic carbon ( $\text{OC}_{\text{petro}}$ ) (Killops and Killops, 2005; Petsch, 2014; Vandenbroucke and Largeau, 2007).

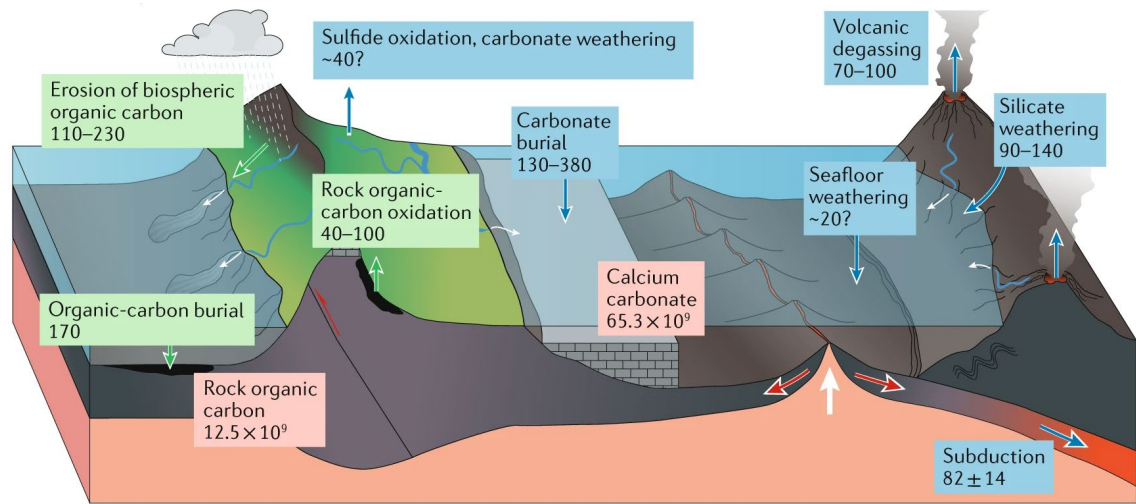


**Figure 1-1. Earth's geological carbon cycle.** Pre-industrial carbon fluxes ( $\text{MtC yr}^{-1}$ ) are denoted with arrows in blue for inorganic carbon and in green for organic carbon, while carbon stocks ( $\text{MtC}$ ) are given in orange boxes. Focus is on carbon fluxes operating on long timescales (greater than hundreds of thousands of years) so that fluxes relevant on shorter timescales (such as primary production, respiration, ocean-atmosphere exchange and carbonate weathering) are not shown. The figure is from Hilton and West (2020).

In contrast, sources of atmospheric carbon are related to the decomposition of carbon stocks in rocks. The subduction of sedimentary rocks and altered oceanic crust and mantle contributes to the deep carbon cycling in Earth's interior (Dasgupta and Hirschmann, 2010; Fischer et al., 2020) that releases carbon to the atmosphere via volcanic outgassing at mid-ocean ridges and subduction zones and via diffusive emission in intraplate volcanic regions, with modern fluxes of  $\sim 70 \text{ MtC yr}^{-1} - 100 \text{ MtC yr}^{-1}$  (Plank and Manning, 2019). On geological timescales, the weathering of carbonate minerals by carbonic acid that is derived from atmospheric  $\text{CO}_2$  is balanced by formation of carbonates elsewhere (Berner, 2004). However, the weathering of carbonate minerals by sulfuric acid that is derived from the oxidation of sulfide minerals (such as pyrite) releases  $\text{CO}_2$  (Calmels et al., 2007; Li et al., 2008; Soulet et al., 2021, 2018; Torres et al., 2016). In the oceans, the balancing precipitation of sulfide minerals producing alkalinity for carbonate precipitation can be delayed over several millions of years,

giving a transient source of carbon to the atmosphere (Torres et al., 2014), with modern fluxes of  $\sim 40 \text{ MtC yr}^{-1}$  (Berner and Berner, 2012; Burke et al., 2018). Likewise during chemical weathering, the oxidation of  $\text{OC}_{\text{petro}}$  releases  $\text{CO}_2$ , with a pre-industrial flux of  $\sim 40 \text{ MtC yr}^{-1} - 100 \text{ MtC yr}^{-1}$  (Petsch, 2014). An exceptional example of  $\text{OC}_{\text{petro}}$  oxidation can be seen in the anthropogenic  $\text{CO}_2$  release that is associated with the combustion of fossil-fuels, with an average global flux during the last decade (2010 – 2019) of  $\sim 9,400 \text{ MtC yr}^{-1}$  (IPCC, 2021), which dwarfs the geological (i.e., pre-industrial) flux by a factor of  $\sim 130$ .

The geological carbon cycle is closely connected to the geochemical cycling of sulfur and oxygen ( $\text{O}_2$ ) (Berner and Berner, 2012; Hayes and Waldbauer, 2006; Holland, 1978). An example is the consumption of  $\text{O}_2$  during oxidative weathering, versus the production of  $\text{O}_2$  by photosynthesis and persistence of organic matter. Over millions of years, the carbon sinks and sources need to be balanced, otherwise unfeasible changes in the atmospheric concentrations of  $\text{CO}_2$  and  $\text{O}_2$  would occur (Berner and Caldeira, 1997; Holland, 1978). Previously, it was assumed that the climate-dependency of silicate weathering acts as the key stabilizing feedback (Berner and Caldeira, 1997; Walker et al., 1981). However, it has been recently emphasized that other erosion and weathering pathways (such as OC burial and oxidative weathering) are of comparable importance in controlling the net balance of carbon release and drawdown (Hilton and West, 2020). Over the past 350 million years, the atmospheric  $\text{CO}_2$  may have varied between 200 ppmv and 3000 ppmv (Berner, 2009; Franks et al., 2014; Mills et al., 2021; Pagani et al., 2005; Rae et al., 2021). Over this time, the atmospheric  $\text{O}_2$  level may have varied between 15 % and 35 % (Belcher and McElwain, 2008; Brand et al., 2021; Husson and Peters, 2017; Krause et al., 2018; Mills et al., 2021; Scott and Glasspool, 2006). For example, a decline of the atmospheric  $\text{O}_2$  concentration over the past 800,000 years may be associated with changes in the global oxidative weathering fluxes (Stolper et al., 2016; Yan et al., 2021). However, the geochemical fluxes associated with oxidative weathering of sedimentary carbon are only partly constrained in respect to size and environmental controls (such as climate change feedbacks). This limits the reconstruction of Earth's geochemical and climatic history (Berner and Berner, 2012; Caves Rugestein et al., 2019; Maffre et al., 2021; Mills et al., 2021) as well as the understanding of the present-day transfer of carbon from the continents to the oceans (Regnier et al., 2022).

## 1.3 Oxidative weathering of sedimentary rocks

### 1.3.1 OC<sub>petro</sub> oxidation

The carbon release from the oxidative weathering of OC<sub>petro</sub> derives globally from a reservoir of  $\sim 12.5 \times 10^9$  MtC (Sundquist and Visser, 2003), with  $\sim 1 \times 10^6$  MtC in the upper 1 m of the continental surface (Copard et al., 2007). The majority of OC<sub>petro</sub> occurs in a solid-phase, macromolecular form (i.e., kerogen), while highly condensed organic matter (such as graphite or black carbon) and bitumen (i.e., liquid or gaseous solvent-soluble OC) are less abundant (Petsch, 2014). Although some rocks (such as coals or black shales) contain large quantities of OC<sub>petro</sub>, commonly the concentration of OC<sub>petro</sub> in sedimentary rocks is below 1 wt.% (Petsch, 2014). When these rocks are introduced to O<sub>2</sub> in air and water, for example, by exhumation during orogenesis (Hilton and West, 2020), oxidative weathering results in the degradation of OC<sub>petro</sub> and the release of CO<sub>2</sub> (Chang and Berner, 1999; Keller and Bacon, 1998; Soulet et al., 2021, 2018).

#### 1.3.1.1 Tracing OC<sub>petro</sub> oxidation

A range of approaches has been used previously to study oxidative weathering. In weathering profiles, loss of OC<sub>petro</sub> occurs towards the surface (Clayton and Swetland, 1978; Jaffe et al., 2002; Marynowski et al., 2011b; Petsch, 2014) that can be accompanied by alteration of its composition (Copard et al., 2006; Graz et al., 2011; Grosjean et al., 2004; Hemingway et al., 2018; Longbottom and Hockaday, 2019; Marynowski et al., 2011a; Petsch et al., 2003, 2000; Wildman, 2004), which is most evident for OC<sub>petro</sub>-rich bedrocks (Figure 1-2). However, the residence time of rock in the oxygen-rich, near-surface weathering zone is challenging to assess so that the calculation of geochemical fluxes from weathering profiles is hindered (Bolton et al., 2006).

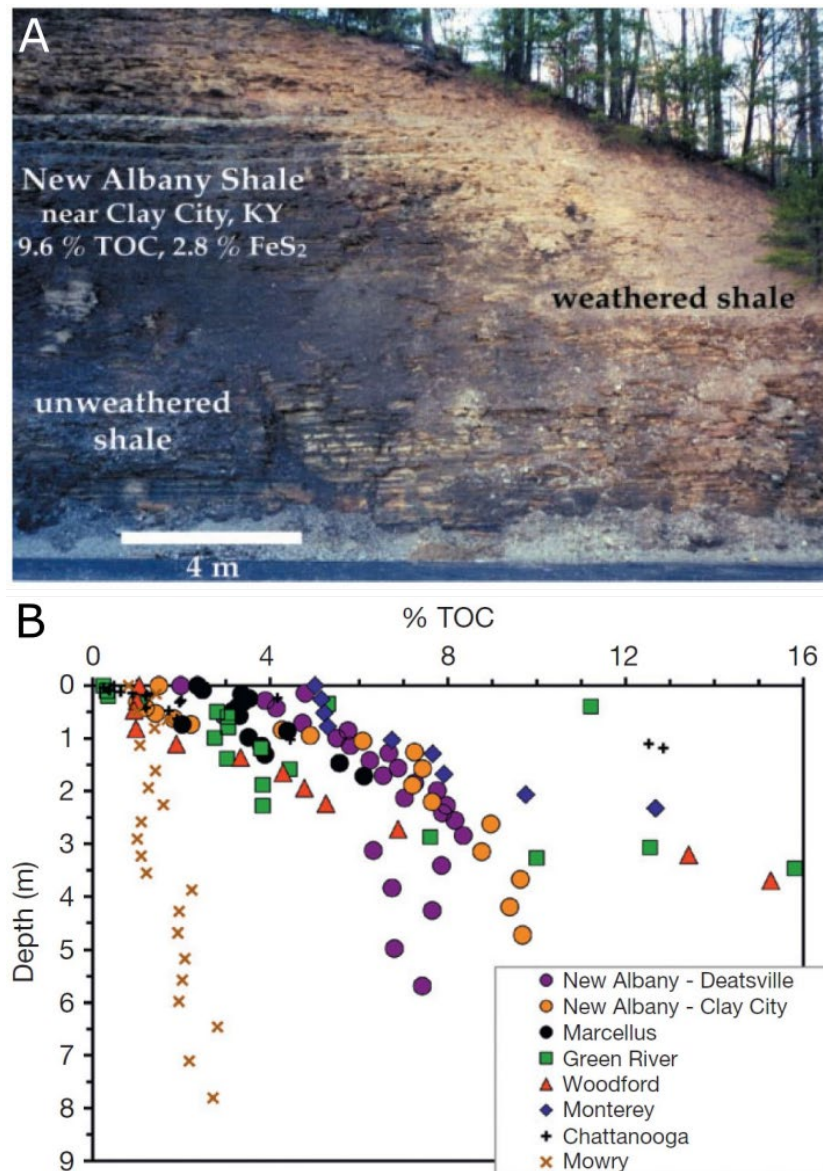


**Figure 1-2. Weathering of  $OC_{\text{petro}}$ -rich sedimentary rocks.** Panel A: image of a weathering profile of New Albany Shale that has been exposed by a recent roadcut (near Clay City, KY, USA), with evidence for weathering including loss of colour,  $OC_{\text{petro}}$  and pyrite, and an increase in friability towards the surface. Image and information are from Petsch et al. (2001). Panel B: decrease of total organic carbon content (TOC, wt.%) in weathering profiles developed on shales, with depth given as distance in meters normal to the surface. The figure is from Petsch (2014).

The oxidation of  $OC_{\text{petro}}$  during exhumation can be incomplete and the subsequent export of eroded material can be traced in rivers (Bouchez et al., 2010; Clark et al., 2017; Galy et al., 2015, 2008; Hilton et al., 2011, 2010; Leithold et al., 2006), in floodplains (Scheingross et al., 2021) and in marine sediments (Blair and Aller, 2012; Leithold et al., 2016). This allows quantification of the oxidation of  $OC_{\text{petro}}$  during transit and the re-burial of organic matter surviving oxidation in riverine and marine sediments, respectively. However, an overall estimate

of the continental oxidation of  $OC_{\text{petro}}$  cannot be based solely on measurements of riverine  $OC_{\text{petro}}$  contents due to the lack of information on the proportion that is lost *in situ* during exhumation of the source rock. Instead, a proxy approach can be applied that relies on the mobilization of a tracer in parallel to the oxidation of  $OC_{\text{petro}}$  and preservation of the tracer during riverine transit. In this way, the trace element rhenium (Re) has been used (Dalai et al., 2002; Hilton et al., 2021, 2014; Horan et al., 2017, 2019; Jaffe et al., 2002). While this indirect approach allows quantification of the oxidation of  $OC_{\text{petro}}$  over large areas, the catchment-wide integration limits the evaluation of local environmental controls on the weathering process.

To investigate the impact of specific environmental conditions on the oxidation of  $OC_{\text{petro}}$ , laboratory experiments have been conducted, for example, to investigate the impact of temperature changes (Chang and Berner, 1999), the formation of dissolved organic matter (Schillawski and Petsch, 2008) or the presence of microorganisms (Matlakowska and Sklodowska, 2011; Petsch et al., 2001; Seifert et al., 2011; Stasiuk et al., 2017). However, so far, research has focused on varying only a small number of environmental factors under controlled, laboratory conditions so that projections to field-based processes of oxidative weathering are not straight-forward (Bolton et al., 2006; Petsch, 2014).

Recently, an approach has been developed to measure the release of  $CO_2$  from oxidative weathering directly in the field (Soulet et al., 2018), which is based on drilling a gas accumulation chamber into sedimentary rock undergoing weathering (Figure 1-3). The  $CO_2$  originating from  $OC_{\text{petro}}$  oxidation can be distinguished from contributions from carbonate dissolution by radiocarbon and stable carbon isotope analyses (Keller and Bacon, 1998; Soulet et al., 2018). This method has the advantage that local effects of environmental changes on the rate of oxidative weathering can be traced holistically with high resolution (Soulet et al., 2021). However, upscaling weathering fluxes to the wider landscape appears to be challenging (Soulet et al., 2021, 2018).

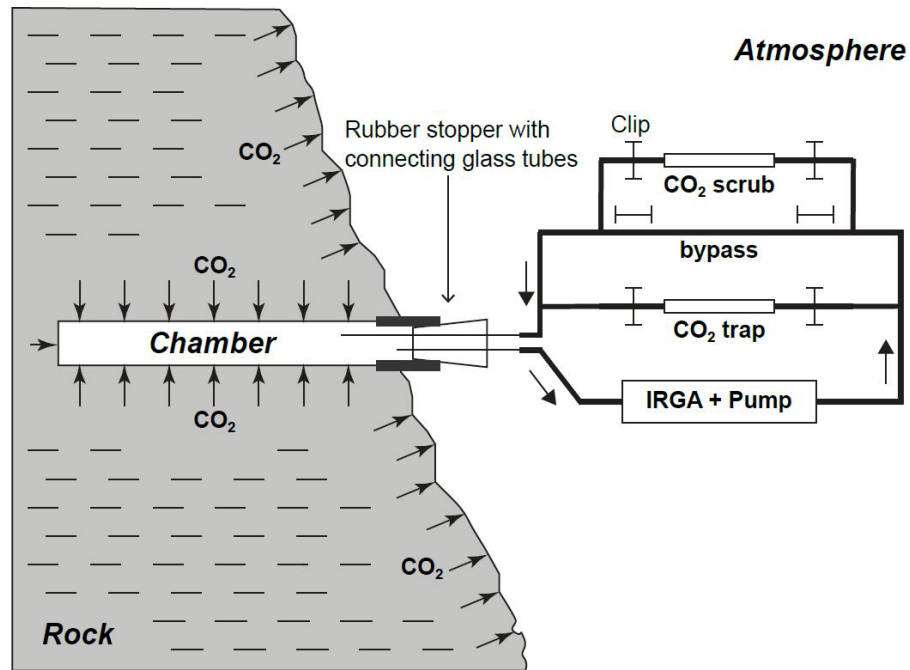


**Figure 1-3. Novel technique for directly measuring CO<sub>2</sub> fluxes from weathering in the field.** A closed-loop monitoring-sampling system is connected to a gas accumulation chamber drilled into a sedimentary rock outcrop. An infra-red gas analyser (IRGA) is used for monitoring CO<sub>2</sub> concentrations of air circulated with a pump through the system and the chamber. Lowering the CO<sub>2</sub> concentration with a soda lime scrub allows measuring a subsequent CO<sub>2</sub> accumulation from the real-time oxidative weathering of the surrounding rock. To identify the source of CO<sub>2</sub> (e.g., OC<sub>petro</sub> vs. inorganic carbon) by analysing its carbon isotope composition, gas can be sampled with zeolite traps. In addition, the monitoring-sampling system incorporates a sensor for measuring the O<sub>2</sub> concentration in the chamber. The figure is modified after Soulet et al. (2018).

### 1.3.1.2 Controls on OC<sub>petro</sub> oxidation

Based on the different methods, insight has been gained into the range of carbon fluxes from OC<sub>petro</sub> oxidation that occur across different environments and their controls. Overall, increases in the flux of oxidized OC<sub>petro</sub> coincide with increases in erosion rate (Figure 1-4), with highly erosive settings being hotspots of OC<sub>petro</sub>-derived CO<sub>2</sub> release (Hilton et al., 2014). This may be controlled by the supply of OC<sub>petro</sub> to the weathering zone (Hilton and West, 2020). However, there is considerable scatter in the global datasets. This may reflect differences in the OC<sub>petro</sub> content of the rock undergoing weathering but could also reflect controls on OC<sub>petro</sub> oxidation by other means, for instance, the supply of O<sub>2</sub> or kinetic limitation.

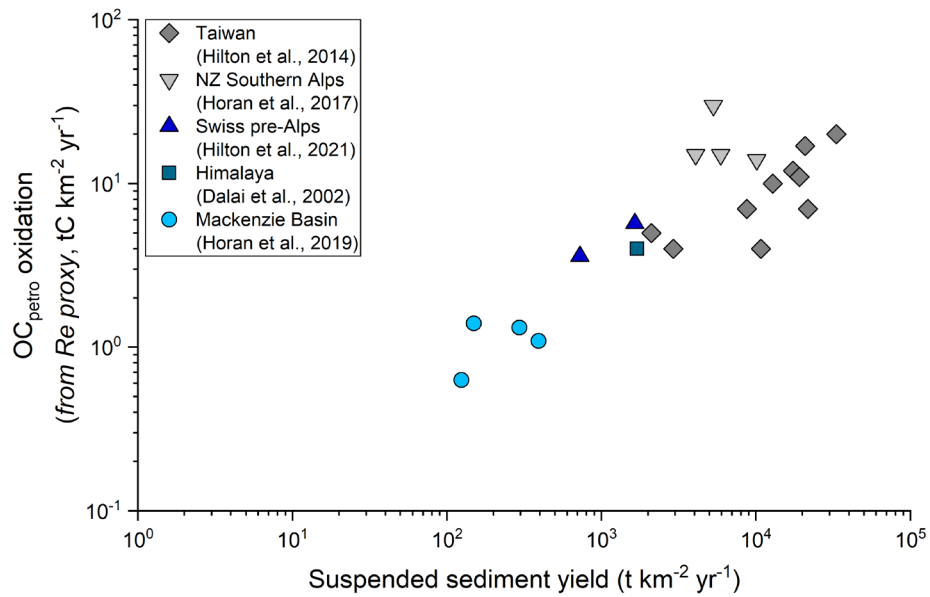


**Figure 1-4. Link of physical erosion and  $OC_{petro}$  oxidation on the catchment-scale.** Carbon fluxes from the oxidation of  $OC_{petro}$  are derived from the dissolved rhenium (Re) proxy, while suspended sediment yield is used as a measure of physical erosion over the integrated area of the studied river-catchments. The figure is modified after Hilton and West (2020) and Hilton et al. (2021).

Indeed, several studies have noted that oxygen supply to the weathering zone must be an important control (Bergman et al., 2004; Bolton et al., 2006; Holland, 1978; Mills et al., 2021), with some limited evidence from laboratory experiments (Chang and Berner, 1999). These experiments also indicated a significant dependence of the oxidation rate of  $OC_{petro}$  to temperature changes by investigating two temperatures. Based on field studies, this control was characterized in more detail, with an exponential increase in  $CO_2$  release when temperature increases (Soulet et al., 2021). In other laboratory studies, it was highlighted that microorganisms have the potential to influence the oxidation (Matlakowska and Sklodowska, 2011; Petsch et al., 2001; Seifert et al., 2011; Stasiuk et al., 2017).

The oxidative weathering of  $OC_{petro}$  can be hindered by mineral association that results in physical protection from the oxygenated environment (Blattmann et al., 2019a; Hemingway et al., 2019; Kleber et al., 2021; Repasch et al., 2021). Furthermore,  $OC_{petro}$  can be stabilized intrinsically by graphitization that follows from high-temperature metamorphism (Beysac et al., 2007; Galvez et al., 2020), with preferential survival of graphite during riverine transit and subsequent burial (Bouchez et al., 2010; Galy et al., 2008; Sparkes et al., 2020).

Generally, these controls are only partly constrained, and it remains unclear how they combine effectively in regulating the oxidation of  $OC_{petro}$  in a given environment. To understand the response of  $OC_{petro}$ -derived  $CO_2$  emissions to varying environmental conditions, more *in situ* constraints are needed that are interpreted in a holistic context.

### 1.3.2 Sulfide oxidation and carbonate dissolution

During weathering of sedimentary rocks, the oxidation of sulfide minerals can coincide with  $OC_{\text{petro}}$  oxidation, which is evidenced in weathering profiles (Figure 1-2A) (Graz et al., 2011; Grosjean et al., 2004; Jaffe et al., 2002; Petsch et al., 2000; Tuttle and Breit, 2009; Wildman, 2004). If the resulting sulfuric acid interacts with carbonate minerals, *in situ*  $CO_2$  release can occur (Soulet et al., 2021, 2018). Analogous to tracing  $OC_{\text{petro}}$  oxidation, sulfide weathering can be assessed with a range of methods. In addition to weathering profiles, chemical analyses of river-water can be used, with dissolved sulfate as a weathering product of sulfide oxidation. However, since sulfate can also derive from other sources, fluxes from the coupled weathering of sulfides and carbonates need to be isolated by geochemical mass balances (Calmels et al., 2007; Das et al., 2012; Galy and France-Lanord, 1999; Li et al., 2008; Spence and Telmer, 2005; Torres et al., 2016, 2014), for example, based on isotope analyses of the dissolved species incorporating carbon, sulfur and/or oxygen. In contrast to this approach that integrates processes on the catchment-scale, local sulfide weathering reactions can be assessed directly based on measurements of  $CO_2$  flux with the gas accumulation chambers mentioned above (Figure 1-3) (Soulet et al., 2021, 2018).

Preliminary evidence on the environmental controls on the oxidation of sulfide minerals suggests similarities to the oxidation of  $OC_{\text{petro}}$  (Hilton and West, 2020). Overall, increases in erosion rate coincide with increases in carbonate weathering by sulfuric acid (Figure 1-5), indicating that the supply of fresh sulfide minerals is a limiting factor to the weathering rate (Bufe et al., 2021; Calmels et al., 2007; Hilton and West, 2020; Torres et al., 2016).

In the weathering zone, the availability of  $O_2$  can control sulfide oxidation (Bolton et al., 2006). However, sulfide minerals can oxidize below  $OC_{\text{petro}}$  in deep weathering zones, which may be linked to a greater reactivity of minerals such as pyrite or a feasibility at lower  $O_2$  levels (Hilton et al., 2021; Petsch, 2014; Petsch et al., 2000; Tuttle and Breit, 2009; Wildman, 2004). The presence of microorganisms has the potential to significantly accelerate the oxidation of sulfide minerals (Percak-Dennett et al., 2017). Furthermore, it was shown that temperature controls the oxidation reaction, similar to  $OC_{\text{petro}}$ , with evidence from laboratory experiments (Nicholson et al., 1988) and from field-based research (Soulet et al., 2021).

Although the environmental controls on the coupled weathering of sulfides and carbonates are only partly constrained, the importance of the associated carbon release for the geological carbon cycle has been emphasized (Bufe et al., 2021; Hilton and West, 2020; Torres et al., 2014). In steep mountainous settings comprised of sedimentary rocks, the  $CO_2$  emissions from sulfide oxidation dominate over the  $CO_2$  drawdown from silicate weathering (Bufe et al.,

2021). There is now an emerging view that mountain building can act as a source of CO<sub>2</sub> to the atmosphere due to the oxidative weathering of sulfide minerals and OC<sub>petro</sub>, with the chemical composition of the exhumated rocks (e.g., igneous vs. sedimentary lithology) controlling the net carbon budget (Hilton and West, 2020).

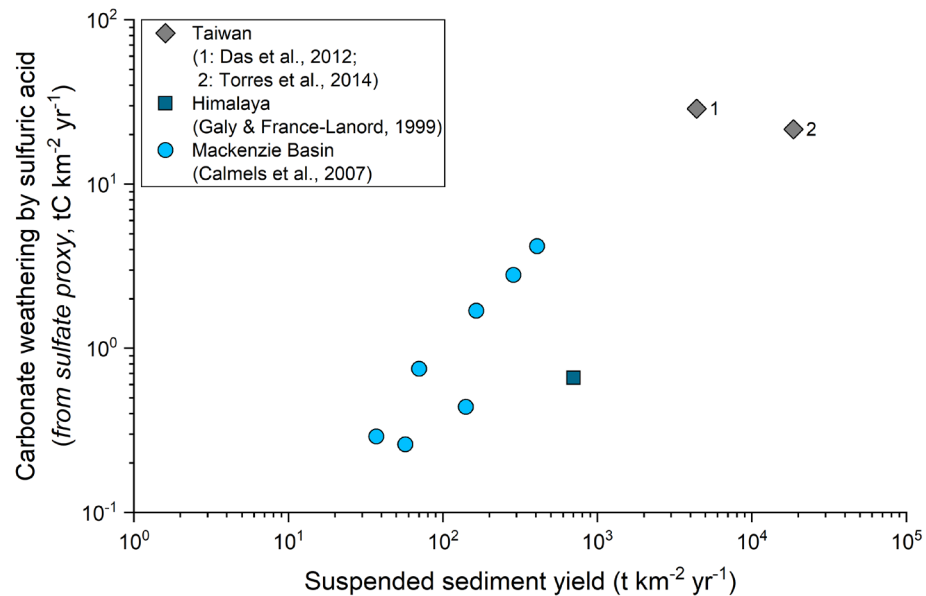


**Figure 1-5. Link of physical erosion and carbonate weathering by sulfuric acid on the catchment-scale.** Carbon fluxes from the dissolution of carbonate minerals by pyrite-derived sulfuric acid are based on partitioned riverine sulfate fluxes. The figure is modified after Hilton and West (2020).

## 1.4 Studying the critical zone

### 1.4.1 The concept of critical zone observatories

To improve the understanding of weathering processes and their role in the geological carbon cycle, it is necessary to investigate them in a holistic and interdisciplinary framework that allows a wide range of effective controls to be examined in parallel. Critical zone observatories provide such a framework. The term “critical zone” refers to a concept that extends from the upper limit of the continental vegetation down to the base of the groundwater zone (Figure 1-6A) and that integrates the entity of physical, chemical, biological and geological processes operating there (Amundson et al., 2007; Anderson et al., 2007; Brantley et al., 2007; Chorover et al., 2007; Derry and Chadwick, 2007). As an interface of lithosphere and atmosphere, the critical zone is crucial to the geological carbon cycle. The flux of materials through the critical zone (Figure 1-6B) is strongly influenced by weathering processes, resulting in the formation of chemical profiles along environmental gradients in, amongst others, mechanical stress, porosity, pore size, water content, biological agents and solution parameters, such as pH (Anderson et al.,

2007; Brantley et al., 2007). To study critical zones locally, observatories including a wide, diverse range of monitoring tools have been established globally, with the aim to improve the understanding of the architecture of the Earth surface system and its dynamics and to sustain the human habitat (Brantley et al., 2017; Gaillardet et al., 2018; Guo and Lin, 2016).

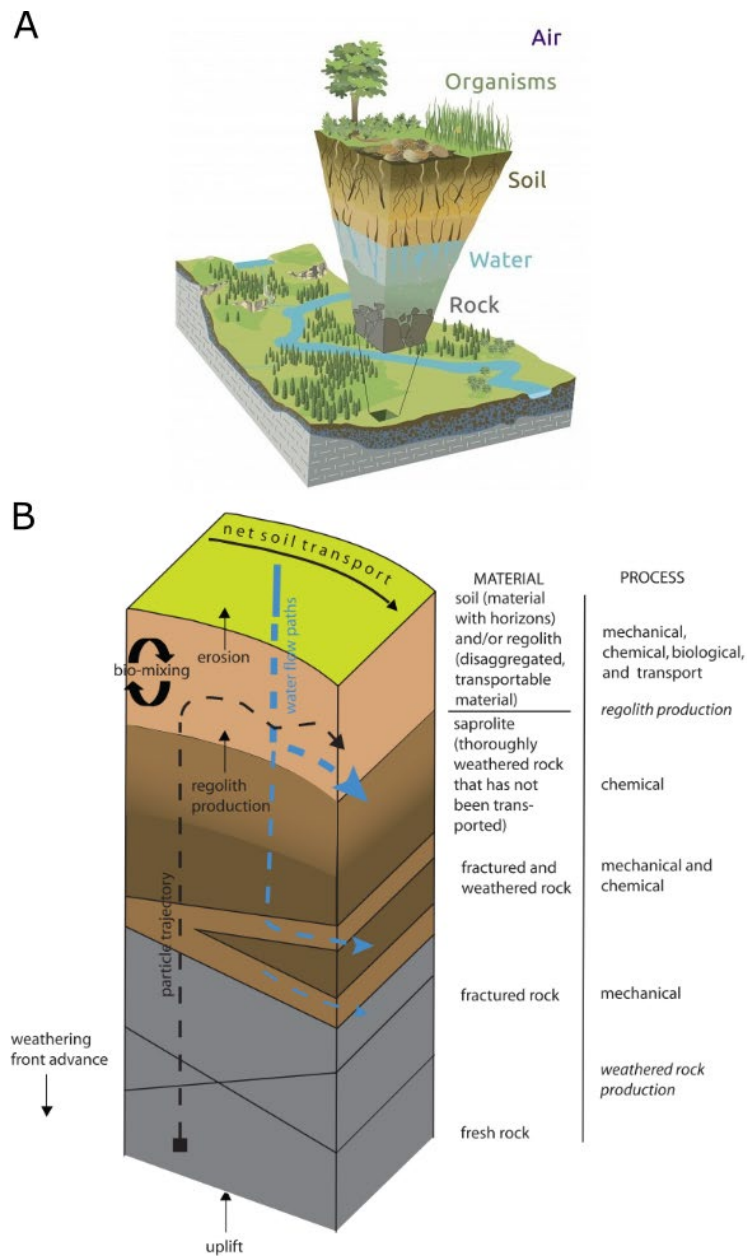


**Figure 1-6. Illustration of Earth's critical zone.** Panel A: the concept of the critical zone extends from the top of the canopy down to the base of the groundwater zone, with a coupling of physical, chemical, biological and geological processes. The figure is from Chorover et al. (2007). Panel B: material and processes in the critical zone can be summarized by vertical layering, with an upward trajectory of rock undergoing weathering in systems with minimal addition of solid material at the top. The figure is from Anderson et al. (2007).

### 1.4.2 The Draix-Bléone observatory

In large parts, this thesis presents research based at a critical zone observatory situated near the village Draix in the Bléone river-catchment in the French southern Alps and that is part of the French network of critical zone observatories (OZCAR) (Gaillardet et al., 2018). The bedrock in the Draix-Bléone observatory is comprised of Jurassic sedimentary rocks experiencing high erosion rates, and the mountainous catchments have been monitored over the last 4 decades (Figure 1-7) (Draix-Bléone Observatory, 2015; Mathys and Klotz, 2008). The data include climate variables (Draix-Bléone Observatory, 2015), near-surface hydrology (Cras et al., 2007; Mallet et al., 2020, 2018) and landcover (Carriere et al., 2020; Cras et al., 2007; Mallet et al., 2020; Mathys and Klotz, 2008). Using gauging-stations with calibrated flumes and sediment traps (Figure 1-7A), the riverine transport of bedload and suspended sediment is measured and used to determine erosion rates on the catchment-scale (Antoine et al., 1995; Carriere et al., 2020; Mathys et al., 2003). Furthermore, erosion processes and their controls have been studied *in situ* (Ariagno et al., 2022; Bechet et al., 2016, 2015; Oostwoud Wijdenes and Ergenzinger, 1998; Rovéra and Robert, 2006).

So far, weathering processes in the catchments of the Draix-Bléone observatory were assessed with chemical weathering profiles (Copard et al., 2006; Graz et al., 2011) and geophysical measurements (Esteves et al., 2005; Maquaire et al., 2002; Travelletti et al., 2012), as well as chemical analyses of river-water (Graz et al., 2012; Ogrič, 2021). For comparison, the unweathered bedrock was examined by deep boreholes (Lofi et al., 2012). Furthermore, direct measurements of CO<sub>2</sub> release from oxidative weathering were conducted at one site (Soulet et al., 2021, 2018). This previous work is a basis for more comprehensive studies on oxidative weathering processes. For example, the variety of lithological settings in the Draix-Bléone observatory (Graz et al., 2011; Mathys and Klotz, 2008) provides an opportunity to investigate differences in the chemical composition (e.g., contents of OC<sub>petro</sub>, sulfide and carbonate minerals) or in the physical properties (e.g., that control the gaseous movement of CO<sub>2</sub> and O<sub>2</sub> in the pore space) of the rocks undergoing weathering. In addition to the Draix-Bléone observatory, this research investigates weathering processes in the likewise rapidly eroding Waiapu catchment, New Zealand (Hicks et al., 2004). The sedimentary rocks outcropping in both study areas share similarities in respect to a formation in a shallow marine, epi- to peri-continental depositional environment (Janjou, 2004; Mazengarb and Speden, 2000), with significant input of terrestrial organic matter, and moderate thermal exposure during burial and subsequent uplift (Copard et al., 2006; Graz et al., 2012; Speden, 1976; Weston et al., 1988). However, while the Cretaceous rocks studied in the Waiapu catchment exhibit a similar range

of  $OC_{\text{petro}}$  (< 1 wt.%) and sulfide contents ( $\sim 0.4$  wt.%) in comparison to the lithologies in the Draix-Bléone observatory, they have significantly lower carbonate contents than the latter (Graz et al., 2011; Kenny, 1984; Leithold et al., 2006; Soulet et al., 2021; Thompson, 2009).

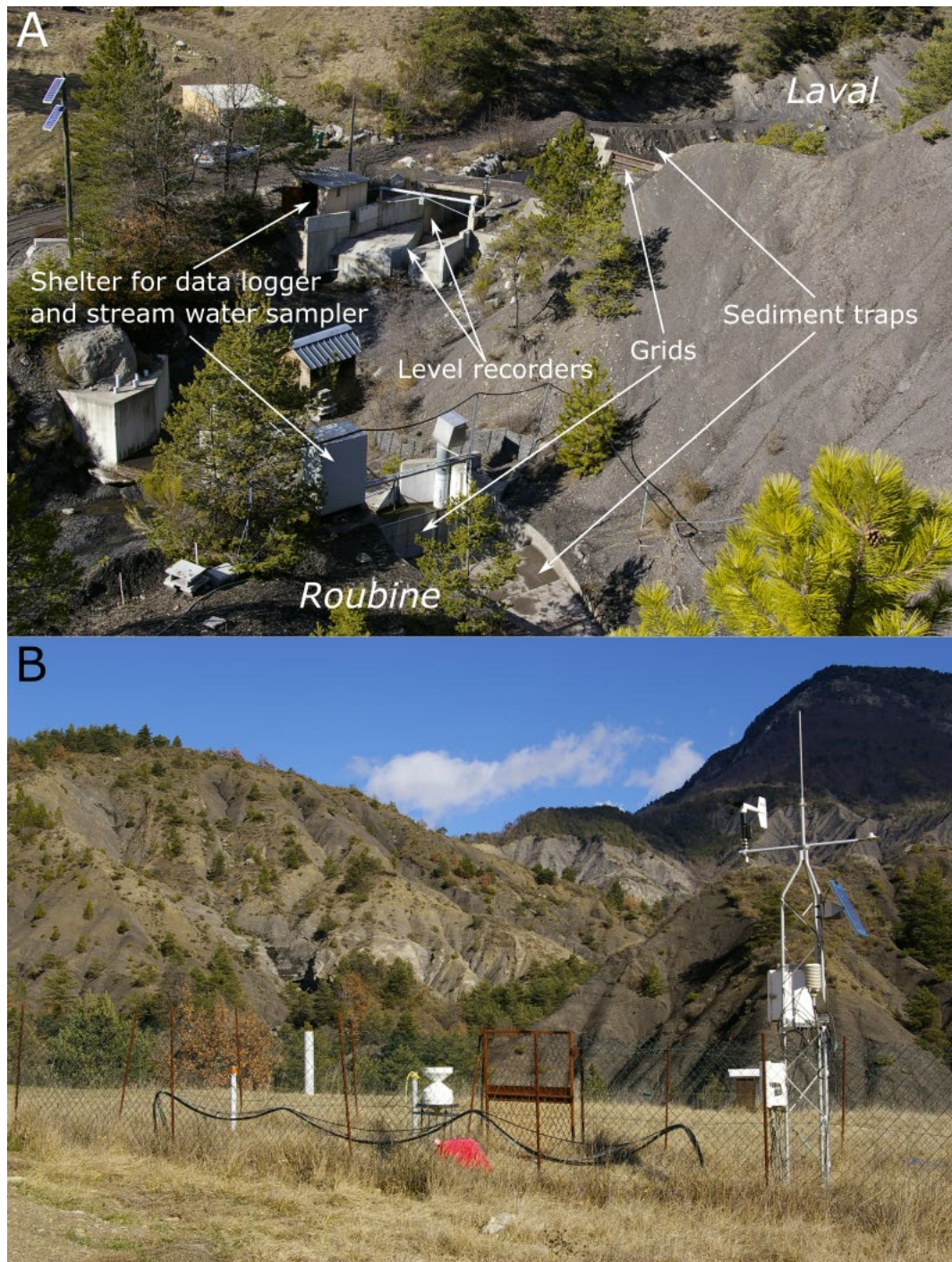


**Figure 1-7. Imagery of the Draix-Bléone observatory in the French southern Alps. Panel A: measurement stations at the outlets of the Laval and Roubine catchments for hydrology and erosion monitoring. The figure is modified after Mathys and Klotz (2008). Panel B: climatological measurement station in front of the Laval catchment extending to the gullied landscape of exposed rocks in the background. Both images are from N. Mathys (Draix-Bléone Observatory, 2015).**

## 1.5 Research aim and questions

The overall aim of this research is to improve the understanding of the release of carbon dioxide to the atmosphere during the oxidative weathering of sedimentary rocks in respect to the size, sources and environmental controls. To address this aim, three main research questions (RQs) have been identified:

- RQ1: Is it possible to quantify the gas exchange of CO<sub>2</sub> and O<sub>2</sub> during weathering of sedimentary rocks in steep terrains by direct *in situ* measurements?
- RQ2: On what timescale do significant changes of CO<sub>2</sub> release from oxidative weathering of OC<sub>petro</sub> and of sulfides in highly erosive settings occur, and how are they linked to environmental changes (e.g., in temperature and precipitation)?
- RQ3: How do differences in the chemical composition of sedimentary rocks undergoing oxidative weathering influence the weathering processes?

To respond to the RQs, the following research objectives (ROs) have been outlined:

- RO1: Conduct direct *in situ* CO<sub>2</sub> measurements at short-term (hours to several days) and long-term (multiple seasons) installations of drilled weathering chambers at multiple sites.
- RO2: Quantify the diffusive exchange of CO<sub>2</sub> and O<sub>2</sub> between the weathering chambers, surrounding rock pores and the overlaying atmosphere.
- RO3: Determine source-specific contributions from OC<sub>petro</sub> oxidation and carbonate dissolution coupled to sulfide oxidation to the bulk rock-derived CO<sub>2</sub> emission based on radiocarbon and stable carbon isotope analyses.
- RO4: Analyse the temporal and spatial variability in source-specific rock-derived CO<sub>2</sub> emissions and investigate links to environmental changes (e.g., in temperature and precipitation) for each study site.
- RO5: Compare the source-specific rock-derived CO<sub>2</sub> emissions at different sites and investigate links to the chemical composition of the studied rocks.

## 1.6 Thesis synopsis

This introduction is followed by three chapters in a self-contained style of a research paper. These works are co-authored, with contributions of each author outlined at the beginning of each chapter.

Chapter 2 explores how CO<sub>2</sub> emissions from oxidative weathering and their environmental controls can be captured using stand-alone, short-term field campaigns. In the remote and rapidly eroding Waiapu catchment, New Zealand, measurements of *in situ* CO<sub>2</sub> release, based on drilled chambers (Figure 1-3), show carbon fluxes that are high compared to other weathering processes (e.g., silicate weathering). Using radiocarbon and stable carbon analyses, it is found that the CO<sub>2</sub> fluxes are dominated by OC<sub>petro</sub> oxidation, with no evidence for carbonate-derived CO<sub>2</sub>. For this, a microbial impact on the carbon isotope composition of CO<sub>2</sub> emitted during weathering of OC<sub>petro</sub> is discussed. Over the installation, variability in CO<sub>2</sub> release is traced and explained in a framework of a quickly responding environmental regulation linked to changes in temperature and humidity. Furthermore, the effect of high CO<sub>2</sub> concentrations in the weathering zone on co-occurring silicate minerals is evaluated, with implications for the understanding of the wider geological carbon cycle.

Chapter 3 presents research conducted in two catchments of the Draix-Bléone observatory that overlay bedrocks with contrasting lithologies. Based on six fieldtrips over one full annual cycle, focus is on the gaseous exchange of CO<sub>2</sub> and O<sub>2</sub> during the oxidative weathering of black shales and marly limestones. For this, the diffusive movement of gases in the rock pore space surrounding drilled gas accumulation chambers is quantified and its variability over space and time is assessed. By doing so, the rock pore volume and rock mass that contribute to a chamber are quantified, providing a basis for upscaling bulk CO<sub>2</sub> and O<sub>2</sub> fluxes associated with oxidative weathering to the wider landscape.

Chapter 4 combines the insights from Chapter 3 with radiocarbon and stable carbon analyses of chamber-derived CO<sub>2</sub> and carbon sources in the local environment of the Draix-Bléone observatory. The source-specific CO<sub>2</sub> release from OC<sub>petro</sub> oxidation and from carbonate dissolution coupled to sulfide oxidation is quantified. Together with chemical analyses of the sedimentary rocks undergoing weathering, this allows a quantitative assessment of the role of the lithology on the geochemical fluxes in the critical zone. This environmental factor, in turn, is separated from the influence of the pronounced seasonality in weather conditions at the study sites. For this, the response of oxidative weathering reactions to temperature changes, which acts as a positive climate change feedback on geological timescales, is specified. In addition, the fate of OC<sub>petro</sub> introduced to shallow weathering zones is examined, and the importance of CO<sub>2</sub>

release in highly erosive mountainous areas for the global carbon cycle is evaluated. This is supported by a wider context including other contrasting rock types, such as the mudstones studied in Chapter 2.

Chapter 5 is the conclusions that provide i) a summary of the research presented here by responding to the main research questions; and ii) an outlook for future studies. In the end of the thesis, references to previous research or external data sources are detailed in a compilation for all chapters.

2 Capturing the short-term variability of carbon dioxide emissions from sedimentary rock weathering in a remote mountainous catchment, New Zealand



*Gully complex in the Waiapu catchment, New Zealand. May 2018 © Robert G. Hilton.*

This chapter is designed for publication in a peer-reviewed journal and is currently under review at *Chemical Geology*, with the following authors:

Tobias Roylands<sup>1</sup>, Robert G. Hilton<sup>1,†</sup>, Mark H. Garnett<sup>2</sup>, Guillaume Soulet<sup>1,3</sup>, Josephine-Anne Newton<sup>2</sup>, Joanne L. Peterkin<sup>4</sup>, Peter Hancock<sup>5</sup>.

**Affiliations:**

<sup>1</sup> Department of Geography, Durham University, South Road, Durham DH1 3LE, United Kingdom

<sup>2</sup> NEIF Radiocarbon Laboratory, Rankine Avenue, East Kilbride, Glasgow G75 0QF, United Kingdom

<sup>3</sup> Geo-Ocean, Brest University, CNRS, Ifremer, F-29280 Plouzané, France

<sup>4</sup> Department of Earth Sciences, Durham University, South Road, Durham DH1 3LE, United Kingdom

<sup>5</sup> Gisborne District Council, 15 Fitzherbert Street, PO Box 747, Gisborne 4010, New Zealand

<sup>†</sup> Present address: Department of Earth Sciences, University of Oxford, South Parks Road, Oxford OX1 3AN, United Kingdom

**Contributions:**

The research was conceptualized by TR and RGH. The main method was designed by RGH, GS and MHG. TR led the field-based measurements, under the supervision of RGH. Laboratory geochemical measurements were led by TR, MHG, JAN and JLP. Climate data was provided by PH. Formal analysis and investigation were carried out by TR, with supervision from RGH, GS and MHG. Data visualization and writing of the original draft were conducted by TR, with help from RGH. All co-authors contributed to subsequent review and editing. Funding was acquired by RGH.

All co-authors confirmed that they agree with the work to be included in this thesis.

## 2.1 Abstract

Weathering of organic carbon contained in sedimentary rocks (petrogenic OC, OC<sub>petro</sub>) is an important control on the concentrations of carbon dioxide (CO<sub>2</sub>) and oxygen in the atmosphere. Of particular significance are steep mountainous catchments, where high rates of physical erosion introduce OC<sub>petro</sub> to the surface, where oxygen in air and water can help drive oxidative weathering reactions, yet measurements of CO<sub>2</sub> emissions from OC<sub>petro</sub> oxidation are still scarce. Here, we show that CO<sub>2</sub> fluxes, and their environmental controls, can be determined using *in situ* accumulation chambers during a stand-alone, short-term (8 days) field campaign, applied to a remote setting. In the rapidly eroding Waiapu River catchment, New Zealand, dominated by mudstones, we measured high rates of CO<sub>2</sub> release (222 mgC m<sup>-2</sup> d<sup>-1</sup> – 1,590 mgC m<sup>-2</sup> d<sup>-1</sup>) in five accumulation chambers in the near-surface of naturally fractured and bedded rock outcrops. The corresponding CO<sub>2</sub> concentrations are very high ( $p\text{CO}_2 \sim 4,700 \text{ ppmv} - 27,100 \text{ ppmv}$ ), and such values could influence acid-hydrolysis reactions during chemical weathering of co-occurring silicate minerals. The CO<sub>2</sub> is radiocarbon depleted (fraction modern,  $F^{14}\text{C} = 0.0122 - 0.0547$ ), confirming it is petrogenic in origin. Stable carbon isotopes suggest a source from OC<sub>petro</sub>, but  $\delta^{13}\text{C}$  values of the CO<sub>2</sub> are lower by  $\sim 3.6 \pm 0.1 \text{ ‰}$  from those of OC<sub>petro</sub> ( $-25.9 \pm 0.1 \text{ ‰}$ ), consistent with isotope fractionation associated with microbial respiration of OC<sub>petro</sub>. Over six days of measurement, we find that CO<sub>2</sub> fluxes respond quickly to changes in temperature and humidity, indicating an environmental regulation that is captured by our short-term installation. The approaches applied here mean that future research can now seek to constrain the climatic, lithological and biological controls on OC<sub>petro</sub> oxidation across regional to global scales.

## 2.2 Introduction

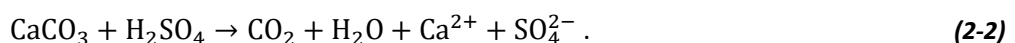
Earth's sedimentary rocks contain around 130,000 times more carbon ( $\sim 75 \times 10^9$  Mt) than the pre-industrial atmosphere, of which  $\sim 80\%$  are present in the form of inorganic minerals (carbonates) and  $\sim 20\%$  organic carbon (OC<sub>petro</sub>), respectively (Petsch, 2014). Over geological timescales, small changes in the balance between the deposition of sedimentary carbon and its weathering on land can alter the concentration of carbon dioxide and oxygen (O<sub>2</sub>) in the atmosphere (Bernier, 1999; Sundquist and Visser, 2003). These govern the planet's habitability, climate and composition of the oceans and atmosphere (Bergman et al., 2004; Bernier, 2004).

Steep mountainous areas are responsible for more than half of the planet's denudation, with rapid rates of physical erosion and chemical weathering (Larsen et al., 2014). As such, these locations are important for the global exchange of carbon between rocks and the atmosphere (Hilton and West, 2020). In terms of silicate weathering by carbonic acid, which acts as a carbon sink when the weathering products are coupled to the precipitation of new carbonate minerals (Bernier, 1999; Chamberlin, 1899; Walker et al., 1981), erosive settings can have high weathering fluxes (Larsen et al., 2014; Milliman and Syvitski, 1992), but more importantly are where the climate-sensitivity of silicate weathering is most pronounced (Maher and Chamberlain, 2014; West et al., 2005). They are also places where the erosion of organic carbon from the biosphere can be rapid (Galy et al., 2015; Hilton, 2017), which, when coupled to burial, acts as a CO<sub>2</sub> sink (Bernier, 1999). However, it is increasingly recognized that, depending on the lithological composition, oxidative weathering reactions can lead to a CO<sub>2</sub> release (Calmels et al., 2007; Hilton et al., 2014; Petsch, 2014; Torres et al., 2014) that can dominate the net rock-atmosphere exchange of CO<sub>2</sub> during weathering and erosion (Hilton and West, 2020).

During chemical weathering, the oxidation of OC<sub>petro</sub> produces CO<sub>2</sub> and consumes O<sub>2</sub>, so-called georespiration (Bernier, 1999; Keller and Bacon, 1998; Petsch, 2014):



Another source of CO<sub>2</sub> during chemical weathering can be via the oxidation of sulfide minerals (Calmels et al., 2007; Li et al., 2008; Torres et al., 2014). In this process, sulfuric acid released from the oxidation of sulfides (e.g., pyrite) can lead to *in situ* emission of CO<sub>2</sub> by dissolving neighbouring carbonates:



Alternatively, the CO<sub>2</sub> can be released elsewhere (e.g., by impacting the carbonate system of stream and river water) and when considering the timescale of carbonate precipitation in the oceans (~ 10<sup>6</sup> yr) (Berner, 2004). This can be described by the equations



and



The global CO<sub>2</sub> fluxes derived from oxidative weathering are known well enough to be recognized as important players in the geological carbon cycle (Hilton and West, 2020), with estimates of OC<sub>petro</sub> oxidation (40 MtC yr<sup>-1</sup> – 100 MtC yr<sup>-1</sup>) (Petsch, 2014) and sulfide oxidation (31 MtC yr<sup>-1</sup> – 36 MtC yr<sup>-1</sup>) (Berner and Berner, 2012; Burke et al., 2018) comparable in size to the CO<sub>2</sub> drawdown by silicate weathering (90 MtC yr<sup>-1</sup> – 140 MtC yr<sup>-1</sup>) (Gaillardet et al., 1999; Moon et al., 2014). Previous research has suggested that oxidative weathering is controlled by various environmental factors, such as temperature, oxygen availability, hydrology, erosion rates and lithology (Bolton et al., 2006; Chang and Berner, 1999; Hemingway et al., 2019; Hilton et al., 2014; Soulet et al., 2021). However, they are not well constrained compared to the analogous controls of silicate weathering (Maher and Chamberlain, 2014; Walker et al., 1981; West et al., 2005). In addition, rock weathering can be affected by microorganisms, which can form biofilms around minerals contributing to and accelerating their breakdown (Ehrlich et al., 2015). This seems to be true for oxidative weathering of sedimentary organic matter, with a growing body of work highlighting the potential for microbes to thrive on and incorporate OC<sub>petro</sub>, with evidence from weathering profiles and laboratory incubations (Bardgett et al., 2007; Berlendis et al., 2014; Matlakowska and Sklodowska, 2011; Petsch et al., 2001; Seifert et al., 2013, 2011). Despite the potential of microorganisms to enzymatically influence the oxidation of OC<sub>petro</sub>, it is unknown how the net weathering rate and CO<sub>2</sub> release are affected in natural environments (Hemingway et al., 2018; Stasiuk et al., 2017; Włodarczyk et al., 2018).

Research addressing the fate of sedimentary organic carbon undergoing weathering has so far focused mostly on indirect approaches, using river data that describe the export of OC<sub>petro</sub> from a catchment, which can be used to estimate the amount of organic matter that escapes oxidation (Bouchez et al., 2010; Hilton et al., 2011), or trace element proxies have been applied at the river catchment scale (e.g., Dalai et al., 2002; Hilton et al., 2014). However, this scale of investigation cannot directly track the reactions *in situ*, thus obscuring how biogeochemical processes and environmental variables, such as temperature, control oxidative weathering processes. In order to better understand regional and global patterns of oxidative weathering and their environmental controls, we require measurements from a variety of settings (Longbottom and Hockaday, 2019). *In situ* measurements of CO<sub>2</sub> emissions that identify a rock-

derived component have only been reported from two sites (Keller and Bacon, 1998; Soulet et al., 2021, 2018). Following the method described by Soulet et al. (2018), rock-derived CO<sub>2</sub> can be differentiated from modern sources (such as soils or the atmosphere) using radiocarbon analyses, whereas radiocarbon-free contributions from OC<sub>petro</sub> and sulfide oxidation coupled to carbonate dissolution can be partitioned using the stable carbon isotope compositions.

Here we explore whether CO<sub>2</sub> emissions from oxidative weathering and their environmental controls can be captured using stand-alone, short-term field campaigns. We do this by installing *in situ* weathering chambers in the remote and rapidly eroding Waiapu catchment, New Zealand. In this area, OC<sub>petro</sub>-bearing rocks are widespread (Leithold et al., 2006; Thompson, 2009) and the physical erosion rates are well described (Hicks et al., 2004; Marden et al., 2012; Parkner et al., 2006), supplying OC<sub>petro</sub> to the weathering zone. We measure CO<sub>2</sub> fluxes that appear rapid when compared to other weathering fluxes (e.g., silicate weathering) and approach values of soil respiration. In contrast to the only other study of this type (Soulet et al., 2021, 2018), we find that the CO<sub>2</sub> fluxes are dominated by OC<sub>petro</sub> oxidation, with no evidence for carbonate-derived CO<sub>2</sub>. The OC<sub>petro</sub> weathering fluxes vary over the installation, and we explore how this variability can be explained by changes in precipitation/hydrology and temperature. In addition, the potential microbial impact on the oxidation of OC<sub>petro</sub> and the carbon isotope composition of emitted CO<sub>2</sub> is discussed. Finally, we examine the wider implications for the understanding of Earth's geological carbon cycle including the weathering of silicate minerals in sedimentary rocks.

## 2.3 Material and methods

### 2.3.1 Study site

The study site (37.85986° S, 178.19028° E) is located within the Waiapu River catchment, North Island, New Zealand (Figure 2-1), situated on the active margin of the converging Pacific and Australian plates and part of the Hikurangi Accretionary Prism (Shulmeister, 2017). This setting is characterized by tectonic uplift of ~ 4 mm yr<sup>-1</sup> in the Late Quaternary (Litchfield and Berryman, 2006) and the tectonic setting results in active fault systems and occasional methane gas and oil seeps in the region (Reyes et al., 2010). Generally, the lithology of the Waiapu catchment is dominated by intensely deformed Cretaceous and Tertiary sedimentary rocks (Mazengarb and Speden, 2000).

In the Northeast of New Zealand, several stations for environmental monitoring are run by the Gisborne District Council including data records on air temperature, rainfall and river flow for the Waiapu catchment (Figure 2-1). The mean annual rainfall is ~ 2 m yr<sup>-1</sup> in a temperate

maritime climate where storms arrive from the tropics around once to twice a year (Chappell, 2016). The combination of these intense rainfall events with easily erodible rocks and high rates of tectonic uplift result in high erosion rates, which have been further increased due to widespread deforestation in the late nineteenth and early twentieth century (Hicks et al., 2004; Marden et al., 2012; Parkner et al., 2006). In the Waiapu River basin, a fifth of the terrain is susceptible to gully erosion and sediment is generated primarily by mass movement processes following oversteepening of gully sidewalls by channel incision, leading to a very high suspended sediment yield of 17,800 t km<sup>-2</sup> yr<sup>-1</sup> (Betts et al., 2003; Hicks et al., 2004). Taking the bedrock density into account, an average erosion rate of ~ 7 mm yr<sup>-1</sup> can be estimated for the Waiapu catchment, indicating short residence times of the abundant exposed bedrock and regolith (Leithold et al., 2006). Chemical weathering fluxes are constrained by long-term discharge data and spot river samples (Lyons et al., 2005), and they are very high (400 t km<sup>-2</sup> yr<sup>-1</sup>), with silicate weathering (1.9 × 10<sup>5</sup> mol km<sup>-2</sup> yr<sup>-1</sup>, total cation yield from silicate minerals) slightly dominating over carbonate weathering (1.2 × 10<sup>5</sup> mol km<sup>-2</sup> yr<sup>-1</sup>, Ca<sup>2+</sup> yield from carbonate minerals).

Our site is located in one of the large gully complexes (0.37 km<sup>2</sup>) that drains into the Tapuaeroa River (Figure 2-1). It is underlain by Early Cretaceous mudstones of the Mokoivi Formation (Ruatoria Group) and part of the Miocene East Coast Allochthon (Mazengarb and Speden, 2000). No gas or oil seep occurs in close proximity to the study site (Francis et al., 1991; Reyes et al., 2010; Scadden et al., 2016). Measurements of rocks from this region (Thompson, 2009) and the stable carbon isotope composition and radiocarbon activity of suspended sediments in the Waiapu River show OC<sub>petro</sub> is widespread in the catchment (Leithold et al., 2006), with a concentration of ~ 0.4 wt.% to 0.5 wt.% in river sediments (Hilton, 2017).

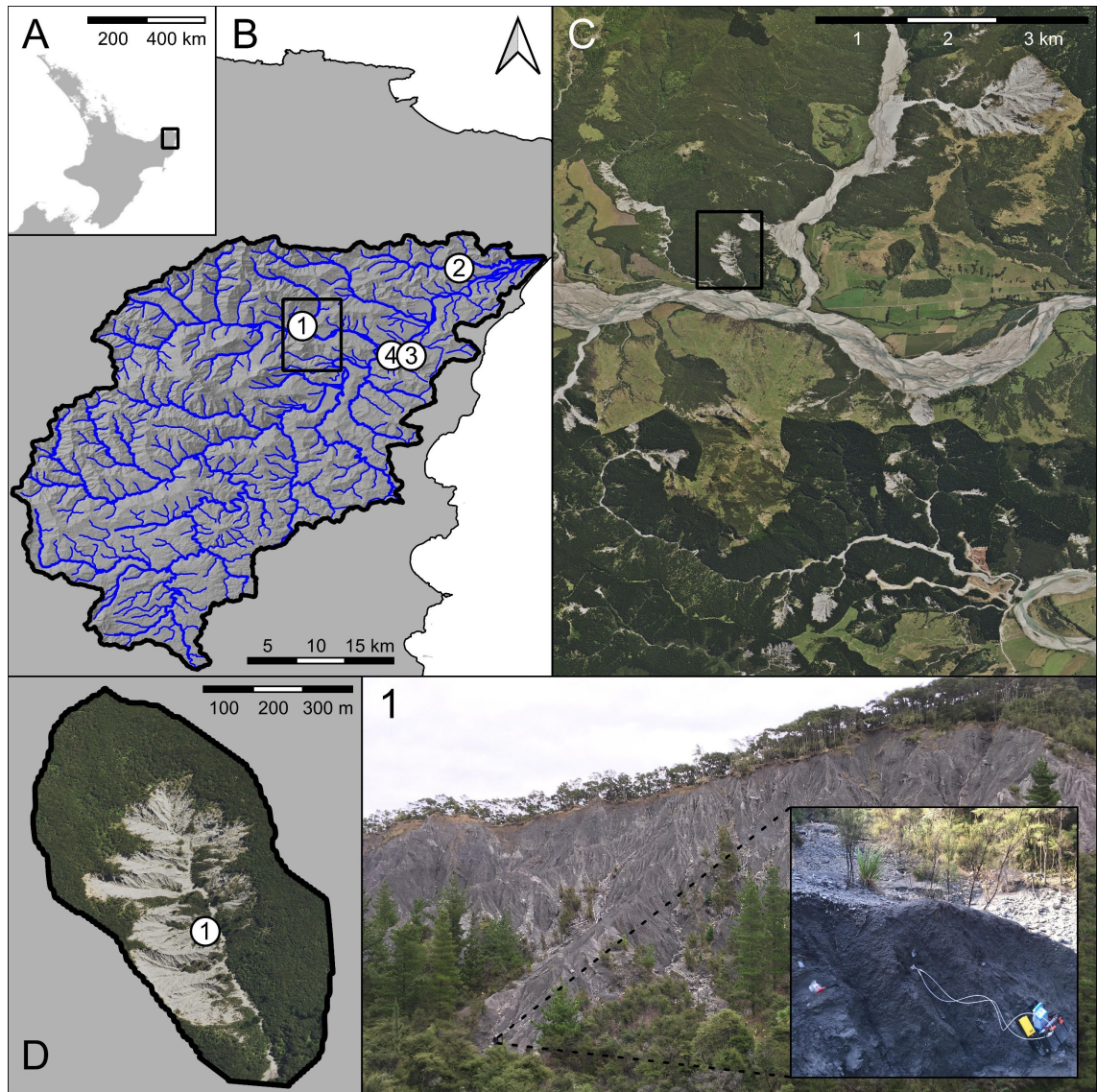


**Figure 2-1. Map and imagery of the study area.** Panel A: location of the Waiapu catchment in the Northeast of New Zealand. Panel B: location of the study site (1) and environmental monitoring stations in the Waiapu catchment: Poroporo Fire Station for air temperatures (2), Ruatoria Telemetry Station for rainfall data (3), and Rotokautuku Bridge for Waiapu River flow (4). Panel C: exposed rocks and regolith occur frequently in the surrounding of the study area. Panel D: location of the experimental setup (1) in a rapidly eroding gully complex. Panels A to D are based on data and satellite imagery provided from the Land Information New Zealand (LINZ) Data Service under the Creative Commons Attribution 4.0 International License.

## 2.3.2 CO<sub>2</sub> measurements

### 2.3.2.1 *In situ* weathering chambers

We installed gas accumulation chambers directly into rock outcrops undergoing weathering (Figure 2-1) following the design established by Soulet et al. (2018). In summary, weathering chambers were drilled horizontally into the exposed rock face which was cleared of loose material beforehand. Their elongated cylinder-like shape ensures a large ratio of surface to volume that benefits CO<sub>2</sub> flux measurements and allows gases to be trapped for isotope analysis (Table 2-1). In order to install the chambers, we used a hand auger with a diameter of 2.6 cm. Then, a small PVC tube is inserted in the entrance of each chamber and closed with a rubber stopper holding two glass tubes fitted with Tygon® tubing, which allows either connection to a gas-sampling system or closure with WeLock® clips to isolate the chamber from the atmosphere. In addition, the intersection of the PVC tube and the surrounding rock is sealed with silicone sealant (Selleys Wet Area Silicone). In this design, the gas exchange between the chamber headspace and the rock pore space happens over the surface of the inner wall of the chamber (Soulet et al., 2018).

We installed seven chambers which were distributed evenly over a transect of ~ 10 m length in a small gully that was free of vegetation or soil (Figure 2-1). A thermocouple meter (Digi-Sense), which was externally calibrated in the range of 5 °C – 25 °C, was placed inside one of the chambers to measure the internal temperature. Another chamber was installed as a back-up in case one was lost, for example, in the event of structural collapse. Four of the chambers had similar depths, but H7 was notably shorter (Table 2-1), which reflected a refusal depth of the hand drill. The chamber array started with H4 at 1.5 m elevation above the riverbed in which the gully drained, followed by H3, H5, H7, and H2 at 4.5 m elevation at the top of the transect, respectively (Table 2-1). The elevation was estimated to the nearest 1 m with a digital elevation model (8 m spatial resolution; Land Information New Zealand (LINZ) Data Service under the Creative Commons Attribution 4.0 International License), verified with GPS-derived altitude measurements, and estimated to the nearest 10 cm with scaled imagery taken in the field.

In addition, we collected rock powder from the drilling of the chambers and stored it in pre-combusted glass vials (4 h at 450 °C) at 4 °C (apart from transport) until freeze-drying.

**Table 2-1. Properties of gas accumulation chambers drilled into weathering sedimentary rocks in the Waiapu catchment, New Zealand.**

Chamber	Elevation above riverbed (m)	Installation date	Depth (cm)	Volume (cm <sup>3</sup> )	Area of exchange with surrounding rock (cm <sup>2</sup> )
H2	4.5	28/04/2018	42	227	334
H3	1.8	28/04/2018	43	229	336
H4	1.5	28/04/2018	44	237	344
H5	2.1	29/04/2018	48	269	361
H7	3.2	29/04/2018	12	64	79

### 2.3.2.2 Rock $p\text{CO}_2$ measurements

The concentrations of CO<sub>2</sub> in the chambers ( $p\text{CO}_2$ ) were measured using an infra-red gas analyser (EGM 5 Portable CO<sub>2</sub> Gas Analyser, PP Systems), which is equipped with an internal pump and calibrated to a  $p\text{CO}_2$  in the range of 0 ppmv to 30,000 ppmv, connected to a closed-loop CO<sub>2</sub> sampling system incorporating a CO<sub>2</sub> scrub (soda lime) and a water trap (magnesium perchlorate) as described by Hardie et al. (2005). Before measuring the CO<sub>2</sub> flux in a chamber, the ambient  $p\text{CO}_2$  was determined by connecting the purged, CO<sub>2</sub>-free sampling system to a chamber that was left closed overnight so that the CO<sub>2</sub> concentration in the surrounding rock pores and the chamber equilibrated. After a short equilibration, the rock  $p\text{CO}_2$  can be calculated from the measured CO<sub>2</sub> concentration in the combined air volume of the chamber and the sampling system by accounting for the dilution introduced from the CO<sub>2</sub>-free air that was originally contained within the sampling system (Soulet et al., 2018).

### 2.3.2.3 CO<sub>2</sub> flux measurements

Flux measurements of CO<sub>2</sub> from *in situ* weathering chambers have been described in detail previously (Soulet et al., 2018). In summary, the accumulation of CO<sub>2</sub> can be recorded over time after lowering the  $p\text{CO}_2$  to a near-atmospheric value by the CO<sub>2</sub> scrub or a zeolite sieve (Section 2.3.2.4) mounted in parallel to the CO<sub>2</sub> monitoring line. One flux measurement consists of a series of repeatedly monitored CO<sub>2</sub> accumulations over ~ 6 min that are separated by short periods where the CO<sub>2</sub> is removed from the chamber to near-atmospheric values. The rate of CO<sub>2</sub> accumulation is then calculated by fitting an exponential model to the recorded  $p\text{CO}_2$  change (Pirk et al., 2016), which considers the diffusivity of carbon from the rock to the chamber and the chamber leakiness (Soulet et al., 2018). The first three repeats are not used in the calculation of the flux, but instead to purge the CO<sub>2</sub> in the rock pores surrounding the chamber. A further three repeats are used to determine an average rate of CO<sub>2</sub> accumulation and its standard deviation. This flux is reported as the CO<sub>2</sub> accumulation rate normalized to the surface

area of exchange with the surrounding rock to account for differences in the depth of the chambers that are related to differences in volume and surface area (Table 2-1).

#### 2.3.2.4 CO<sub>2</sub> sampling and isotopic analyses

The CO<sub>2</sub> accumulations of a flux measurement can be sampled by circulating the chamber air through a zeolite molecular sieve sampling cartridge mounted in parallel to the CO<sub>2</sub> monitoring line (Hardie et al., 2005). In the chambers, CO<sub>2</sub> was sampled between day 5 (02/05/2018) and day 8 (05/05/2018) of the trip, and a total of 10 samples was collected. To yield a sufficient amount of CO<sub>2</sub> for isotopic analyses, a greater number of repeats was sampled for some measurements with lower fluxes. The volume of carbon loaded onto the sieves was quantified by adding up the *p*CO<sub>2</sub> maxima of the repeated accumulations of a flux measurement minus the near-atmospheric value (lower boundary of an accumulation) while accounting for the combined volume of the chamber and the sampling system.

The gas trapped onto the zeolite sieves was recovered in the laboratory by heating to 425 °C, while purging with high-purity nitrogen gas. The CO<sub>2</sub> was purified cryogenically under vacuum and its volume quantified (Garnett et al., 2019; Garnett and Murray, 2013). The stable carbon isotope composition of the CO<sub>2</sub> was measured using Isotope Ratio Mass Spectrometry (IRMS; Thermo Fisher Delta V). The results are reported in standard delta (δ) notation in per mil (‰) relative to Vienna Pee Dee Belemnite (VPDB) standard. To determine the radiocarbon activity of CO<sub>2</sub>, aliquots were graphitized by iron/zinc reduction and measured with Accelerator Mass Spectrometry at the Scottish Universities Environmental Research Centre (SUERC). Radiocarbon measurements were corrected for isotopic fractionation using the sample-specific δ<sup>13</sup>C value and reported in the form of the fraction modern (i.e., in the F<sup>14</sup>C notation) (Reimer et al., 2004; Stuiver and Polach, 1977).

In addition, an atmospheric CO<sub>2</sub> sample was collected by circulating the atmosphere sampled at ~ 3 m above ground through a zeolite molecular sieve using the CO<sub>2</sub> sampling system and analysed for its stable carbon isotope composition as described above.

#### 2.3.3 Bulk geochemistry

The rock powder collected during the drilling of the accumulation chambers was analysed for its bulk geochemical composition. After freeze-drying, it was ground and homogenized using a pestle and mortar. The stable carbon isotope composition of organic carbon and its content were obtained using an Elemental Analyser (Costech) coupled to an IRMS (Thermo Fisher Delta V Advantage) after inorganic carbon removal from the samples with aqueous HCl (4 mol L<sup>-1</sup>). In summary, a known sample mass was weighed into pre-combusted silver capsules (combusted at 450 °C within a week of analysis) loaded into a Teflon tray, with

acid added to each capsule and then placed in the oven at 80 °C until the liquid was evaporated (~ 2 h), and the acid step and drying repeated twice. Capsules were folded closed prior to analysis. The stable carbon isotope composition of inorganic carbon and its content were measured with a carbonate dissolution device (Thermo Scientific Gas Bench II) coupled to an IRMS (Thermo Scientific MAT 253). Furthermore, total sulfur measurements were performed with an Elemental Analyser (Costech) coupled to an IRMS (Thermo Fisher Delta V Plus). Both stable carbon isotope compositions are reported in standard delta ( $\delta$ ) notation in per mil (‰) relative to Vienna Pee Dee Belemnite (VPDB) standard, whereas carbon and sulfur contents are reported in % weight.

Because the studied rocks are of Cretaceous origin, they should not contain any radiocarbon. We assume that their F<sup>14</sup>C values are zero when studying the carbon isotope mass balance in the weathering zone (Equation 2-5) (Soulet et al., 2018).

## 2.4 Results

### 2.4.1 Bulk geochemistry

The rocks of the Mokoivi Formation are characterized by an average organic carbon concentration of  $0.76 \pm 0.23$  wt.% ( $\pm$  standard deviation, unless otherwise stated), with a  $\delta^{13}\text{C}$  of  $-25.9 \pm 0.1$  ‰. In contrast, for most of the rock samples, the inorganic carbon content was below the detection threshold (0.1 wt.%). For the remaining samples, they had inorganic carbon concentrations of  $0.17 \pm 0.06$  wt.% with a  $\delta^{13}\text{C}$  of  $-10.7 \pm 0.1$  ‰. This  $\delta^{13}\text{C}$  value is significantly more negative than typical  $\delta^{13}\text{C}$  values from Early Cretaceous marine carbonates ranging between  $\sim 0$  ‰ and  $+5$  ‰ (Erba, 2004; Gröcke et al., 2003; Weissert et al., 1998). This discrepancy could be the result of diagenesis and tectonic deformation of carbonate concretions, which are widespread in several outcropping lithologies in the Waiapu catchment (Mazengarb and Speden, 2000), and which occur with a wide range of  $\delta^{13}\text{C}$  values between  $-50$  ‰ and  $+15$  ‰ in Cretaceous and Cenozoic rocks in New Zealand (Nelson and Smith, 1996; Pearson and Nelson, 2005). Furthermore, total sulfur measurements revealed a content of  $0.33 \pm 0.04$  wt.%.

### 2.4.2 Environmental variables

The start of the field trip coincided with a storm event in the Waiapu catchment, which delivered  $\sim 45$  mm rainfall within three days, and resulted in an increase in the water discharge of the Waiapu River and its tributaries (Figure 2-2A). This peaked on 30/04/2018. The chambers were installed between 28/04/2018 and 29/04/2018 (Table 2-1). In the following days, no significant precipitation occurred and the bare surface of the studied mudstones dried visibly.

Over the six days of CO<sub>2</sub> measurements and the two days before, significant changes in air temperatures were recorded ranging from 9.5 °C to 19.9 °C at the Poroporo Fire station (~ 18 km from the site at ~ 164 m.a.s.l.) (Figure 2-2B). The temperature record at Poroporo Fire station closely mirrors that measured in the rock face (dummy accumulation chamber at ~ 160 m.a.s.l.). Due to the short and incomplete character of the latter, this study benefits from including the more detailed air temperature record. The agreement between the datasets is best when considering a lag of around 2 h from the Poroporo Fire station to the rock chamber (Figure 2-3).

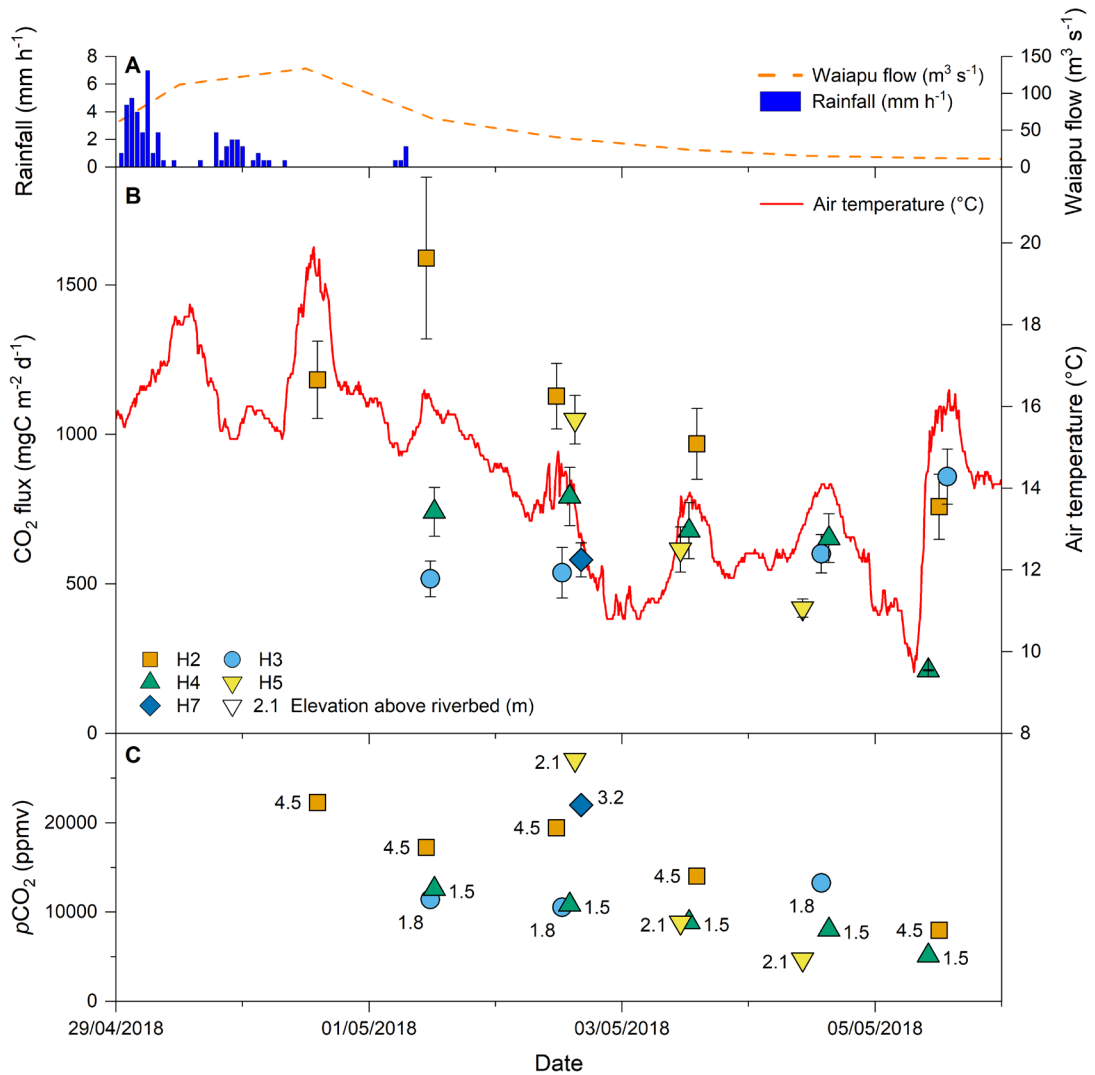


**Figure 2-2. Time series of carbon dioxide fluxes and partial pressures alongside environmental variables.** Panel A: rainfall and flow of the Waiapu River. Panel B: CO<sub>2</sub> fluxes ( $\pm$  standard deviation) from in situ weathering chambers alongside air temperature. Panel C: pCO<sub>2</sub> measured prior to each flux measurement. The elevation of the chambers above the riverbed (m) is denoted next to each pCO<sub>2</sub> symbol.

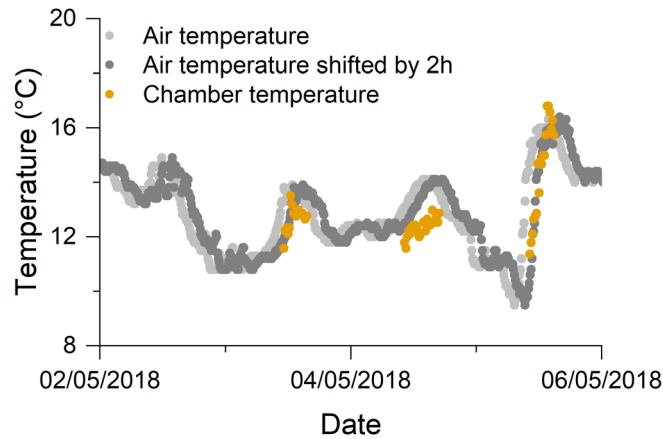


**Figure 2-3. Time series of air temperatures and chamber temperatures.** Temperatures within the weathering chambers can be described by shifting the air temperature record by 2 h for three tested intervals.

### 2.4.3 CO<sub>2</sub> fluxes

Over the sampling period, the measured CO<sub>2</sub> fluxes varied between the gas accumulation chambers, and over time at each single chamber (Figure 2-2B). Overall, the CO<sub>2</sub> fluxes ranged between 222 mgC m<sup>-2</sup> d<sup>-1</sup> and 1,590 mgC m<sup>-2</sup> d<sup>-1</sup> (Table 2-2), with fluxes in each chamber varying by, on average, a factor of  $2.5 \pm 0.8$ .

**Table 2-2. Summary table of CO<sub>2</sub> fluxes.** Standard deviations (SD) for the smallest and the largest flux measured at each chamber are reflecting the uncertainty of a single flux measurement, which consists of a series of repeated accumulations. The standard deviation for the average flux at each chamber is based on the average rate of accumulation for each flux measurement.

Chamber	Average flux (mgC m <sup>-2</sup> d <sup>-1</sup> ± SD)	Minimum flux (mgC m <sup>-2</sup> d <sup>-1</sup> ± SD)	Maximum flux (mgC m <sup>-2</sup> d <sup>-1</sup> ± SD)
H2	1,125 ± 275 (n=5)	758 ± 109	1,590 ± 270
H3	662 ± 144 (n=4)	544 ± 63	904 ± 97
H4	647 ± 219 (n=5)	222 ± 2	834 ± 102
H5	731 ± 277 (n=3)	441 ± 32	1,105 ± 86
H7	611 (n=1)		

The CO<sub>2</sub> fluxes of the chambers in the studied gully complex were broadly correlated with their elevation above the riverbed (Figure 2-4). Chamber H2 recorded the highest fluxes, on average, while the chambers H4 and H7 had the lowest fluxes on average. Overall, the data reveal a positive relationship ( $R^2 = 0.40$ ,  $p = 0.005$ ,  $n = 18$ ; Figure 2-4). The correlation is weaker when the measurements made before the 03/05/2018 (first 3 days following the storm event) are excluded from this comparison ( $R^2 = 0.25$ ,  $p = 0.170$ ,  $n = 9$ ).

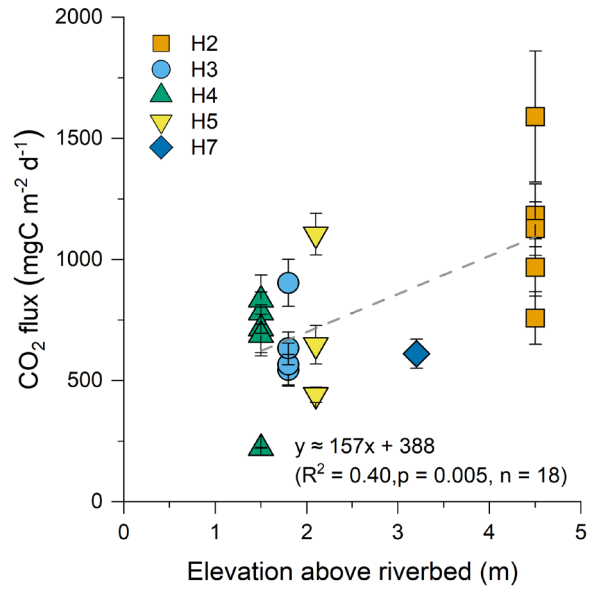


**Figure 2-4. Carbon dioxide flux from weathering chambers versus their elevation above the riverbed.** CO<sub>2</sub> fluxes and their standard deviation are shown from five in situ weathering chambers as a linear function of the chamber elevation above the riverbed.

The CO<sub>2</sub> fluxes were broadly linearly correlated with instantaneous air temperature at the start of each measurement ( $R^2 = 0.17$ ,  $p = 0.091$ ,  $n = 18$ ; Figure 2-5A). This correlation is improved using the average temperature of the last 24 h before a measurement ( $R^2 = 0.22$ ,  $p = 0.049$ ,  $n = 18$ ; Figure 2-5B), and further improved when considering a lag of 2 h from the timing of the CO<sub>2</sub> flux measurement and the air temperature ( $R^2 = 0.35$ ,  $p = 0.010$ ,  $n = 18$ ; Figure 2-5C). This is the same lag found between the air temperature record and the rock chambers (Figure 2-3). Furthermore, when the measurements made before the 03/05/2018 are excluded (first 3 days following the storm event) the correlation between CO<sub>2</sub> fluxes and air temperature is further improved ( $R^2 = 0.67$ ,  $p = 0.007$ ,  $n = 9$ ; Figure 2-5D).

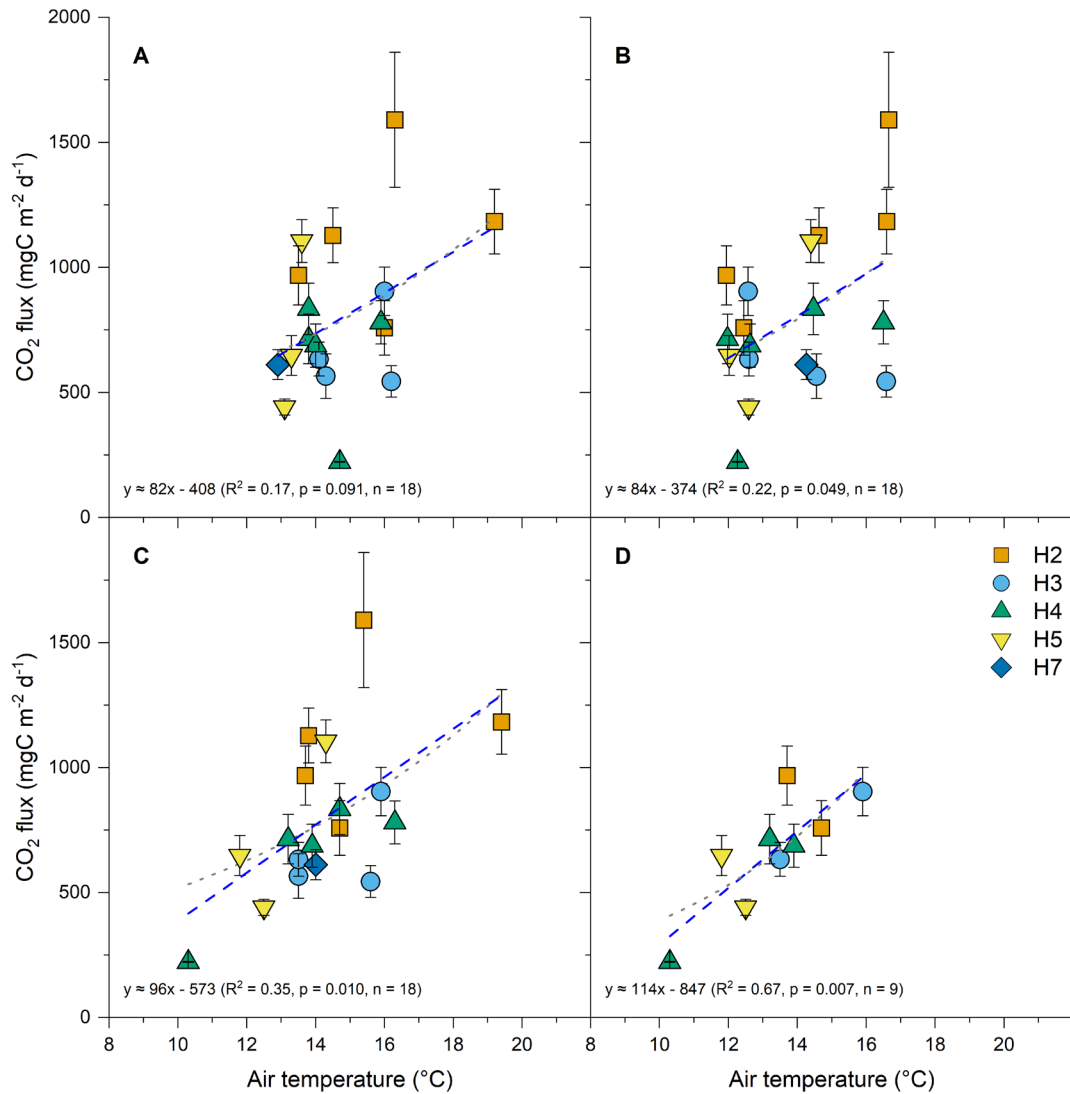


**Figure 2-5. Carbon dioxide flux versus temperature.** CO<sub>2</sub> fluxes and their standard deviation are shown from five in situ weathering chambers as a function of the air temperature record treated in different ways. Panel A: all measurements versus the air temperature at the start of each measurement. Panel B: all measurements versus the average air temperature over the last 24 h of a measurement. Panel C: all measurements versus the air temperature delayed by 2 h from the timing of each measurement. Panel D: CO<sub>2</sub> fluxes without measurements made before the 03/05/2018 (excluding the first 3 days following the storm event) versus the air temperature delayed by 2 h from the timing of each measurement. Details of linear functions (dashed blue lines) are given in each panel. As an alternative (Section 2.5.2.2), exponential functions (dotted grey lines) are delineated in the background.

#### 2.4.4 Rock chamber $p\text{CO}_2$

The measured rock  $p\text{CO}_2$  varied between the gas accumulation chambers and over time (Figure 2-2C). Overall, the  $p\text{CO}_2$  values ranged between  $\sim 4,700$  ppmv and 27,100 ppmv with an average temporal variability for a single chamber of a factor of  $3.1 \pm 1.6$ . Generally, the rock  $p\text{CO}_2$  declined steadily following the storm event in all chambers although this trend is somewhat more evident for higher elevations above the riverbed (Figure 2-2C). Furthermore, changes in rock  $p\text{CO}_2$  correlate well with changes in CO<sub>2</sub> fluxes ( $R^2 = 0.44$ ,  $p = 0.004$ ,  $n = 17$ ; Figure 2-6). It is worth noting that a measurement artifact of the flux measurements by incomplete purging, which could lead to residual CO<sub>2</sub> in the gas accumulation chambers or connected rock pores, can be excluded because the standard deviations of the flux measurements correlate less with the flux values ( $R^2 = 0.22$ ,  $p = 0.050$ ,  $n = 18$ ).

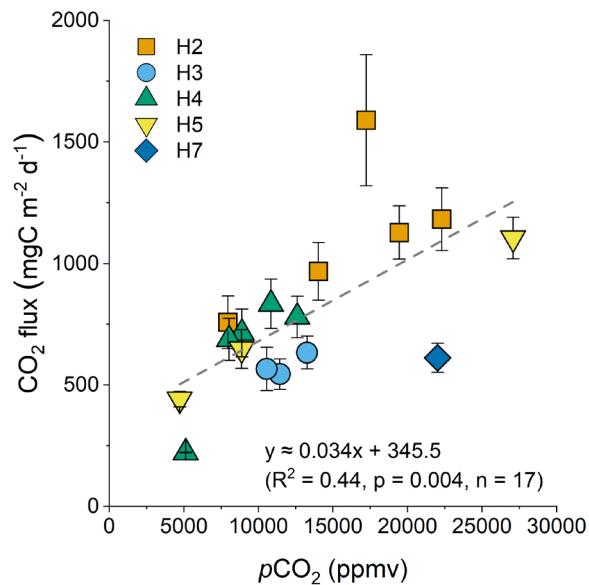


**Figure 2-6. Carbon dioxide flux versus partial pressure of carbon dioxide in the weathering zone.**  $p\text{CO}_2$  values from five *in situ* weathering chambers are correlated with  $\text{CO}_2$  fluxes. Standard deviations are given for  $\text{CO}_2$  flux measurements while the standard deviation of a single  $p\text{CO}_2$  measurement cannot be determined with the applied method.

#### 2.4.5 Carbon isotope composition of CO<sub>2</sub>

The stable carbon isotopic composition of the CO<sub>2</sub> sampled from the *in situ* weathering chambers revealed three samples with notably high  $\delta^{13}\text{C}$  values, ranging from  $-5.5$  ‰ to  $+22.3$  ‰. These samples were all collected four days after the chamber installation (02/03/2018 for H2 and H3, and 03/03/2018 for H5, respectively). The remaining samples had  $\delta^{13}\text{C}$  values between  $-29.3$  ‰ and  $-16.3$  ‰.

Overall, these high  $\delta^{13}\text{C}$  values correlate with a metric of excess carbon trapped on the molecular sieves. This is the ratio of the volume of CO<sub>2</sub> recovered from the zeolite molecular sieve cartridges (MSC), compared to that trapped based on the estimate of the volume of CO<sub>2</sub> loaded onto the sieves using the  $p\text{CO}_2$  recorded with the infra-red gas analyser (IRGA<sub>CO2</sub>) (Figure 2-7). This trend also reflects the time passed since the installation of each chamber. Together, this indicates the presence of a contaminant in the trapped gases of the initial samples that was not detected by the IRGA as CO<sub>2</sub> but that behaves in a similar way to CO<sub>2</sub> during the CO<sub>2</sub> recovery and purification in the laboratory. Laboratory experiments following the field trip identified that the silicone sealant used was the source of some contamination, releasing an unidentified gas during the curing process that interferes heavily on the IRMS (at m/z value 45). However, it was found that curing finishes mostly within three days and that no contamination of the stable carbon isotope measurement occurs when the sealant has dried for one week under outside conditions similar to the field setup.

Therefore, only CO<sub>2</sub> sampled from the end of the fieldtrip is used for further interpretations in this study. In contrast, the CO<sub>2</sub> volumes and  $\delta^{13}\text{C}$  values of samples collected before the sealant dried are tainted and likely to be only an apparent signal consisting of naturally emitted CO<sub>2</sub> and the contaminant (Figure 2-7). It is important to note that the CO<sub>2</sub> flux measurements are not affected by the contaminant.

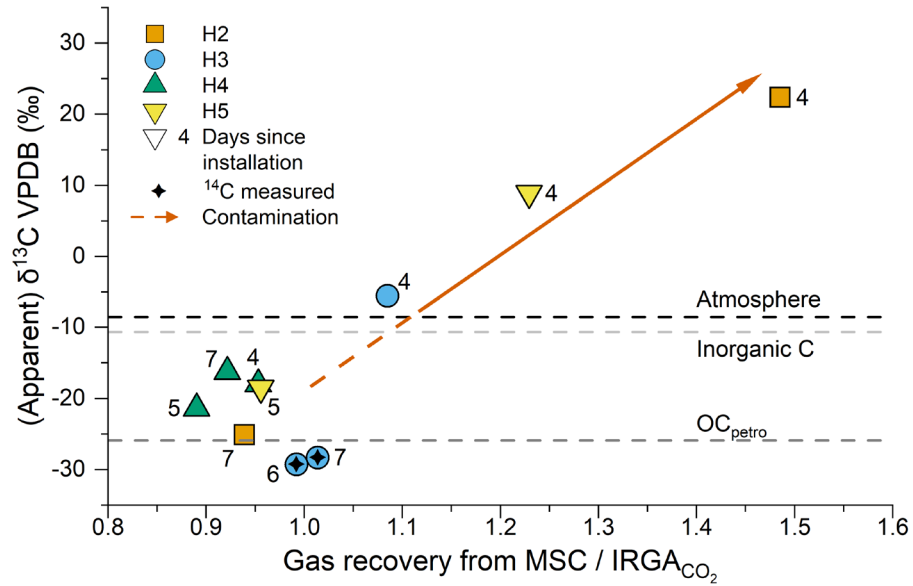


**Figure 2-7. Stable carbon isotope measurement of CO<sub>2</sub> from weathering chambers versus sampling efficiency.** Excess of gas recovered from the molecular sieve cartridges (MSC) compared to the amount of CO<sub>2</sub>, which theoretically should have been trapped in the field according to the infra-red gas analyser (IRGA), correlates with the δ<sup>13</sup>C (‰ VPDB) of the sample. This trend coincides with the time passed since the installation of the particular chamber, which is denoted next to each data point (days), indicating a contamination of the trapped CO<sub>2</sub> associated with the chamber set-up. This contaminant is not detected by the IRGA but behaved similar to CO<sub>2</sub> during the CO<sub>2</sub> recovery and purification in the laboratory, and interferes heavily on isotopic measurements. An uncontaminated sample has typically a sampling efficiency of ~95 % with the applied methods.

Stable carbon isotope analyses revealed a δ<sup>13</sup>C of -29.3 ‰ for CO<sub>2</sub> collected from chamber H3 on the 04/05/2018 (6 days after the installation) and a δ<sup>13</sup>C of -28.3 ‰ for the following day. The radiocarbon activities for this CO<sub>2</sub> from chamber H3 were  $F^{14}\text{C} = 0.0122 \pm 0.0049$  and  $F^{14}\text{C} = 0.0547 \pm 0.0047$ , respectively (Table 2-3). The radiocarbon content is used to assess the contributions from the atmosphere (mass fraction;  $f_{\text{Atm}}$ ) and from petrogenic carbon (that is the combined pool of inorganic and organic carbon;  $f_{\text{Petrogenic C}}$ ) to the sampled gases by solving the following isotope mass balance system:

$$\begin{cases} f_{\text{Atm}} + f_{\text{Petrogenic C}} = 1 \\ f_{\text{Atm}} \times F^{14}\text{C}_{\text{Atm}} + f_{\text{Petrogenic C}} \times F^{14}\text{C}_{\text{Petrogenic C}} = F^{14}\text{C}_{\text{Chamber}} \end{cases} \quad (2-5)$$

Based on the assumption that the declining trend of the atmospheric radiocarbon content over the last few decades can be described by a linear regression (Cerling et al., 2016; Hua et al., 2013), we estimate the radiocarbon content of the local atmospheric CO<sub>2</sub> to be  $F^{14}\text{C}_{\text{Atm}} = 1.0216$  during the sampling period, by extrapolating an atmospheric record of radiocarbon dioxide measurements from Wellington, New Zealand, for the years 2013 – 2017 (Turnbull et al., 2017).

This estimated value is close to the latest report of  $F^{14}C = 1.0226$  for 20/09/2017 (Turnbull et al., 2017). Correcting for the atmospheric contributions ( $f_{Atm} \approx 1.2\%$  and  $5.4\%$ , respectively) by taking its  $\delta^{13}C_{Atm}$  value of  $-8.6\text{‰}$  into account indicates that the petrogenic carbon pools in the two CO<sub>2</sub> samples have very similar  $\delta^{13}C$  signatures ( $\delta^{13}C_{Petrogenic\ C}$ ) of  $-29.5 \pm 0.1\text{‰}$  within the measurement uncertainties (Table 2-3), following the equation

$$f_{Atm} \times \delta^{13}C_{Atm} + f_{Petrogenic\ C} \times \delta^{13}C_{Petrogenic\ C} = \delta^{13}C_{Chamber} . \quad (2-6)$$

Since the radiocarbon activities of the sampled CO<sub>2</sub> are very low, we estimate any uncertainty of the atmospheric correction that is associated with extrapolating the atmospheric radiocarbon content to be negligible.

**Table 2-3. Carbon isotope composition of sampled CO<sub>2</sub>.** The atmospheric contributions to chamber H3 are corrected using an extrapolated fraction modern based on a published record for the years 2013 – 2017 (Turnbull et al., 2017) (\*).

Sample	Date	Publication code	$\delta^{13}C$ (‰ VPDB, $\pm 0.1$ )	Fraction modern ( $\pm$ SD)	$\delta^{13}C$ corrected for atm. contribution (‰ VPDB $\pm 0.1$ )
Atmosphere	03/05/2018	-	-8.6	1.0216*	-
H3	04/05/2018	SUERC-84238	-29.3	0.0122 $\pm$ 0.0049	-29.6
H3	05/05/2018	SUERC-84239	-28.3	0.0547 $\pm$ 0.0047	-29.4

## 2.5 Discussion

### 2.5.1 Source of rock-derived CO<sub>2</sub>

To quantify the CO<sub>2</sub> emissions from weathering of mudstones exposed in the Waiapu catchment (Figure 2-1), it is crucial to first constrain the source of carbon. To do this, we rely on the stable and radioactive carbon isotopic composition of the emitted CO<sub>2</sub>, which is used alongside measurements of the rocks undergoing weathering. This allows us to track the contributions from OC<sub>petro</sub>, carbonates and the atmosphere. The very low radiocarbon content of the sampled CO<sub>2</sub> ( $F^{14}C = 0.0122$  to  $0.0547$ ) indicates only minor contributions ( $f_{Atm} < 6\%$ ) from modern atmospheric CO<sub>2</sub>, and also confirms the underlying assumption that neither soil organic matter nor plants incorporating modern carbon contribute any CO<sub>2</sub> in the rock outcrops we studied (Figure 2-1).

The mudstones that make up the study site contain very little inorganic carbon (IC) as disseminated carbonate ( $< 0.2\text{ wt.}\%$ ). The OC<sub>petro</sub>/IC ratio is  $\geq 4.5$ . This could suggest that the contribution of IC to the CO<sub>2</sub> emissions (Equation 2-2) is negligible in this setting. Indeed, the  $\delta^{13}C$  values of trapped CO<sub>2</sub> ( $\sim -29.5\text{‰}$ , corrected for atmospheric contribution; Table 2-3) confirm this hypothesis because they are significantly more negative than that of typical

Cretaceous marine carbonates (~ 0 ‰ to +5 ‰) (Erba, 2004; Gröcke et al., 2003; Weissert et al., 1998) or that of IC from the study site (-10.7 ‰). This contrasts notably with the carbonate-rich marly rocks of the Laval catchment in the Draix-Bléone Critical Zone Observatory (CZO; France) where carbonate dissolution by sulfuric acid derived from the oxidation of sulfide minerals (Equation 2-2) contributes more than 70 % of the emitted CO<sub>2</sub> (Soulet et al., 2021, 2018). However, we do not exclude that carbonate dissolution could contribute to the carbon fluxes from weathering in the Waiapu catchment because carbonate concretions are a common feature in several outcropping lithologies (Mazengarb and Speden, 2000; Speden, 1976) and dissolved ion fluxes suggest high carbonate weathering rates (Lyons et al., 2005).

The  $\delta^{13}\text{C}$  values of CO<sub>2</sub> from our accumulation chambers are more negative than the  $\delta^{13}\text{C}$  values of OC<sub>petro</sub> (-25.9 ‰) in rock samples. Having corrected for carbon input from atmospheric CO<sub>2</sub>, the offset is ~ 3.6 ‰ (Table 2-3). It is important to note that previous work did not find any carbon isotope fractionation associated with the methods used for gas sampling and processing (Garnett et al., 2019; Hardie et al., 2005). In addition, any contamination of the trapped gases associated with the setup of the accumulation chambers (silicone sealant) is avoided by considering samples collected approximately one week after installation (Figure 2-7). Indeed, if present, such a contamination would lead to an apparently heavier stable carbon isotope composition and thus could not explain the lower  $\delta^{13}\text{C}$  values of emitted CO<sub>2</sub> compared to OC<sub>petro</sub>. In addition, the  $\delta^{13}\text{C}$  values of OC<sub>petro</sub> reported here are verified by comparison with previous work in the Waiapu catchment (Thompson, 2009). Therefore, we explore two remaining scenarios for why the  $\delta^{13}\text{C}$  signatures of CO<sub>2</sub> from mudstone weathering are offset from OC<sub>petro</sub>: i) an additional fossil carbon source with a more negative  $\delta^{13}\text{C}$  value; and/or ii) carbon isotope fractionation associated with the weathering processes.

#### 2.5.1.1 Geothermal contributions of CO<sub>2</sub> and CH<sub>4</sub> oxidation

One explanation for the <sup>13</sup>C-depleted nature of the sampled CO<sub>2</sub> compared to the  $\delta^{13}\text{C}$  values of the OC<sub>petro</sub> in the mudstones could be that geothermal sources contribute either CO<sub>2</sub> or methane (CH<sub>4</sub>) that is oxidized to CO<sub>2</sub> below (or around) the accumulation chambers. Gas seeps occasionally occur in the northeast of New Zealand but none are reported in close proximity to our study site (Francis et al., 1991; Reyes et al., 2010; Scadden et al., 2016). While a geothermal carbon source would most likely be <sup>14</sup>C-free, geothermal CO<sub>2</sub> reported in the region has high  $\delta^{13}\text{C}$  values of ~ -12.0 ‰ (ranging from -6.7 ‰ to -17.3 ‰) which is ~ 17.5 ‰ more positive than the  $\delta^{13}\text{C}$  values of CO<sub>2</sub> that we sampled (Giggenbach et al., 1995; Lyon and Giggenbach, 1992). Thus, even if missed, a geothermal CO<sub>2</sub> source could not explain our observations.

Gas seeps in the northeast of New Zealand can be dominated by thermogenic CH<sub>4</sub> and only contain trace amounts of CO<sub>2</sub> (Giggenbach et al., 1993; Lowry et al., 1998). Taking into account the reported δ<sup>13</sup>C values of CH<sub>4</sub> of -34 ‰ to -42 ‰ for this area (Giggenbach et al., 1995; Lyon and Giggenbach, 1992) and a carbon isotope fractionation during aerobic or anaerobic methane oxidation of 5 ‰ to 30 ‰ (Whiticar, 1999), a CH<sub>4</sub> source that is oxidized and degassing into our chambers would have a δ<sup>13</sup>C value of CO<sub>2</sub> between -39 ‰ and -72 ‰. If oxidation of thermogenic CH<sub>4</sub> was occurring, this process alone cannot explain the measured δ<sup>13</sup>C values of chamber CO<sub>2</sub>. Instead, we would have to invoke a mixture with contributions from an isotopically heavier source (e.g., OC<sub>petro</sub>). However, to shift the CO<sub>2</sub> stable isotopic composition by 3.6 ‰, we calculate that the mass of thermogenic CH<sub>4</sub> flux would have to be very large ranging from ~ 62 mgC m<sup>-2</sup> d<sup>-1</sup> to 218 mgC m<sup>-2</sup> d<sup>-1</sup>, and represent 7.8 % to 27.4 % of the average CO<sub>2</sub> release from the chambers (795 mgC m<sup>-2</sup> d<sup>-1</sup>). This would be similar in size to the globally highest CH<sub>4</sub> fluxes from sub-tropical wetland soils (Oertel et al., 2016). Furthermore, it would greatly exceed the mean CH<sub>4</sub> flux of ~ 6 mgC m<sup>-2</sup> d<sup>-1</sup> from microseepage in soils over near-surface oil-gas reservoirs or active geothermal areas (Etiope and Klusman, 2010). Indeed, it would be comparable only to the highest fluxes associated with macro-seeps in such settings (Etiope and Klusman, 2010, 2002). Thus, a significant geothermal carbon contribution to the CO<sub>2</sub> emissions measured in our accumulation chambers appears to be unlikely.

#### 2.5.1.2 Microbial impact on OC<sub>petro</sub> oxidation and carbon isotope fractionation

An alternative explanation for the δ<sup>13</sup>C values of the CO<sub>2</sub> would be via carbon isotope fractionation associated with microbial heterotrophic respiration (Petsch et al., 2001) which can produce CO<sub>2</sub> that is <sup>13</sup>C-depleted compared to the substrate (Blair et al., 1985; Werth and Kuzyakov, 2010). However, although previous studies have shown that microorganisms can thrive aerobically on OC<sub>petro</sub> as a sole carbon source (Matlakowska and Sklodowska, 2011; Petsch et al., 2001; Stasiuk et al., 2017), to our knowledge, no report exists yet on carbon isotope fractionation during the CO<sub>2</sub> release from microbial degradation of OC<sub>petro</sub>. In contrast, this process is well described for soil organic matter. As reviewed by Werth and Kuzyakov (2010), the <sup>13</sup>C-depletion in soil microbial respiration is an apparent isotope fractionation as the combined result of three effects: i) kinetic <sup>13</sup>C-fractionation; ii) preferential substrate utilization; and iii) heterogeneity and activity of microorganisms. The ~ 3.6 ‰ <sup>13</sup>C-depletion of CO<sub>2</sub> emissions compared to OC<sub>petro</sub> reported here is well within range of the kinetic carbon isotope fractionation during microbial catabolism, leading to a <sup>13</sup>C-depletion in respired CO<sub>2</sub> that is balanced typically by a 0.1 ‰ – 5.7 ‰ <sup>13</sup>C-enrichment of the microbial biomass in soils (Blair et al., 1985; Šantrůčková et al., 2000).

Thus, our measurements would be consistent with a microbial process that leads to a <sup>13</sup>C-depletion in CO<sub>2</sub> produced during oxidative weathering. However, further research is needed to constrain the detail and magnitude of the offsets. Ramped temperature pyrolysis or oxidation, coupled with stable carbon analysis, could be used to determine whether <sup>13</sup>C-depleted fractions of OC<sub>petro</sub> are oxidized preferentially (Hemingway et al., 2018, 2017). This signature may be present in organic biomarkers associated with microbial activity (e.g., phospholipid fatty acids) (Petsch et al., 2001; Schwab et al., 2019; Seifert et al., 2013, 2011). Modification of OC<sub>petro</sub> oxidation experiments (Chang and Berner, 1999) could also be informative, when coupled to an apparatus to measure the isotopic composition of evolved gases (Beaupré et al., 2016). In summary, we conclude that the oxidation of OC<sub>petro</sub> is the sole contributor of CO<sub>2</sub> in this case, with lower δ<sup>13</sup>C values of the CO<sub>2</sub> possibly relating to isotopic fractionation associated with microbial respiration of OC<sub>petro</sub> during weathering.

## 2.5.2 Rock-derived CO<sub>2</sub> fluxes and their environmental controls

In general, the large CO<sub>2</sub> emissions from oxidative weathering of OC<sub>petro</sub> in mudstones of northern New Zealand have a similar magnitude as fluxes from soil respiration reported for various soil types and climates (Oertel et al., 2016; Raich and Schlesinger, 1992). Likewise, they are comparable in size to OC<sub>petro</sub>-derived CO<sub>2</sub> fluxes measured in marly rocks exposed in the French Alps ranging from ~ 1 mgC m<sup>-2</sup> d<sup>-1</sup> to 795 mgC m<sup>-2</sup> d<sup>-1</sup>, which, however, are lower by a factor of ~ 5.5 than CO<sub>2</sub> fluxes from carbonate dissolution (Soulet et al., 2021). Both locations experience very high erosion rates. In the Waiapu catchment, the sediment export rates are ~ 17,800 t km<sup>-2</sup> yr<sup>-1</sup> (Betts et al., 2003; Hicks et al., 2004), whereas in the Laval catchment in the Draix-Bléone CZO they are ~ 11,200 t km<sup>-2</sup> yr<sup>-1</sup> (Mathys et al., 2003). Estimates of OC<sub>petro</sub> oxidation using the rhenium-proxy suggest that high erosion rates could sustain rapid rates of oxidation (Hilton et al., 2014), and this could explain the apparent, broad similarity between the sites. We also note that the rocks in the Waiapu River basin contain slightly more OC<sub>petro</sub> (0.76 wt.%) than the rocks in the Laval catchment (~ 0.54 wt.%) (Soulet et al., 2021), but again they are broadly similar. These features are interesting and call on more studies that quantify OC<sub>petro</sub> oxidation and their CO<sub>2</sub> emissions in this way. However, to make more detailed comparisons requires a larger dataset than is presently available. Here, instead, we focus on the observation that OC<sub>petro</sub> fluxes appear to respond quickly to environmental changes.

### 2.5.2.1 Local topographic position and moisture

The relationship between CO<sub>2</sub> fluxes and the elevation of the chambers above the riverbed (Figure 2-4) can be explained in terms of diffusive processes operating in a hydrological

framework. The degree of water-saturation generally decreases with increasing elevation above the riverbed (Lu and Godt, 2013; Mason et al., 2016), which allows for more diffusive exchange of any connected pore space around the chamber (Bao et al., 2017; Bolton et al., 2006; Feng et al., 2002; Tremosa et al., 2020; Voroney and Heck, 2015). This provides greater amounts of oxygen for the oxidation of OC<sub>petro</sub> (Equation 2-1), and, if present, the oxidation of pyrite that can lead to dissolution of carbonate minerals (Equation 2-2 and Equation 2-3). Furthermore, lower degrees of water-saturation in the weathering zone increase the amount of CO<sub>2</sub> that escapes in gaseous form while the export of dissolved inorganic carbon to the river decreases (Hasenmueller et al., 2015; Neu et al., 2016; Tune et al., 2020). These inferences can explain the first order correlation between chamber elevation and CO<sub>2</sub> flux (Figure 2-4), and confirm findings from the French Alps where five gas accumulation chambers were installed within 2.5 m elevation above a riverbed (Soulet et al., 2021).

Another way to examine these controls is to categorize our data set into “wet” and “dry” measurement periods. We do this based on a threshold of three days after the rain event (Figure 2-2A). This categorization highlights the importance of the hydrological control on CO<sub>2</sub> fluxes since their correlation with the chamber elevation is significantly lower when “wet” samples are excluded ( $R^2 = 0.40$  and  $R^2 = 0.25$ , respectively). This also affects the  $p\text{CO}_2$  within the weathering zone (Figure 2-2C) similar to findings in soils where high levels of moisture act as a diffusion barrier that leads to greater accumulations of CO<sub>2</sub> (Hasenmueller et al., 2015).

Previous studies have indicated that the presence of water is crucial for microbial life in the weathering zone. In the laboratory, dissolved OC<sub>petro</sub> derived from an aqueous kerogen dissolution can be rapidly assimilated and biodegraded by aerobic heterotrophic bacteria (Schillawski and Petsch, 2008). The authors suggested that the dissolution could be the rate limiting step of respiration of OC<sub>petro</sub>. Furthermore, recent research highlighted the importance of aqueous subaerial biofilms for the degradation of OC<sub>petro</sub>, which act to incorporate enzymes crucial for aerobic heterotrophic metabolism (Stasiuk et al., 2017). Taken together, this could mean that the CO<sub>2</sub> fluxes from OC<sub>petro</sub> oxidation relate to moisture in a bell-shaped curve. At low levels of moisture, CO<sub>2</sub> production is inhibited due to a lack of an aqueous transport and reactant medium that is also needed to create epilithic biofilms. At high levels of moisture, the CO<sub>2</sub> production is hampered due to a limited oxygen supply.

#### 2.5.2.2 Temperature

Our 6 day measurement period revealed a positive relationship between CO<sub>2</sub> flux from OC<sub>petro</sub> and regional air temperatures (Figure 2-5). Daily-averaged air temperatures indicate a broadly positive relationship. However, the correlation is stronger when considering a 2 h lag

between the measurements and air temperature record (Figure 2-5C). This time lag was observed between the local climate station and the rock chambers (Figure 2-3). The correlation is further improved when “wet” measurements are excluded (Figure 2-5D). Despite the influence of precipitation and of the topographic position of the chambers on the CO<sub>2</sub> fluxes, the evidence for an important temperature control on the oxidative weathering of OC<sub>petro</sub> is unambiguous. It should be noted that single chambers respond comparably to temperature, such as H3 and H4 located at similar elevation above the riverbed, and the trend of this relationship is confirmed by comparing the combined CO<sub>2</sub> fluxes of all chambers with the temperature record (Figure 2-5).

Previous research has indicated the presence of such an environmental control by investigating the oxidation of coal in laboratory experiments but this was restricted to two temperatures at 24 °C and 50 °C (Chang and Berner, 1999). Only recently, seasonal investigations of *in situ* oxidative weathering of OC<sub>petro</sub> contained in marly rocks have specified this relationship as highly sensitive and exponential (Soulet et al., 2021). To provide an exponential measure of the change in flux as the consequence of increasing the reaction temperature by 10 °C, a dimensionless  $Q_{10}$  value can be calculated:

$$Q_{10} = \exp(10 \text{ }^{\circ}\text{C} \times \gamma) \quad (2-7)$$

where  $\gamma$  is the growth rate parameter (°C<sup>-1</sup>) that can be derived from a growth exponential model:

$$F = F_0 \times \exp(\gamma \times T) \quad (2-8)$$

where  $F$  is the CO<sub>2</sub> flux (mgC m<sup>-2</sup> d<sup>-1</sup>),  $T$  is the temperature (°C) and  $F_0$  is the CO<sub>2</sub> flux at 0 °C. The  $Q_{10}$  coefficient of Soulet et al. (2021) can be compared with our dataset, although we note that the data from the Waiapu basin can be described sufficiently by a linear relation (Figure 2-5). By using an exponential model, we find a  $Q_{10}$  value of  $2.7 \pm 1.0$  ( $F_0 = 195 \pm 108$  mgC m<sup>-2</sup> d<sup>-1</sup>;  $\pm$  standard error;  $R^2 = 0.30$ ,  $p < 0.001$ ,  $n = 18$ ), based on the air temperatures delayed by 2 h (Figure 2-5C). Interestingly, this is similar, albeit slightly higher, to the OC<sub>petro</sub> oxidation  $Q_{10}$  value of  $2.2 \pm 0.5$  reported for the Laval catchment, based on daily-averaged chamber temperatures (Soulet et al., 2021). It is well within the global range of CO<sub>2</sub> fluxes from soil respiration with a mean  $Q_{10}$  value of  $3.0 \pm 1.1$  for the 0 °C – 20 °C temperature range (Bond-Lamberty and Thomson, 2010). However, when considering only the “dry” fluxes (Figure 2-5D), which were measured in the range of around 10 °C – 16 °C, the  $Q_{10}$  temperature coefficient is higher, at  $4.8 \pm 2.5$  ( $R^2 = 0.61$ ,  $p < 0.001$ ,  $n = 9$ ).

The similarity of  $Q_{10}$  values of petrogenic CO<sub>2</sub> fluxes and of soil respiration suggests a microbial control on the kinetics of the oxidation of OC<sub>petro</sub>, analogous to soils (Bond-Lamberty and Thomson, 2010; Oertel et al., 2016). Since microbial enzymes have the potential to increase

the rate of breakdown of organic matter by several orders of magnitude, small changes in microbial activity (e.g., by changes in humidity) have the potential to induce large changes in the associated CO<sub>2</sub> production (Leifeld and von Lützow, 2014). The number of enzymatic steps that are required to release a carbon atom from organic matter as CO<sub>2</sub> is assumed to depend on its reactivity which in turn is controlled by various factors such as solubility, molecular size and functionalization, and association with fine-grained minerals (Bosatta and Ågren, 1999; Schmidt et al., 2011). Accordingly, it can be expected that oxidative weathering of OC<sub>petro</sub> depends not only on environmental and microbial variables but also strongly on the characteristics of the organic matter and its surrounding rock matrix (i.e., its mineral association) (Hemingway et al., 2019). This could explain differences in CO<sub>2</sub> emissions in contrasting lithologies. Overall, as highlighted by Soulet et al. (2021), our  $Q_{10}$  value identifies oxidative weathering of OC<sub>petro</sub> as a positive feedback to warming, most relevant to the geological carbon cycle. At present, models of chemical weathering fluxes in the geological carbon cycle do not attempt to parametrize OC<sub>petro</sub> oxidation with a temperature control (Caves Rügenstein et al., 2019; Isson et al., 2020) and the measurements here support the finding of Soulet et al. (2021) that this modification is necessary.

### 2.5.3 Wider implications for understanding Earth's carbon cycle

We have identified the oxidation of OC<sub>petro</sub> as the source of rapid rates of CO<sub>2</sub> release measured in rock outcrops of the Waiapu catchment. We find environmental controls on these fluxes that are analogous to those reported in a setting with contrasting bedrock (Soulet et al., 2021, 2018). Thus, we propose that the studied gully complex should not only be representative of a large portion of the Waiapu catchment and neighbouring watersheds in New Zealand (Gomez et al., 2004; Hicks et al., 2000; Leithold et al., 2006; Mazengarb and Speden, 2000; Thompson, 2009), but also for similar lithologies in rapidly eroding settings elsewhere.

### 2.5.3.1 Feasibility of short-term investigations to reveal environmental controls on rock-derived CO<sub>2</sub> fluxes

There have been only two studies that attempt to establish long-term records (months to years) of rock-derived CO<sub>2</sub> fluxes to help constrain their environmental controls (Keller and Bacon, 1998; Soulet et al., 2021, 2018). Using gas sampling wells over ~ 7 m depth in shallow soil underlain by glacial till dominated by shales, Keller and Bacon (1998) provided the first *in situ* evidence for petrogenic CO<sub>2</sub>, differentiating it from soil respiration over a 1 year period at monthly intervals. More recently, at the Draix-Bléone CZO, CO<sub>2</sub> flux measurements were made on seasonal visits over 2.5 years (Soulet et al., 2021) from rock chambers drilled into rock outcrops undergoing weathering (the design used in this study).

Here, we show that the design for *in situ* CO<sub>2</sub> measurements of Soulet et al. (2018) can be applied in stand-alone investigations without a conceptual framework of repeated visits. The potential to capture significant short-term changes in temperature and hydrology, which can be linked to changes in CO<sub>2</sub> fluxes (Figure 2-2B and Figure 2-5), was previously indicated by findings in the Draix-Bléone CZO (Soulet et al., 2021). The approach used in this study is feasible even in remote locations. The general location of the field site was explored from remote sensing imagery prior to fieldwork. The first two days of the trip were used to search for a suitable location within the study area and install the chambers (using only portable drilling equipment). At the end of the measurement period, the setup can be easily dismantled within a few minutes and all material removed from the environment. To exclude the possibility of contamination of the molecular sieves used for trapping the CO<sub>2</sub>, we recommend starting CO<sub>2</sub> collection approximately one week after the chamber setup when using a sealant containing drying agents (Figure 2-7). In the future, automation of the flux measurements, for instance using electrically-actuated valves, could allow several recordings in parallel and provide further detail in the dataset.

One drawback of a stand-alone trip is the limited range in environmental variables that can be observed, which could potentially be extended significantly by repeated visits over various seasons (depending on the seasonality in the study area), as performed in the Draix-Bléone CZO (Soulet et al., 2021). Nevertheless, our work shows that short field campaigns are viable and provide new insight on the environmental controls on OC<sub>petro</sub> oxidation for a given substrate. This approach can now be used to study *in situ* CO<sub>2</sub> emissions and their controls across climatic, lithological and biological variables.

### 2.5.3.2 Rock $p\text{CO}_2$ and silicate weathering

The oxidation of  $\text{OC}_{\text{petro}}$  in the critical zone also bears relevance to other chemical weathering processes because it can influence the partial pressure of  $\text{CO}_2$  within the weathering zone. In the Waiapu catchment, the temperature and humidity combine to control the accumulation of  $\text{CO}_2$  within the chambers (Figure 2-4 and Figure 2-5), and thus the  $p\text{CO}_2$  in the surrounding rock pores (Figure 2-6). Since these mudstones have low inorganic carbon contents (< 0.2 wt.%), the consumption of  $\text{CO}_2$  produced by  $\text{OC}_{\text{petro}}$  oxidation cannot be negated by the dissolution of carbonate minerals as it would in carbonate-rich lithologies (Calmels et al., 2014). In contrast, the high  $p\text{CO}_2$  values that we measured could have the strong potential to drive the weathering of co-occurring silicate minerals, which can contain more than 25 wt.% feldspar (mostly plagioclase) and 15 wt.% chlorite (Kenny, 1984), by acid hydrolysis reactions. In this process, a high  $p\text{CO}_2$  is expected to be associated with a low pH, which facilitates the dissolution of silicate minerals by carbonic acid, which itself is transformed into bicarbonate (Drever, 1994; Ebelmen, 1845). The dissolution should be further amplified by organic acids formed by microorganisms during the breakdown of  $\text{OC}_{\text{petro}}$  as it is within soils (Stasiuk et al., 2017; Waksman and Starkey, 1931).

We found that almost all the  $\text{CO}_2$  within the pore space of the mudstones in the Waiapu River gully complex is rock-derived. Thus, atmospheric  $\text{CO}_2$  is not likely to have been involved in any silicate weathering reactions in the shallow subsurface of these bare rock outcrops. As such, chemical weathering of silicate minerals cannot act as an atmospheric  $\text{CO}_2$  sink mechanism (Berner, 1999; Gaillardet et al., 1999; Moon et al., 2014). Instead, rock-derived carbon that is transformed during silicate weathering is likely to be exported by the Waiapu River as bicarbonate. This may be released as  $\text{CO}_2$  during river transport (Raymond et al., 2013), and/or eventually precipitate as  $\text{CaCO}_3$  in the oceans (Berner, 1999; Walker et al., 1981). If the newly precipitated carbonates form from carbon originally derived from  $\text{OC}_{\text{petro}}$ , their formation would represent no modern-day carbon transfer to the carbonate mineral. In fact, half of the exported bicarbonates would return to the atmosphere as  $\text{CO}_2$  based on the stoichiometry of this process (Berner, 1999). This would minimize the overall carbon sink linked to silicate weathering in locations that share similarities with our study area, with high erosion rates, sedimentary rocks and oxidative weathering (Bufe et al., 2021). Furthermore, this would also mean that the dissolved cations derived from silicate weathering, which are transferred from the weathering zone into the Waiapu River, could in fact be linked back to oxidative weathering of  $\text{OC}_{\text{petro}}$ .

For the study area, we can explore this further using our one-time estimates of  $\text{OC}_{\text{petro}}$  oxidation to compare with those of silicate weathering and carbonate weathering. There are several caveats to be noted here. First, our chamber-based measurements show systematic

variation between chambers (linked to their topographic position; Figure 2-4) and within a chamber over 6 days due to ambient temperature and precipitation conditions (Figure 2-2). Therefore, it is difficult to provide an estimate of flux that would be representative of a longer-term flux, over a wider area. Second, we normalize the measured fluxes to the chambers internal area, which allows chambers to be compared meaningfully. However, this is not the same as normalizing fluxes to the surface area exposed in a catchment (Soulet et al., 2021). Finally, the published silicate and carbonate weathering fluxes for the Waiapu catchment are based on only a single assessment (Lyons et al., 2005). Nevertheless, the comparison is informative. The published carbon flux of silicate weathering is  $5.7 \times 10^5 \text{ mol CO}_2 \text{ km}^{-2} \text{ yr}^{-1}$ , which translates to an average of  $\sim 18.8 \text{ mgC m}^{-2} \text{ d}^{-1}$  over the catchment area. Similarly, the carbonate weathering flux is  $1.2 \times 10^5 \text{ mol CO}_2 \text{ km}^{-2} \text{ yr}^{-1}$ , which translates to an average of  $\sim 4 \text{ mgC m}^{-2} \text{ d}^{-1}$ . These catchment-wide estimates are much lower than the OC<sub>petro</sub> oxidation fluxes we measured in chambers of the gully complex, which ranged from 222 mgC m<sup>-2</sup> d<sup>-1</sup> to 1,590 mgC m<sup>-2</sup> d<sup>-1</sup> (Table 2-2). Depending on the wider rates of OC<sub>petro</sub> oxidation that occur throughout the catchment, for which trace metal proxies such as rhenium in river water could shed light (Hilton et al., 2014), it appears that the CO<sub>2</sub> supply from OC<sub>petro</sub> oxidation could play a major role in silicate and carbonate weathering fluxes by carbonic acid in this type of setting.

Overall, a direct impact of the oxidation of OC<sub>petro</sub> on silicate and/or carbonate dissolution suggests that differentiating the carbon cycle into a silicate-carbonate subcycle and an organic matter subcycle as it has been suggested by Berner (1999) oversimplifies the complexity of chemical weathering and calls for a more holistic view. Together with identifying the carbon sources associated with oxidative weathering, the parallel dissolution of silicate minerals needs to be considered in any overall assessment of chemical weathering of sedimentary rocks (Bufe et al., 2021; Hilton and West, 2020; Jin et al., 2014). However, while the high rock-derived CO<sub>2</sub> fluxes and pCO<sub>2</sub> values identify the mudstones studied here as a clear carbon source, future research is needed to constrain weathering pathways at larger scales, and through the inorganic carbon pool of river catchments.

## 2.6 Conclusions

We have measured CO<sub>2</sub> release during weathering of mudstones in the Waiapu catchment, New Zealand, using a short-term installation of accumulation chambers installed directly into exposed rock outcrops. They reveal rapid instantaneous fluxes that range from 222 mgC m<sup>-2</sup> d<sup>-1</sup> to 1,590 mgC m<sup>-2</sup> d<sup>-1</sup> over the study period of six days. The setting experiences rapid erosion rates, and these measurements confirm that steep mountain catchments comprised of sedimentary rocks can act as hotspots of carbon cycling between the lithosphere and the atmosphere.

Based on the magnitude of the CO<sub>2</sub> fluxes and the stable and radioactive carbon isotopic composition of CO<sub>2</sub> sampled from the chambers, OC<sub>petro</sub> is the sole contributor of carbon in this setting. There is a depletion of ~ 3.6 ‰ in the δ<sup>13</sup>C values of CO<sub>2</sub> when compared to OC<sub>petro</sub> in rocks. We suggest this may reflect carbon isotope fractionation associated with microbial respiration of OC<sub>petro</sub>. In addition, CO<sub>2</sub> fluxes responded quickly to changes in temperature and humidity. Together, this supports the importance of environmental controls on chemical weathering and climate change feedbacks.

We measure very high pCO<sub>2</sub> in the shallow weathering zone of these rock outcrops, with negligible input from atmospheric CO<sub>2</sub>. This high pCO<sub>2</sub> could induce the weathering of silicate minerals using the rock-derived CO<sub>2</sub>. Any subsequent transfer of carbon in the bicarbonate pool of rivers would represent a leak of carbon derived from OC<sub>petro</sub> oxidation to the atmosphere elsewhere, and silicate weathering would not act as an atmospheric CO<sub>2</sub> sink. This suggests the need to consider a direct connection of OC<sub>petro</sub> oxidation and silicate weathering in rapidly eroding mudstones, and for how these play out in the wider carbon cycle. Overall, this study provides a framework for future work regarding a better understanding of the chemical weathering of sedimentary rocks and their climatic, lithological and biological interrelations which can now be addressed with short field campaigns even in remote areas following the presented methodology.

## 2.7 Acknowledgements

This work was supported by the European Research Council (Starting Grant to RGH, ROC-CO<sub>2</sub> project, grant 678779). We thank M. A. Barton, M. Dellinger, C. Delport, D. R. Gröcke, M. Ogrič and H. Roil for assistance during fieldwork and/or help with data acquisition.

### 3 Probing the exchange of CO<sub>2</sub> and O<sub>2</sub> in the shallow critical zone during weathering of marl and black shale



*Study site in the Moulin catchment, Draix-Bléone observatory, France. January 2019.*

This chapter is designed for submission to a peer-reviewed journal, with the following authors:

Tobias Roylands<sup>1</sup>, Robert G. Hilton<sup>1,2</sup>, Erin L. McClymont<sup>1</sup>, Mark H. Garnett<sup>3</sup>, Guillaume Soulet<sup>1,4</sup>, Sébastien Klotz<sup>5</sup>, Mathis Degler<sup>6</sup>, Felipe Napoleoni<sup>1</sup>, Caroline Le Bouteiller<sup>5</sup>.

Affiliations:

<sup>1</sup> Department of Geography, Durham University, South Road, Durham DH1 3LE, United Kingdom

<sup>2</sup> Department of Earth Sciences, University of Oxford, South Parks Road, Oxford OX1 3AN, United Kingdom

<sup>3</sup> NEIF Radiocarbon Laboratory, Rankine Avenue, East Kilbride, Glasgow G75 0QF, United Kingdom

<sup>4</sup> Geo-Ocean, Brest University, CNRS, Ifremer, F-29280 Plouzané, France

<sup>5</sup> Univ. Grenoble Alpes, INRAE, UR ETNA, 2 rue de la papeterie, BP 76, 38402 Saint-Martin-d'Hères, Cedex, France

<sup>6</sup> Institute of Geosciences, Christian-Albrechts-University, Ludewig-Meyn-Straße 10, 24118 Kiel, Germany

Contributions:

The research was conceptualized by TR, with help from RGH and ELM. The main methods were designed by TR, with help from RGH, GS, MHG and ELM. Field-based and/or laboratory geochemical measurements were led by TR, with contributions from MHG, RGH, SK, MD and FN, and climate data and aerial imagery were provided by SK and CLB. TR led the formal analysis, investigation, data visualization and writing of the original draft, under the supervision of RGH and ELM. All authors contributed to subsequent review and editing, led by TR, RGH, ELM and GS. Funding was acquired by RGH.

All co-authors confirmed that they agree with the work to be included in this thesis.

### 3.1 Abstract

Chemical weathering of sedimentary rocks can release carbon dioxide (CO<sub>2</sub>) and consume oxygen (O<sub>2</sub>) via the oxidation of petrogenic organic carbon or the oxidation of sulfide minerals, which, in turn, can be coupled to the dissolution of carbonate minerals. These pathways govern Earth's surface system and climate over geological timescales, but the corresponding present-day weathering fluxes and their environmental controls are only partly constrained due to a lack of *in situ* measurements. Here, we investigate the gaseous exchange of CO<sub>2</sub> and O<sub>2</sub> during the oxidative weathering of black shales and marly limestones exposed in two rapidly eroding river catchments in the French southern Alps, based on six fieldtrips over one year. We use drilled headspace chambers to measure the CO<sub>2</sub> concentrations in the shallow critical zone, and quantify CO<sub>2</sub> fluxes in real-time. In addition, we can quantify the mass of CO<sub>2</sub> that is stored in a chamber and connected rock pores, which allows us to estimate the volume of rock that contributes CO<sub>2</sub> to a chamber and assess effective diffusive gas exchange. Both rock types are characterized by similar contributing rock volumes and diffusive movement of CO<sub>2</sub>, with variations over time coinciding with changes in temperature and precipitation. However, CO<sub>2</sub> emissions differed between the rock types, with yields over rock outcrop surfaces (inferred from the quantified contributing rock volume and the local weathering depths) ranging on average between 166 tC km<sup>-2</sup> yr<sup>-1</sup> and 2,416 tC km<sup>-2</sup> yr<sup>-1</sup> for black shales and between 83 tC km<sup>-2</sup> yr<sup>-1</sup> and 1,558 tC km<sup>-2</sup> yr<sup>-1</sup> for marly limestones over the study period, which may be linked to differences in the rock chemistry. Following the quantification of the diffusive processes, chamber-based O<sub>2</sub> concentration measurements are used to calculate O<sub>2</sub> fluxes. The rate of O<sub>2</sub> consumption increased with production of CO<sub>2</sub>, and with increased temperature, but the O<sub>2</sub> : CO<sub>2</sub> molar ratios were on average 10 : 1. If O<sub>2</sub> consumption occurs by both rock organic carbon oxidation and sulfide oxidation, these measurements suggest an additional O<sub>2</sub> sink that needs to be identified, or could be explained by a significant export of dissolved inorganic carbon from the weathering zone. Together, our findings refine the tools we have to probe CO<sub>2</sub> and O<sub>2</sub> exchange in rocks at Earth's surface and shed new light on CO<sub>2</sub> and O<sub>2</sub> fluxes, their drivers and the fate of rock-derived carbon.

## 3.2 Introduction

Sedimentary rocks cover ~ 64 % of the present-day continental surface of Earth (Hartmann and Moosdorf, 2012) and contain vast amounts of carbon in the form of either carbonate minerals or organic matter (Petsch, 2014). The physical and chemical breakdown of these rocks can act as a source of carbon to the near-surface reservoirs (hydrosphere-biosphere-pedosphere-atmosphere) and can be a sink of oxygen, in turn exerting an important control on the evolution of climate and life (Berner and Berner, 2012; Berner, 1999; Sundquist and Visser, 2003). The rates of physical erosion and chemical weathering tend to be high in steep mountainous areas where more than half of Earth's total denudation occurs (Larsen et al., 2014). During mountain building, sedimentary rocks exhumed and exposed to the surface typically release CO<sub>2</sub> and consume O<sub>2</sub> from air or water via oxidative weathering (Hilton and West, 2020). In the global present-day carbon cycle, the oxidation of petrogenic organic carbon (OC<sub>petro</sub>) contributes ~ 40 MtC yr<sup>-1</sup> – 100 MtC yr<sup>-1</sup> to the atmosphere (Petsch, 2014). Another major source of carbon and sink of oxygen is the oxidation of sedimentary sulfide minerals that produce sulfuric acid that can, in turn, dissolve carbonate minerals (Calmels et al., 2007; Li et al., 2008; Torres et al., 2014), contributing ~ 31 MtC yr<sup>-1</sup> – 36 MtC yr<sup>-1</sup> to the atmosphere (Berner and Berner, 2012; Burke et al., 2018) and representing a major input of sulfate to the oceans (Burke et al., 2018; Halevy et al., 2012). On a global scale, these two chemical weathering pathways together emit roughly as much carbon to the atmosphere as is removed by the weathering of silicate minerals with a flux of ~ 90 MtC yr<sup>-1</sup> – 140 MtC yr<sup>-1</sup> (Gaillardet et al., 1999; Moon et al., 2014). Furthermore, there is an apparent dominance of CO<sub>2</sub> release from chemical weathering of sulfide and carbonate minerals over CO<sub>2</sub> drawdown via silicate dissolution where high erosion rates of sedimentary rocks are recorded (Bufe et al., 2021). Over the past 800,000 years, a decline of the atmospheric O<sub>2</sub> concentration may be associated with changes in the global oxidative weathering fluxes (Stolper et al., 2016; Yan et al., 2021).

To improve the understanding of the changes of Earth's surface conditions over geological timescales, it is crucial to better constrain the modern contributions of the different weathering pathways to the global carbon, oxygen and sulfur cycles, their spatial distribution and the mechanisms that control them (Berner and Berner, 2012; Mills et al., 2021). To do this, we must consider sedimentary rocks in the holistic framework of the critical zone that extends from the top of the canopy down to the base of the groundwater zone and that is controlled by a coupling of physical, chemical, biological and geological processes (Brantley et al., 2007; Gaillardet et al., 2018). The evolution of the critical zone over timescales relevant to weathering reactions (i.e., 100s to 1,000s of years) (White and Brantley, 2003) can be investigated by

theoretical modeling based on weathering profiles (measured depletion of elements of interest towards the surface) and relies on input kinetics of the weathering reactions (Bao et al., 2017; Bolton et al., 2006). Field-based observations are needed to constrain the weathering kinetics and what is controlling them, and to validate the model outcomes describing the modern weathering fluxes. Nevertheless, reports on *in situ* measurements of the gas exchange between rocks undergoing weathering and the atmosphere remain scarce.

The first field-based fluxes of weathering-derived CO<sub>2</sub> were reported by Keller and Bacon (1998) for shallow soils underlain by glacial till dominated by shales, using radiocarbon and stable carbon isotopes to differentiate the shale-derived CO<sub>2</sub> from modern carbon cycled by soil respiration. More recently, Tune et al. (2020) found substantial CO<sub>2</sub> release and O<sub>2</sub> depletion in bedrock undergoing weathering below a forested hillslope, with carbon sourced from superficial soils, deep roots or OC<sub>petro</sub> oxidation. Both studies determined the gaseous fluxes on the basis of profiles of the CO<sub>2</sub> concentration in air sampled from boreholes extending to depths of ~ 7 m (Keller and Bacon, 1998) and of ~ 15 m (Tune et al., 2020), using Fick's law:

$$j_X = -D_X \times \frac{dC_X}{dz} \quad (3-1)$$

where  $j_X$  is the molar flux (mol m<sup>-2</sup> s<sup>-1</sup>) of the particular gas species  $X$  and  $D_X$  its diffusivity (i.e., the capability to allow diffusion, m<sup>2</sup> s<sup>-1</sup>) in the studied vadose zone, and where  $\frac{dC_X}{dz}$  describes the change of the concentration (mol m<sup>-3</sup>) over depth (m). An alternative approach was introduced by Soulet et al. (2018) using gas accumulation chambers drilled into shallow weathering zones. Instead of calculating a carbon flux from a presupposed diffusion coefficient, which can introduce uncertainties (Maier and Schack-Kirchner, 2014), this method allows direct monitoring of the CO<sub>2</sub> release in real-time, similar to surface chambers that are commonly used for soil surfaces (Oertel et al., 2016). Drilled chambers have some additional benefits because they allow studying weathering processes in settings with high erosion rates that would pose a threat to the longevity of surface chambers (Soulet et al., 2021, 2018). Direct measurements of CO<sub>2</sub> fluxes have recently provided new insights into how temperature, precipitation and topography control the size of CO<sub>2</sub> emissions from marly limestones (Soulet et al., 2021) and mudstones (Chapter 2). However, for weathering chambers installed within the rock face, three aspects have remained unexplored: i) the rock volume that contributes to the CO<sub>2</sub> accumulation measured in the chamber; ii) how the diffusive movement of CO<sub>2</sub> in the shallow weathering zone is impacted by short-term environmental changes (e.g., in temperature and hydrology); and iii) the quantification of O<sub>2</sub> depletion during oxidative weathering.

In this study, we investigate the weathering driven exchange of CO<sub>2</sub> and O<sub>2</sub> by installing chambers into black shales and marly limestones undergoing oxidation at two study sites in the

steep terrains of the Draix-Bléone observatory, France (Draix-Bléone Observatory, 2015; Gaillardet et al., 2018; Mathys and Klotz, 2008). In support of previous research from an outcrop at the same observatory (Soulet et al., 2021), we find that chamber-based CO<sub>2</sub> emissions vary significantly over one year, linked to changes in temperature and precipitation. A new theoretical framework is developed and applied to quantify the rock pore space that is probed during CO<sub>2</sub> flux measurements. This allows us to normalize CO<sub>2</sub> accumulation rates based on a contributing rock volume, and return estimates of fluxes emitted from the surface of rock outcrops. We are also able to characterize the diffusive movement of CO<sub>2</sub>. Using Fick's law (Equation 3-1), measurements of the O<sub>2</sub> concentration in the chambers are then used to quantify the O<sub>2</sub> consumption in the studied rocks. Together, we provide new insights into the exchange of CO<sub>2</sub> and O<sub>2</sub> in the shallow weathering zone of sedimentary rocks.

### 3.3 Material and methods

#### 3.3.1 Study area

The two study sites are located in the catchments of the Brusquet (catchment area 1.08 km<sup>2</sup>) and Moulin (0.08 km<sup>2</sup>) of the Draix-Bléone observatory (Draix-Bléone Observatory, 2015; Mathys and Klotz, 2008), which is part of the French network of critical zone observatories (OZCAR) (Gaillardet et al., 2018). The Brusquet site is located at 44.16251° N 6.32330° E at 847 m.a.s.l. and the Moulin site at 44.14146° N 6.36095° E at 874 m.a.s.l. (Figure 3-1). The catchments of the Draix-Bléone observatory are well monitored, including continuous measurements of river water discharge, river suspended load and bedload transport, and meteorological data over the last 4 decades (Carriere et al., 2020; Cras et al., 2007; Draix-Bléone Observatory, 2015; Mallet et al., 2020; Mathys et al., 2003; Mathys and Klotz, 2008). This data provides climatic, hydrodynamic and geomorphic contexts for studies of oxidative weathering. Prior work has examined the occurrence of OC<sub>petro</sub> in the Brusquet, Moulin and Laval catchments (Copard et al., 2006; Graz et al., 2012, 2011). The Laval catchment (0.86 km<sup>2</sup>), which neighbours the Moulin catchment (Figure 3-1), is the location of previous *in situ* measurements of rock-derived CO<sub>2</sub> (Soulet et al., 2021, 2018).

The Moulin catchment overlays Callovian to Oxfordian marly limestones (Graz et al., 2012; Mathys et al., 2003). In contrast, the lithology of the Brusquet catchment consists of a sequence of Bajocian marly limestones, Aalenian grey shales and limestones to Toarcian black shales (Copard et al., 2006; Graz et al., 2011), with the study site located on the latter (Figure 3-1).

The climate is transitional between Alpine and Mediterranean with a hot and dry summer, including short and intense rainfall events during thunderstorms (up to 150 mm h<sup>-1</sup>),

with rainfall events of lower intensity typically during spring and autumn (Carriere et al., 2020; Mallet et al., 2020; Mathys et al., 2003; Soulet et al., 2021). During winter, more than 100 days of frost can occur (Oostwoud Wijdenes and Ergenzinger, 1998; Rovéra and Robert, 2006) and frost-cracking from ice-segregation was found to control hillslope regolith production (Ariagno et al., 2022). The mean annual rainfall is  $\sim 900$  mm and the mean annual air temperature is  $\sim 11$  °C defined by high solar radiation ( $> 2,300$  h yr<sup>-1</sup>) (Mallet et al., 2020; Mathys and Klotz, 2008; Soulet et al., 2021).

Together, the climate and the erodible lithology of finely bedded, mechanically weak rocks result in a badland morphology with V-shaped gullies, high physical weathering rates and abrupt, sediment-loaded floods (Antoine et al., 1995; Cras et al., 2007; Le Bouteiller et al., 2021; Mathys et al., 2003). These features limit the development of soils and vegetation cover. In the late 19<sup>th</sup> century, following overgrazing in the wider area of the observatory, the Brusquet catchment was reforested (Cras et al., 2007; Mathys et al., 2003). Today  $\sim 87$  % of the catchment area of Brusquet is vegetated, in contrast to  $\sim 46$  % and  $\sim 32$  % of the Moulin and Laval catchments, respectively (Carriere et al., 2020; Cras et al., 2007). The sediment export fluxes of the Brusquet catchment are on average  $\sim 70$  t km<sup>-2</sup> yr<sup>-1</sup>, and  $\sim 5,700$  t km<sup>-2</sup> yr<sup>-1</sup> and  $\sim 14,300$  t km<sup>-2</sup> yr<sup>-1</sup> for the Moulin and Laval catchments, respectively (Carriere et al., 2020; Mathys et al., 2003). Taking a regolith bulk density of  $\sim 1.3$  t m<sup>-3</sup> –  $1.8$  t m<sup>-3</sup> into account (Bechet et al., 2016; Mallet et al., 2020; Mathys and Klotz, 2008; Oostwoud Wijdenes and Ergenzinger, 1998), a physical erosion rate of  $\sim 0.04$  mm yr<sup>-1</sup> –  $0.05$  mm yr<sup>-1</sup>,  $\sim 3.2$  mm yr<sup>-1</sup> –  $4.4$  mm yr<sup>-1</sup> and  $\sim 8$  mm yr<sup>-1</sup> –  $11$  mm yr<sup>-1</sup> can be estimated for the Brusquet, Moulin and Laval catchments, respectively. However, these values are catchment-scale averages, and the physical erosion can significantly vary spatially. On steep, bare slopes, the erosion rates may be more comparable between the catchments of the Draix-Bléone observatory (Bechet et al., 2016; Carriere et al., 2020; Mathys et al., 2003).

The bare surfaces in the catchments are characterized by four morphologically different layers: i) near surface, loose detrital cover of locally produced clasts or colluvial material with a thickness of  $\sim 0$  cm –  $10$  cm; ii) below, the upper, fine regolith with a thickness of  $\sim 5$  cm –  $20$  cm; and iii) the lower, coarse regolith with a thickness of  $\sim 10$  cm –  $20$  cm; iv) the unweathered bedrock at the bottom (Maquaire et al., 2002; Mathys and Klotz, 2008; Oostwoud Wijdenes and Ergenzinger, 1998; Rovéra and Robert, 2006). The compactness and density of these layers increase, while the porosity decreases (from values of up to  $\sim 50$  %), over depth towards the unweathered marl bedrock (grain density  $\sim 2.7$  t m<sup>-3</sup>, porosity  $\sim 10$  % –  $20$  %) (Bechet et al., 2016; Lofi et al., 2012; Mallet et al., 2020; Maquaire et al., 2002; Mathys and Klotz,

2008; Travelletti et al., 2012). The thickness of the weathering profile varies laterally with the thickest regolith layers and detrital cover on crests, minimal development in thalwegs and intermediate in gullies (Esteves et al., 2005; Maquaire et al., 2002).

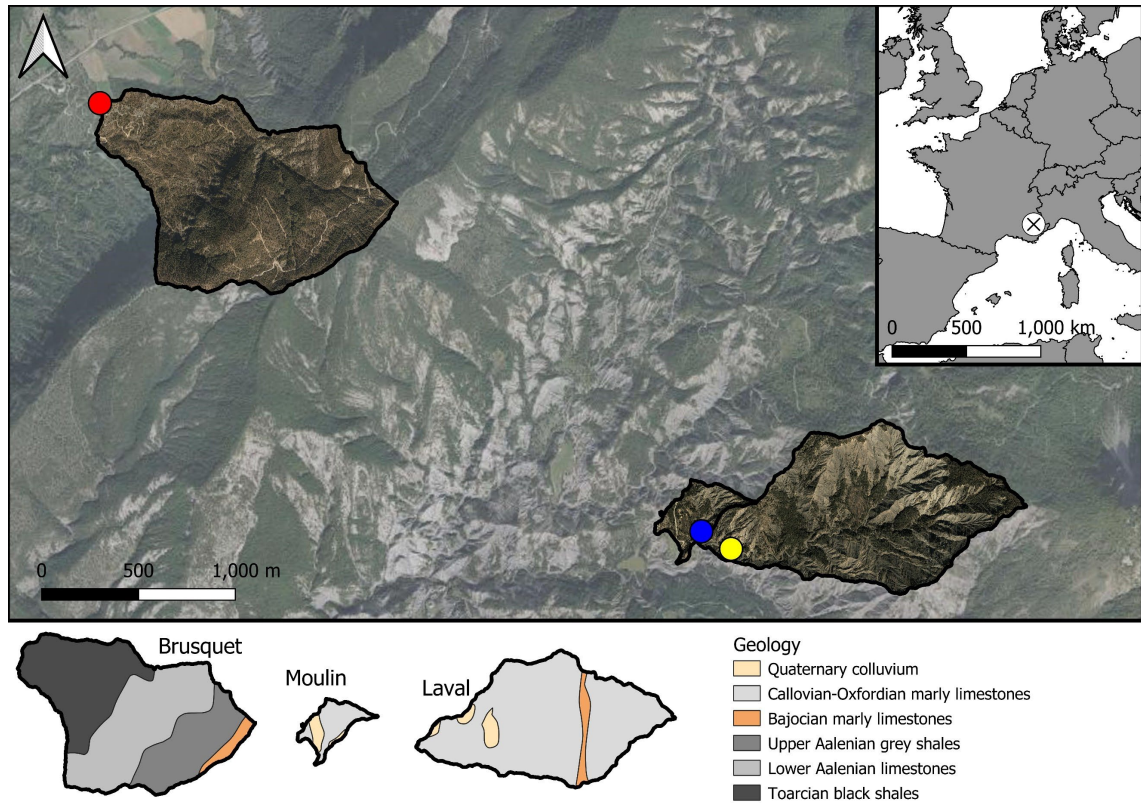


**Figure 3-1. Location of the French Draix-Bléone observatory and of the study sites for CO<sub>2</sub> and O<sub>2</sub> monitoring.** Study sites are located in the Brusquet catchment (red circle) and in the Moulin catchment (blue circle). The location of previous research in the Laval catchment is given for reference (yellow circle) (Soulet et al., 2021, 2018), alongside geological maps of these catchments (Janjou, 2004). Meteorological stations are present at each of the catchment outlets with a maximum distance to the study sites of 200 m (Draix-Bléone Observatory, 2015). Catchment-specific aerial imagery (2015) (Draix-Bléone Observatory, 2015) is shown alongside transparent aerial imagery of the wider area (2018 © IGN).

### 3.3.2 Drilled gas accumulation chambers

To measure the *in situ* production of CO<sub>2</sub> and consumption of O<sub>2</sub> by oxidative weathering reactions, we use drilled chambers. The chambers were visited 6 times over the study to capture seasonal changes in weather conditions, on 27/09/2018, 11/01 – 14/01/2019, 11/04 – 15/04/2019, 27/05 – 29/05/2019, 05/07 – 12/07/2019 and 27/09 – 02/10/2019. Their design has been previously detailed (Soulet et al., 2018). In summary, a horizontal chamber is drilled directly into the exposed rock which has been cleared of detrital cover. The shape ensures a large surface to volume ratio to benefit measurement of gas concentrations and enable

efficient trapping of CO<sub>2</sub>. To install the chambers of ~ 38 cm depth, a mechanical drill was used with a diameter of 2.9 cm. Rock powder left inside the chambers was blown away with a compressed-air gun. A small PVC tube is inserted in the entrance of each chamber that is closed with a rubber stopper holding two glass tubes fitted with Tygon® tubing. The latter allow either connection to a gas-sampling system or sealing with WeLock® clips. To further isolate the chamber from the atmosphere, the intersection of the PVC tube and regolith is sealed with a silicone sealant (Unibond® Outdoor), which we previously tested to be free of potential contaminants for gas sampling (Chapter 2).

At both the Brusquet and Moulin study sites, we installed one array of 4 chambers placed in a square (2 × 2) (Table 3-1; Figure 3-2). In each array, 2 chambers were placed in the same rock bed with a roughly horizontal orientation at the Brusquet site and roughly vertical at the Moulin site. The minimum distance between chambers was 70 cm. The aspect, hydrological and geomorphic setting of the location of both arrays is similar: they were placed at the upper margin of the watersheds in steep walls of gullies on a Southwest- (Brusquet) and South-facing aspect (Moulin). The chambers were drilled into bare rock faces devoid of roots and with minimal soil or vegetation cover in the vicinity to exclude a contribution by them to the CO<sub>2</sub> measurements (Figure 3-2).

**Table 3-1. Properties of gas accumulation chambers drilled into weathering sedimentary rocks in the Brusquet catchment and in the Moulin catchment.** For calculation of volume and inner surface area of the chambers, length and insertion depth of the PVC tube and rubber stopper are taken into account.

Chamber identifiers	Site	Same bed as chamber	Installation date	Depth (cm)	Volume (cm <sup>3</sup> )	Inner surface area (cm <sup>2</sup> )	
							short
1	M-C-1	Moulin	3	24/09/2018	41.0	278	367
2	M-A-2	Moulin	4	24/09/2018	39.5	263	346
3	M-D-3	Moulin	1	24/09/2018	38.0	255	335
4	M-B-4	Moulin	2	24/09/2018	39.0	262	345
5	B-F-5	Brusquet	6	25/09/2018	38.0	255	335
6	B-G-6	Brusquet	5	25/09/2018	37.0	255	335
7	B-H-7	Brusquet	8	25/09/2018	35.0	229	299
8	B-I-8	Brusquet	7	25/09/2018	35.0	235	308

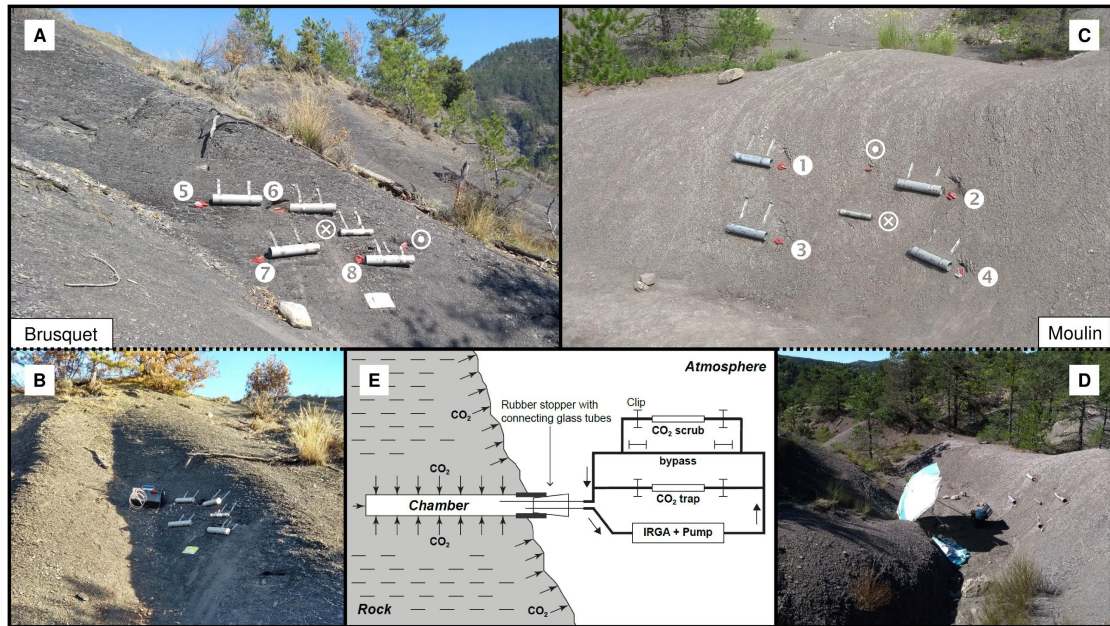


**Figure 3-2.** The study sites in the Brusquet catchment and in the Moulin catchment. Panels A and B: imagery of the Brusquet site. Panels C and D: imagery of the Moulin site. Identifiers of the CO<sub>2</sub> accumulation chambers (Table 3-1) are given next to their entrance. Furthermore, the location of temperature and relative humidity loggers in a further chamber with similar properties (circled dot) and on the rock surface (circled X) are shown. For scale, the grey cases (not used in the present study) next to the chambers are of ~40 cm length. Panel E: design of the chambers and the sampling system, adapted from Soulet et al. (2018).

### 3.3.3 Rock temperature and humidity

At both sites, a chamber with the same design was installed to hold a temperature and relative humidity logger (Lascar® EL-USB-2) (Figure 3-2) from 27/09/2018 onwards. A second logger was placed on the rock surface (monitoring the air directly above it) with the main body fitted inside a small PVC tube for physical protection and an aluminium foil wrapping around the tube to avoid alteration of the temperature measurement due to the dark colour of the housing of the sensor and the PVC tube.

Over the study period, technical issues with batteries of the temperature and relative humidity loggers prevented occasionally data collection. To fill the gaps in the direct chamber temperature measurements, we assess whether air temperatures from a local weather station can be used as a proxy. For this, we modify a modeling framework that describes soil temperatures at an hourly resolution by, amongst other variables, air temperature (Liang et al., 2014). The approach combines measured air temperatures with a Fourier-fitted function that describes the daily average temperature inside the rock chambers by weighting averaged air temperatures by the fractional duration of daylight ( $L$ ) at the latitude of the Draix-Bléone

observatory. In more detail, we estimate the current chamber temperature  $T_{\text{Chamber}}$  at an hourly resolution as follows:

$$T_{\text{Chamber}} = T_{\text{mean}} \times \text{coeff}_A + (T_{\text{Air}-6\text{h}} - T_{\text{mean}}) \times \text{coeff}_B \quad (3-2)$$

where  $T_{\text{Air}-6\text{h}}$  is the hourly air temperature from nearby meteorological stations (Draix-Bléone Observatory, 2015) delayed by 6 hours,  $\text{coeff}_A$  and  $\text{coeff}_B$  are site-specific fitting coefficients, and  $T_{\text{mean}}$  is the long-term trend of rock temperature described by:

$$T_{\text{mean}} = \text{coeff}_{C1} + \text{coeff}_{C2} \times \cos(\text{coeff}_{C3} \times T_{\text{Air},7\text{d}} \times L) \\ + \text{coeff}_{C4} \times \sin(\text{coeff}_{C3} \times T_{\text{Air},7\text{d}} \times L) \quad (3-3)$$

where  $\text{coeff}_{C1}$  to  $\text{coeff}_{C4}$  are site-specific fitting coefficients in a 1<sup>st</sup> order Fourier-model, and  $T_{\text{Air},7\text{d}}$  is the 7 day average of the past air temperatures at hourly resolution. Using the site-specific air temperatures, this approach simulates  $T_{\text{Chamber}}$  well, with a root-mean-square error (RMSE) of 1.8 °C for the Brusquet catchment and 2.2 °C for the Moulin catchment (Figure 3-3) (Supplementary Section 3.8.1).

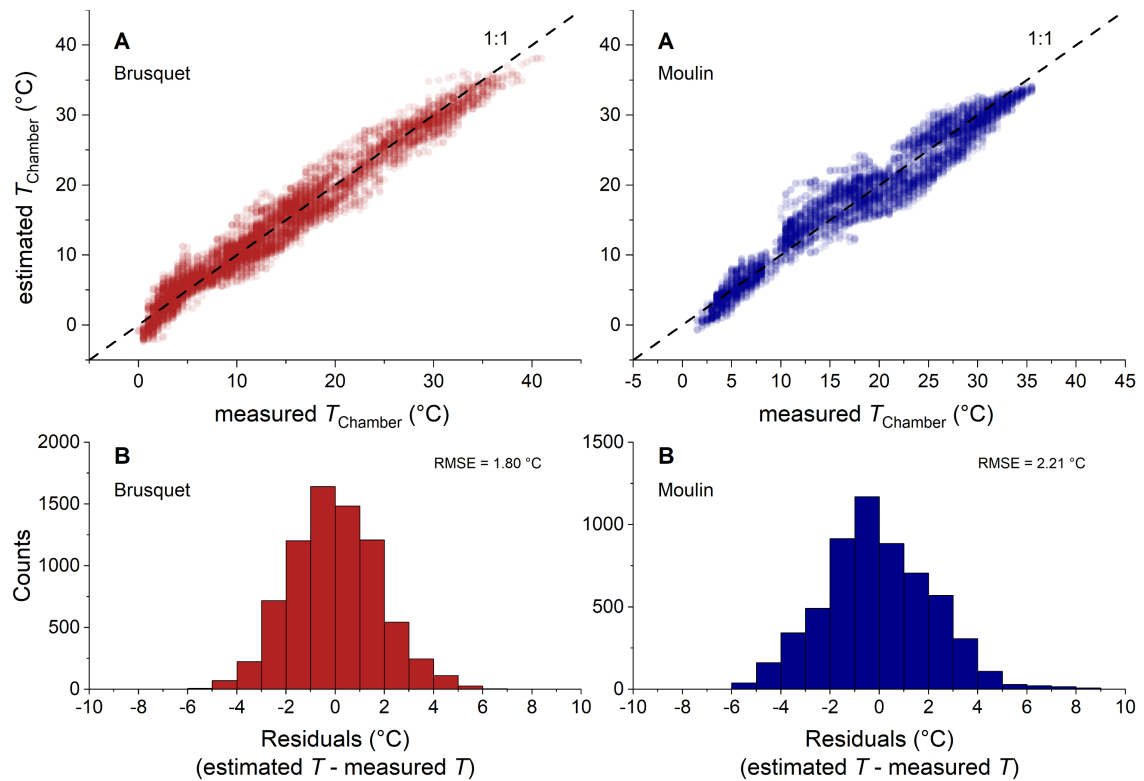


**Figure 3-3. Overview of modeled chamber temperatures.** Panels A: comparison of chamber temperatures measured and estimated by a modeling framework based on air temperature and the fractional duration of daylight at the latitude of the Draix-Bléone observatory at hourly resolution for the Brusquet catchment (red) and the Moulin catchment (blue), which agree with a 1 : 1 relation (dashed line). Panels B: normally distributed residuals between the measured temperatures and the modeling framework.

### 3.3.4 Partial pressure of rock CO<sub>2</sub>

The partial pressure of CO<sub>2</sub> ( $p\text{CO}_2$ ) was measured alongside air pressure to determine the concentrations of CO<sub>2</sub> in the rock chambers with an infra-red gas analyser (IRGA; EGM-5 Portable Gas Analyser, PP Systems). This is equipped with an internal pump and calibrated to  $p\text{CO}_2$  in the range of 0 ppmv to 30,000 ppmv. First, the closed-loop sampling system is purged of CO<sub>2</sub> using an inline CO<sub>2</sub> scrub (soda lime) (Hardie et al., 2005). This is then connected to a chamber to measure the ambient  $p\text{CO}_2$ . After a short equilibration, the  $p\text{CO}_2$  in the chamber ( $p\text{CO}_{2\text{ Chamber}}$ ) is calculated from the CO<sub>2</sub> concentration in the combined air volume of the chamber and the sampling system by accounting for the dilution introduced from the CO<sub>2</sub>-free air that was originally contained within the sampling system (Chapter 2) (Soulet et al., 2018). To ensure that the determined  $p\text{CO}_{2\text{ Chamber}}$  is representative of the ambient  $p\text{CO}_2$  in the rock pores around the chamber ( $p\text{CO}_{2\text{ Rock}}$ ), measurements are only considered if the chambers were left closed overnight so that the production of CO<sub>2</sub> from oxidative weathering could reach a steady-state in respect to diffusion between rock pores, chamber and atmosphere.

### 3.3.5 CO<sub>2</sub> flux measurements

Real-time measurements of CO<sub>2</sub> release in drilled chambers have been previously described in detail (Soulet et al., 2018) and used to quantify CO<sub>2</sub> flux (Chapter 2) (Soulet et al., 2021). In summary, one CO<sub>2</sub> flux measurement consists of a series of repeated accumulations (typically 8 or more) that are recorded over time after determining the  $p\text{CO}_{2\text{ Rock}}$ . First, the  $p\text{CO}_{2\text{ Chamber}}$  is lowered to a value close to that of the local atmosphere value using soda lime or a zeolite sieve (Section 3.3.6) (Figure 3-2E). Then, CO<sub>2</sub> is allowed to build up, typically over ~ 6 min, before the CO<sub>2</sub> in the chamber is again removed to a near-atmospheric value. For each repeat, the rate of CO<sub>2</sub> accumulation  $q$  (mgC min<sup>-1</sup>) is calculated by fitting an exponential model to the recorded  $p\text{CO}_2$  change, following (Pirk et al., 2016):

$$\frac{dm(t)}{dt} = q - \lambda \times (m(t) - m_0) \quad (3-4)$$

where  $\frac{dm(t)}{dt}$  is the carbon mass change (mgC) in the chamber with time (min),  $m_0$  is the initial carbon mass in the chamber (mgC), and  $\lambda$  (min<sup>-1</sup>) is the curvature of the mass change that relates to diffusion of CO<sub>2</sub> between rock pores, chamber and atmosphere (Soulet et al., 2018). For this, the carbon mass ( $m$ , mgC) in the chamber is obtained from:

$$m = p\text{CO}_{2\text{ Chamber}} \times V \times \frac{P}{R \times T} \times M_C \times 10^{-9} \quad (3-5)$$

where the measured  $p\text{CO}_{2\text{ Chamber}}$  is in ppmv (cm<sup>3</sup> m<sup>-3</sup>),  $V$  is the combined volume (cm<sup>3</sup>) of the chamber and the sampling system,  $P$  is the pressure (Pa),  $R$  is the universal gas constant (m<sup>3</sup> Pa K<sup>-1</sup> mol<sup>-1</sup>),  $T$  is the chamber temperature (K), and  $M_C$  is the molar mass of carbon (g mol<sup>-1</sup>).

The CO<sub>2</sub> accumulation rate  $q$  can be normalized to the internal surface area of the chamber  $S_{\text{Chamber}}$  (i.e., area of exchange with the surrounding rock, m<sup>2</sup>) to account for differences in the depth of the chambers, which are related to differences in volume and surface area, giving a repeat-specific flux  $Q$  (mgC min<sup>-1</sup> m<sup>-2</sup>):

$$Q = \frac{q}{S_{\text{Chamber}}} . \quad (3-6)$$

Alternatively, the CO<sub>2</sub> accumulation can be reported as a molar-based flux  $J_{\text{CO}_2}$  (mmol CO<sub>2</sub> m<sup>-2</sup> min<sup>-1</sup>):

$$J_{\text{CO}_2} = \frac{j_{\text{CO}_2}}{S_{\text{Chamber}}} = \frac{q}{M_{\text{C}} \times S_{\text{Chamber}}} \quad (3-7)$$

where  $j_{\text{CO}_2}$  (mmol CO<sub>2</sub> min<sup>-1</sup>) is the molar-based analogue to  $q$ .

Previous work has noted that the CO<sub>2</sub> accumulation rate during the first measurements is typically higher than subsequent repeats (Soulet et al., 2018). To calculate a CO<sub>2</sub> flux from these repeated accumulations (consisting of  $n$  repeats), previous work excluded the first 3 repeats ( $q_1$  to  $q_3$ ), and took the average of a minimum of 3 further repeats ( $q_4$  to  $q_{n \geq 6}$ ) (Chapter 2) (Soulet et al., 2021, 2018). We examine this further using new data collected here, which also provides constraint on the nature of the gas exchange around the chambers.

### 3.3.6 CO<sub>2</sub> sampling

During a CO<sub>2</sub> flux measurement, the CO<sub>2</sub> in the chamber can be sampled by circulating it through a zeolite molecular sieve cartridge (MSC) mounted in parallel to the monitoring line (Hardie et al., 2005; Soulet et al., 2018). This is typically done when lowering the  $p\text{CO}_2$  Chamber to a near-atmospheric value by using the zeolite sieve instead of the CO<sub>2</sub> scrub. The theoretical volume of carbon loaded onto a sieve is estimated by adding up the  $p\text{CO}_2$  maxima for each trapping episode minus the final  $p\text{CO}_2$  after trapping (near-atmospheric value), while accounting for the combined volume of the chamber and the sampling system.

The zeolite sieves were heated in the laboratory to 425 °C and purged with high-purity nitrogen gas to release the CO<sub>2</sub> trapped onto them prior to cryogenic purification under vacuum (Garnett and Murray, 2013). The theoretically estimated sampled volume of CO<sub>2</sub> from the chamber-based  $p\text{CO}_2$  measurements ( $V_{\text{CO}_2\text{-IRGA}}$ , mL) can be compared with the volume recovered in the laboratory ( $V_{\text{CO}_2\text{-MSC}}$ , mL) giving a sampling ratio ( $SR$ , unitless) (Chapter 2):

$$SR = \frac{V_{\text{CO}_2\text{-MSC}}}{V_{\text{CO}_2\text{-IRGA}}} . \quad (3-8)$$

For this, all volumes of CO<sub>2</sub> are normalized to 0 °C and 1,013 mbar.

The  $SR$  thus allows us to independently check calculations of carbon mass using the  $p\text{CO}_2$  data combined with the gas line and chamber volume measurements (Equation 3-4 and Equation 3-5).

### 3.3.7 Measuring $pO_2$ and O<sub>2</sub> fluxes

While measuring  $pCO_2$ , the EGM-5 Portable Gas Analyser, incorporating the IRGA, also records the partial pressure of oxygen in the chamber ( $pO_{2 \text{ Chamber}}$ , % v/v) with an electrochemical O<sub>2</sub> sensor. Previous work in the Laval catchment noted O<sub>2</sub> consumption relative to the local atmosphere, but did not seek to quantify an O<sub>2</sub> flux (Soulet et al., 2018). The methods used to measure CO<sub>2</sub> accumulation do not allow observation of a clear change of  $pO_{2 \text{ Chamber}}$  over time because of two reasons. First, the precision of the O<sub>2</sub> sensor of  $\geq 0.1$  % (v/v) is not high enough to observe any real-time change of the  $pO_{2 \text{ Chamber}}$ . Second, oxygen should be consumed during oxidative weathering of sulfide minerals and OC<sub>petro</sub>, and so we would require a method that replenishes oxygen, which was not done while measuring CO<sub>2</sub> accumulation.

However, an alternative method to calculate an O<sub>2</sub> flux is based on Fick's law, using the diffusive gradient of the partial pressure of O<sub>2</sub> in the rock ( $pO_{2 \text{ Rock}}$ ) towards the atmospheric O<sub>2</sub> concentration ( $pO_{2 \text{ Atm}}$ ). To obtain  $pO_{2 \text{ Rock}}$ , the  $pO_{2 \text{ Chamber}}$  measured after connecting the sampling system to the chamber has to be corrected for the oxygen concentration in the line of the sampling system (because we do not operate with an O<sub>2</sub> scrub), while accounting for the volumes of the chamber and the sampling line. Furthermore, the  $pO_2$  recorded before and during a measurement is corrected for instrument drift. The drift correction is based on measuring the  $pO_{2 \text{ Atm}}$  directly before or after a chamber-based measurement and assuming an average atmospheric oxygen concentration of 20.95 % (v/v).

To quantify the exchange of O<sub>2</sub> between the chamber, connected rock pores and the atmosphere ( $j_{O_2}$ , mmol O<sub>2</sub> min<sup>-1</sup>), we describe the process via a diffusive transfer controlled by the diffusivity of O<sub>2</sub> ( $D_{O_2}$ , cm<sup>2</sup> min<sup>-1</sup>) across a spatial parameter  $\omega$  (describing a combined movement over depth and area, cm<sup>1</sup> cm<sup>-2</sup>), according to Fick's law (Equation 3-1):

$$j_{O_2} = \frac{D_{O_2}}{\omega} \times (pO_{2 \text{ Rock}} - pO_{2 \text{ Atm}}) \times \frac{P}{R \times T} \times 10^{-3} . \quad (3-9)$$

If we assume that  $\omega$  is the same for O<sub>2</sub> and CO<sub>2</sub>, linking the space of oxygen consumption and carbon dioxide release,  $D_{O_2}$  can be related to the diffusivity of CO<sub>2</sub> ( $D_{CO_2}$ , cm<sup>2</sup> min<sup>-1</sup>) based on their ideal relation in air, which is independent of temperature (Angert et al., 2015):

$$\frac{D_{CO_2}}{D_{O_2}} = 0.76 = \frac{D_{CO_2}}{\omega} \div \frac{D_{O_2}}{\omega} . \quad (3-10)$$

In more detail, differences in the effective diffusivities of gas species in air and in the shallow weathering zone depend on the structure of the air-filled pore space, which is expected to have identical impacts on the gaseous movement of O<sub>2</sub> and CO<sub>2</sub> (Angert et al., 2015; Millington, 1959; Penman, 1940). Thus, if the term  $\frac{D_{CO_2}}{\omega}$  (cm<sup>3</sup> min<sup>-1</sup>) can be quantified by other means (for instance, through analysis of the  $pCO_{2 \text{ Rock}}$  and CO<sub>2</sub> flux data), we have the ability to quantify  $j_{O_2}$ . These themes will be discussed later (Section 3.5.1 and Section 3.5.4). An uncertainty of  $j_{O_2}$  can

be estimated from propagating the uncertainties of the input variables, including the uncertainty associated with the drift correction which is obtained from monitoring the atmosphere over similar time intervals compared to the chamber-based measurement.

## 3.4 Results

### 3.4.1 Chamber temperature and meteorological conditions

Over the study period (27/09/2018 – 02/10/2019), the variability in environmental conditions at the Brusquet catchment was similar to the Moulin catchment. The temperatures of the local atmosphere, in the chambers and at the rock surface exhibited pronounced daily and seasonal changes (Table 3-2) (Figure 3-4A – F). In general, the occurrence and extent of rainfall events was comparable at both sites, but the Brusquet catchment received on average less rainfall than the Moulin catchment, with cumulative precipitations over the study period of 773 mm and 1,033 mm, respectively (Figure 3-4G – H). In addition, the relative air humidity in the chambers was high and constant with values of  $\sim 93.1 \pm 4.5$  % ( $\pm$  standard deviation, SD) and  $\sim 91.3 \pm 4.1$  % at the Brusquet and Moulin sites, respectively (not considering gaps in the record) (Figure 3-4I – J).

**Table 3-2. Overview of the variability of air temperature, chamber temperature and rock surface temperature.** Considered is the study period (27/09/2018 – 02/10/2019) (Figure 3-4). A gap in the record of rock surface temperatures at the Moulin site (25/10/2018 – 11/01/2019) is not considered.

Variable	Daily averages			Hourly resolution	
	Average ( $\pm$ SD)	Min.	Max.	Min.	Max.
Air temperature					
<i>Brusquet</i>	10.5 $\pm$ 7.4	-4.9	29.5	-9.5	41.5
<i>Moulin</i>	10.5 $\pm$ 7.3	-4.0	27.9	-9.1	38.3
Chamber temperature					
<i>Brusquet</i>	15.7 $\pm$ 9.4	0.7	34.6	-1.1	41.0
<i>Moulin</i>	16.6 $\pm$ 9.7	0.2	33.0	-1.5	36.1
Rock surface temperature					
<i>Brusquet</i>	14.4 $\pm$ 8.7	-1.6	35.3	-7.0	56.0
<i>Moulin</i>	17.9 $\pm$ 9.0	-1.4	37.3	-8.5	62.5

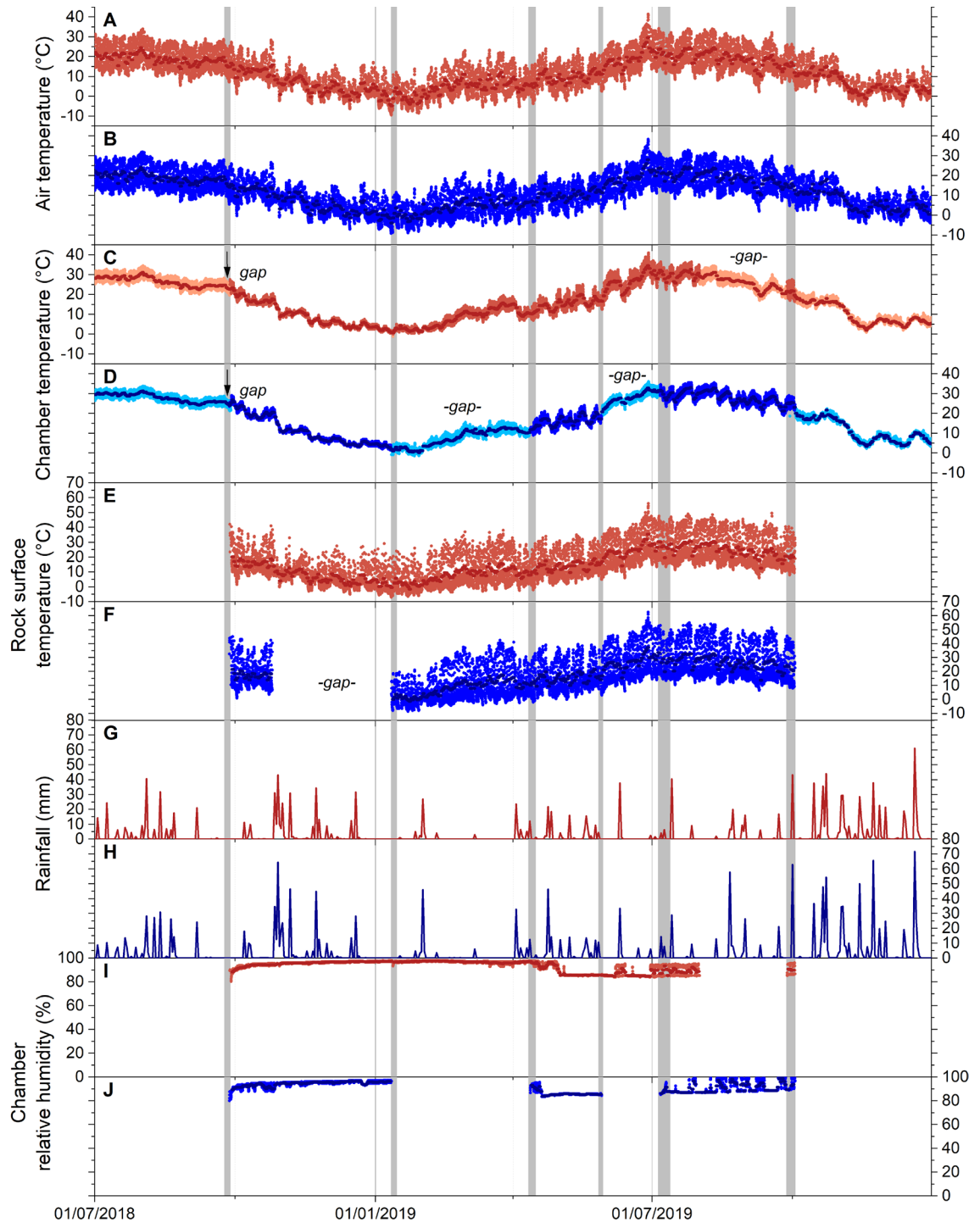


**Figure 3-4. Environmental variables for weathering chambers in 2018 and 2019.** Grey shaded areas show fieldwork visits in the Brusquet catchment (red) and in the Moulin catchment (blue). Daily averages are shown by darker colours in all panels. Panels A and B: hourly air temperatures from meteorological stations (Draix-Bléone Observatory, 2015). Panels C and D: hourly chamber temperatures. Estimated chamber temperatures are indicated by lighter colours (Section 3.4.1) and are shown for gaps in the logger record (denoted). Panels E and F: hourly rock surface temperatures. Panels G and H: daily rainfall. Panels I and J: relative humidity in the chambers, with gaps in the record similar to the chamber temperatures.

### 3.4.2 $p\text{CO}_2$ measurements and CO<sub>2</sub> collection

Over the sampling period, the  $p\text{CO}_{2\text{Rock}}$  varied between the chambers and over time. In the Brusquet catchment, the observed  $p\text{CO}_{2\text{Rock}}$  values ranged from 588 ppmv to 3,378 ppmv with an average of  $1,490 \pm 743$  ppmv ( $\pm$  SD, if not reported otherwise,  $n = 28$ ), and from 543 ppmv to 2,680 ppmv with an average of  $1,492 \pm 633$  ( $n = 32$ ) in the Moulin catchment (Table 3-3).

**Table 3-3. Chamber-specific overview of CO<sub>2</sub> partial pressures in the shallow weathering zone. Variations are reported as 1 SD.**

Chamber identifiers		Site	$p\text{CO}_{2\text{Rock}}$ (ppmv)			
<i>short</i>	<i>long</i>		Average ( $\pm$ SD)	n	Min.	Max.
5	B-F-5	Brusquet	861 $\pm$ 254	5	588	1,167
6	B-G-6	Brusquet	1,985 $\pm$ 771	12	936	3,378
7	B-H-7	Brusquet	936 $\pm$ 340	4	588	1,399
8	B-I-8	Brusquet	1,405 $\pm$ 438	7	721	2,000
<i>Brusquet totals</i>			<i>1,490 <math>\pm</math> 743</i>	<i>28</i>		
1	M-C-1	Moulin	1,740 $\pm$ 654	10	551	2,499
2	M-A-2	Moulin	720 $\pm$ 110	4	543	834
3	M-D-3	Moulin	1,881 $\pm$ 127	3	1,755	2,054
4	M-B-4	Moulin	1,456 $\pm$ 576	15	681	2,680
<i>Moulin totals</i>			<i>1,492 <math>\pm</math> 633</i>	<i>32</i>		

Following the determination of  $p\text{CO}_{2\text{Rock}}$ , a total of 78 CO<sub>2</sub> flux measurements were conducted, and each chamber was visited at least once each season during the study period. In the Brusquet catchment, 37 measurements were performed, of which 26 consisted of 8 – 10 repeats and 6 of more than 10 repeats. In the Moulin catchment, 41 measurements were made, of which 26 consisted of 8 – 10 repeats and 11 of more than 10 repeats. Every one of the CO<sub>2</sub> flux measurements showed an initial decline of accumulation rates that approached a constant value of peak CO<sub>2</sub> concentrations (Figure 3-5). Considering the repeats 6 – 8, averages of the CO<sub>2</sub> accumulation rates varied between chambers and over time at each single chamber, with occurrence of the lowest accumulation rates in winter and highest in summer. In more detail, on four visits, a chamber was measured twice a day and the observed CO<sub>2</sub> release was higher in the afternoon than in the morning, coinciding with an increase of the chamber temperature. Overall, the observed CO<sub>2</sub> accumulation rates (averages of  $q_6$  to  $q_8$ ) ranged from  $1.2 \mu\text{gC min}^{-1}$  to  $48.2 \mu\text{gC min}^{-1}$  with an average of  $15.2 \pm 11.7 \mu\text{gC min}^{-1}$  ( $n = 32$ ), and from  $1.1 \mu\text{gC min}^{-1}$  to  $28.8 \mu\text{gC min}^{-1}$  with an average of  $11.5 \pm 8.0 \mu\text{gC min}^{-1}$  ( $n = 37$ ) in the Brusquet catchment and in the Moulin catchment, respectively. The associated values of the fitting parameter  $\lambda$  (Equation 3-4) ranged from  $0.061 \text{ min}^{-1}$  to  $0.336 \text{ min}^{-1}$  with an average of

0.179 ± 0.076 min<sup>-1</sup> (n = 32), and from 0.018 min<sup>-1</sup> to 0.242 min<sup>-1</sup> with an average of 0.140 ± 0.061 min<sup>-1</sup> (n = 37) in the Brusquet catchment and in the Moulin catchment, respectively.

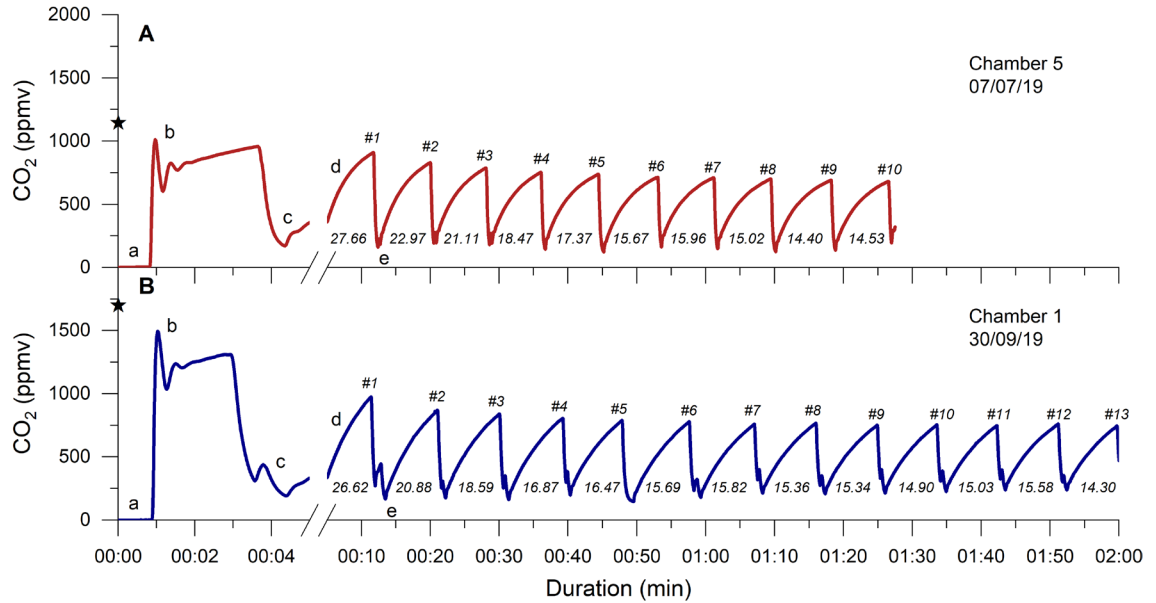


**Figure 3-5. Two examples of monitoring the CO<sub>2</sub> concentration in a chamber during a flux measurement.** Following connection, the CO<sub>2</sub>-free air of the sampling system (a) equilibrates with the partial pressure of CO<sub>2</sub> in the chamber (b), which is representative of pCO<sub>2</sub>Rock (denoted by ★). After the CO<sub>2</sub> in the chamber is removed to a near-atmospheric value (c), the first accumulation (d) is monitored (with a change in axis scale), followed by further removal (sometimes stepwise, e) and accumulation events (~6 min, numbers denoted with #). The measured accumulation rates (q, mgC min<sup>-1</sup> per chamber) are given for each repeat. The CO<sub>2</sub> flux measurement of chamber 5 on the 07/07/19 (Brusquet catchment, Panel A, red) consisted of 10 repeats, and the measurement of chamber 1 on the 30/09/19 (Moulin catchment, Panel B, blue) consisted of 13 repeats.

At each study site, CO<sub>2</sub> was sampled from two chambers. Following recovery from the zeolite sieves in the laboratory, the sampling ratio (SR, Equation 3-8) was quantified with an overall median of 1.03 (Table 3-4). Within the uncertainties, the SR is similar for samples from both study sites with somewhat higher values for samples from the Brusquet catchment compared to samples from the Moulin catchment.

**Table 3-4. Overview of the chamber-specific sampling ratio.** The SR (Equation 3-8) compares the estimated volumes of CO<sub>2</sub> sampled in the Brusquet catchment and in the Moulin catchment with volumes recovered in the laboratory from zeolite sieves.

Chamber identifiers		Site	Number of samples	Sampling ratio (SR, unitless)	
<i>short</i>	<i>long</i>			Median	Average ( $\pm$ SD)
1	M-C-1	Moulin	4	0.90	0.98 $\pm$ 0.25
4	M-B-4	Moulin	7	0.93	0.94 $\pm$ 0.10
6	B-G-6	Brusquet	7	1.04	1.05 $\pm$ 0.09
8	B-I-8	Brusquet	2	1.12	1.12 $\pm$ 0.04
<i>Total</i>			<i>20</i>	<i>1.03</i>	<i>1.00 <math>\pm</math> 0.15</i>

### 3.4.3 $pO_2$ measurements

The total number of usable  $pO_{2\text{ Chamber}}$  measurements was limited to 15. This was due to a malfunction of the oxygen sensor in one of two EGM-5 devices used in the field and by the availability of accompanying measurements of the  $pO_2$  of the atmosphere that are needed for the drift correction. Overall,  $pO_{2\text{ Chamber}}$  values in the Brusquet catchment and in the Moulin catchment were similar or lower than the O<sub>2</sub> concentration of the atmosphere. The difference in  $pO_2$  between the chambers and the atmosphere ( $pO_{2\text{ Chamber}} - pO_{2\text{ Atm}}$ ) varied over time, ranging from zero within uncertainty ( $0.18 \pm 0.36\%$ , v/v,  $\pm 95\%$  confidence interval, CI) to  $-1.50 \pm 0.30\%$  (v/v), with the lowest  $pO_{2\text{ Chamber}}$  values in summer and higher values (lower gradient) in winter at both sites.

## 3.5 Discussion

Carbon dioxide release during oxidative weathering of sedimentary rocks exposed in steep mountainous areas has been shown to vary with changes in temperature, precipitation and local topography (Chapter 2) (Soulet et al., 2021). Furthermore, previous studies on weathering profiles (Bolton et al., 2006; Petsch, 2014) and on the chemical composition of rivers (Hilton and West, 2020) indicated that geological and geomorphological factors are an important control on the release of CO<sub>2</sub> and the consumption of O<sub>2</sub> during oxidative weathering. Differences in the release of carbon can be related to erosion rates and the concentration of reactive mineral phases in rocks (Hilton and West, 2020; Petsch, 2014), but should also depend on the pore space characteristics of the weathering zone, such as porosity and tortuosity (Bolton et al., 2006; Brantley et al., 2013; Gu et al., 2020a, 2020b; Soulet et al., 2021). However, we lack direct observations of how these chemical and physical properties affect the *in situ* weathering fluxes of CO<sub>2</sub> and O<sub>2</sub>, which are necessary to understand spatial variability in fluxes. In addition,

only with information on the contributing rock volume can we upscale and quantify CO<sub>2</sub> and O<sub>2</sub> fluxes from the measurement site to the landscape scale.

In the following discussion, we first propose a new approach of interpreting *in situ* CO<sub>2</sub> flux measurements that allows us to assess the diffusion of CO<sub>2</sub> and O<sub>2</sub> in the shallow critical zone and that can be used to quantify the rock volume contributing to the measured fluxes. This is based on data obtained from installations of drilled chambers in rapidly eroding marly limestones and black shales at similar topographic and hydrological settings (Figure 3-1 and Figure 3-2), which experience notable seasonal variations in temperature and precipitation (Figure 3-4). We then examine the implications of these new insights for quantifying the rock-derived CO<sub>2</sub> release, and then determine the coinciding O<sub>2</sub> consumption to investigate an overall redox budget of oxidative weathering in an erosive environment.

### 3.5.1 Probing the gas exchange of the shallow critical zone

#### 3.5.1.1 Explaining the patterns of CO<sub>2</sub> accumulation during a single flux measurement

To explain the initial decline of CO<sub>2</sub> accumulation rates during a flux measurement that stabilize over time (Figure 3-5), we consider the known volume of a drilled chamber and distinguish it from the unknown rock pore space around it. After arriving at a chamber to start a CO<sub>2</sub> flux measurement, we assume that the initial scrubbing (before the first repeat  $q_1$ ) removes CO<sub>2</sub> from the chamber (i.e.,  $p\text{CO}_2^{\text{Chamber}}$ ) to a near-atmospheric level, but does not remove the CO<sub>2</sub> from the connected pore space to a similar  $p\text{CO}_2$  value. Further scrubbing and removal of CO<sub>2</sub> to near-atmospheric value, associated with repeated CO<sub>2</sub> accumulations (Figure 3-5), then acts to lower the CO<sub>2</sub> concentration in the rock pore space connected to the chamber ( $p\text{CO}_2^{\text{Rock}}$ ). Once this pool of “excess” CO<sub>2</sub> has been exhausted, subsequent CO<sub>2</sub> accumulation rates ( $\text{CO}_2^{\text{Plateau}}$ ) are assumed to be representative of the real-time production of CO<sub>2</sub> in the rock surrounding the chamber. This explanation requires that the air volume processed by the sampling system equals the chamber volume, whereas the gas exchange between chamber and connected rock pores happens solely via diffusion. This assumption is supported by the measured CO<sub>2</sub> sampling ratio,  $SR$  (Equation 3-8), with an average  $SR = 1.03 \pm 0.15$  (Table 3-4). This is similar to the recovery efficiency of ~ 95 % of CO<sub>2</sub> standards in the laboratory (Garnett et al., 2019).

To interpret the period where we consider there is an excess of CO<sub>2</sub> diffusing into the chamber from a connected pore space, rather than real-time production of gas and diffusion, we introduce an exponential fitting model that describes the decrease of CO<sub>2</sub> accumulation rates ( $q$ ) over time (Figure 3-6):

$$q(t) = \alpha \times \exp(-\beta \times t) + q_{\text{plateau}} \quad (3-11)$$

where  $q_{\text{plateau}}$  is a constant value of the CO<sub>2</sub> <sub>plateau</sub> accumulation rate, the sum of  $\alpha$  and  $q_{\text{plateau}}$  is the initial rate of accumulation ( $\approx q_1$ , mgC min<sup>-1</sup>) at the start of the flux measurement ( $t = 0$ ),  $\beta$  is the measurement-specific removal constant (min<sup>-1</sup>), and the term  $\alpha \times \exp(-\beta \times t)$  describes the purging of the initially stored  $p\text{CO}_2$  from the rock pore space connected to the chamber over time.

In more detail, to ensure reliable results from fitting the exponential model to the measured rates of accumulation over time, measurements are only considered if the last 3 of at least 8 repeats ( $q_{n-2}$  to  $q_n$  for  $n \geq 8$ ) are “stabilized”, which we define as having a relative standard deviation of less than 5 %. To interpret the remaining CO<sub>2</sub> flux measurements, chamber-specific averages of the removal constant  $\beta$  from stabilized measurements are used to extrapolate  $q_{\text{plateau}}$  for measurements that did not stabilize.

The outputs of this analysis provide a CO<sub>2</sub> flux that represents the real-time production of CO<sub>2</sub> ( $q_{\text{plateau}}$ ), while quantifying the scrubbing of CO<sub>2</sub> stored initially in the connected volume of pore space around each chamber. This allows us to assess the diffusive movement of CO<sub>2</sub> in the shallow weathering zone (Section 3.5.1.2) and to estimate the contributing rock volume (Section 3.5.2).

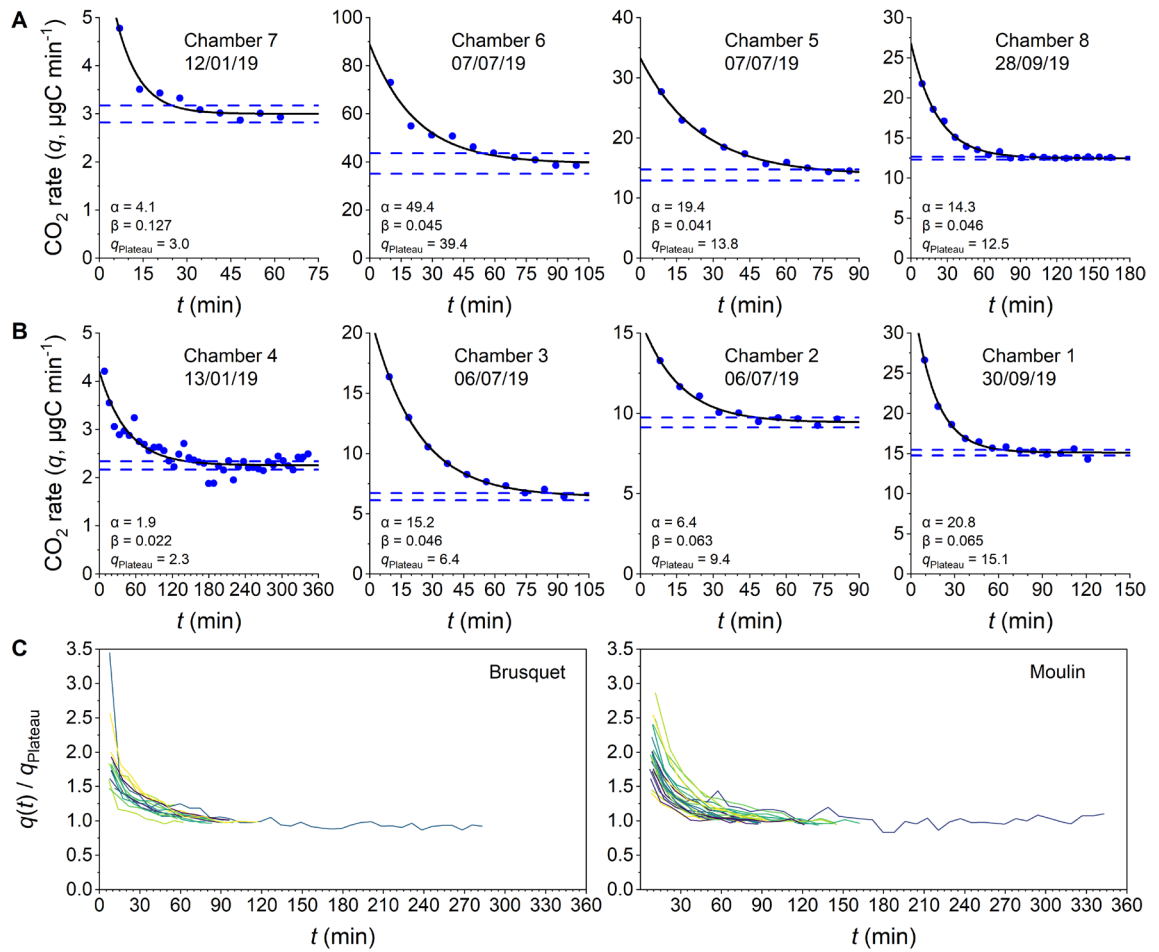


**Figure 3-6. Examples of CO<sub>2</sub> flux measurements consisting of several repeated accumulation rate measurements.** Panels A and B: measured accumulation rates ( $q$ ,  $\mu\text{gC min}^{-1}$  per chamber, y-axis) are shown alongside exponential fits (Equation 3-11) describing their evolution over time (x-axis) and alongside the 95 % confidence intervals of the modeled level at which the rates plateau ( $q_{\text{plateau}}$ ,  $\mu\text{gC min}^{-1}$ ) for chambers in the Brusquet catchment (Panel A) and in the Moulin catchment (Panel B). Dates and fitting parameters  $\alpha$  ( $\mu\text{gC min}^{-1}$ ) and  $\beta$  ( $\text{min}^{-1}$ ) of the single flux measurements are denoted. Panel C: for a comparison of the stabilizing evolution of different CO<sub>2</sub> flux measurements, indicated by varying colours,  $q(t)$  is normalized to  $q_{\text{plateau}}$  for both study sites in separate plots.

### 3.5.1.2 Assessing the diffusivity of the shallow weathering zone

After a CO<sub>2</sub> flux measurement, the chamber is re-sealed, and the chamber interior and surrounding pore space will evolve to reflect a steady-state of diffusive movement of CO<sub>2</sub> along a concentration gradient between the surface of the rock outcrop and the atmosphere so that  $p\text{CO}_{2\text{ Chamber}} = p\text{CO}_{2\text{ Rock}}$ . Thus, this steady-state of a closed chamber differs from the manipulated environment of a CO<sub>2</sub> flux measurement that is associated with repeats of CO<sub>2</sub> accumulation and removal with the sampling system (Figure 3-5). The comparison of the two states can shed light on gas movement and the physical properties of the rocks undergoing weathering. Here, we explore how the observed changes in  $p\text{CO}_{2\text{ Rock}}$  and CO<sub>2</sub> fluxes can be explained by a

framework of diffusive processes in the shallow critical zone, and assess the degree to which these are modulated by weather conditions.

According to Fick's law (Equation 3-1), diffusion of gases in a porous media is controlled by: i) the production and accumulation of CO<sub>2</sub>; ii) the volume of space (rock pores and/or chamber) and length scale over which molecules travel towards the low  $p\text{CO}_2$  reservoir; and iii) the diffusivity of CO<sub>2</sub> along their path. We find a co-variation of  $p\text{CO}_2$  Rock and the CO<sub>2</sub> fluxes that is similar for both sites, a relationship that can be explained by a linear regression model (Supplementary Section 3.8.2), with high  $p\text{CO}_2$  Rock values coinciding with high CO<sub>2</sub> accumulation rates (Figure 3-7A). This indicates that the contributing volume of rock pores and the diffusivity (the remaining variables from Fick's law) may be relatively stable at both sites over the study period.

However, in more detail, the ambient hydroclimate appears to modify their response. We consider measurements as being made during "wet" or "dry" periods, whereby "wet" measurements are those where the cumulative precipitation over the last 3 days was  $\geq 5$  mm. At a given  $p\text{CO}_2$  Rock value, "dry" conditions are associated with lower CO<sub>2</sub> production compared to "wet" conditions (Figure 3-7A). However, previous research has shown that rock-derived CO<sub>2</sub> fluxes from drilled chambers are lower following rain events, but recover subsequently over a few dry days (Chapter 2) (Soulet et al., 2021). This observation has been linked to the degree of water saturation controlling the gas motion of O<sub>2</sub> and CO<sub>2</sub>, as well as to dissolution of weathering-derived carbon and subsequent export of dissolved inorganic carbon (Chapter 2) (Soulet et al., 2021). It is important to note that a decrease of the production of CO<sub>2</sub>, associated with a lower O<sub>2</sub> supply required for the oxidative weathering reactions and/or with a greater uptake of carbon into the DIC, would also decrease  $p\text{CO}_2$  Rock (Chapter 2) (Soulet et al., 2021). Thus, a change in the relationship between  $p\text{CO}_2$  Rock and CO<sub>2</sub> flux may be better explained by differences in the diffusivity or the contributing rock volume during "wet" and "dry" conditions.

According to Fick's law, a lower diffusivity at a constant contributing volume of rock results in higher  $p\text{CO}_2$  Rock values. Thus, "wet" conditions may be associated with a decrease in the diffusivity of gases in the weathering rocks. This is in agreement with a simple model describing the effective diffusivity  $D_{\text{Rock}}$  (m<sup>2</sup> s<sup>-1</sup>) of a given gas in porous media (such as rocks and soils) at a given temperature by

$$D_{\text{Rock}} = D_{\text{Air}} \times \phi_{\text{Air-filled}} \times \tau \quad (3-12)$$

where  $D_{\text{Air}}$  is the diffusion coefficient (m<sup>2</sup> s<sup>-1</sup>) of the particular gas in air,  $\tau$  is a dimensionless tortuosity factor, and  $\phi_{\text{Air-filled}}$  is the air-filled porosity (v/v %) (Davidson and Trumbore, 1995; Penman, 1940). If  $\phi_{\text{Air-filled}}$  decreases due to meteoric water filling the pore space, precipitation events are likely to lower the effective diffusivity of CO<sub>2</sub> within the critical zone. An increase of

moisture in porous media also leads to more tortuous pathways (Davidson and Trumbore, 1995; Millington, 1959), which could further lower  $D_{\text{Rock}}$  under wet conditions. Analogously, rock moisture would also affect the diffusion of atmospheric O<sub>2</sub> into the rock pore space, so that this framework can explain the observed decrease of CO<sub>2</sub> production following rain events (Chapter 2) (Soulet et al., 2021).

To describe the diffusion of CO<sub>2</sub> during the steady-state of a closed chamber, we use Fick's law (Equation 3-1) and the measured CO<sub>2</sub> flux ( $q_{\text{Plateau}}$ ) and the concentration gradient of CO<sub>2</sub> ( $p\text{CO}_{2\text{Rock}} - p\text{CO}_{2\text{Atm}}$ ) to define a measure ( $\frac{D_{\text{CO}_2}}{\omega}$ , cm<sup>3</sup> min<sup>-1</sup>) that describes the effective diffusivity  $D_{\text{CO}_2}$  (cm<sup>2</sup> min<sup>-1</sup>) of the CO<sub>2</sub> flux towards the atmosphere over the unknown effective depth and area  $\omega$  (cm<sup>1</sup> cm<sup>-2</sup>):

$$\frac{D_{\text{CO}_2}}{\omega} = \frac{q_{\text{Plateau}}}{p\text{CO}_{2\text{Rock}} - p\text{CO}_{2\text{Atm}}} \times \frac{R \times T}{P} \times \frac{10^9}{M_{\text{C}}} . \quad (3-13)$$

The calculated values (based on repeats 6 - 8) range from 5.0 cm<sup>3</sup> min<sup>-1</sup> to 47.1 cm<sup>3</sup> min<sup>-1</sup> with an average of  $27.5 \pm 12.4$  cm<sup>3</sup> min<sup>-1</sup> (n = 25) and from 3.3 cm<sup>3</sup> min<sup>-1</sup> to 51.9 cm<sup>3</sup> min<sup>-1</sup> with an average of  $21.8 \pm 13.2$  cm<sup>3</sup> min<sup>-1</sup> (n = 30) in the Brusquet catchment and in the Moulin catchment, respectively.

An alternative way to assess diffusivity is to use the constant  $\lambda$  (Equation 3-4) that is representative for the curvature of the repeated accumulations during a CO<sub>2</sub> flux measurement (Figure 3-5) (Pirk et al., 2016). Differences between  $\lambda$  and  $\frac{D_{\text{CO}_2}}{\omega}$  may be expected because  $\lambda$  is representative of short intervals during one flux measurement (~ 6 min observations), while  $\frac{D_{\text{CO}_2}}{\omega}$  represents a period of a few hours (because this measure is based on linking a CO<sub>2</sub> flux determined in the end of a measurement and the  $p\text{CO}_{2\text{Rock}}$  determined beforehand). We find a significant linear correlation of  $\lambda$  and  $\frac{D_{\text{CO}_2}}{\omega}$  for all samples irrespective of the study site (Figure 3-7B) (Supplementary Section 3.8.3). The similarities of both metrics affirm that the accumulation rates determined during flux measurements are representative for the longer-term CO<sub>2</sub> release from the studied rocks towards the atmosphere.

The concordance of changes in  $\lambda$  and in  $\frac{D_{\text{CO}_2}}{\omega}$  suggests that the rock pore space is relatively homogenous in porosity and tortuosity, since the diffusive pathways of the steady-state during a stabilized flux measurement differ from that of a closed chamber (Supplementary Section 3.8.4). Minor heterogeneities may explain some scatter in the correlation of  $\lambda$  and  $\frac{D_{\text{CO}_2}}{\omega}$ , as well as short-term changes in the effective rock space contributing CO<sub>2</sub> to a chamber induced by percolation of meteoric waters.

However, we find some variability in the measures of diffusivity that is linked to the hydroclimatic conditions. “Wet” conditions coincide generally with somewhat lower  $\frac{D_{CO_2}}{\omega}$  values for a given  $\lambda$  (Figure 3-7B) (Supplementary Section 3.8.3). Because the atmosphere is acting as the low  $pCO_2$  reservoir during the steady-state of a closed chamber,  $\frac{D_{CO_2}}{\omega}$  is likely to be more influenced by surficial processes than  $\lambda$ , which is affected by CO<sub>2</sub> migration pathways towards the chamber (Supplementary Section 3.8.4). For example, lower  $\frac{D_{CO_2}}{\omega}$  values for a given  $\lambda$  may be the result of filling of surficial cracks with water, or micro-landslides, swelling of the surface rock material and lateral expansion following rainfall events (Bechet et al., 2015), which may hinder the migration of gas. During drier conditions, cracks may significantly increase gas exchange between the rocks and the atmosphere (Maier and Schack-Kirchner, 2014; Weisbrod et al., 2009). In the study area, desiccation cracks typically appear at steep slopes during summer, when erosion by runoff is less prevailing than in spring and autumn, whereas a thick layer of loose detrital cover can be accumulated during winter due to frost weathering (Ariagno et al., 2022), when movement of surface materials is limited to solifluction (Bechet et al., 2016). Thus, the diffusivity of the rock surface presumably changes over time, with greater values during dry summer conditions (Figure 3-7F – I).

The  $\lambda$  and  $\frac{D_{CO_2}}{\omega}$  values can also be explored as a function of temperature inside the chambers (Figure 3-7F – I). In air, the diffusion coefficient of CO<sub>2</sub> is strongly controlled by temperature with an increase by a factor of  $\sim 1.25$  at 35 °C compared to 0 °C (Massman, 1998). However, we find a much larger change of  $\lambda$  and  $\frac{D_{CO_2}}{\omega}$ , with an average increase by a factor of  $\sim 3.5$  between 0 °C and 35 °C (Figure 3-7F - I). This relation between temperature and diffusivity could be explained by a coinciding decrease of rock moisture. In the marls of the Laval catchment, neighbouring the studied Moulin catchment, lower near-surface water contents were observed during dry summer periods, with values as low as  $\sim 10\%$  contrasting to values of up to  $\sim 25\%$  in winter (Mallet et al., 2020). However, the relation of rock moisture and temperature is not straightforward (Soulet et al., 2021), with precipitation an important control on surface rock moisture. In addition, we observe high and constant relative air humidity in the chambers over the year (Figure 3-4). Together, a complex hydrological control on  $D_{Rock}$ , which includes surface processes, may explain some part of the high apparent temperature sensitivity of  $\lambda$  and  $\frac{D_{CO_2}}{\omega}$  by modifying  $\tau$  and  $\phi_{Air-filled}$  (Equation 3-12), alongside changes of  $D_{Air}$  forced solely by temperature.

In summary, disentangling diffusive processes in the shallow weathering zone is complicated by drivers that can be interrelated and co-vary (Figure 3-7). This is also commonly

observed in soils (Davidson and Trumbore, 1995; Hashimoto and Komatsu, 2006; Maier and Schack-Kirchner, 2014; Tokunaga et al., 2016). Generally, hydrology and temperature are important controls on  $p\text{CO}_2$  Rock, CO<sub>2</sub> flux, diffusivity and potentially rock pore space, all of which contribute to the release of CO<sub>2</sub> to the atmosphere. Interestingly, similar responses to changes in environmental controls are observed at both study sites, and they appear to have similar diffusivity measures. Here, changes in precipitation and temperature coincide with changes in the diffusion parameters that are greater than differences between chambers at one site, or between sites. However, the CO<sub>2</sub> fluxes differ significantly between sites, with greater CO<sub>2</sub> efflux at a given rock temperature from the chambers in the Brusquet catchment compared to the Moulin catchment (Figure 3-7C), which may be explained by a difference in the source of CO<sub>2</sub> or by differences in the contributing rock volume (Section 3.5.2).

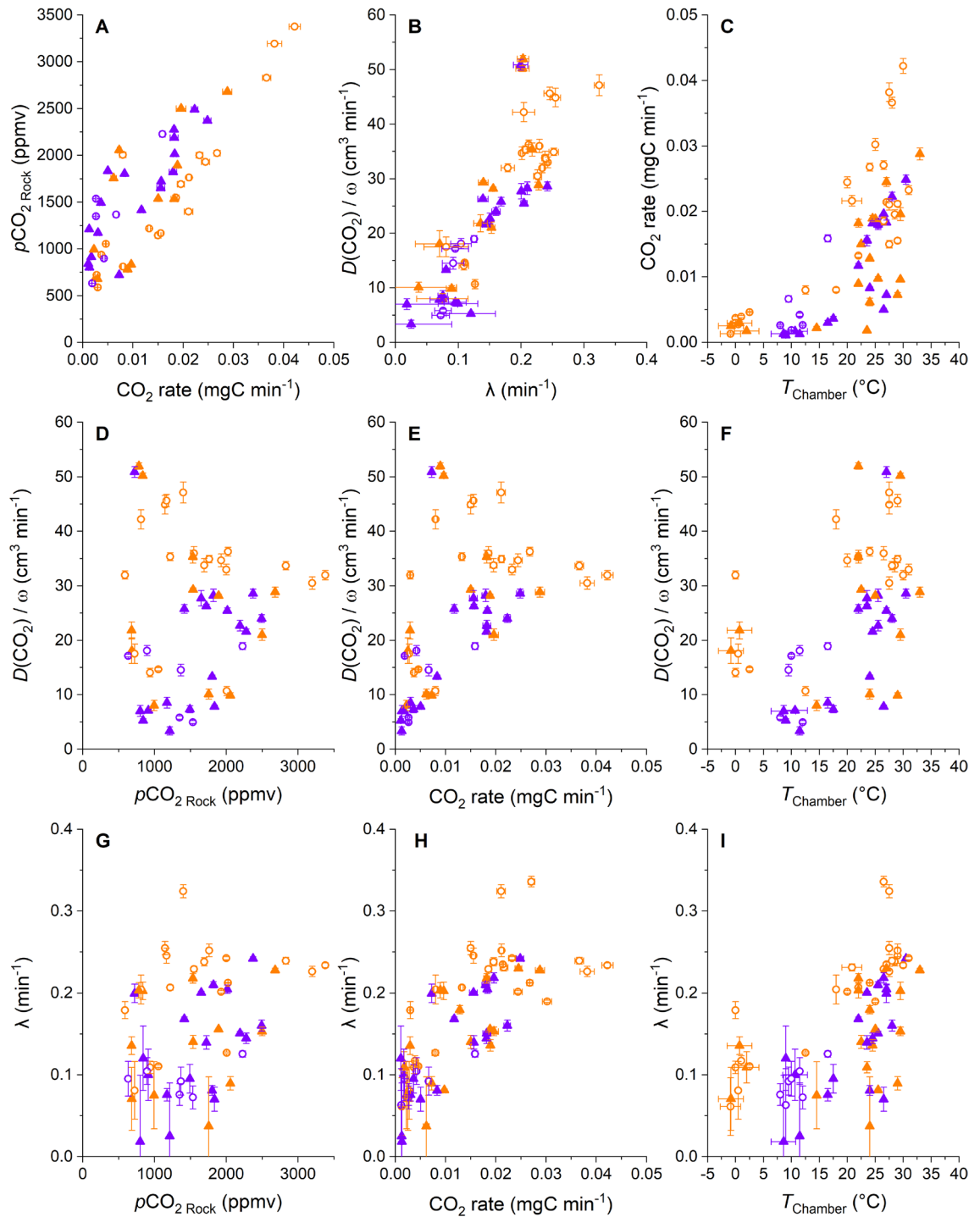


**Figure 3-7. Comparisons of diffusivity, CO<sub>2</sub> partial pressures and accumulation rates, and chamber temperatures.** Diffusivity is assessed with the measures  $\lambda$  and  $\frac{D_{CO_2}}{\omega}$ . Colour coding differentiates “dry” (orange) from “wet” samples (violet) using a threshold of a cumulative precipitation of 5 mm over the last 3 days. The origin of samples is indicated with open circles for the Brusquet catchment and filled triangles for the Moulin catchment. For consistency, all parameters determined during CO<sub>2</sub> flux measurements are calculated on the basis of the repeats 6–8 ( $\pm 1$  SD). Estimated temperatures are indicated by accompanying error bars (RMSE).

### 3.5.2 Assessing the contributing rock pore volume

#### 3.5.2.1 Quantification of the contributing rock pore volume

Chamber-based measurements of CO<sub>2</sub> flux provide insight on the variability of fluxes over time and the environmental controls that force them (Chapter 2) (e.g., Bond-Lamberty and Thomson, 2010; Oertel et al., 2016; Pirk et al., 2016; Soulet et al., 2021). However, the volume of material that contributes to the measured CO<sub>2</sub> fluxes is rarely quantified. If this could be determined, it may be possible to consider the production of CO<sub>2</sub> as a function of the mass of reactants, allowing comparisons between different field sites and laboratory experiments (e.g., Angert et al., 2015; Kalks et al., 2021; Lefèvre et al., 2014; Soucémariadin et al., 2018; Tokunaga et al., 2016). In the case of the internal rock chambers used here, quantification of the contributing rock volume would allow us to potentially upscale the fluxes over an outcrop surface area. To do this, here, we use the exponential fitting model (Equation 3-11) that describes the transition between a closed chamber and the manipulated state during flux measurements as a way to quantify the carbon mass derived from the rock pore space (Figure 3-5 and Figure 3-6). By doing so, we can use the  $p\text{CO}_{2\text{ Rock}}$  to calculate the corresponding air volume in the rock volume contributing CO<sub>2</sub>. The volume of rock pores, in turn, can be used to estimate the corresponding rock volume and its geometry, and, ultimately, the rock mass to determine an absolute weathering flux.

To do so, first the mass of CO<sub>2</sub> purged during a flux measurement from the rock pore space around the chamber can be described as an excess of CO<sub>2</sub> (CO<sub>2 Excess</sub>, mgC) that exceeds the contribution from the CO<sub>2 Plateau</sub> accumulation rate:

$$\text{CO}_{2\text{ Excess}} = \int_{t(0)}^{t(\text{Plateau})} \alpha \times \exp(-\beta \times t) \quad (3-14)$$

with  $\alpha$  and  $\beta$  being the fitting parameters from the same fitting procedure used to calculate  $q_{\text{Plateau}}$  (Equation 3-11) over time, starting at the beginning of the flux measurement ( $t = 0$ ) and ending when the integrated term approaches zero ( $t_{\text{Plateau}}$ , when  $q(t)$  equals  $q_{\text{Plateau}}$ ). Furthermore, we assume that the air volume of the rock pores, from which CO<sub>2</sub> diffuses to the chamber within the time intervals of the single repeats of a flux measurement, can be estimated from CO<sub>2 Excess</sub> by taking into account the  $p\text{CO}_{2\text{ Rock}}$  at the start of the flux measurement (when  $p\text{CO}_{2\text{ Rock}}$  equals  $p\text{CO}_{2\text{ Chamber}}$ ). This air volume ( $V_{\text{Rock pores}}$ , cm<sup>3</sup>) is calculated by modifying Equation 3-5:

$$V_{\text{Rock pores}} = \text{CO}_{2\text{ Excess}} \times \frac{R \times T}{P} \times \frac{10^9}{M_C \times p\text{CO}_{2\text{ Rock}}} \quad (3-15)$$

The uncertainties of CO<sub>2 Excess</sub> and  $V_{\text{Rock pores}}$  can be derived from propagating the 95 % confidence intervals of the fitting parameters (Equation 3-11).

Overall, the calculated values of  $V_{\text{Rock pores}}$  are similar for both study sites with  $365 \pm 208 \text{ cm}^3$  ( $\pm 1$  SD of the average of measurement-specific values) for the chambers in the Brusquet catchment, and  $322 \pm 174 \text{ cm}^3$  for the chambers in the Moulin catchment (Figure 3-8) (Table 3-5). However, significant variation is observed over time for each chamber (Figure 3-9), while each measurement-specific value of  $V_{\text{Rock pores}}$  is associated with a high uncertainty (Table 3-5). These uncertainties are not normally distributed, with an average upper relative uncertainty of  $125.8 \pm 140.1 \%$  (average of 95 % CI  $\pm 1$  SD) and an average lower relative uncertainty of  $47.8 \pm 42.3 \%$  for all samples.

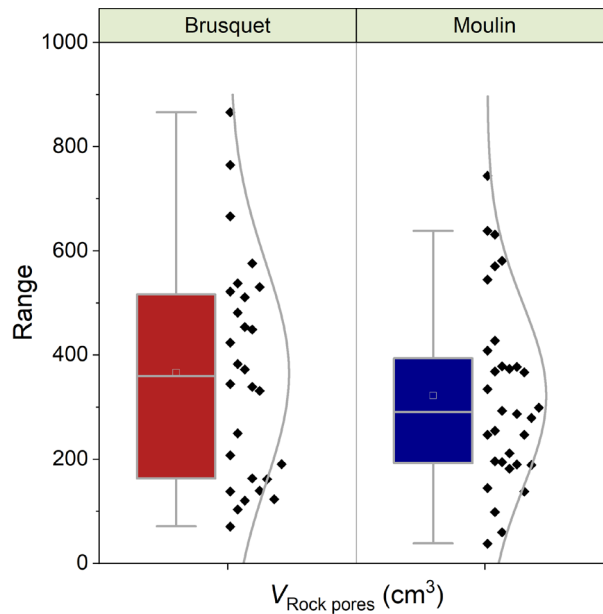


**Figure 3-8. Catchment-specific summary of measured volumes of rock pores.** Box plots and distribution curves summarize catchment-specifically the volume of rock pores ( $V_{\text{Rock pores}}$ ) connected to each chamber determined during CO<sub>2</sub> flux measurements including 4 chambers at each site. Boxes indicate the 25 % – 75 % range alongside the 1.5 interquartile ranges with mean (open square) and median (line). Colours indicate the origin (Brusquet: red, Moulin: blue).

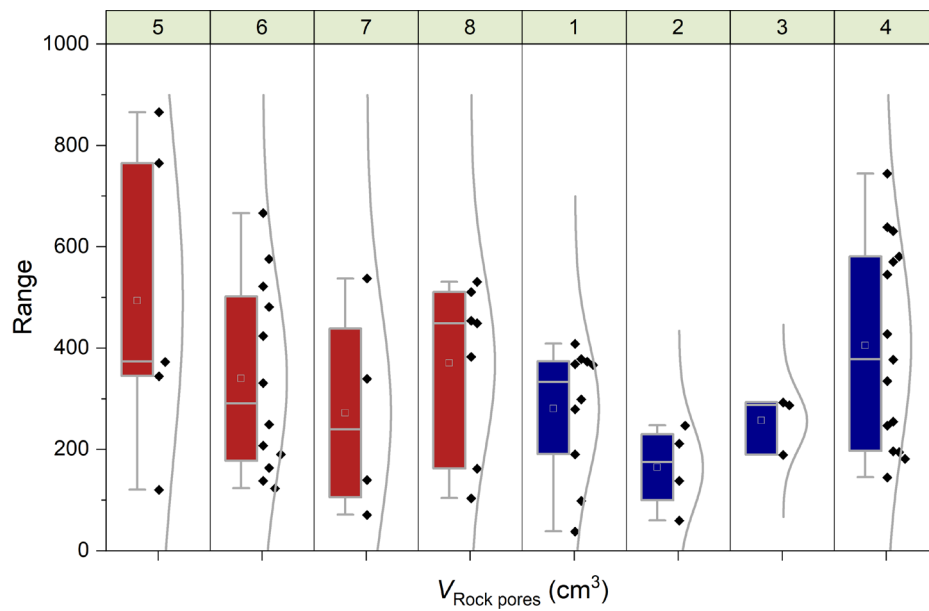


**Figure 3-9. Chamber-specific summary of measured volumes of rock pores.** Box plots and distribution curves summarize chamber-specifically the volume of rock pores ( $V_{\text{Rock pores}}$ ) connected to each chamber determined during CO<sub>2</sub> flux measurements. Boxes indicate the 25%–75% range alongside the 1.5 interquartile ranges with mean (open square) and median (line). Panels at the top show the chamber identifiers (Table 3-1) and colours indicate the origin (Brusquet: red, Moulin: blue).

### 3.5.2.2 Environmental controls on the contributing rock pore volume

The variation of  $V_{\text{Rock pores}}$  may be linked to changes in the diffusive processes and weather conditions (Figure 3-10). Overall, higher values of  $\lambda$  coincide with greater values of  $V_{\text{Rock pores}}$  (all samples:  $R^2$  of a linear regression = 0.52,  $p < 0.001$ ,  $n = 55$ ) (Figure 3-10A). This is also true for the relation between  $V_{\text{Rock pores}}$  and  $\frac{D_{\text{CO}_2}}{\omega}$  (Figure 3-10B), which itself is positively correlated to  $\lambda$  (Section 3.5.1). These relationships are similar for both sites, and for “wet” and “dry” conditions. The latter observation indicates that rock moisture impacts the diffusivity of CO<sub>2</sub> and  $V_{\text{Rock pores}}$  in equal measure. This, in turn, is in line with Fick’s law, with the extent of the rock pore space that contributes CO<sub>2</sub> to a chamber depending on the potential of gas to move within the rocks undergoing weathering. In this process, the degree to which changes in the diffusivity impact the contributing rock volume is driven by the effective change in length of the diffusion paths. Here, a change of  $\lambda$  from 0.1 min<sup>-1</sup> to 0.2 min<sup>-1</sup> is associated with a change of  $V_{\text{Rock pores}}$  by a factor of  $\sim 3.5$  and this roughly fits the modification of the geometry of a cylinder-shaped rock pore space around a drilled chamber when doubling its effective radius.

Furthermore, differences in  $V_{\text{Rock pores}}$  coincide also with changes in temperature (all samples:  $R^2$  of a linear regression = 0.47,  $p < 0.001$ ,  $n = 60$ ) (Figure 3-10C), which is likely

associated with the apparent relation of temperature and diffusivity (Section 3.5.1). This coincidence is important to consider when assessing the control of temperature on the CO<sub>2</sub> production from chemical weathering (i.e., weathering kinetics), and is discussed later (Section 3.5.3). The coincidence of positive correlations of temperature and CO<sub>2</sub> production, and of temperature and the extent of  $V_{\text{Rock pores}}$  (indirectly connected by  $D_{\text{CO}_2}$ ) also means that changes in CO<sub>2</sub> flux are associated with changes in the contributing rock pore space (all samples:  $R^2$  of a linear regression = 0.42,  $p = <0.001$ ,  $n = 60$ ) (Figure 3-10D).

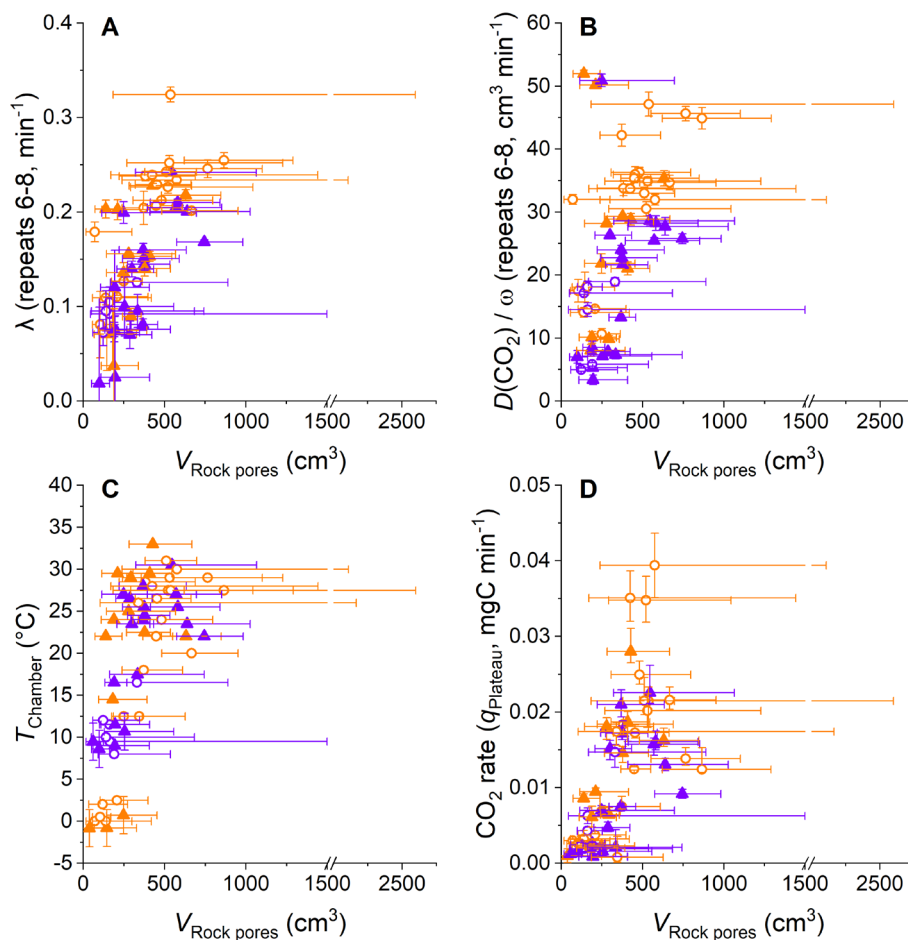


**Figure 3-10. Comparisons of  $V_{\text{Rock pores}}$ , diffusivity, CO<sub>2</sub> accumulation rates, and chamber temperatures.**

Diffusivity is assessed with the measures  $\lambda$  and  $\frac{D_{\text{CO}_2}}{\omega}$ . Colour coding differentiates “dry” (orange) from “wet” samples (violet) using a threshold of a cumulative precipitation of 5 mm over the last 3 days. The origin of samples is indicated with open circles for the Brusquet catchment and filled triangles for the Moulin catchment. Reported values of  $\lambda$  and  $\frac{D_{\text{CO}_2}}{\omega}$  are based on the repeats 6 - 8 of a CO<sub>2</sub> flux measurement ( $\pm 1$  SD), whereas the calculation of  $V_{\text{Rock pores}}$  and CO<sub>2</sub> accumulation rates are based on the fitting model ( $\pm 95\%$  CI). Estimated temperatures are indicated by accompanying error bars (RMSE).

### 3.5.2.3 Upscaling chamber-based CO<sub>2</sub> fluxes

The determined  $V_{\text{Rock pores}}$  can be combined with the porosity of the rocks undergoing weathering to allow a better understanding of the volume of rock contributing CO<sub>2</sub> to a chamber-based flux measurement ( $V_{\text{Rock}}$ , cm<sup>3</sup>):

$$V_{\text{Rock}} = \frac{V_{\text{Rock pores}}}{\varphi_{\text{Air-filled}}}. \quad (3-16)$$

This assumes that the majority of rock pores are well connected (total porosity  $\approx$  connected porosity), and that no significant amount of water is filling the pore space. To consider the range of potential porosities occurring in the weathering rocks of the Draix-Bléone observatory (Garel et al., 2012) and variable rock moisture contents (Mallet et al., 2020), the following evaluation is based on assigning an effective air-filled porosity of 30 % within a 95 % confidence interval of 20 % – 40 %.

On average, CO<sub>2</sub> fluxes from chambers in the Brusquet catchment derive from a rock volume of  $1,216.0_{-690.2}^{+3,081.0}$  cm<sup>3</sup> (within 95 % confidence interval based on propagating the uncertainties of the fitting procedure and of the assigned porosity), which is similar to the release of CO<sub>2</sub> in the Moulin catchment from rock volumes of  $1,071.8_{-555.4}^{+1,606.1}$  cm<sup>3</sup>. If we visualize this volume as a cylindrical rock layer around the drilled chambers (Figure 3-2E: sampling distance indicated by arrows pointing towards the chamber), its thickness would be  $\sim 1.9_{-0.9}^{+2.1}$  cm. However, the exact geometry of this space is unknown. Instead, considering that porosities are highest at the surface of rock outcrops in the study area (Lofi et al., 2012; Mallet et al., 2020; Maquaire et al., 2002; Mathys and Klotz, 2008; Travelletti et al., 2012), where unloading and climatic controls on physical weathering act most efficiently (Ariagno et al., 2022; Bechet et al., 2016, 2015; Cras et al., 2007; Mathys and Klotz, 2008), it seems likely that the shape of the porous and permeable rock that contributes to gas exchange represents a cone with a radius that declines over depth of a drilled chamber.

The knowledge of the probed layer thickness can be combined with the inner surface area of the chambers to valuate the spatial parameter  $\omega$  (Equation 3-13), and thus to calculate the effective diffusivity of CO<sub>2</sub> in the air-filled rock pores zone. Overall, we find values of  $D_{\text{CO}_2}$  ranging between  $\sim 0.02$  cm<sup>2</sup> min<sup>-1</sup> and  $0.30$  cm<sup>2</sup> min<sup>-1</sup> (considering the range of  $\frac{D_{\text{CO}_2}}{\omega}$  at both study sites; Section 3.5.1). Interestingly, these values are similar to diffusion coefficients that were determined by laboratory experiments at 22.5 °C, with O<sub>2</sub> as the tracer gas, which correspond to  $D_{\text{CO}_2}$  values of  $0.34$  cm<sup>2</sup> min<sup>-1</sup> and  $0.43$  cm<sup>2</sup> min<sup>-1</sup> for limestones with porosities of 0.40 % and 0.46 %, and of  $0.04$  cm<sup>2</sup> min<sup>-1</sup> and  $0.17$  cm<sup>2</sup> min<sup>-1</sup> for mudstones with porosities of 0.33 % and 0.38 %, respectively (Peng et al., 2012).

In addition, the rock volume around a chamber can be “unwrapped” to represent a comparable surface area on an outcrop that would have the same contributing rock pore volume ( $S_{\text{Rock}}$ , cm<sup>2</sup>) if the weathering depth  $z_{\text{Rock}}$  (cm), over which CO<sub>2</sub> is thought to be produced by oxidative weathering, is considered:

$$S_{\text{Rock}} = \frac{V_{\text{Rock}}}{z_{\text{Rock}}} \quad (3-17)$$

The  $z_{\text{Rock}}$  value can be inferred from the morphology of bare surfaces in the study area (Maquaire et al., 2002; Mathys and Klotz, 2008; Oostwoud Wijdenes and Ergenzinger, 1998; Rovéra and Robert, 2006), based on the assumption that chemical weathering of sedimentary rocks occurs at the same depths where physical properties are altered (Brantley et al., 2013; Gu et al., 2020b, 2020a; Lebedeva and Brantley, 2020). Accordingly, based on previous research in a neighbouring catchment reporting physical alteration that extends to depths of  $\sim 20.0_{-10.0}^{+10.0}$  cm at slopes similar to our study sites (Maquaire et al., 2002), we estimate the chemical weathering to extend to similar depths at both study sites.

The corresponding values calculated for  $S_{\text{Rock}}$  can be compared to the inner surface area of the chambers (Table 3-1). On average  $S_{\text{Rock}}$  is smaller than the inner surface area of the drilled chambers, by a factor of  $6.4_{-5.3}^{+16.1}$ . This means that CO<sub>2</sub> fluxes from chambers drilled into rocks and normalized to the chamber inner surface area (Equation 3-6) cannot be compared directly with topographic surface fluxes (e.g., from surface chambers), which are typically reported for soils (Bond-Lamberty and Thomson, 2010; Oertel et al., 2016), as suggested by (Soulet et al., 2021). Instead, CO<sub>2</sub> fluxes from a drilled chamber need to be corrected by considering  $V_{\text{Rock}}$  and the weathering depth. On average, the measured CO<sub>2</sub> fluxes (Table 3-5) equate to a topographic surface efflux of  $\sim 1,215$  tC km<sup>-2</sup> yr<sup>-1</sup> and of  $\sim 885$  tC km<sup>-2</sup> yr<sup>-1</sup> in the Brusquet catchment and in the Moulin catchment, respectively, which is similar to the global mean emissions of CO<sub>2</sub> from soils with different land cover (Oertel et al., 2016).

In the Laval catchment, two short-term surface chamber experiments carried out alongside measurements of CO<sub>2</sub> fluxes from chambers drilled into exposed marly limestones (with a normalization to the inner surface area) indicate roughly consistent fluxes from both chamber types under similar environmental conditions (Soulet et al., 2021). An explanation for the difference between the study site in the Laval catchment and the chambers in the Brusquet and Moulin catchments could be that the chambers at the Laval site were installed in a different topographic setting that is much closer to the main streambed (Soulet et al., 2021). Since weathering profiles closer to a thalweg are typically less developed (Esteves et al., 2005; Maquaire et al., 2002; Mathys and Klotz, 2008), this could mean that the porosities and weathering depths around the chambers at the Laval site are lower, which, in turn, would lower

the calculated difference between outer and inner surface areas for a given  $V_{\text{Rock pores}}$ . For example, if the chambers in the Laval catchment would have comparable values of  $V_{\text{Rock pores}}$  to the chambers in the Brusquet and Moulin catchments, a local effective porosity of 15 % and a weathering depth of 10 cm correspond to a difference by a factor of  $\sim 1.6$  that is significantly closer to a consistency of outer and inner surface areas compared to the findings from the Brusquet and Moulin catchments. However, future work combining the approach of the present study with surface chamber measurements is needed to investigate whether the calculated outer surface flux derived from drilled chambers fits the measured flux from surface chambers.

Carbon fluxes from oxidative weathering can be linked to a rock mass, allowing fluxes to be interpreted in terms of the overall kinetics of the oxidative weathering reactions as a function of environmental variables. This is essential for theoretical carbon cycle modeling (Bao et al., 2017; Bolton et al., 2006). Following calculation of  $V_{\text{Rock}}$ , the rock mass emitting CO<sub>2</sub> ( $m_{\text{Rock}}$ , g) can be estimated by using an average estimate of the density of the rock grains surrounding the chambers ( $\rho_{\text{Rock}}$ , g cm<sup>-3</sup> = t m<sup>-3</sup>):

$$m_{\text{Rock}} = (V_{\text{Rock}} - V_{\text{Rock pores}}) \times \rho_{\text{Rock}} \quad (3-18)$$

Considering a grain density of  $2.7_{-0.02}^{+0.02}$  t m<sup>-3</sup> (Lofi et al., 2012), we find that an average rock mass of  $2,153.0_{-1,315.5}^{+5,318.4}$  g produces the CO<sub>2</sub> fluxes derived from chambers in the Brusquet catchment and in the Moulin catchment. To our knowledge, this allows for the first time an absolute report of weathering-derived CO<sub>2</sub> fluxes that are measured in real-time and *in situ*.

The combined quantification of CO<sub>2</sub> fluxes and of the corresponding rock mass undergoing oxidative weathering means that there is an opportunity for future research to include investigations of the internal surface area of the studied rocks, which would allow reporting field-based CO<sub>2</sub> fluxes normalized to the reacting surface areas. Such normalizations are typically considered during modeling (Bao et al., 2017; Bolton et al., 2006) to acknowledge that the internal surface area can change significantly during sedimentary rock weathering (Fischer and Gaupp, 2005). Analogously to silicate weathering rates, variations in OC<sub>petro</sub> and carbonate weathering rates obtained from different field and laboratory conditions may be related to the conceptualization and parametrization of the reactive surface area, which needs to be considered when comparing them (Brantley et al., 2007; White and Brantley, 2003).

**Table 3-5. Chamber-specific overview of CO<sub>2</sub> Excess, V<sub>Rock pores</sub> and CO<sub>2</sub> accumulation rate (q<sub>plateau</sub>).** Uncertainties of minima and maxima are representing the 95 % CI, whereas averages are reported with 1 SD.

Chamber identifiers		Site	CO <sub>2</sub> Excess (µgC)				V <sub>Rock pores</sub> (cm <sup>3</sup> )				CO <sub>2</sub> rate (µgC min <sup>-1</sup> )			
<i>short</i>	<i>long</i>		Average (± SD)	n	Min. (± CI)	Max. (± CI)	Average (± SD)	n	Min. (± CI)	Max. (± CI)	Average (± SD)	n	Min. (± CI)	Max. (± CI)
5	B-F-5	Brusquet	222 ± 166	5	34 <sup>+44</sup> <sub>-24</sub>	444 <sup>+78</sup> <sub>-44</sub>	493 ± 279	5	120 <sup>+153</sup> <sub>-85</sub>	866 <sup>+424</sup> <sub>-244</sub>	6.6 ± 5.9	10	0.8 <sup>+2.8</sup> <sub>-0.7</sub>	18.5 <sup>+5.0</sup> <sub>-1.5</sub>
6	B-G-6	Brusquet	353 ± 267	12	64 <sup>+130</sup> <sub>-37</sub>	863 <sup>+1,709</sup> <sub>-505</sub>	339 ± 180	12	123 <sup>+223</sup> <sub>-64</sub>	666 <sup>+286</sup> <sub>-183</sub>	17.1 ± 13.5	13	2.0 <sup>+0.2</sup> <sub>-0.4</sub>	39.4 <sup>+4.3</sup> <sub>-4.3</sub>
7	B-H-7	Brusquet	142 ± 126	4	20 <sup>+66</sup> <sub>-16</sub>	336 <sup>+1,352</sup> <sub>-222</sub>	272 ± 182	4	71 <sup>+229</sup> <sub>-54</sub>	537 <sup>+2,159</sup> <sub>-354</sub>	13.8 ± 9.6	5	1.9 <sup>+0.1</sup> <sub>-0.3</sub>	25.4 <sup>+3.3</sup> <sub>-2.4</sub>
8	B-I-8	Brusquet	261 ± 147	7	37 <sup>+24</sup> <sub>-16</sub>	450 <sup>+164</sup> <sub>-115</sub>	370 ± 157	7	103 <sup>+67</sup> <sub>-46</sub>	530 <sup>+697</sup> <sub>-262</sub>	14.7 ± 7.0	8	2.6 <sup>+0.3</sup> <sub>-0.3</sub>	21.5 <sup>+3.1</sup> <sub>-1.8</sub>
<i>Brusquet totals</i>			<i>277 ± 221</i>	<i>28</i>			<i>365 ± 208</i>	<i>28</i>			<i>13.2 ± 10.8</i>	<i>36</i>		
1	M-C-1	Moulin	252 ± 150	10	10 <sup>+57</sup> <sub>-10</sub>	453 <sup>+152</sup> <sub>-113</sub>	280 ± 122	10	38 <sup>+210</sup> <sub>-38</sub>	408 <sup>+137</sup> <sub>-102</sub>	12.5 ± 7.4	11	1.0 <sup>+0.9</sup> <sub>-0.9</sub>	21.0 <sup>+1.9</sup> <sub>-1.6</sub>
2	M-A-2	Moulin	55 ± 26	4	15 <sup>+17</sup> <sub>-11</sub>	79 <sup>+144</sup> <sub>-42</sub>	164 ± 72	4	60 <sup>+65</sup> <sub>-42</sub>	247 <sup>+449</sup> <sub>-133</sub>	5.0 ± 3.5	6	1.2 <sup>+0.3</sup> <sub>-0.3</sub>	9.4 <sup>+0.5</sup> <sub>-0.4</sub>
3	M-D-3	Moulin	217 ± 50	3	149 <sup>+119</sup> <sub>-62</sub>	267 <sup>+59</sup> <sub>-46</sub>	256 ± 48	3	189 <sup>+150</sup> <sub>-79</sub>	293 <sup>+64</sup> <sub>-51</sub>	4.6 ± 3.1	6	0.5 <sup>+0.4</sup> <sub>-0.4</sub>	9.3 <sup>+1.2</sup> <sub>-0.3</sub>
4	M-B-4	Moulin	296 ± 192	15	48 <sup>+62</sup> <sub>-26</sub>	569 <sup>+544</sup> <sub>-232</sub>	404 ± 193	15	145 <sup>+184</sup> <sub>-77</sub>	744 <sup>+238</sup> <sub>-169</sub>	11.1 ± 8.4	18	0.9 <sup>+0.1</sup> <sub>-0.3</sub>	28.0 <sup>+3.0</sup> <sub>-1.5</sub>
<i>Moulin totals</i>			<i>245 ± 174</i>	<i>32</i>			<i>322 ± 174</i>	<i>32</i>			<i>9.6 ± 7.7</i>	<i>41</i>		

### 3.5.3 Implications for CO<sub>2</sub> flux measurements

#### 3.5.3.1 Accuracy and precision of CO<sub>2</sub> flux measurements

The time-dependency of carbon accumulations during the CO<sub>2</sub> flux measurements (Figure 3-5 and Figure 3-6) has provided new insights into the nature of the shallow weathering zone (Section 3.5.1 and Section 3.5.2). It also has important implications for how CO<sub>2</sub> fluxes are quantified, and the associated accuracy and precision.

In short, changes of  $p\text{CO}_2^{\text{Chamber}}$  during the field operations are interpreted as the combination of: i) purging of CO<sub>2</sub> stored initially in the chamber and surrounding rock pores ( $p\text{CO}_2^{\text{Rock}}$ ); and ii) the real-time production of CO<sub>2</sub> from oxidative weathering. At the start of a CO<sub>2</sub> flux measurement, CO<sub>2</sub> accumulations have important contributions from i), which led previous studies to use the later repeats ( $q_4$  to  $q_{n \geq 6}$ ) to quantify ii) (Chapter 2) (Soulet et al., 2021, 2018). Here, longer measurements at each chamber allow us to explore this in more detail. As discussed earlier, the CO<sub>2</sub> accumulation rates from a single chamber at each visit over a year at the Brusquet and the Moulin sites show an exponential decline, and the assumption that a CO<sub>2</sub><sup>Plateau</sup> accumulation rate can be observed, if a measurement is long enough, has been affirmed, based on performing more repeats than previous studies (Figure 3-6).

The time it takes for the CO<sub>2</sub> accumulation rates to decline and stabilize within the 95 % confidence interval of the  $q_{\text{plateau}}$  value derived from fitting CO<sub>2</sub> accumulation rates over time (Equation 3-11) differs between flux measurements, but is ~ 90 min corresponding to ~ 10 repeats (Figure 3-6). This observation implies that treating only the first 3 repeats of a measurement as combined signals of purging and production of CO<sub>2</sub>, as it was done previously in similar studies (Chapter 2) (Soulet et al., 2021, 2018), returns a greater flux than  $q_{\text{plateau}}$ . Here, we quantify this impact by assuming that  $q_{\text{plateau}}$  provides an accurate value of CO<sub>2</sub> accumulation. In respect to the wide range of CO<sub>2</sub> fluxes occurring at the study sites over a year, we find that any overestimate is rather modest and not biased across this range.

The average accumulation rate of the measured repeats 4 – 6 is ~ 15 % higher than the  $q_{\text{plateau}}$  value (Figure 3-11A). This is true for the entire data set, including stabilized and extrapolated measurements (slope of linear regression =  $1.151 \pm 0.013$ ,  $R^2 = 0.99$ ,  $n = 74$ ,  $p = <0.001$ ) and also for the site-specific samples (slope =  $1.152 \pm 0.017$  and  $1.150 \pm 0.021$  for the Brusquet catchment and Moulin catchment, respectively). It is important to note that this relative offset is constant irrespective of the overall size of the CO<sub>2</sub> accumulation (Figure 3-11A), which means that flux data including non-plateaued accumulations can be corrected. It also means that any link between CO<sub>2</sub> flux and measured environmental variables is robust (Chapter 2) (Soulet et al., 2021). This finding also confirms that the purging of the chamber and

connected rock pores is systematic and predictable. When taking the average of the measured repeats 6 – 8 (Figure 3-11B), the value is ~ 7 % higher than  $q_{\text{plateau}}$  (all samples: slope of linear regression =  $1.066 \pm 0.009$ ,  $R^2 = 0.99$ ,  $n = 69$ ,  $p = <0.001$ ; Brusquet: slope =  $1.068 \pm 0.012$ ; Moulin: slope =  $1.062 \pm 0.016$ ).

In addition to accuracy, the precision needs to be considered to evaluate the overall uncertainty of CO<sub>2</sub> flux measurements using drilled chambers. However, the precision cannot be determined on the basis of replicated measurements because CO<sub>2</sub> fluxes are established over a few hours, over which time ambient environmental conditions such as temperature and precipitation may change. Here, we assess the precision using the exponential fitting model and the uncertainty of the calculated  $q_{\text{plateau}}$  values. For this, we consider the uncertainty of the CO<sub>2</sub> Plateau accumulation rates as the greater value of either the variability of the last 3 measured repeats (2 SD added to the mean) or the 95 % confidence interval of  $q_{\text{plateau}}$  derived from the fitting procedure. On average, this corresponds to a relative uncertainty of  $6.0 \pm 2.8 \%$  ( $\pm 1$  SD,  $n = 40$ , stabilized measurements), which is similar for both study sites (Brusquet:  $7.3 \pm 3.4 \%$ ,  $n = 17$ , Moulin:  $5.1 \pm 1.9 \%$ ,  $n = 23$ ). Extrapolations using chamber-specific averages of the removal constant  $\beta$  from stabilized measurements (that were performed for measurements considered as not stabilized) introduced a larger uncertainty of  $q_{\text{plateau}}$  of on average  $17.4 \pm 21.8 \%$  ( $n = 37$ ). For comparison, the combined uncertainty of accuracy and precision of the averaged repeats 4 – 6 is  $\sim 11.6 \pm 7.6 \%$  (average of 2 SD of the repeated accumulations  $\pm 1$  SD of this average,  $n = 74$ ), which is similar for both study sites (Brusquet:  $10.4 \pm 5.2 \%$ ,  $n = 35$ , Moulin:  $12.7 \pm 9.1 \%$ ,  $n = 39$ ). The averaged repeats 6 – 8 have an uncertainty of  $\sim 9.0 \pm 7.6 \%$  ( $n = 69$ ), which is similar for both study sites (Brusquet:  $8.2 \pm 4.8 \%$ ,  $n = 32$ , Moulin:  $9.7 \pm 9.3 \%$ ,  $n = 37$ ). Overall, the uncertainties associated with the precision found in this study are small compared to the range of chamber-derived CO<sub>2</sub> fluxes occurring at both study sites over time (Figure 3-11, Table 3-5).

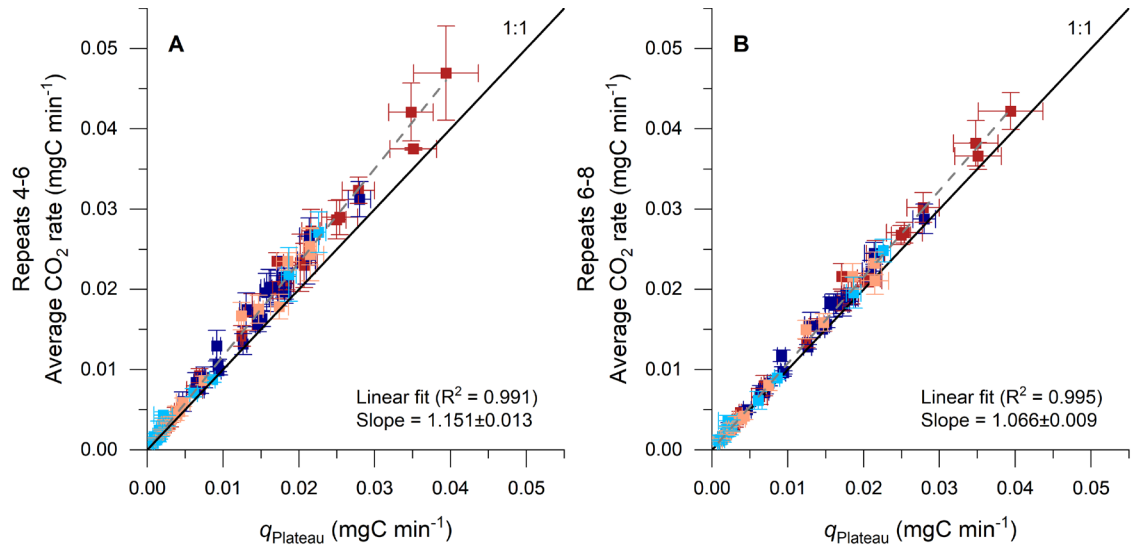


**Figure 3-11. Comparison of CO<sub>2</sub> fluxes determined by using the average of repeated accumulation rates and by an exponential fitting model.** Results from the proposed model are given on the x-axis ( $q_{\text{plateau}}$ , Equation 3-11;  $\pm 95\%$  CI) and are compared with the averages of the repeats 4 – 6 (Panel A) and of the repeats 6 – 8 (Panel B) on the y-axis ( $\pm 2$  SD), alongside a linear regression and a 1 : 1 line for reference. Red colours indicate samples from the Brusquet catchment (stabilized: dark, extrapolated fitting: light), and blue colours indicate samples from the Moulin catchment (stabilized: dark, extrapolated fitting: light).

### 3.5.3.2 Reporting CO<sub>2</sub> flux as a function of temperature

Recent research has highlighted that temperature controls the release of CO<sub>2</sub> from chambers drilled into the shallow weathering zone of sedimentary rocks (Soulet et al., 2021), with an exponential response:

$$F = F_0 \times \exp(\gamma \times T) \quad (3-19)$$

where  $F$  is the CO<sub>2</sub> flux ( $\text{mgC m}^{-2} \text{d}^{-1}$ , using the chamber-specific inner surface area),  $T$  is the temperature ( $^{\circ}\text{C}$ ),  $F_0$  is the CO<sub>2</sub> flux at  $0^{\circ}\text{C}$  and  $\gamma$  is the growth rate parameter ( $^{\circ}\text{C}^{-1}$ ) that is derived from an exponential model. For the oxidation of marly limestones, Soulet et al. (2021) found a value for  $\gamma$  of  $0.070 \pm 0.007^{\circ}\text{C}^{-1}$  ( $\pm$  standard error) considering five different chambers independent of their  $F_0$  values, based on daily-averaged chamber temperatures. Across differences in the hydrological setting of these chambers,  $F_0$  values ranged from  $35 \pm 7 \text{ mgC m}^{-2} \text{d}^{-1}$  to  $626 \pm 113 \text{ mgC m}^{-2} \text{d}^{-1}$  with the lowest CO<sub>2</sub> fluxes in close proximity to a riverbed (Soulet et al., 2021).

Here, at different installation sites, we find a similar exponential response of CO<sub>2</sub> release to temperature with a  $\gamma$  of  $0.065 \pm 0.012^{\circ}\text{C}^{-1}$  at the Brusquet site and a  $\gamma$  of  $0.067 \pm 0.018^{\circ}\text{C}^{-1}$  at the Moulin site. However, using an hourly resolution for the chamber temperature (Figure 3-12A) returns a  $\gamma$  of  $0.077 \pm 0.013^{\circ}\text{C}^{-1}$  at the Brusquet site and a  $\gamma$  of  $0.085 \pm 0.016^{\circ}\text{C}^{-1}$  at the Moulin site. This can be explained by an instantaneous response of weathering reactions to *in*

*situ* temperature changes, and that daily average temperatures capture lower night-time temperatures when flux measurements were not carried out. This also fits to the observation that CO<sub>2</sub> fluxes increased over a few hours alongside increases of chamber temperature for chambers visited twice a day: for chamber 5 at the Brusquet site,  $q_{\text{plateau}}$  increased from 1.1  $\mu\text{gC min}^{-1}$  to 3.8  $\mu\text{gC min}^{-1}$  and from 2.6  $\mu\text{gC min}^{-1}$  to 4.7  $\mu\text{gC min}^{-1}$  coinciding with temperature increases from -0.9 °C to 1.0 °C and from 2.0 °C to 5.0 °C, respectively; for chamber 4 at the Moulin site,  $q_{\text{plateau}}$  increased from 14.6  $\mu\text{gC min}^{-1}$  to 18.0  $\mu\text{gC min}^{-1}$  and from 16.3  $\mu\text{gC min}^{-1}$  to 21.4  $\mu\text{gC min}^{-1}$  coinciding with temperature increases from 22.5 °C to 26.5 °C and from 22.0 °C to 27.0 °C, respectively. Overall, this evidence highlights the importance of considering the *in situ* environmental conditions with a high temporal resolution (Section 3.4.1).

Furthermore, despite the similarities of the topography, hydrology and erosion rates (Figure 3-1 and Figure 3-2), we find site-specific differences in the bulk CO<sub>2</sub> production at a given temperature, which may be linked to differences in the source of carbon associated with the different rock types outcropping in the Brusquet catchment (black shales;  $F_0 = 122.2 \pm 41.3 \text{ mgC m}^{-2} \text{ d}^{-1}$ ) and in the Moulin catchment (marly limestones;  $F_0 = 45.6 \pm 20.3 \text{ mgC m}^{-2} \text{ d}^{-1}$ ) (Figure 3-12).

We also find that changes in temperature coincide with changes in the diffusive processes in the rocks surrounding a chamber (Section 3.5.1). To differentiate changes in the diffusive framework from the CO<sub>2</sub> production at a given temperature (i.e., weathering kinetics), the CO<sub>2</sub> fluxes can be set in context with  $V_{\text{Rock pores}}$ , which is representative for the contributing amount of rock grains undergoing oxidation (Section 3.5.2). Since the observed CO<sub>2</sub> fluxes range by a factor of  $\sim 18.2$ , while values of  $V_{\text{Rock pores}}$  exhibit a lower range of a factor of  $\sim 5.9$  (Table 3-5), a normalization of the CO<sub>2</sub> fluxes to the measurement-specific value of  $V_{\text{Rock pores}}$  does not diminish the importance of the temperature control on the CO<sub>2</sub> release (Figure 3-12C). However, due to large measurement-specific uncertainties that are associated with the calculation of  $V_{\text{Rock pores}}$ , a full assessment of whether higher chamber-derived CO<sub>2</sub> fluxes at higher temperatures are partly a result of greater contributing rock volumes is hindered.

Considering the large uncertainties of  $V_{\text{Rock pores}}$ , we suggest normalizing to the chamber-specific averages of  $V_{\text{Rock pores}}$ . This allows investigation of how CO<sub>2</sub> release from a given rock volume scales with temperature and of how site-specific differences may be related to differences in the rock chemistry (Figure 3-12B). The corresponding  $\gamma$  values are  $0.077 \pm 0.016 \text{ } ^\circ\text{C}^{-1}$  and  $0.085 \pm 0.015 \text{ } ^\circ\text{C}^{-1}$  for a  $F_0$  of  $7.86 \pm 3.37 \text{ mgC m}^{-3} \text{ min}^{-1}$  and  $4.63 \pm 1.83 \text{ mgC m}^{-3} \text{ min}^{-1}$  at the Brusquet site and the Moulin site, respectively. To better understand these different weathering fluxes, future research is needed to assess the carbon source(s) and the response of the weathering reactions to changes in temperature at both study

sites in more detail, for instance, by studying the chemical composition of the rocks (i.e., contents of OC<sub>petro</sub>, carbonates and sulfides) alongside the radiocarbon and stable carbon isotope composition of the released CO<sub>2</sub>, analogously to previous research in the neighbouring Laval catchment (Soulet et al., 2021, 2018) and in the Waiapu catchment in New Zealand (Chapter 2).

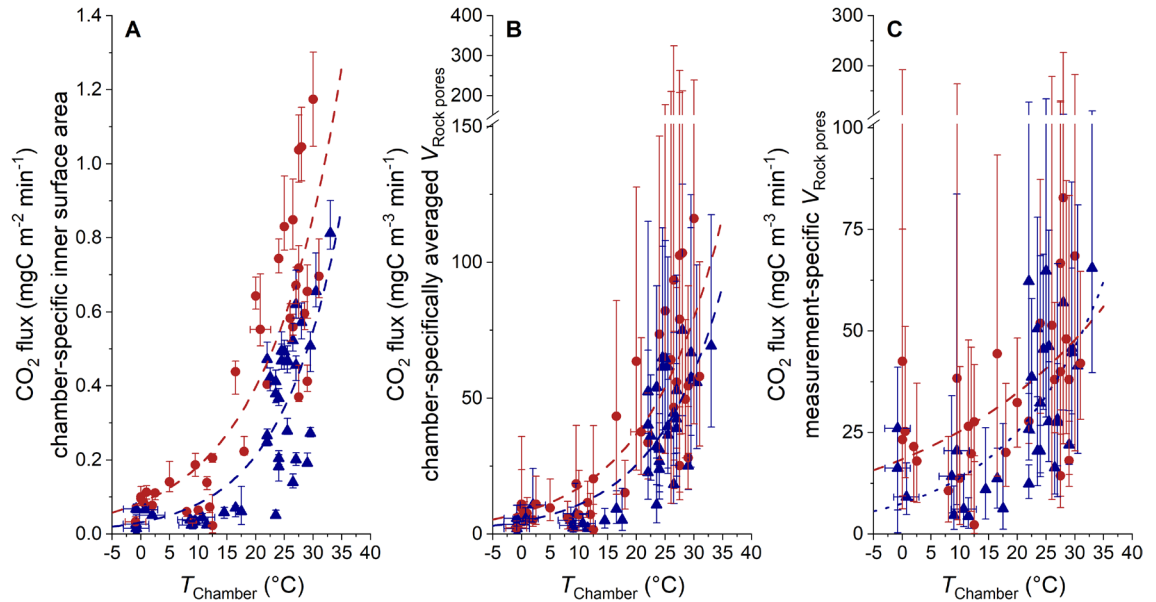


**Figure 3-12. Comparison of CO<sub>2</sub> fluxes with different normalizations and chamber temperature.** Panel A: normalization to the chamber-specific inner surface area (Table 3-1) (including the 95 % CI of  $q_{\text{plateau}}$ ). Panel B: normalization to chamber-specifically averaged  $V_{\text{Rock pores}}$  (Table 3-5) (including the combined uncertainty of  $q_{\text{plateau}}$  and the averaged 95 % CI of  $V_{\text{Rock pores}}$ ). Panel C: normalization to measurement-specific  $V_{\text{Rock pores}}$  (including the combined uncertainty of  $q_{\text{plateau}}$  and the measurement-specific 95 % CI of  $V_{\text{Rock pores}}$ ). Estimated temperatures are indicated by accompanying error bars (RMSE). Colours indicate the site of measurement (Brusquet: red, Moulin: blue).

### 3.5.4 Linking CO<sub>2</sub> and O<sub>2</sub> fluxes

In addition to CO<sub>2</sub> flux measurements, another tool for investigating the kinetics of oxidative weathering of sedimentary rocks is to assess the O<sub>2</sub> consumption in the weathering zone (Tune et al., 2020), analogous to previous research on soils (Angert et al., 2015; Hicks Pries et al., 2020). Overall,  $p\text{O}_2_{\text{Chamber}}$  values in the Brusquet catchment and in the Moulin catchment were similar or lower than the O<sub>2</sub> concentration of the atmosphere, confirming that the studied weathering zones are sinks of oxygen. The variation of  $p\text{O}_2_{\text{Chamber}}$  over time coincides with a variation in temperature within the chambers (Figure 3-13A), with roughly similar relationships for both study sites. This observation fits to the recently proposed importance of temperature controlling oxidative weathering kinetics (Soulet et al., 2021). However, due to a limited number

of samples and a large measurement uncertainty, neither chamber-specific differences nor the impact of precipitation on  $pO_{2\text{ Chamber}}$  can be evaluated accurately.

The observed  $pO_{2\text{ Chamber}}$  values can be used to calculate a diffusive flux of O<sub>2</sub> between the chamber, connected rock pores and the atmosphere (Equation 3-9 and Equation 3-10). For this, the insights into the diffusive processes of the chambers and the connected rock space, which are derived from the CO<sub>2</sub> measurements, are used (Section 3.3.7 and Section 3.5.1). Previous work on porous media has established that the effective diffusivities of CO<sub>2</sub> and O<sub>2</sub> can be expected to be influenced similarly by the structure of the air-filled pore space (Angert et al., 2015; Millington, 1959; Penman, 1940), which allows determination of the effective diffusivity of O<sub>2</sub> from that of CO<sub>2</sub> in the shallow weathering zone.

The calculated O<sub>2</sub> fluxes are representative of the same rock volume that is releasing CO<sub>2</sub>, which also means that a report of absolute fluxes is possible (Section 3.5.2). Altogether, the chamber-specific O<sub>2</sub> exchange rate in the Brusquet catchment and the Moulin catchment range between zero within uncertainty ( $0.42^{+0.58}_{-0.88}$   $\mu\text{mol O}_2 \text{ min}^{-1}$ ) to a maximum consumption of O<sub>2</sub> of  $-16.33^{+5.72}_{-7.75}$   $\mu\text{mol O}_2 \text{ min}^{-1}$ , with increasing O<sub>2</sub> consumption with increasing temperature (Figure 3-13B). It should be noted that reporting O<sub>2</sub> fluxes is associated with a greater relative uncertainty compared to the  $pO_2$  gradient because the uncertainties associated with the determination of the measurement-specific diffusivity are included in the O<sub>2</sub> flux calculation.

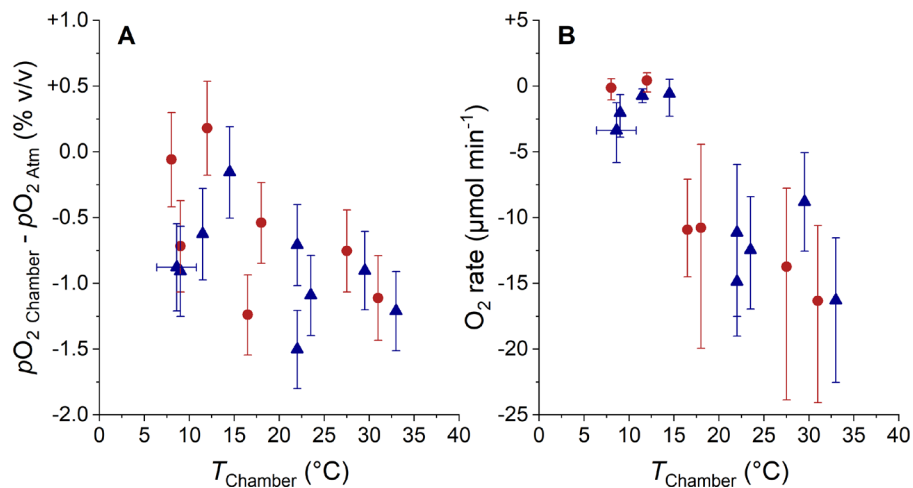


**Figure 3-13. Comparison of O<sub>2</sub> partial pressure and O<sub>2</sub> flux with temperature.** Panel A:  $pO_{2\text{ Chamber}}$  (normalized to atmospheric  $pO_2$ ,  $\pm$  RMSE) and chamber temperature. Panel B: O<sub>2</sub> consumption rate (per chamber,  $\pm$  95 % CI) and chamber temperature. The origin of samples is indicated with red circles for the Brusquet catchment and blue triangles for the Moulin catchment. Estimated temperatures are indicated by accompanying error bars (RMSE).

The O<sub>2</sub> flux into the chambers and their connected rock pores can be compared with the CO<sub>2</sub> flux from this space. At 20 °C, an O<sub>2</sub> consumption rate of ~8.7 μmol O<sub>2</sub> min<sup>-1</sup> coincides with an average CO<sub>2</sub> accumulation rate of ~1.1 μmol CO<sub>2</sub> min<sup>-1</sup> in the Brusquet catchment and of ~0.6 μmol CO<sub>2</sub> min<sup>-1</sup> in the Moulin catchment. This is an average ratio of ~10 mol O<sub>2</sub> : 1 mol CO<sub>2</sub>. This field-based molar ratio of O<sub>2</sub> consumption and CO<sub>2</sub> release is significantly lower than the theoretical ratio of weathering reactions describing the oxidation of sedimentary rocks. For example, the oxidation of OC<sub>petro</sub> is theoretically described by a ratio of 1 mol O<sub>2</sub> : 1 mol CO<sub>2</sub> (Petsch, 2014). In addition, the oxidation of pyrite minerals coupled to the dissolution of carbonates is theoretically characterized by a ratio of up to 1.875 mol O<sub>2</sub> : 1 mol CO<sub>2</sub> if the CO<sub>2</sub> release occurs *in situ* (Soulet et al., 2021; Torres et al., 2014). To investigate this discrepancy, here we discuss several mechanisms that could influence the consumption of O<sub>2</sub> and the release of CO<sub>2</sub> in the shallow weathering zone.

In addition to OC<sub>petro</sub> and pyrite minerals, other minerals, such as illite, chlorite, and ankerite, can be a sink of oxygen during the weathering of sedimentary rocks (Brantley et al., 2013; Sullivan et al., 2016). However, in settings where pyrite minerals are present, the chemical weathering of these other ferrous iron bearing minerals progresses relatively slowly and advances only more rapidly following the complete oxidation of pyrite minerals (Gu et al., 2020a, 2020b). Accordingly, pyrite minerals should be the dominating inorganic O<sub>2</sub> sink at the two study sites.

It has been previously suggested that the oxidation of OC<sub>petro</sub> progresses in a stepwise manner, with the formation of oxygenated compounds of organic matter prior to the release of CO<sub>2</sub> (Chang and Berner, 1999), typically resulting in an increase of the relative oxygen content of OC<sub>petro</sub> during chemical weathering (Longbottom and Hockaday, 2019; Petsch, 2014; Tamamura et al., 2015). If the oxidation of OC<sub>petro</sub> progresses more rapidly than the separate process of CO<sub>2</sub> release from oxygenated OC<sub>petro</sub> in the Draix-Bléone observatory, this could partly explain the lower ratio of CO<sub>2</sub> released compared to the O<sub>2</sub> uptake. However, for rocks exposed in rapidly eroding terrains in the Draix-Bléone observatory, previous studies did not find a significant effect of weathering on the chemical composition of OC<sub>petro</sub>, despite a decrease in the quantities of OC<sub>petro</sub> and pyrite minerals (Copard et al., 2006; Graz et al., 2011). Thus, it seems unlikely that the oxidation of OC<sub>petro</sub> at both study sites deviates notably from the theoretical stoichiometry mentioned above.

Furthermore, if the sulfuric acid derived from the oxidation of pyrite minerals interacts with silicate minerals (Blattmann et al., 2019b; Bufe et al., 2021), this would lead to O<sub>2</sub> consumption but no CO<sub>2</sub> release. In addition, sulfuric acid could interact with OC<sub>petro</sub> and be

neutralized, yet the vast majority of OC<sub>petro</sub> is typically made of kerogen, which is resistant to acid hydrolysis, and only minor amounts of more labile organic matter can be prone to this type of degradation (Killops and Killops, 2005; Petsch, 2014; Seifert et al., 2011; Włodarczyk et al., 2018).

Another explanation may involve the lateral transport of CO<sub>2</sub> as part of the dissolved load, lowering the gaseous release of carbon. The oxidation of OC<sub>petro</sub> and pyrite minerals coupled to the dissolution of carbonates occur in a humid weathering zone (Figure 3-4), where CO<sub>2</sub> may be incorporated into the dissolved inorganic carbon (DIC) pool (Chapter 2) (Bao et al., 2017; Soulet et al., 2021; Torres et al., 2014). A recent study has quantified the export of DIC using the molar ratio of O<sub>2</sub> and CO<sub>2</sub> fluxes for sedimentary rocks undergoing weathering below a forested hillslope (Tune et al., 2020). There, carbon is sourced from soils, roots or OC<sub>petro</sub>, with an absence of an inorganic carbon source and of pyrite minerals. If a part of the CO<sub>2</sub> from oxidative weathering is exported as DIC in the Brusquet and the Moulin catchments, this would raise the observed gaseous O<sub>2</sub> to CO<sub>2</sub> ratio, and would have to do so by a factor in the range of ~ 4 and 15. This is worthy of future research towards understanding O<sub>2</sub> consumption in the weathering zone. Here, a more accurate quantification is hindered because the proportions of inorganic carbon release versus organic carbon release (which derive from weathering reactions with a different stoichiometry as described above) are unknown. This again calls for future work to assess the carbon sources in more detail.

Overall, we have developed the tools needed to quantify the production or consumption, storage and movement of CO<sub>2</sub> and O<sub>2</sub> in the near-surface of rocks undergoing weathering. If combined, for example, with surface chambers (for gaseous exchange) and boreholes extending below the oxidation front (profiling gaseous and dissolved processes) (Tokunaga et al., 2016), alongside radiocarbon and stable carbon isotope analyses (for partitioning the weathering reactions) (Chapter 2) (Keller and Bacon, 1998; Soulet et al., 2021), the cycling of carbon and oxygen in the total critical zone and its environmental controls could be investigated comprehensively. Using drilled chambers benefits investigations using the gradient method for profiles of gas concentrations, because with the approach suggested here the diffusivity measures can be determined *in situ* and in real-time, which else are typically estimated (Keller and Bacon, 1998; Maier and Schack-Kirchner, 2014; Tokunaga et al., 2016; Tune et al., 2020). Furthermore, by assessing the release and movement of nitrous oxide from the subsurface (Wan et al., 2021), an overall greenhouse gas budget could be developed for sedimentary rocks undergoing weathering. This would be especially valuable for sites with a thin soil cover, which typically dominate more widespread terrains at lower slopes compared to the study sites presented here (Heimsath et al., 2012; Milodowski et al., 2015). There, the additional,

modern carbon pool complicates disentangling biogeochemical processes and the corresponding source-specific CO<sub>2</sub> and O<sub>2</sub> fluxes, however, they mark a potential hotspot of carbon cycling between the lithosphere and recent atmosphere (Copard et al., 2006; Hemingway et al., 2018; Keller and Bacon, 1998; Longbottom and Hockaday, 2019; Tune et al., 2020).

### 3.6 Conclusions

The present study has further developed and assessed methods for *in situ* constraints on the release of CO<sub>2</sub> and the consumption of O<sub>2</sub> during oxidative weathering of exposed sedimentary rocks. Our new method framework allows for both accurate quantification of weathering fluxes over hourly to daily timescales, while also constraining diffusive processes in the shallow weathering zone. At two sites of the Draix-Bléone observatory (France), accumulation chambers were installed by drilling holes directly into rocks undergoing weathering in the Brusquet catchment (black shales) and in the Moulin catchment (marly limestones). At each site, using an array of 4 chambers, measurements of  $p\text{CO}_{2\text{Rock}}$  and CO<sub>2</sub> fluxes were carried out alongside  $p\text{O}_{2\text{Rock}}$  measurements during six fieldtrips over one year.

We find that during a single visit to a chamber, the accumulation rates decline over a few measurement cycles, before reaching a stable CO<sub>2</sub> accumulation rate. This pattern is consistent across the fieldtrips, and can be described by an exponential model. To explain these observations, we outline a framework which considers the measured CO<sub>2</sub> accumulation as a combination of the real-time production during weathering, with the release of excess CO<sub>2</sub> built up in pore space surrounding the chambers. By doing so, we can assess the rock pore volume and rock mass that produce CO<sub>2</sub>. For the first time, this allows an absolute report of rock-derived CO<sub>2</sub> fluxes measured *in situ* and in real-time, providing input data for future studies modeling the chemical weathering of sedimentary rocks. The assessment of contributing rock pore space allows us also to normalize the fluxes to an outcrop surface area, enabling comparison of the weathering fluxes at the study sites to other rock types and soils across different terrains and climates. Furthermore, by studying the accumulation of CO<sub>2</sub> in a chamber and the connected rock pore space over time, the diffusivity of gases in the shallow weathering zone and its environmental controls are investigated, including an absolute, *in situ* determination of the diffusion coefficients.

In addition to these insights into the CO<sub>2</sub> release,  $p\text{O}_2$  values for the studied rocks are presented and used together with the quantification of the diffusive processes in the weathering zone to calculate O<sub>2</sub> fluxes. It is shown that the consumption of O<sub>2</sub> co-varies with changes in the emission of CO<sub>2</sub> over time, which are driven by changes in temperature. However, the O<sub>2</sub> fluxes indicate significantly greater oxidative weathering rates compared to the CO<sub>2</sub> fluxes. We suggest

this discrepancy results of the export of inorganic carbon by the dissolved load of percolating waters lowering the effective release of gaseous CO<sub>2</sub>.

A site-specific difference in the magnitude of CO<sub>2</sub> emissions at the two study sites cannot be explained by differences in the lithological properties influencing the diffusion of gas within the rock space surrounding the chambers as both study sites have similar characteristics, which is evidenced by diffusivity measures changing similarly alongside temperature and precipitation. This finding suggests that differences in the source of carbon are the main reason for the observed CO<sub>2</sub> flux differences, providing an opportunity for future research to investigate the control of the chemical composition of the rocks (i.e., contents of OC<sub>petro</sub>, carbonates and sulfides) on the CO<sub>2</sub> flux size.

### **3.7 Acknowledgements**

This work was supported by the European Research Council (Starting Grant to RGH, ROC-CO<sub>2</sub> project, grant 678779).

## 3.8 Supplementary

### 3.8.1 Details of the fitting model for chamber temperatures

Overview of site-specific fitting coefficients used for modeling chamber temperatures based on air temperature and fractional duration of daylight (Equation 3-2 and Equation 3-3) and details of the goodness of the fitting model based on comparisons to measured chamber temperatures with hourly and daily resolution.

Site	R <sup>2</sup>	p-value	n	RMSE (hourly) (°C)	RMSE (daily) (°C)	<i>coeff</i> <sub>A</sub>	<i>coeff</i> <sub>B</sub>	<i>coeff</i> <sub>c1</sub>	<i>coeff</i> <sub>c2</sub>	<i>coeff</i> <sub>c3</sub>	<i>coeff</i> <sub>c4</sub>
Brusquet	0.96	<0.001	7,392	1.80	1.58	1.147	0.361	0.408	2.364	0.080	30.106
Moulin	0.94	<0.001	5,664	2.21	1.99	1.222	0.298	0.362	2.074	0.093	26.407

### 3.8.2 Linear regression of $p\text{CO}_2$ Rock and CO<sub>2</sub> accumulation rates

Details of linear regressions comparing measurement-specific values of  $p\text{CO}_2$  Rock and CO<sub>2</sub> accumulation (based on repeats 6 – 8) (with  $p\text{CO}_2$  (ppmv) =  $a_1 \times \text{CO}_2\text{rate}$  ( $\mu\text{gC min}^{-1}$ ) +  $a_2$ ) including the standard errors of the fitting parameters. Differentiations into “dry” and “wet” samples are based on a threshold of a cumulative precipitation of 5 mm over 3 days prior to the measurement. Both sites have similar linear regressions with overlapping standard errors.

Data set	$a_1$	$a_2$	R <sup>2</sup>	p-value	n
all	55.1 ± 5.1	848.7 ± 83.5	0.69	<0.001	55
<i>Brusquet</i>	55.0 ± 6.3	741.6 ± 120.5	0.77	<0.001	25
<i>Moulin</i>	61.1 ± 8.5	872.5 ± 117.0	0.64	<0.001	30
all - dry	59.1 ± 6.4	664.3 ± 122.2	0.75	<0.001	31
all - wet	61.0 ± 8.3	948.7 ± 101.0	0.71	<0.001	24

### 3.8.3 Linear regression of diffusivity measures

Details of linear regressions comparing the diffusivity measures  $\frac{D_{\text{CO}_2}}{\omega}$  and  $\lambda$  (with  $\frac{D_{\text{CO}_2}}{\omega}$  ( $\text{cm}^3 \text{min}^{-1}$ ) =  $b_1 \times \lambda$  ( $\text{min}^{-1}$ ) +  $b_2$ ) including the standard errors of the fitting parameters. Differentiations into “dry” and “wet” samples are based on a threshold of a cumulative precipitation of 5 mm over 3 days prior to the measurement. The regressions are based on using the average values from the repeats 6 – 8 of the flux measurements, which is typically close to stabilization of the CO<sub>2</sub> accumulation rate, because a significant number of the measurements was limited to 8 repeats. Both sites have comparable linear regressions with overlapping standard errors.

Data set	$b_1$	$b_2$	R <sup>2</sup>	p-value	n
all	163.4 ± 13.2	-1.13 ± 2.25	0.74	<0.001	55
<i>Brusquet</i>	162.1 ± 13.9	-1.54 ± 2.67	0.86	<0.001	25
<i>Moulin</i>	170.4 ± 24.0	-1.57 ± 3.61	0.64	<0.001	30
all - dry	151.4 ± 18.5	2.25 ± 3.58	0.71	<0.001	31
all - wet	157.2 ± 22.9	-1.94 ± 3.13	0.68	<0.001	24

### 3.8.4 Different diffusion pathways of a closed versus manipulated chamber

The diffusion pathways of a closed chamber differ from that of a manipulated chamber. During a flux measurement, CO<sub>2</sub>, which is released from a rock grain undergoing oxidative weathering into the pore space, moves via diffusion along a concentration gradient, which is initiated by lowering repeatedly the  $p\text{CO}_2$  Chamber to a near-atmospheric level (Soulet et al., 2018), from the rock pores towards the manipulated chamber if they are connected more effectively to the chamber than to the rock-atmosphere boundary. In contrast, without a sampling system acting as the receiving reservoir, rock-derived CO<sub>2</sub> travels along the concentration gradient towards the atmosphere. In the latter scenario, rock pores that contribute CO<sub>2</sub> during a flux measurement to a chamber either contribute the CO<sub>2</sub> via diffusion directly to the atmosphere (without a pathway through the chamber) or through the chamber towards the atmosphere.

#### 4 Carbon dioxide emissions during sedimentary rock weathering scale with organic matter content and temperature



*Gullied landscape in the Laval catchment, Draix-Bléone observatory, France. May 2018.*

This chapter is designed for submission to a peer-reviewed journal, with the following authors:

Tobias Roylands<sup>1</sup>, Mark H. Garnett<sup>2</sup>, Guillaume Soulet<sup>1,3</sup>, Erin L. McClymont<sup>1</sup>, Sébastien Klotz<sup>4</sup>, Josephine-Anne Newton<sup>2</sup>, Caroline Le Bouteiller<sup>4</sup>, Robert G. Hilton<sup>1,5</sup>.

Affiliations:

<sup>1</sup> Department of Geography, Durham University, South Road, Durham DH1 3LE, United Kingdom

<sup>2</sup> NEIF Radiocarbon Laboratory, Rankine Avenue, East Kilbride, Glasgow G75 0QF, United Kingdom

<sup>3</sup> Geo-Ocean, Brest University, CNRS, Ifremer, F-29280 Plouzané, France

<sup>4</sup> Univ. Grenoble Alpes, INRAE, UR ETNA, 2 rue de la papeterie, BP 76, 38402 Saint-Martin-d'Hères, Cedex, France

<sup>5</sup> Department of Earth Sciences, University of Oxford, South Parks Road, Oxford OX1 3AN, United Kingdom

Contributions:

The research was conceptualized by TR, with help from RGH, ELM and GS. The main methods were designed by TR, with help from MHG, GS, RGH and ELM. Field-based analyses were described previously (Chapter 3). The laboratory geochemical measurements were led by MHG, JAN and TR, and climate-related information was provided by SK and CLB. TR led the formal analysis, investigation, data visualization and writing of the original draft, under supervision of RGH and ELM. All authors contributed to subsequent review and editing, led by TR, RGH, ELM and GS. Funding was acquired by TR, RGH, and MHG.

All co-authors confirmed that they agree with the work to be included in this thesis.

## 4.1 Abstract

Oxidative weathering is an important source of carbon dioxide (CO<sub>2</sub>) in the geological carbon cycle, occurring through transformation of petrogenic organic carbon (OC<sub>petro</sub>) or of pyrite coupled to the dissolution of carbonates minerals. Recent field-based measurements show an exponential growth in CO<sub>2</sub> release as the temperature of exposed sedimentary rocks increases. This suggests that oxidative weathering could act as a positive feedback to warming. To constrain the potential of this response at the regional to global scale, we require measurements that isolate the CO<sub>2</sub> from OC<sub>petro</sub> versus pyrite oxidation, while also assessing rocks of varying chemical composition. Here, we use weathering chambers to study black shales and marly limestones exposed in neighbouring catchments in the French southern Alps that share similar physical properties but have contrasting contents of OC<sub>petro</sub>. The contributions to chamber-derived CO<sub>2</sub> fluxes from different carbon sources are determined via radiocarbon and stable carbon isotope analyses. Following investigations across multiple seasons, it is possible to separate lithological and climatic controls on the source-specific CO<sub>2</sub> fluxes. We measure a common temperature response of CO<sub>2</sub> release from the oxidation of OC<sub>petro</sub> and pyrite minerals, which increases on average by a factor of 2.3 with a temperature increase of 10 °C in line with previous research. Differences in the OC<sub>petro</sub>-derived CO<sub>2</sub> flux at a given temperature between the two rock types scale with their OC<sub>petro</sub> contents, with an apparent 1 : 1 ratio between the concentration of weathering reactants and products. In contrast, the CO<sub>2</sub> flux derived from pyrite oxidation coupled to the dissolution of carbonates is not controlled by the quantity of these minerals, but the concentration of OC<sub>petro</sub>. This may be the result of a microbial link of both weathering pathways. Considering the temperature sensitivity and the extent of the rock volume contributing CO<sub>2</sub> to a chamber, we find high mean annual topographic CO<sub>2</sub> fluxes derived from OC<sub>petro</sub>, ranging between 13 gC m<sup>-2</sup> yr<sup>-1</sup> and 180 gC m<sup>-2</sup> yr<sup>-1</sup>. For the oxygenated part of the weathering zone, we estimate a rapid degradation of OC<sub>petro</sub> with a lifetime of ~ 15 yr, while annually ~ 1.0 % of the total rock mass is dissolved in the form of carbonates following the oxidation of pyrite at both study sites. Together, these findings highlight that erosive areas are hotspots of oxidative weathering whose contributions need to be considered in Earth system models due to the dual control of OC<sub>petro</sub> content and temperature on the resultant CO<sub>2</sub> fluxes.

## 4.2 Introduction

There are vast amounts of carbon stored in Earth’s sedimentary rocks, which cover ~ 64 % of the present-day continental surface (Hartmann and Moosdorf, 2012), in the form of either organic carbon (petrogenic OC) or carbonate minerals (Petsch, 2014). The uppermost meter of the planet’s surface alone contains ~ 10<sup>6</sup> MtC of OC<sub>petro</sub> (Copard et al., 2007) and its chemical breakdown is an important source of carbon dioxide to the atmosphere on geological timescales, with an estimated global flux of ~ 40 MtC yr<sup>-1</sup> – 100 MtC yr<sup>-1</sup> (Petsch, 2014). Of particular significance for the exchange of carbon between rocks and the atmosphere are steep mountainous areas due to a link between physical erosion and oxidative weathering via a rapid supply and exposure of OC<sub>petro</sub> to oxygen (O<sub>2</sub>) in air or water (Hilton et al., 2014; Hilton and West, 2020), resulting in “georespiration” (pathway abbreviation: OC) (Berner, 1999; Keller and Bacon, 1998; Petsch, 2014):

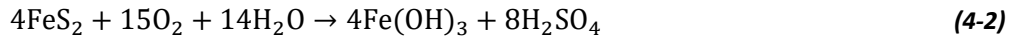


However, estimates of OC<sub>petro</sub> fluxes typically rely on indirect tracers (Hilton and West, 2020; Petsch, 2014), such as dissolved rhenium in river waters as a residual of oxidative weathering (Hilton et al., 2014; Horan et al., 2019). Tracer approaches integrate processes on a catchment-scale and thus hinder evaluation of local reactions operating under varying environmental conditions and controls (Hilton et al., 2021).

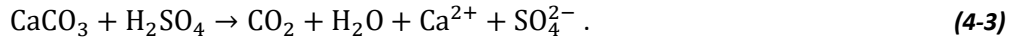
Recently, a method for direct CO<sub>2</sub> measurements was developed to quantify the carbon release from chemical weathering and investigate its environmental controls *in situ* (Soulet et al., 2018). By measuring the evolution of CO<sub>2</sub> efflux from chambers drilled into highly eroding marly limestones, Soulet et al. (2021) identified a temperature control on the flux of carbon emission from shallow weathering zones. These observations led to the proposal for a previously unrecognized, positive feedback to warming by sedimentary rock weathering. In addition to temperature, it was shown that moisture impacts the release of CO<sub>2</sub> from different fine-grained sedimentary rock types, associated with precipitation and location in a catchment (Chapter 2 and Chapter 3) (Soulet et al., 2021). In contrast, in settings with lower erosion rates, temperature changes less pronounced in the deeper weathering zones, and the effect of warming on oxidative weathering remains unclear (Gu et al., 2020b; Tune et al., 2020). For terrains with lower slopes, preliminary research indicates that water flow across the fractured bedrock vadose zone is the dominant control on CO<sub>2</sub> evasion by influencing O<sub>2</sub> delivery and wash-out of CO<sub>2</sub> via the dissolved load (Tremosa et al., 2020; Tune et al., 2020). However, carbon and oxygen cycling by soil organisms and vegetation complicates quantifying the rock-derived

component and its environmental controls in these settings (Keller and Bacon, 1998; Tune et al., 2020).

In parallel with OC<sub>petro</sub> oxidation, sedimentary rock weathering can result in another source of CO<sub>2</sub> via carbonate dissolution following pyrite oxidation (pathway abbreviation: SA) that releases sulfuric acid (Calmels et al., 2007; Torres et al., 2014):



and



Alternatively, the sulfuric acid can interact with carbonic acid from meteoric waters to dissolve carbonate minerals (pathway abbreviation: CSA), leading similarly to immediate CO<sub>2</sub> release (Soulet et al., 2021):



and



Due to the widespread co-occurrence of OC<sub>petro</sub>, carbonate and pyrite minerals (Berner and Berner, 2012), and because the oxidative weathering of these different materials may (co-)vary with changes in temperature, O<sub>2</sub> availability and water flow (Chang and Berner, 1999; Hilton et al., 2021; Kemeny et al., 2021; Nicholson et al., 1988; Soulet et al., 2021), source-specific contributions need to be carefully partitioned. Radiocarbon and stable carbon isotope analyses allow this, by considering the carbon isotope composition of both the produced CO<sub>2</sub> and the modern and rock-derived sources (Keller and Bacon, 1998; Soulet et al., 2018).

Building on the previous work by Soulet et al. (2021), we use new installations to directly assess the impact of temperature and lithology on both OC<sub>petro</sub>- and sulfide-derived CO<sub>2</sub> emissions during oxidative weathering (Equations 4-1 – 4-5). To do this, we study black shales and marly limestones as two rock types with contrasting contents of OC<sub>petro</sub>, from study sites located in similar hydrological settings in rapidly eroding terrains in the French southern Alps. For drilled weathering chambers installed at these sites, the volume of rock that contributes to bulk CO<sub>2</sub> fluxes has been previously estimated, based on quantifying the mass of CO<sub>2</sub> stored in a chamber and connected rock pores (Chapter 3). By investigating the carbon isotope compositions of CO<sub>2</sub> and its potential sources, we here partition the CO<sub>2</sub> release for contributions from OC<sub>petro</sub> (Equation 4-1) and carbonate dissolution coupled to pyrite oxidation (Equations 4-2 – 4-5). Together, this allows source-specific reporting of absolute CO<sub>2</sub> fluxes, with normalization to the mass and surface area of the contributing rock volumes. We discuss the importance of the chemical composition of bedrock, especially OC<sub>petro</sub> content, for scaling the CO<sub>2</sub> production alongside climatic controls that are traced across multiple seasons. In addition,

we examine the fate of OC<sub>petro</sub> introduced to shallow weathering zones and evaluate the importance of CO<sub>2</sub> release in steep mountainous areas for the global turnover of OC<sub>petro</sub>.

## 4.3 Material and methods

### 4.3.1 Study area

The study sites are located in two catchments with contrasting lithologies in the Draix-Bléone observatory (Draix-Bléone Observatory, 2015), which is part of the French network of critical zone observatories (OZCAR) (Gaillardet et al., 2018), and have been previously described in detail (Chapter 3). In summary, we installed weathering chambers into rapidly eroding, bare surfaces in the Brusquet catchment, overlaying Toarcian black shales, and in the Moulin catchment, overlaying Callovian to Oxfordian marly limestones (Copard et al., 2006; Graz et al., 2011). The Moulin catchment neighbours the Laval catchment, having a similar lithology to previous studies at the Draix-Bléone observatory (Soulet et al., 2021, 2018). The climatic, hydrodynamic and geomorphic context is provided by continuous monitoring of river water discharge, river suspended load and bedload transport at the observatory, alongside meteorological data (Draix-Bléone Observatory, 2015). The combination of erodible lithologies with a transitional climate between Alpine and Mediterranean of hot and dry summers, with short and intense rainfall events, and frequent freeze-thaw cycles in winter result in high physical weathering and erosion rates and a badland morphology (Ariagno et al., 2022; Bechet et al., 2016; Mathys et al., 2003; Mathys and Klotz, 2008; Rovéra and Robert, 2006). Experiencing high erosion rates of up to  $\sim 10 \text{ mm yr}^{-1}$  (Carriere et al., 2020; Mathys et al., 2003), surfaces devoid of soil and vegetation are widespread in the study area, with  $\sim 54 \%$  of the Moulin catchment exposed rock. In the Brusquet catchment, reforestation in the late 19<sup>th</sup> century has resulted in  $\sim 87 \%$  of its area now being vegetated (Carriere et al., 2020; Cras et al., 2007). On bare surfaces, pyrite minerals and OC<sub>petro</sub> occur often in quantities approaching those of unweathered bedrock with minimal chemical alteration (Copard et al., 2006; Graz et al., 2012, 2011). These settings are characterized by a thin weathering zone with elevated porosities extending to depths of  $\sim 15 \text{ cm}$  to  $\sim 50 \text{ cm}$ , consisting of detrital cover above fine and coarse regolith overlaying the bedrock (Maquaire et al., 2002; Mathys and Klotz, 2008; Oostwoud Wijdenes and Ergenzinger, 1998; Rovéra and Robert, 2006). The thickest detrital cover is found on crests, intermediate at gullies and minimal in thalwegs (Esteves et al., 2005; Maquaire et al., 2002).

### 4.3.2 Rock bulk chemistry

To assess the chemical composition of the rocks undergoing weathering, rock powder was collected during the drilling of the weathering chambers. The samples were then freeze-dried, ground and homogenized, and the carbon content and stable carbon isotope composition of organic carbon and inorganic carbon were determined, as detailed previously (Chapter 2). For organic carbon, an Elemental Analyser (Costech) coupled to an Isotope Ratio Mass Spectrometry (IRMS; Thermo Fisher Delta V Advantage) was used after inorganic carbon removal from the samples with aqueous HCl (4 mol L<sup>-1</sup>). For inorganic carbon, a carbonate dissolution device (Thermo Scientific Gas Bench II) coupled to an IRMS (Thermo Scientific MAT 253) was used. In addition, total sulfur measurements were performed on further aliquots of the homogenized material with an Elemental Analyser (Costech) coupled to an IRMS (Thermo Fisher Delta V Plus). The stable carbon isotope compositions are reported in per mil ( $\delta^{13}\text{C}$ , ‰) relative to Vienna Pee Dee Belemnite (VPDB) standard, with an analytical uncertainty in  $\delta^{13}\text{C}$  of  $\pm 0.1$  ‰ (2 standard deviations, 2 SD) for replicate analyses of the international standards and duplicates, whereas carbon and sulfur contents are reported in % weight, with a standard deviation of  $\sim 3$  wt.% of the measured values.

### 4.3.3 CO<sub>2</sub> fluxes

#### 4.3.3.1 Total CO<sub>2</sub> fluxes

The installation of weathering chambers and measurements of total CO<sub>2</sub> fluxes following Soulet et al. (2018) have been previously detailed for these installations (Chapter 3). In summary, at both the Brusquet and Moulin study sites, an array of 4 chambers was installed in the steep walls of gullies, with a minimal distance of 70 cm between chambers, by drilling horizontally into bare rock faces devoid of roots and with minimal soil or vegetation cover in the vicinity. Each chamber was drilled to a depth of  $\sim 38$  cm using a mechanical drill with a diameter of 2.9 cm and was isolated from the atmosphere following the design by Soulet et al. (2018) after removal of residual rock powder left inside. The seal of a chamber allows connection to a gas-sampling system. The latter consists of an infra-red gas analyser (IRGA; EGM-5 Portable Gas Analyser, PP Systems), which is calibrated to a partial pressure of CO<sub>2</sub> ( $p\text{CO}_2$ ) in the range of 0 ppmv to 30,000 ppmv and equipped with an internal pump as well as an electrochemical O<sub>2</sub> sensor. In the gas-sampling system, the IRGA is placed in a closed-loop incorporating also a CO<sub>2</sub> scrub (soda lime) and a connector for CO<sub>2</sub> trapping with zeolite molecular sieve cartridges (MSC) (Section 4.3.3.2) (Hardie et al., 2005).

At the start of a CO<sub>2</sub> flux measurement, the  $p\text{CO}_2$  in the chamber ( $p\text{CO}_2^{\text{Chamber}}$ ) is determined, which is representative of the ambient  $p\text{CO}_2$  in the rock pores ( $p\text{CO}_2^{\text{Rock}}$ ) around

the chamber associated with diffusive equilibration prior to the measurement (Chapter 3). Subsequently, a series of repeated accumulations is recorded to determine the CO<sub>2</sub> flux into ambient atmosphere: first, the  $p\text{CO}_2$  Chamber is lowered to a near-atmospheric value using the CO<sub>2</sub> scrub or MSC, and CO<sub>2</sub> is allowed to build up, typically over ~ 6 min, before the  $p\text{CO}_2$  Chamber is lowered again. For each repeat, the recorded  $p\text{CO}_2$  change is converted to a rate of CO<sub>2</sub> accumulation  $q$  (mgC min<sup>-1</sup>) (Pirk et al., 2016; Soulet et al., 2018). During a flux measurement, previous work has noted that the CO<sub>2</sub> accumulation rates decline until a constant value is reached ( $q_{\text{plateau}}$ ) (Chapter 3) (Soulet et al., 2021, 2018). This process has been explained as an initial purging of stored CO<sub>2</sub> from the rock pore space connected to the chamber, coinciding with the real-time produced CO<sub>2</sub> (Chapter 3), which is the primary measurement of interest, and is described by:

$$q(t) = \alpha \times \exp(-\beta \times t) + q_{\text{plateau}} \quad (4-6)$$

where the sum of  $\alpha$  and  $q_{\text{plateau}}$  is the initial rate of accumulation at the start of the flux measurement ( $t = 0$ ),  $\beta$  is the measurement-specific removal constant (min<sup>-1</sup>), and the term  $\alpha \times \exp(-\beta \times t)$  describes the decrease of the pore-space CO<sub>2</sub> over several repeated accumulations (Chapter 3).

Based on quantifying the carbon mass purged from the rock pore space of a weathering chamber (CO<sub>2</sub> Excess) after the initial removal of  $p\text{CO}_2$  Chamber, the volume of connected rock pores ( $V_{\text{Rock pores}}$ , cm<sup>3</sup>) can be estimated considering the initial  $p\text{CO}_2$  Rock:

$$V_{\text{Rock pores}} = \text{CO}_2 \text{ Excess} \times \frac{R \times T}{P} \times \frac{10^9}{p\text{CO}_2 \text{ Rock} \times M_C} \quad (4-7)$$

with

$$\text{CO}_2 \text{ Excess} = \int \alpha \times \exp(-\beta \times t) \quad (4-8)$$

where  $R$  is the universal gas constant (m<sup>3</sup> Pa K<sup>-1</sup> mol<sup>-1</sup>),  $T$  is the chamber temperature (K),  $P$  is the pressure (Pa) and  $M_C$  is the molar mass of carbon (g mol<sup>-1</sup>) (Chapter 3). In addition, considering the air-filled porosity in the shallow weathering zone (Garel et al., 2012; Mallet et al., 2020) and the density of the rock undergoing weathering (Lofi et al., 2012; Mathys and Klotz, 2008),  $V_{\text{Rock pores}}$  can be used to estimate the rock volume and mass contributing CO<sub>2</sub> to a weathering chamber (Chapter 3). This allows us to report CO<sub>2</sub> fluxes relative to the contributing rock mass (i.e., a chamber-specific normalization of  $q_{\text{plateau}}$  to rock mass). Finally, this rock volume contributing to the measured CO<sub>2</sub> efflux ( $V_{\text{Rock}}$ , cm<sup>3</sup>) can be used to estimate the corresponding surface area of an exposed outcrop ( $S_{\text{Rock}}$ , cm<sup>2</sup>) as a function of the weathering depth of the landscape ( $z_{\text{Rock}}$ , cm) (Chapter 3):

$$S_{\text{Rock}} = \frac{V_{\text{Rock}}}{z_{\text{Rock}}} \quad (4-9)$$

4.3.3.2 C<sub>CO2</sub> isotope measurements and source partitioning

During a CO<sub>2</sub> flux measurement, CO<sub>2</sub> can be collected using the gas sampling system and a zeolite MSC (Type 13X) (Hardie et al., 2005; Soulet et al., 2018). In the laboratory, the sampled gas was released by heating the zeolite MSC to 425 °C while purging with high-purity nitrogen prior to cryogenic purification under vacuum (Garnett et al., 2019; Garnett and Murray, 2013). The stable carbon isotope composition of the CO<sub>2</sub> samples was analysed using IRMS (Thermo Fisher Delta V; results expressed in δ<sup>13</sup>C notation relative to VPDB standard). In addition, the radiocarbon (<sup>14</sup>C) activity of CO<sub>2</sub> was measured with Accelerator Mass Spectrometry at the Scottish Universities Environmental Research Centre (SUERC) after graphitization by iron/zinc reduction (Garnett et al., 2019; Garnett and Murray, 2013). Using the sample-specific δ<sup>13</sup>C value, the <sup>14</sup>C measurements were corrected and reported in the form of the fraction modern (i.e., F<sup>14</sup>C notation) (Reimer et al., 2004; Stuiver and Polach, 1977).

The δ<sup>13</sup>C and F<sup>14</sup>C values of rock-derived CO<sub>2</sub> can be used to partition the contributions of carbon from OC<sub>petro</sub>, carbonate minerals and the atmosphere (Subscript: Atm), with an isotope-mass balance system as previously detailed by Soulet et al. (2021):

$$\begin{cases} f_{OC} + f_{SA} + f_{CSA} = 1 \\ f_{OC} \times \delta^{13}C_{OC} + f_{SA} \times \delta^{13}C_{SA} + f_{CSA} \times \delta^{13}C_{CSA} = \delta^{13}C_{Chamber} \\ f_{OC} \times F^{14}C_{OC} + f_{SA} \times F^{14}C_{SA} + f_{CSA} \times F^{14}C_{CSA} = F^{14}C_{Chamber} \end{cases} \quad (4-10)$$

where  $f$  is the mass fraction of CO<sub>2</sub> from OC<sub>petro</sub> ( $f_{OC}$ ; Equation 4-1), the dissolution of carbonate minerals by sulfuric acid ( $f_{SA}$ ; Equation 4-2 and Equation 4-3) and the dissolution of carbonate minerals by carbonic acid (sourced from meteoric waters incorporating atmospheric CO<sub>2</sub>) coupled to sulfuric-acid-driven degassing ( $f_{CSA}$ ; Equation 4-4 and Equation 4-5), and the terms δ<sup>13</sup>C and F<sup>14</sup>C represent the carbon isotope composition of these possible sources. For the oxidation of OC<sub>petro</sub>, we consider a possible microbial impact that may result in isotope fractionation shifting the δ<sup>13</sup>C<sub>OC</sub> value by up to ~ 3.6 ‰ (Chapter 2), by assigning a δ<sup>13</sup>C value of CO<sub>2</sub> that is lower by 1.8 ± 1.8 ‰ compared to that of OC<sub>petro</sub>. Furthermore, we assume that the F<sup>14</sup>C of carbonate minerals and OC<sub>petro</sub> are zero (Soulet et al., 2018). For the coupled carbonic acid and sulfuric acid pathway, a temperature-dependent isotope fractionation factor between bicarbonate and CO<sub>2</sub> (Δ) is considered (Mook et al., 1974):

$$\delta^{13}C_{CSA} = \frac{1}{2} \times (\delta^{13}C_{Atm} + \Delta_{Atm} + \delta^{13}C_{CaCO_3}) - \Delta_{Rock} \quad (4-11)$$

where Δ<sub>Atm</sub> represents the isotope fractionation during the formation of carbonic acid, considering the average atmospheric temperature of 30 d prior to the sampling of rock-derived CO<sub>2</sub> (i.e., formation of meteoric waters from precipitation over the past month), and Δ<sub>Rock</sub> represents the isotope fractionation during the sulfuric-acid driven degassing in the weathering

zone, considering the chamber temperature during the CO<sub>2</sub> sampling (i.e., real-time, rock-derived CO<sub>2</sub> emission). In addition, the <sup>14</sup>C activity of this pathway is described as:

$$F^{14}C_{CSA} = \frac{1}{2} \times (F^{14}C_{Atm} + F^{14}C_{CaCO_3}) = \frac{1}{2} \times F^{14}C_{Atm} . \quad (4-12)$$

To determine the carbon isotope composition of the atmospheric CO<sub>2</sub>, atmospheric samples were collected at each site in each season of the study period by circulating the atmosphere from ~ 3 m above ground through a zeolite MSC using the CO<sub>2</sub> sampling system and by extracting and analysing as described above. For the source-partitioning of each rock-derived CO<sub>2</sub> sample, the δ<sup>13</sup>C<sub>Atm</sub> value is based on averaging the values of the seasonal atmospheric samples over one year and considering the annual variability for the overall uncertainty. The F<sup>14</sup>C<sub>Atm</sub> value is based on the sample that is closest in time while considering an uncertainty that is based on the annual variability of the site-specific atmospheric samples. In addition, to describe the uncertainties of the source partitioning, the uncertainties of the δ<sup>13</sup>C and F<sup>14</sup>C measurements are considered as well as the variability in the temperature record on hourly resolution for the atmosphere and the chambers, which are considered for the calculation of Δ<sub>Atm</sub> and Δ<sub>Rock</sub>. Direct contributions of atmospheric CO<sub>2</sub> to the rock interior are excluded in the isotope-mass balance system (Soulet et al., 2021) because pCO<sub>2</sub> Chamber values were generally higher than the atmospheric pCO<sub>2</sub> resulting in a unidirectional diffusion gradient (Chapter 3) (Soulet et al., 2021, 2018).

#### 4.3.3.3 Temperature sensitivity of CO<sub>2</sub> fluxes

To capture seasonal changes in weather conditions, the field installations were visited 6 times: 27/09/2018, 11/01 – 14/01/2019, 11/04 – 15/04/2019, 27/05 – 29/05/2019, 05/07 – 12/07/2019 and 27/09 – 02/10/2019. Over the study period, temperature and relative humidity in the weathering chambers were monitored with loggers (Lascar® EL-USB-2) placed in additional chambers with similar design. To fill gaps in the data record due to technical issues, air temperatures from local weather stations (Draix-Bléone Observatory, 2015) are used to estimate chamber temperatures with a previously developed modeling framework on hourly resolution (Chapter 3). Following previous research, changes in the chamber temperature alongside changes in the total or partitioned rock-derived CO<sub>2</sub> flux ( $F$ , e.g., mgC kg<sub>Rock</sub><sup>-1</sup> yr<sup>-1</sup>) can be described through a growth exponential model (Soulet et al., 2021):

$$F = F_0 \times \exp(\gamma \times T) \quad (4-13)$$

where  $T$  is the chamber temperature (°C),  $F_0$  is the CO<sub>2</sub> flux at 0 °C and  $\gamma$  is the growth-rate parameter (°C<sup>-1</sup>).

After establishing the relation of chamber temperature and CO<sub>2</sub> emissions found during the flux measurements, Equation 4-13 can be used to estimate an annual release of CO<sub>2</sub> using the chamber temperatures between the measurements. The growth-rate parameter  $\gamma$  can also

be used to describe the sensitivity of CO<sub>2</sub> release as a result of a 10 °C rise in temperature with the dimensionless  $Q_{10}$  factor:

$$Q_{10} = \exp(10 \text{ °C} \times \gamma). \quad (4-14)$$

Furthermore, using the Arrhenius equation, the activation energy ( $E_A$ ) of the reactions underlying the rock-derived CO<sub>2</sub> release can be determined:

$$F = A \times \exp\left(\frac{-E_A}{R \times T}\right) \quad (4-15)$$

where  $T$  is the chamber temperature (K) and  $A$  is a pre-exponential factor, which returns  $E_A$  based on linear fitting  $-R \times \ln(F)$  as a function of  $\frac{1}{T}$ .

## 4.4 Results

### 4.4.1 Carbon isotope composition of rock-derived CO<sub>2</sub> and source partitioning

During 21 of a total of 78 CO<sub>2</sub> flux measurements, which were regularly carried out over the study period, CO<sub>2</sub> was sampled for carbon isotope analyses. On average, chamber-derived CO<sub>2</sub> had  $F^{14}\text{C}$  values of  $0.41 \pm 0.12$  ( $\pm 2$  SD,  $n = 10$ ) and  $0.35 \pm 0.08$  ( $n = 11$ ) in the Brusquet catchment and in the Moulin catchment, and  $\delta^{13}\text{C}$  values of  $-10.8 \pm 3.4$  ‰ and  $-10.8 \pm 2.6$  ‰, respectively (Figure 4-1A; Supplementary Section 4.8.1).

The carbon isotope composition of CO<sub>2</sub> sourced from OC<sub>petro</sub> (Equation 4-1) differed notably in comparison with CO<sub>2</sub> from the two pathways of carbonate dissolution (Equations 4-2 – 4-5), with  $\delta^{13}\text{C}$  values of: i)  $-28.7 \pm 2.0$  ‰ and  $-29.1 \pm 2.0$  ‰ for OC<sub>petro</sub> oxidation; ii)  $0.8 \pm 0.2$  ‰ and  $0.2 \pm 0.2$  ‰ for the SA pathway; and iii)  $-8.2 \pm 2.5$  ‰ and  $-8.5 \pm 2.6$  ‰ for the CSA pathway at the Brusquet site and Moulin site, respectively (Figure 4-1A). Furthermore, we estimated  $F^{14}\text{C}$  values for CO<sub>2</sub> released from the CSA pathway of  $0.503 \pm 0.014$  and  $0.503 \pm 0.010$  at these sites, respectively (Figure 4-1A).

Based on the carbon isotope compositions of the chamber-derived CO<sub>2</sub> and of the possible sources, we estimate the source-specific contributions with a carbon isotope mass balance system considering contributions via the OC, SA and CSA pathways (Equation 4-10). However, five samples cannot be described completely by these sources without introducing large uncertainties. This could reflect contribution of atmospheric CO<sub>2</sub> from leaks around the chamber entrance or within the sampling system (Soulet et al., 2021), although the sample compositions are still close to the CSA endmember (Figure 4-1A). Alternatively, they could result from heterogeneities in the rock composition that are not captured by the average of our measurements. For the remaining samples ( $n = 16$ ), the proportion of CO<sub>2</sub> from OC<sub>petro</sub> oxidation compared to the inorganic sources (total of CSA and SA) was remarkably stable over time (Figure 4-1B), with averages of: i)  $15.3 \pm 3.4$  % ( $\pm$  SD) and  $16.5 \pm 3.1$  % from OC<sub>petro</sub> oxidation;

ii)  $11.3 \pm 7.7$  % and  $15.1 \pm 7.3$  % via the SA pathway; and iii)  $73.4 \pm 5.6$  % and  $68.4 \pm 6.4$  % via the CSA pathway at the Brusquet site and Moulin site, respectively.

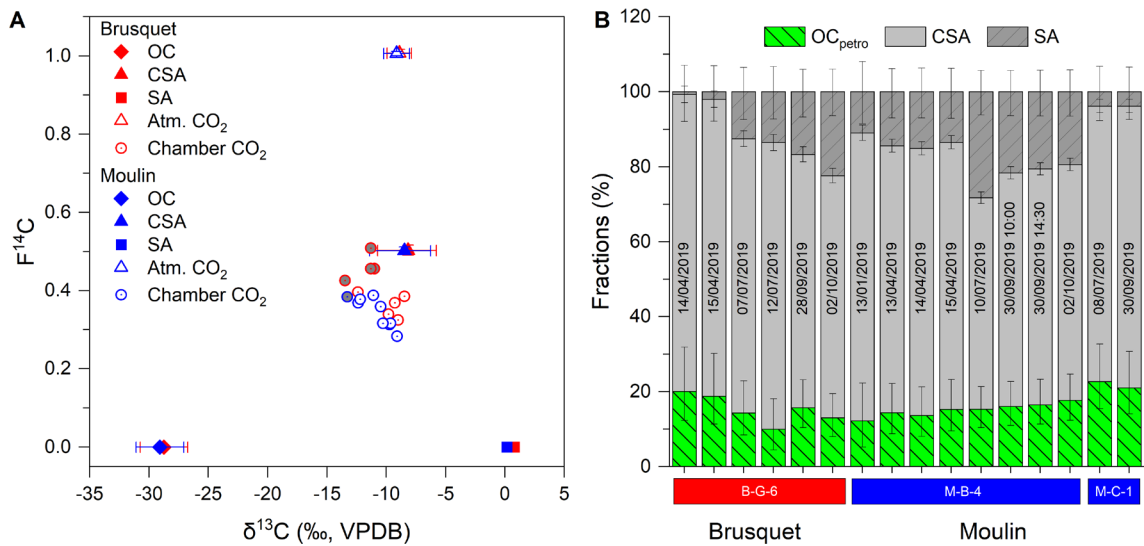


**Figure 4-1. The source of chamber-derived CO<sub>2</sub> inferred from carbon isotope compositions.** Panel A:  $F^{14}C$  and  $\delta^{13}C$  values of chamber-derived and atmospheric CO<sub>2</sub> (open symbols) and carbon sources (closed symbols) at the Brusquet (red) and Moulin (blue) sites. Samples that cannot be described completely by the carbon isotope-mass balance system (Equations 4-10 – 4-12) are grey. Panel B: relative measurement-specific contributions from OC<sub>petro</sub> oxidation (OC), carbonate dissolution by sulfuric acid from pyrite oxidation (SA) or interaction of sulfuric acid with carbonic acid from meteoric waters (CSA) for chambers at the Brusquet site (B-G-6) and Moulin site (M-B-4, M-C-1). Uncertainties of 2 SD are shown when larger than the symbol size.

#### 4.4.2 Source-specific CO<sub>2</sub> fluxes and their response to temperature

The total rock-derived CO<sub>2</sub> fluxes have been previously presented (Chapter 3). On average, a total CO<sub>2</sub> flux of  $13.2 \pm 10.8 \mu\text{gC min}^{-1}$  ( $\pm$  SD) and  $9.6 \pm 7.7 \mu\text{gC min}^{-1}$  was measured, which originated from rock masses of  $2.3 \pm 1.3 \text{ kg}$  ( $\pm$  SD) and  $2.0 \pm 1.1 \text{ kg}$  at the Brusquet site and the Moulin site, respectively. There is a pronounced seasonal variability in the measured CO<sub>2</sub> fluxes, with significantly higher fluxes in summer than winter (Chapter 3) in agreement with measurements from the nearby Laval site (Soulet et al., 2021). Given that the isotope partitioning does not show pronounced seasonal changes (Figure 4-1B), we partition all CO<sub>2</sub> fluxes using the site-specific averages so that each sample has the same relative source-specific contributions (Section 4.4.1). This implies that all pathways (OC, SA and CSA; Equations 4-1 – 4-5) have pronounced seasonal changes in their CO<sub>2</sub> emissions (Table 4-1). Together, considering the measured CO<sub>2</sub> fluxes and their temperature sensitivity, the black shales of the Brusquet catchment have a greater CO<sub>2</sub> release than the marly limestones of the

Moulin catchment. The difference is a factor of ~ 1.7, using the  $F_0$  values of the temperature versus CO<sub>2</sub> flux relationship (Equation 4-13), or ~ 1.3, considering the site-specific annual release (Table 4-1).

**Table 4-1. Overview of the total rock-derived CO<sub>2</sub> fluxes from marly limestones and black shales and their temperature sensitivity in comparison with the contribution from OC<sub>petro</sub> oxidation.** Annual CO<sub>2</sub> fluxes are based on extrapolating the response to changes in chamber temperature (derived from regular measurements; n = 78; Equations 4-13 – 4-15), on hourly resolution over the study period (Oct. 2018 – Sep. 2019). CO<sub>2</sub> fluxes are normalized to the chamber-specific contributing rock mass or to the landscape surface considering different depths of origin of the CO<sub>2</sub> (Equation 4-9). To describe the contribution of OC<sub>petro</sub> oxidation for the entire dataset, source-specific contributions (Figure 4-1) are site-specifically averaged (\*) and extrapolated. Uncertainties are given as standard deviations (SD), or as standard errors (SE) for non-linear relations.

Rock type	Site	Mean annual chamber temperature (°C)	Measurements: average (↔ range) (mgC kg <sub>Rock</sub> <sup>-1</sup> yr <sup>-1</sup> ± SD)	Temperature sensitivity				Annual rock-mass-specific CO <sub>2</sub> flux (mgC kg <sub>Rock</sub> <sup>-1</sup> yr <sup>-1</sup> )	Annual topographic CO <sub>2</sub> efflux (gC m <sup>-2</sup> yr <sup>-1</sup> ) based on weathering depth of:		
				F <sub>0</sub> (mgC kg <sub>Rock</sub> <sup>-1</sup> yr <sup>-1</sup> ± SE)	γ (°C <sup>-1</sup> ± SE)	Q <sub>10</sub> (± SE)	E <sub>A</sub> (kJ mol <sup>-1</sup> ± SE)		2 cm	5 cm	20 cm
Total CO <sub>2</sub> flux											
Marly limestones	Moulin	16.48	2,596 ± 1,953 (164 ↔ 6,258)	386 ± 153	0.085 ± 0.015	2.3 ± 0.3	70.3 ± 7.0	~ 2,215	84	209	837
Black shales	Brusquet	15.59	3,159 ± 2,786 (130 ↔ 9,690)	656 ± 281	0.077 ± 0.016	2.2 ± 0.3	63.0 ± 7.5	~ 2,889	109	273	1,092
OC <sub>petro</sub> -derived CO <sub>2</sub> flux											
Marly limestones	Moulin	16.48	397 ± 299 (25 ↔ 958)	59 ± 23 (7 ± 8)*	0.085 ± 0.015 (0.188 ± 0.048)*	2.3 ± 0.3 (6.5 ± 3.2)*	70.3 ± 7.0 (102.1 ± 20.7)*	~ 339	13	32	128
Black shales	Brusquet	15.59	520 ± 459 (21 ↔ 1,596)	108 ± 46 (106 ± 67)*	0.077 ± 0.016 (0.083 ± 0.023)*	2.2 ± 0.3 (2.3 ± 0.5)*	63.0 ± 7.5 (85.5 ± 16.1)*	~ 476	18	45	180

#### 4.4.3 Relation of the lithological composition and source-specific CO<sub>2</sub> fluxes

The source-specific CO<sub>2</sub> fluxes via the OC, SA and CSA pathways can be compared with the chemical composition of the rocks undergoing weathering. The black shales of the Brusquet site have a higher OC<sub>petro</sub> content of  $0.78 \pm 0.01$  wt.% ( $\pm$  SD,  $n = 4$ ) than the marly limestones of the Moulin site, with OC<sub>petro</sub> contents of  $0.46 \pm 0.02$  wt.%. The inorganic carbon contents are lower in the Brusquet catchment ( $3.8 \pm 0.3$  wt.%, i.e., CaCO<sub>3</sub> contents of 31.6 wt.%) than in the Moulin catchment ( $5.3 \pm 0.1$  wt.%, i.e., CaCO<sub>3</sub> contents of 44.0 wt.%), while their total sulfur contents were more similar, at  $0.40 \pm 0.05$  wt.% and  $0.47 \pm 0.09$  wt.% at the Brusquet site and the Moulin site, respectively.

These characteristics can be used to normalize the measured CO<sub>2</sub> fluxes and compare the two sites. For OC<sub>petro</sub>-derived CO<sub>2</sub>, we find a common relationship of increased CO<sub>2</sub> release with increased temperature when considering the OC<sub>petro</sub> contents of the contributing rock mass (Figure 4-2), with a georespiration rate that is described by a  $F_0$  value of  $13.4 \pm 3.9$  mgC<sub>CO2</sub> gC<sub>OCpetro</sub><sup>-1</sup> yr<sup>-1</sup> ( $\pm$  SE) and a  $\gamma$  value of  $0.082 \pm 0.011$  °C<sup>-1</sup>, based on the extrapolation for the entire dataset from the Brusquet and Moulin sites. The corresponding annual release of OC<sub>petro</sub>-derived CO<sub>2</sub> is  $\sim 0.068$  gC<sub>CO2</sub> gC<sub>OCpetro</sub><sup>-1</sup> yr<sup>-1</sup>, which can be described as  $\sim 6.8$  % of the OC<sub>petro</sub> in the oxidative weathering zone being lost per year.

In contrast, CO<sub>2</sub> fluxes derived from the dissolution of carbonate minerals do not scale (i.e., they are not positively correlated) with the contents of carbonate or sulfides, which are the minerals involved in the SA and CSA pathways (Equations 4-2 – 4-5). The rock-mass-specific CO<sub>2</sub> fluxes can be described with  $F_0$  values of  $449 \pm 192$  mgC kg<sub>Rock</sub><sup>-1</sup> yr<sup>-1</sup> and  $99 \pm 43$  mgC kg<sub>Rock</sub><sup>-1</sup> yr<sup>-1</sup> at the Brusquet site, and  $283 \pm 112$  mgC kg<sub>Rock</sub><sup>-1</sup> yr<sup>-1</sup> and  $44 \pm 17$  mgC kg<sub>Rock</sub><sup>-1</sup> yr<sup>-1</sup> at the Moulin site for the CSA and SA pathways, respectively. These values are based on the extrapolation for the entire dataset, with  $\gamma$  values identical to the total CO<sub>2</sub> fluxes (Table 4-1). Considering the carbonate content of the rock mass contributing CO<sub>2</sub> to a chamber, and the contribution of atmospheric carbon via meteoric waters to the CSA pathway (Equation 4-4 and Equation 4-5), these values correspond to a total annual carbonate dissolution of  $\sim 0.012$  g<sub>Carbonate</sub> g<sub>Rock</sub><sup>-1</sup> yr<sup>-1</sup> and  $\sim 0.009$  g<sub>Carbonate</sub> g<sub>Rock</sub><sup>-1</sup> yr<sup>-1</sup> at the Brusquet site and the Moulin site, respectively. Likewise based on the CO<sub>2</sub> fluxes from the SA and CSA pathways, a relative annual loss of pyrite minerals in the oxidative weathering zone of  $\sim 95$  % and  $\sim 60$  % can be estimated at the Brusquet site and the Moulin site, respectively, when assuming that all sulfur in the rocks is present in the form of pyrite minerals.

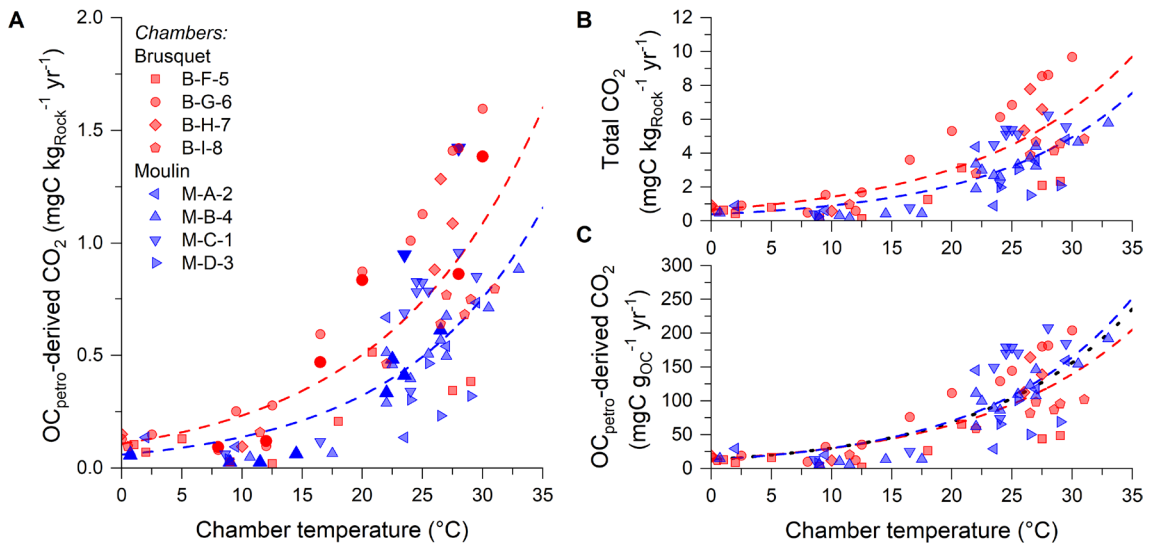


**Figure 4-2. Response of  $OC_{petro}$ -derived CO<sub>2</sub> release to changes in chamber temperature.** Panel A: chamber-specific  $OC_{petro}$ -derived CO<sub>2</sub> fluxes normalized to the contributing rock mass for the Brusquet (red) and Moulin (blue) sites, with darker colours for samples that are considered in the measurement-specific carbon isotope-based source partitioning (Figure 4-1B) and that are the basis for site-specific extrapolations (lighter colours). Panel B: total rock-derived CO<sub>2</sub> fluxes normalized to the contributing rock mass for comparison. Panel C: normalization of  $OC_{petro}$ -derived CO<sub>2</sub> fluxes to the mass of  $OC_{petro}$  in the contributing rock volume. Dashed lines (Panels A – C) indicate site-specific growth exponential models (Equation 4-13; Table 4-1), whereas a black dotted line (Panel A) describes a common temperature sensitivity for both sites.

## 4.5 Discussion

To better understand the magnitude of and environmental controls on CO<sub>2</sub> release from oxidative weathering in steep mountainous areas, we compare CO<sub>2</sub> emissions from sedimentary rocks with differing chemical composition. In the Brusquet catchment and the Moulin catchment in the Draix-Bléone observatory (France), CO<sub>2</sub> fluxes were measured with regularly repeated, *in situ* flux measurements over one complete annual cycle of pronounced seasonal weather changes. We find a pronounced growth of total CO<sub>2</sub> releases alongside increase in chamber temperature at both study sites (Table 4-1; Figure 4-2B), supporting previous findings from marly limes in the neighbouring Laval catchment (Soulet et al., 2021), and for carbonate-poor mudstones in the Waiapu catchment (New Zealand) (Chapter 2). All these sites share a temperature sensitivity of total CO<sub>2</sub> release that is described by  $Q_{10}$  values in the range of ~ 2.0 – 2.7. Furthermore, all sites show a common response to rainfall events with a reduction in CO<sub>2</sub> fluxes that recover over a few days (Chapter 2 and Chapter 3) (Soulet et al., 2021). However, we do not directly compare the results of this study with previous CO<sub>2</sub> flux measurements in the neighbouring Laval catchment (Soulet et al., 2021) and in New Zealand

(Chapter 2) because we use a new framework which allows us to assess the contributing rock volume (Chapter 3).

In contrast to these commonalities, we here find significant differences in the CO<sub>2</sub> release from black shales and marly limestones (Table 4-1; Figure 4-2B). These differences in flux occur despite similarities of the study sites in respect to the relative source-specific contributions (Figure 4-1) from the OC, CSA and SA pathways (Equations 4-1 – 4-5). In the following, we explain this finding by the chemical compositions of the source rocks (Section 4.5.1). Based on the quantitative approach, we then evaluate the breakdown of OC<sub>petro</sub> during oxidative weathering (Section 4.5.2) and discuss the implications of fluxes of oxidized OC<sub>petro</sub> from highly erosive settings for the global carbon cycle and feedbacks to climate (Section 4.5.3).

#### 4.5.1 OC<sub>petro</sub> content in shallow weathering rocks scales CO<sub>2</sub> emission

##### 4.5.1.1 OC<sub>petro</sub>-derived CO<sub>2</sub>

The surplus of OC<sub>petro</sub>-derived CO<sub>2</sub> release from black shales (Brusquet site) undergoing weathering compared to that of marly limestones (Moulin site) (Table 4-1, Figure 4-2A) scales with the OC<sub>petro</sub> contents of these rocks (Figure 4-2C) that differ by a factor of ~ 1.7. This finding corresponds to an apparent 1 : 1 ratio between the concentration of weathering reactants and products, and confirms a fundamental assumption on the conservation of mass and reaction rate in existing models of organic carbon cycling in weathering profiles (Bao et al., 2017; Bolton et al., 2006) and on the catchment to global scale (Bergman et al., 2004; Berner and Berner, 2012; Copard et al., 2007). Furthermore, the common temperature response of OC<sub>petro</sub>-derived CO<sub>2</sub> fluxes normalized to the OC<sub>petro</sub> content of the contributing rock mass (Figure 4-3) provides the possibility to globally upscale locally quantified weathering fluxes, which may be based on small-scale *in situ* work as presented here or on catchment-wide assessments via riverine proxies.

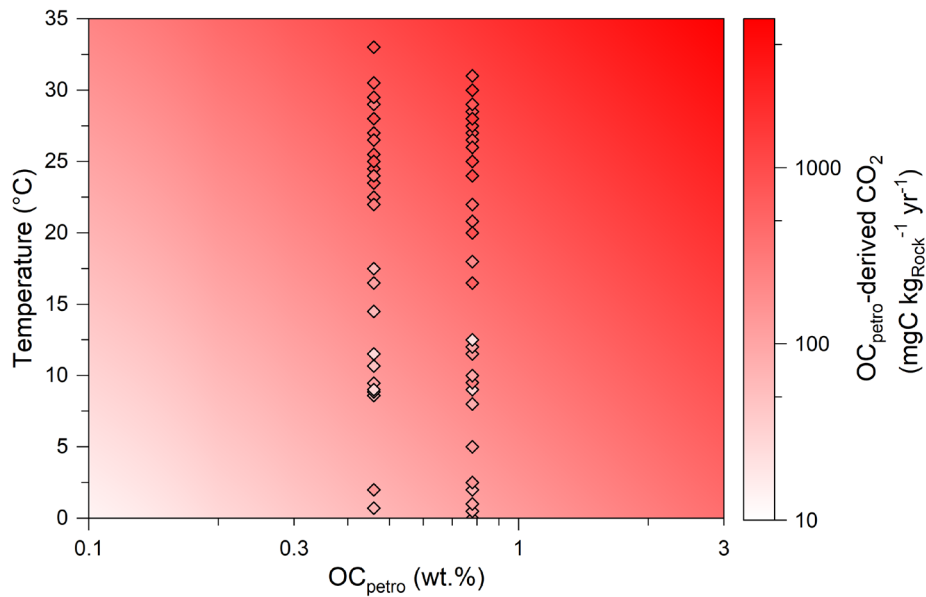


**Figure 4-3. Dual control of  $OC_{\text{petro}}$  content and temperature in shallow, aerated weathering zones on  $OC_{\text{petro}}$ -derived  $CO_2$  release.** The shared rate of georespiration found in the Brusquet catchment (0.78 wt.%  $OC_{\text{petro}}$ ) and in the Moulin catchment (0.46 wt.%  $OC_{\text{petro}}$ ) is projected with sequential colour mixing (white – red) alongside the underlying dataset indicated with diamonds (using the same colourmap). The  $OC_{\text{petro}}$  content as well as the  $CO_2$  fluxes are presented on logarithmic scale.

#### 4.5.1.2 Carbonate-sourced CO<sub>2</sub>

In contrast to the oxidation of  $OC_{\text{petro}}$ , the chemical breakdown of carbonate minerals coupled to the oxidative weathering of pyrite minerals does not appear to be scaled by the quantity of reactants involved (Equations 4-2 – 4-5) at these study sites. For example, despite similar total sulfur contents, around 1.5 times more inorganic carbon is released from black shales via the combined CSA and SA pathways in comparison with marly limestones. This discrepancy between the rock chemistry and measured CSA- and SA-derived  $CO_2$  fluxes is even more notable when one considers that the carbonate mineral content of the marly limestones at the Moulin site is  $\sim 1.4$  times higher than that of the black shales at the Brusquet site.

Surprisingly, the  $CO_2$  release from carbonate dissolution by sulfuric acid scales approximately with the  $OC_{\text{petro}}$  content of the rocks undergoing weathering. We propose that microbial activity could explain this finding. Previous research has highlighted the presence of microorganisms in weathering zones (Bardgett et al., 2007; Berlendis et al., 2014; Seifert et al., 2013) and their potentials to incorporate  $OC_{\text{petro}}$  (Matlakowska and Sklodowska, 2011; Petsch et al., 2001; Stasiuk et al., 2017). Furthermore, sulfide oxidation can be promoted enzymatically by microorganisms, increasing the oxidation rate by approximately one order of magnitude in respect to abiotic reactions, with microbial oxidation of  $\sim 20\%$  of pyrite-sulfide within a month in laboratory experiments (Percak-Dennett et al., 2017), which is roughly similar to the field-

based oxidation rates of pyrite minerals during oxidative weathering in the Draix-Bléone observatory. If a chemoheterotrophic microbial consortium controls the oxidation of sulfide minerals at the study sites, and this relies on OC<sub>petro</sub> to thrive, the availability of the organic substrate could limit the microbial mediation of pyrite oxidation. Such a bottleneck in sulfuric acid release by OC<sub>petro</sub> content does not only control the overall size of carbonate-sourced CO<sub>2</sub> fluxes (combined CSA and SA pathways) but could also affect their sensitivity to changes in temperature, including the activation energy. The control of OC<sub>petro</sub> oxidation on inorganic carbon weathering implies that the temperature sensitivity of carbonate-sourced CO<sub>2</sub> release equals that of OC<sub>petro</sub> oxidation, as well as that of the total flux (Table 4-1).

The linkage of organic and inorganic carbon release presented here could be more widespread in shallow weathering zones on shales and marls. However, for locations where weathering zones extend deeper into the substrate, it has been shown that the oxidation of pyrite can occur in deeper reaction fronts compared to OC<sub>petro</sub> (Hilton et al., 2021; Petsch et al., 2000; Tuttle and Breit, 2009; Wildman, 2004), where higher degrees of water saturation hinder the supply of O<sub>2</sub> to depth (Tremosa et al., 2020). Accordingly, it has been previously interpreted that pyrite minerals are less resistant to oxidation compared to OC<sub>petro</sub> at low O<sub>2</sub> levels (Bolton et al., 2006; Petsch, 2014). Together, this indicates that the coupling of carbonate-sourced CO<sub>2</sub> release to OC<sub>petro</sub> oxidation may be less pronounced in settings with deeper weathering fronts compared to our study sites. In addition, the sensitivity to changes in water saturation and O<sub>2</sub> supply in deeper weathering zones could also reduce the importance of temperature as a control on CO<sub>2</sub> release from carbonate dissolution coupled to pyrite oxidation compared to hydrological parameters (Kemeny et al., 2021).

Following weathering, the released carbon may be washed out of the weathering zone as dissolved inorganic carbon (DIC) instead of being directly released as gaseous CO<sub>2</sub> (Tune et al., 2020). Preliminary O<sub>2</sub> fluxes that were measured alongside CO<sub>2</sub> fluxes at the Brusquet site and the Moulin site indicate a significantly higher oxygen consumption compared to CO<sub>2</sub> release, with a ratio of ~ 10 mol O<sub>2</sub> : 1 mol CO<sub>2</sub> at a given temperature (Chapter 3). Based on the source-specific contributions (Figure 4-1), we estimate that the molar ratio of the theoretical chemical weathering (Equations 4-1 – 4-5) at our study sites is ~ 10 mol O<sub>2</sub> : 9.3 mol CO<sub>2</sub>, and the discrepancy to the observed gas exchange of O<sub>2</sub> and CO<sub>2</sub> could indicate a significant incorporation of CO<sub>2</sub> (originating from both OC<sub>petro</sub> and pyrite oxidation coupled to carbonate dissolution) into the dissolved load at the study sites. This carbon may be partially degassed and precipitated into secondary carbonates after equilibration with the lower pCO<sub>2</sub> of the atmosphere (Bickle et al., 2015; Erlanger et al., 2021). The fate of this carbon is relevant to better understanding the source of evaded CO<sub>2</sub> from streams and rivers (Raymond et al., 2013).

#### 4.5.2 Fate of OC<sub>petro</sub> during oxidative weathering

The *in situ* OC<sub>petro</sub>-derived CO<sub>2</sub> emissions from black shales and marly limestones undergoing oxidative weathering corresponds to an annual oxidation of ~ 6.8 % of OC<sub>petro</sub> contained in the sampled rock volume (Table 4-1). The observed stoichiometry of O<sub>2</sub> consumption versus CO<sub>2</sub> production suggests that some carbon released from oxidative weathering may not be released directly as gaseous CO<sub>2</sub>, but instead exported as DIC, so that the total annual oxidation of OC<sub>petro</sub> may be higher than we calculate here. Laboratory experiments on the oxidation of pyrite-free bituminous coal show an OC<sub>petro</sub> loss of ~ 0.4 % yr<sup>-1</sup> at 24 °C and O<sub>2</sub> concentrations equivalent to the present-day atmosphere (Chang and Berner, 1999), which is ~ 25 times lower than the oxidation rate we measure at the Draix-Bléone observatory at these conditions. As suggested by Chang and Berner (1999), higher field-based oxidation rates compared to laboratory experiments could be due to the lack of microbial activity in the latter. Furthermore, OC<sub>petro</sub> at the study sites consists dominantly of a type III kerogen (Graz et al., 2012) and, because the average grainsize of coal is larger than that of kerogen, a surface reaction control on the oxidation of OC<sub>petro</sub> may explain the greater field-based CO<sub>2</sub> release compared to the laboratory experiments as a result of differences in the area of reacting surfaces (Chang and Berner, 1999). Furthermore, our respiration rates for OC<sub>petro</sub>-derived CO<sub>2</sub> release are around a magnitude larger compared to that for a mixed soil OC- and petrogenic OC-derived CO<sub>2</sub> release from different sediments underlying soils in incubation experiments (Kalks et al., 2021). However, it remains unclear at which O<sub>2</sub> concentration the breakdown of soil and petrogenic organic carbon occurred in the incubation experiments, while the *p*O<sub>2</sub> values in the weathering chambers remained close to that of the atmosphere over the study period (Chapter 3).

The lifetime of OC<sub>petro</sub> in the oxygenated weathering zone can be assessed using the oxidation rate of OC<sub>petro</sub> as a proportion of the contributing rock mass, giving ~ 15 yr. This relatively short lifespan may seem at odds with the observations that particulate OC<sub>petro</sub> is widespread at the surface in the catchments of the Draix-Bléone observatory (Copard et al., 2006; Graz et al., 2011) and the rivers export significant quantities of this matter (Graz et al., 2012). To explain the apparent widespread escape of OC<sub>petro</sub> from oxidation, we suggest that the oxidation in the wider landscape occurs only in the uppermost few centimetres, and that a depletion of O<sub>2</sub> below this shallow oxidation front limits further oxidation at depth. Together with the high physical erosion rates at the study sites, this would mean that the residence time of OC<sub>petro</sub> on steep slopes is lower than our estimated OC<sub>petro</sub> lifetime in an oxygenated layer. For example, with an erosion rate of ~ 1 cm yr<sup>-1</sup> (Carriere et al., 2020; Mathys et al., 2003), OC<sub>petro</sub>

would reside in the upper 2 cm for only 2 years, and lose < 15 % of its initial mass. Given the variability in OC<sub>petro</sub> contents in the wider catchment area (Copard et al., 2006; Graz et al., 2011), it may not be possible to observe this loss in the riverine particulate OC<sub>petro</sub> pool.

Previous research has shown that, if OC<sub>petro</sub> escapes the rapid degradation in the near-surface by physical erosion, it may be deposited over millennial timescales in floodplains (Repasch et al., 2021; Scheingross et al., 2021), whereas significant oxidation may occur during the fluvial transport with oxidation rates similar to ours. Depending on the total sediment transit in the floodplain (Scheingross et al., 2019), OC<sub>petro</sub> may be further degraded, or re-buried and preserved in marine sediments, with large preservations in steep mountains systems (Blair and Aller, 2012; Leithold et al., 2016).

In general, an important control on the preservation of natural organic carbon in the marine and continental realms is protection resulting from interactions with mineral matrices, with intrinsic differences in the chemical composition of the organic matter being of secondary impact (Blattmann et al., 2019a; Hemingway et al., 2019; Kleber et al., 2021; Repasch et al., 2021). An exception are highly stabile graphitized materials (Bouchez et al., 2010; Galvez et al., 2020; Galy et al., 2008), which may survive multiple orogenic cycles (Sparkes et al., 2020). In the Draix-Bléone observatory, the rapid oxidation of OC<sub>petro</sub> is likely facilitated by a decline in mineral protection of kerogen alongside increased porosity towards the surface that is driven by unloading and dissolution of carbonates coupled to sulfide oxidation (Section 4.5.1.2), which results annually in ~ 1.0 % dissolution of the total rock mass at both study sites. Future research on differing rock types is needed to further address the impact of the mineral matrix on the *in situ* degradation of OC<sub>petro</sub> in the oxygenated weathering zone. However, based on the previous discussion, the OC<sub>petro</sub> oxidation rates for sedimentary rocks in highly erosive settings and their controls presented here (Figure 4-3) should be representative for a wide range of types of kerogen that make up the vast majority of Earth's OC<sub>petro</sub> (Killops and Killops, 2005; Vandenbroucke and Largeau, 2007).

### 4.5.3 Highly erosive sedimentary rocks as hotspots of oxidative weathering

To understand what the implications of the rapid OC<sub>petro</sub> oxidation rates in shallow weathering zones are for the global carbon cycle, it is crucial to estimate the CO<sub>2</sub> efflux from the surface of the studied outcrops. This can be done based on assumptions on the depth of the oxidative weathering front (Equation 4-9). However, as previously indicated (Section 4.5.2), the oxidation reactions may occur only over the uppermost part of the total weathering zone that is described by elevated porosities towards the surface. This zone has been assessed at the Draix-Bléone observatory on similar slopes compared to our study sites to correspond to depths

of ~ 20 cm (Maquaire et al., 2002; Mathys and Klotz, 2008; Oostwoud Wijdenes and Ergenzinger, 1998; Rovéra and Robert, 2006). In addition to this deeper boundary, a minimum depth of the oxidation front of ~ 2 cm can be inferred from the average depth of the rock volume that is probed by the weathering chambers (Chapter 2). Using these thicknesses and normalizing the CO<sub>2</sub> fluxes to  $S_{\text{Rock}}$  (Equation 4-9), the corresponding mean annual topographic OC<sub>petro</sub>-derived CO<sub>2</sub> fluxes range between 13 gC m<sup>-2</sup> yr<sup>-1</sup> and 180 gC m<sup>-2</sup> yr<sup>-1</sup> (Table 4-1) for the study sites. Considering that a portion of the total carbon release from oxidative weathering may degas from the exported DIC pool elsewhere, these values may underestimate the overall OC<sub>petro</sub>-derived CO<sub>2</sub> release from the studied landscapes.

As reviewed by Hilton and West (2020), previous research using the trace element rhenium as a proxy for OC<sub>petro</sub>-oxidation over river catchments returned fluxes ranging between 4 gC m<sup>-2</sup> yr<sup>-1</sup> and 30 gC m<sup>-2</sup> yr<sup>-1</sup> for settings with high erosion rates in Taiwan and New Zealand (Hilton et al., 2014; Horan et al., 2017). These are similar to the lower end of our estimates on the carbon release from oxidation of OC<sub>petro</sub> on bare rock surfaces in these catchments. In contrast, a significantly lower value of ~ 0.3 gC m<sup>-2</sup> yr<sup>-1</sup> to 0.7 gC m<sup>-2</sup> yr<sup>-1</sup> can be estimated for the average global OC<sub>petro</sub>-derived carbon release from oxidative weathering for Earth's total continental surface without ice (Petsch, 2014). Thus, we here confirm the proxy-based identification of highly erosive sedimentary rocks as hotspots of CO<sub>2</sub> release from oxidative weathering (Hilton et al., 2014; Hilton and West, 2020) by using direct measurements.

The high fluxes of oxidized OC<sub>petro</sub> in steep terrains also bear important implications for other weathering pathways. In lithologies that contain only marginal contents of carbonate minerals, the oxidation of OC<sub>petro</sub> can induce high CO<sub>2</sub> fluxes resulting in high  $p\text{CO}_2$  Rock values that may influence acid-hydrolysis reactions to increase the chemical weathering of co-occurring silicate minerals in the absence of buffering carbonates (Chapter 2). In contrast, CO<sub>2</sub> derived from OC<sub>petro</sub> oxidation may impact the dissolution of carbonate minerals in carbonate-rich lithologies by constituting an additional proton source analogous to CO<sub>2</sub> derived from soil respiration (Calmels et al., 2014; Gaillardet et al., 2019; Romero-Mujalli et al., 2019). This theory is supported by similarities of the CO<sub>2</sub> flux size from georespiration and soil respiration (Table 4-1) (Soulet et al., 2021). Furthermore, in the presence of pyrite minerals, the linkage between organic and inorganic carbon releases may be further distinct due to the influence of OC<sub>petro</sub> content on CO<sub>2</sub> release from pyrite oxidation coupled to carbonate dissolution by sulfuric acid (Section 4.5.1.2). At present, OC<sub>petro</sub> oxidation is typically not included as a control of acidity in river-chemistry-based constraints of chemical weathering (Bufe et al., 2021; Emberson et al., 2018; Gaillardet et al., 2019), while our findings emphasize the importance of doing so.

Together, the identification of highly erosive settings as hotspots of OC<sub>petro</sub> oxidation, its potential to be rapidly degraded under optimal conditions and the pronounced positive feedback of CO<sub>2</sub> release to temperature increases mean that steep mountainous areas need to be carefully considered in geological carbon cycle models. Small changes in the extent of bare rock faces, local temperatures and the OC<sub>petro</sub> content of the rocks undergoing weathering have the potential to induce larger-scale changes in the flux of oxidized OC<sub>petro</sub>. However, large imbalances in the geological carbon cycle cannot be sustained on a million year timescale without destabilizing Earth's atmospheric composition and climate (Berner and Berner, 2012; Berner and Caldeira, 1997), which poses the question of how changes in OC<sub>petro</sub> oxidation are linked to those of carbon sink processes during the transformation of a landscape.

## 4.6 Conclusions

This study investigates the lithological and climatic controls on the CO<sub>2</sub> release from oxidative weathering in steep terrains. We use direct *in situ* measurements across multiple seasons for two contrasting rock types: black shales and marly limestones. The relative contributions of CO<sub>2</sub> from organic and inorganic carbon and the role of different weathering pathways were determined using radiocarbon and stable carbon isotopes. We find high fluxes from both OC<sub>petro</sub> oxidation and carbonate dissolution coupled to pyrite oxidation that share a pronounced seasonality shown by the highest CO<sub>2</sub> fluxes at high temperatures, with an increase of CO<sub>2</sub> flux by a factor of 2.3 with a temperature increase of 10 °C. The OC<sub>petro</sub>-derived CO<sub>2</sub> fluxes are higher at the site where black shales outcrop, with an increase that follows a 1 : 1 ratio with the higher concentration of OC<sub>petro</sub> at that site. Furthermore, the OC<sub>petro</sub> content scales the release of CO<sub>2</sub> from carbonate dissolution coupled to pyrite oxidation, which may be the result of a microbial link of both weathering pathways.

Considering the OC<sub>petro</sub> content of the rock volume contributing to the CO<sub>2</sub> flux, we estimate that 6.8 % of the OC<sub>petro</sub> in the oxidative weathering zone are oxidized per year. This represents a lifetime of ~ 15 yr, which indicates that it is degraded rapidly as soon as the rocks enter the uppermost, oxygenated part of the weathering zone. The time that rocks spend in the upper few centimetres is much shorter due to the rapid erosion rates at these sites, meaning that a large proportion of OC<sub>petro</sub> can escape oxidation despite high fluxes of CO<sub>2</sub>. The quantified high OC<sub>petro</sub>-derived CO<sub>2</sub> surface efflux of rocks exposed in highly erosive settings confirms their previous identification as hotspots of carbon release in the geological carbon cycle using riverine proxy-based approaches. We also show that the sensitivity to environmental changes is important to capture in Earth system models. For highly erosive settings, we present a dual framework that allows estimating the carbon release from rock types with different contents of

OC<sub>petro</sub> and/or situated in different climates by separating the lithological and climatic controls on the CO<sub>2</sub> release during oxidative weathering. For a more detailed understanding of the oxidative weathering processes, future research directions may aim at the role of microbial communities, the physical and chemical structure of the shallow weathering zone and the link to porewater chemistry including the aqueous export of weathering-derived carbon.

## 4.7 Acknowledgements

This work was supported by the Natural Environment Research Council (NERC), UK (NEIF Radiocarbon Grant to TR, RGH and MHG, grant 2201.1019), and by the European Research Council (Starting Grant to RGH, ROC-CO<sub>2</sub> project, grant 678779). We thank M. Degler, D. R. Gröcke, F. Napoleoni and J. L. Peterkin for assistance during fieldwork or help with data acquisition.

## 4.8 Supplementary

### 4.8.1 Carbon isotope data of rock-derived and atmospheric CO<sub>2</sub> samples

Site	Sample (Chamber or atmosphere)	Sampling date and time	Publication code	F <sup>14</sup> C ± 1 SD	δ <sup>13</sup> C (‰ VPDB) ± 1 SD
Brusquet	B-G-6	14/01/2019 13:07	SUERC-88827	0.4262 0.0034	-13.5 0.1
	B-G-6	14/04/2019 14:36	SUERC-88838	0.3962 0.0034	-12.4 0.1
	B-G-6	15/04/2019 10:32	SUERC-88838	0.3962 0.0034	-12.4 0.1
	B-G-6	29/05/2019 09:13	SUERC-88849	0.4564 0.0034	-11.0 0.1
	B-G-6	07/07/2019 09:07	SUERC-91865	0.3688 0.0036	-9.3 0.1
	B-G-6	12/07/2019 13:56	SUERC-91870	0.3852 0.0035	-8.5 0.1
	B-G-6	28/09/2019 11:50	SUERC-91890	0.3393 0.0036	-9.8 0.1
	B-G-6	02/10/2019 09:01	SUERC-91891	0.3248 0.0036	-9.0 0.1
	B-I-8	12/07/2019 15:27	SUERC-91871	0.5091 0.0034	-11.3 0.1
	B-I-8	28/09/2019 14:06	SUERC-91880	0.4567 0.0035	-11.3 0.1
	Atm.	14/01/2019 16:06	SUERC-95113	1.0138 0.0047	-9.4 0.1
	Atm.	14/04/2019 15:49	SUERC-95114	1.0002 0.0046	-9.3 0.1
	Atm.	07/07/2019 12:01	SUERC-95115	1.0081 0.0046	-8.1 0.1
	Atm.	28/09/2019 17:04	SUERC-95116	1.0053 0.0046	-8.8 0.1
	Moulin	M-B-4	13/01/2019 12:36	UCIAMS-223881	0.3879 0.0048
M-B-4		13/04/2019 11:54	SUERC-88837	0.3585 0.0036	-10.5 0.1
M-B-4		14/04/2019 10:24	SUERC-88837	0.3585 0.0036	-10.5 0.1
M-B-4		15/04/2019 14:59	SUERC-88837	0.3585 0.0036	-10.5 0.1
M-B-4		10/07/2019 09:05	SUERC-91872	0.2829 0.0038	-9.1 0.1
M-B-4		30/09/2019 10:03	SUERC-91883	0.3129 0.0037	-9.7 0.1
M-B-4		30/09/2019 14:32	SUERC-91881	0.3161 0.0037	-9.6 0.1
M-B-4		02/10/2019 11:57	SUERC-91885	0.3162 0.0037	-10.3 0.1
M-C-1		08/07/2019 11:57	SUERC-91864	0.3683 0.0036	-12.4 0.1
M-C-1		30/09/2019 12:27	SUERC-91882	0.3776 0.0035	-12.2 0.1
M-C-1		02/10/2019 14:38	SUERC-91889	0.3843 0.0035	-13.3 0.1
Atm.		13/01/2019 16:07	SUERC-91852	1.0098 0.0047	-9.3 0.1
Atm.		14/04/2019 12:15	SUERC-91855	1.0064 0.0047	-9.5 0.1
Atm.		08/07/2019 13:03	SUERC-91869	1.0027 0.0046	-8.2 0.1
Atm.		30/09/2019 15:50	SUERC-91884	1.0047 0.0046	-9.5 0.1

## 5 Conclusions



*Laval riverbed, Draix-Bléone observatory, France. September 2018.*

The aim of this thesis was to improve the understanding of the release of carbon dioxide to the atmosphere during the oxidative weathering of sedimentary rocks in respect to the size, sources and environmental controls. To address this aim, three main research questions (RQs) were outlined (Chapter 1):

- RQ1: Is it possible to quantify the gas exchange of CO<sub>2</sub> and O<sub>2</sub> during weathering of sedimentary rocks in steep terrains by direct *in situ* measurements?
- RQ2: On what timescale do significant changes of CO<sub>2</sub> release from oxidative weathering of organic matter (OC<sub>petro</sub>) and of sulfides in highly erosive settings occur, and how are they linked to environmental changes (e.g., in temperature and precipitation)?
- RQ3: How do differences in the chemical composition of sedimentary rocks undergoing oxidative weathering influence the weathering processes?

This concluding chapter summarizes the main research findings (Section 5.1) and presents potential directions for future research (Section 5.2).

## 5.1 Main research findings

### 5.1.1 RQ1: Is it possible to quantify the gas exchange of CO<sub>2</sub> and O<sub>2</sub> during weathering of sedimentary rocks in steep terrains by direct *in situ* measurements?

For the research presented in this thesis, direct *in situ* measurements of CO<sub>2</sub> release were performed in steep, rapidly eroding terrains of the Waiapu catchment, North Island, New Zealand, and of two neighbouring catchments in the French southern Alps. The rock-derived CO<sub>2</sub> release was measured in weathering chambers installed into bare rock outcrops, using previous designs of a gas sampling system (Hardie et al., 2005) and a drilled headspace chamber (Soulet et al., 2018). In the Waiapu catchment, it was shown that measurements of chamber-derived CO<sub>2</sub> flux are feasible during stand-alone, short-term ( $\geq 1$  week) field campaigns in remote areas (Chapter 2), while providing insights on the variability of CO<sub>2</sub> fluxes and their environmental controls (Section 5.1.2 and Section 5.1.3). In addition to the short-term variability, the long-term variability of CO<sub>2</sub> release from weathering chambers that occurs across multiple seasons was investigated in the Draix-Bléone observatory in the French southern Alps, based on six fieldtrips over one year (Chapter 3 and Chapter 4).

At the three study sites, the partial pressure of CO<sub>2</sub> in the shallow weathering zone ( $p\text{CO}_{2\text{Rock}}$ ) was determined (Chapter 2 and Chapter 3). In the case of the chamber method described here, a new framework was introduced, building on the previously developed method (Soulet et al., 2018), to assess the storage of gaseous CO<sub>2</sub> in the probed rock pore space at the start of a CO<sub>2</sub> flux measurement. Considering the movement of CO<sub>2</sub> between the rock pore space, a chamber and the atmosphere, a relationship between chamber-derived CO<sub>2</sub> fluxes and  $p\text{CO}_{2\text{Rock}}$  values was found that is consistent with Fick's law of diffusion. In this process, changes in the diffusivity of CO<sub>2</sub> in the shallow weathering zone are linked to changes in rock temperature and moisture, which was quantified with the long-term records obtained in the Draix-Bléone observatory (Chapter 3).

Following quantification of the diffusivity of CO<sub>2</sub>, specific to a measurement visit to a chamber, the diffusivity of O<sub>2</sub> can be estimated. In Chapter 3, it was shown that the partial pressure of O<sub>2</sub> ( $p\text{O}_2$ ) in the studied rocks can be combined with the diffusivity of O<sub>2</sub> to estimate an O<sub>2</sub> consumption in the weathering zone. For this, the  $p\text{O}_2$  value was determined simultaneously while measuring  $p\text{CO}_2$ . Assuming that O<sub>2</sub> consumption and CO<sub>2</sub> release occur over the same pore space during chemical weathering of OC<sub>petro</sub> and of sulfides coupled to carbonate dissolution, the measured O<sub>2</sub> : CO<sub>2</sub> molar ratios can be compared with the theoretical stoichiometry of the chemical weathering reactions. The expected ratio was ~ 10 mol O<sub>2</sub> : 9.3 mol CO<sub>2</sub> at both study sites in the Draix-Bléone observatory. There was thus a stark discrepancy with the apparent measured O<sub>2</sub> : CO<sub>2</sub> molar ratios of ~ 10 : 1. While this warrants further research into the consumption of O<sub>2</sub> during weathering, a possible explanation may be significant export of dissolved inorganic carbon (DIC) from pore waters in the studied rocks, lowering the measured release of gaseous CO<sub>2</sub> (Chapter 3 and Chapter 4).

Finally, the volume of rock responsible for producing the measured CO<sub>2</sub> fluxes was estimated, using a quantification of the mass of CO<sub>2</sub> present in the pore space around a chamber (Chapter 3). In turn, by quantifying the rock volume that contributes to a CO<sub>2</sub> flux measurement, it is possible to estimate the CO<sub>2</sub> flux through the surface of the studied rock outcrops (a topographic CO<sub>2</sub> efflux). This forms an important basis for upscaling chamber-based weathering fluxes across wider landscapes (Chapter 3 and Chapter 4).

Following this approach, high rock-derived CO<sub>2</sub> emissions were reported that identify steep terrains as hotspots of oxidative weathering in Earth's geological carbon cycle – especially if considering that the export of DIC from the highly erosive settings may result in CO<sub>2</sub> emission elsewhere (Chapter 2 and Chapter 4).

### 5.1.2 RQ2: On what timescale do significant changes of CO<sub>2</sub> release from oxidative weathering of organic matter and of sulfides in highly erosive settings occur, and how are they linked to environmental changes?

During chemical weathering of sedimentary rocks, the oxidation of OC<sub>petro</sub> and of sulfide minerals coupled to the dissolution of carbonate minerals can both be a source of CO<sub>2</sub> to the atmosphere. Over one week in the Waiapu catchment, the CO<sub>2</sub> release measured in the weathering chambers varied by a factor of ~ 2.5 (Chapter 2), while CO<sub>2</sub> fluxes varied by a factor of ~ 18 over one year of observations at the two study sites in the French southern Alps (Chapter 3). As a first step towards understanding this variability, and its link to environmental changes (e.g., in temperature and precipitation), the source of CO<sub>2</sub> was determined using radiocarbon and stable carbon isotope analyses of CO<sub>2</sub>, alongside the isotopic composition of organic and inorganic carbon in the studied environments. In the Waiapu catchment, dominated by mudstones, it was found that the CO<sub>2</sub> flux derived completely from the oxidation of OC<sub>petro</sub> (Chapter 2). In contrast, ~ 84 % of the bulk CO<sub>2</sub> release from black shales and marly limestones in the Draix-Bléone observatory were attributed to pyrite oxidation coupled to carbonate dissolution, and ~ 16 % to OC<sub>petro</sub> oxidation, with stable contributions from both sources over time (Chapter 4).

Changes in the temperature of the rocks undergoing weathering were found to explain the most significant changes in CO<sub>2</sub> efflux derived from both weathering pathways (Figure 5-1). CO<sub>2</sub> flux increased exponentially by a factor of ~ 2.3 with a temperature increase of 10 °C at all three study sites (Chapter 2 and Chapter 4). This finding confirms previous research based on one study site in a neighbouring catchment in the Draix-Bléone observatory (Soulet et al., 2021). Together, they show that the CO<sub>2</sub> release from oxidative weathering of sedimentary rocks can act as a positive feedback to warming in the geological carbon cycle (Figure 5-1) (Soulet et al., 2021). The apparent response is opposite to the weathering-driven CO<sub>2</sub> sink by silicate weathering, and raises questions about how erosion and weathering impact the global carbon cycle. Together, the identification of highly erosive settings as hotspots of oxidative weathering (Section 5.1.1), and the pronounced temperature sensitivity of CO<sub>2</sub> release mean that highly erosive areas need to be carefully considered in Earth system models (Chapter 4).

In more detail, it was shown in Chapter 2 and Chapter 3 that the response of the CO<sub>2</sub> release to changes in rock temperature occurs rapidly on timescales  $\leq 1$  h. Furthermore, a model was developed that allows calculation of the rock temperature based on the air temperature and the duration of day light (Chapter 3). In addition to CO<sub>2</sub> measurements, the results from pO<sub>2</sub> and O<sub>2</sub> flux analyses in the weathering chambers present evidence on the temperature

sensitivity of oxidative weathering reactions, with an agreement of relative changes in  $O_2$  consumption and  $CO_2$  production with changes in rock temperature (Chapter 3).

In addition to temperature, precipitation impacts rock moisture and was found to control the size of  $CO_2$  emissions from shallow weathering zones (Figure 5-1). Following rain events, the bulk  $CO_2$  release decreases but recovers subsequently over a few days. This was attributed to the dissolution of weathering-derived carbon and export of DIC, in addition to the role of increased rock moisture in hindering the diffusive release of  $CO_2$  and supply of  $O_2$  needed for the oxidative weathering reactions (Chapter 2 and Chapter 3) (Soulet et al., 2021).

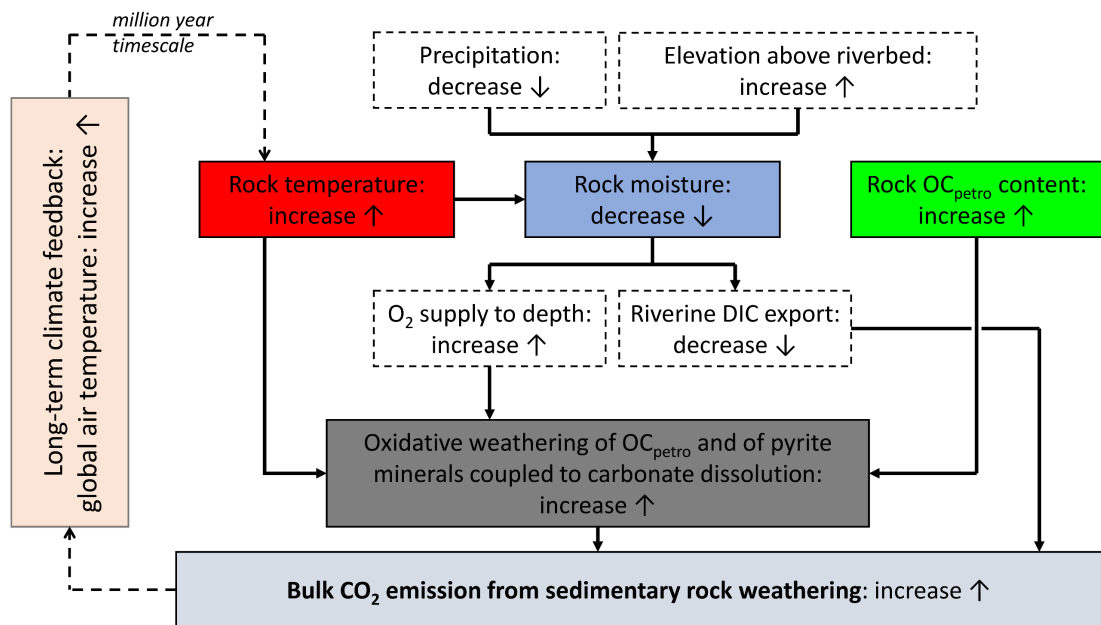


**Figure 5-1. Generalized diagram for the response of  $CO_2$  emissions from oxidative weathering of sedimentary rocks to environmental changes in highly erosive terrains.**

The impact of changes in temperature and precipitation on the  $CO_2$  release during oxidative weathering of sedimentary rocks may be facilitated by microorganisms (Hemingway et al., 2018; Matlakowska and Sklodowska, 2011; Petsch et al., 2001; Seifert et al., 2013; Stasiuk et al., 2017). The new findings here provide multiple lines of evidence that indicate their involvement in the weathering processes at the three study sites. First, differences between the carbon isotope composition of  $CO_2$  derived from the oxidation of  $OC_{\text{petro}}$  and of  $OC_{\text{petro}}$  itself are consistent with carbon isotope fractionation during microbial heterotrophic respiration (Chapter 2). Secondly, in the Draix-Bléone observatory, the  $CO_2$  fluxes from sulfide oxidation coupled to carbonate dissolution correspond to an oxidation rate of pyrite minerals that is similar to that of microbially accelerated pyrite oxidation found previously in laboratory experiments (Chapter 4). Furthermore, a coupling of the  $CO_2$  release from the oxidation of  $OC_{\text{petro}}$  and of sulfide minerals (Section 5.1.3) indicates the presence of a chemoheterotrophic

microbial consortium controlling the oxidation of sulfide minerals at the study sites that relies on  $OC_{\text{petro}}$  to thrive (Chapter 4). Finally, it was shown that the oxidation of  $OC_{\text{petro}}$  shares similarities with the degradation of soil organic matter that is controlled by microorganisms in respect to the temperature sensitivity and to the quantity of organic material that is oxidized (i.e., respired) over time (Chapter 2 and Chapter 4).

### 5.1.3 RQ3: How do differences in the chemical composition of sedimentary rocks undergoing oxidative weathering influence the weathering processes?

To understand how differences in the chemical composition of the studied sedimentary rocks influence the weathering processes, their contents of  $OC_{\text{petro}}$ , carbonate minerals and sulfide minerals were determined. The source-specific contributions of  $CO_2$  release from oxidation of  $OC_{\text{petro}}$  and of sulfides coupled to carbonate dissolution were then compared to the bulk rock-derived  $CO_2$  efflux (Section 5.1.2). A separation of climatic controls (Section 5.1.2) from lithological influences is possible with the year-long monitoring of source-specific  $CO_2$  release from black shales and marly limestones outcropping in neighbouring catchments of the Draix-Bléone observatory, which experienced similar changes in temperature and precipitation. There, it was also found that the capability of the studied rocks to allow diffusion is similar, which implies that differences in  $CO_2$  efflux between study sites cannot be explained by potential differences of the structure of the pore space (e.g., porosity and tortuosity) (Chapter 3).

The surplus of  $OC_{\text{petro}}$ -derived  $CO_2$  release was higher from black shales compared to marly limestones. The difference scaled with the  $OC_{\text{petro}}$  contents of these rocks, which varied by a factor of  $\sim 1.7$  (Chapter 4), suggesting a 1 : 1 ratio between the  $OC_{\text{petro}}$  concentration of weathering reactants and products (Figure 5-1). This finding was combined with the quantified temperature sensitivity of the oxidative weathering reactions (Section 5.1.2) to present a dual framework that allows the carbon release from rock types with different contents of  $OC_{\text{petro}}$  and/or situated in different climates to be estimated. Following quantification of the contributing rock volume (Section 5.1.1), high mean annual topographic  $CO_2$  fluxes from oxidative weathering of  $OC_{\text{petro}}$  were found, ranging between  $13 \text{ gC m}^{-2} \text{ yr}^{-1}$  and  $180 \text{ gC m}^{-2} \text{ yr}^{-1}$  in the highly erosive settings of the Draix-Bléone observatory.

The  $CO_2$  flux derived from the oxidation of sulfide minerals coupled to dissolution of carbonates did not scale with the quantity of these minerals. Instead, they scaled with the  $OC_{\text{petro}}$  content (Figure 5-1). It was suggested that this may be the result of a microbial link of both weathering pathways (Chapter 4). The coupled oxidative weathering reactions result in extensive weathering of carbonate minerals that corresponds to  $\sim 1 \text{ \% yr}^{-1}$  dissolution of the total rock mass of the studied black shales and marly limestones.

In contrast, the mudstones undergoing oxidative weathering in the Waiapu catchment did not contain significant quantities of carbonate minerals, resulting in a lack of CO<sub>2</sub> release from weathering of inorganic carbon (Section 5.1.2), while high CO<sub>2</sub> fluxes derived from the oxidation of OC<sub>petro</sub> were found (Chapter 2). The absence of carbonate minerals and the buffer their reactants can provide appeared to allow very high CO<sub>2</sub> fluxes and *p*CO<sub>2</sub> values. These may promote acid-hydrolysis reactions that increase the chemical weathering of co-occurring silicate minerals. Such a link implies that the uptake of atmospheric CO<sub>2</sub> during weathering of silicate minerals is hindered in the presence of OC<sub>petro</sub>-derived CO<sub>2</sub>. If this is a wider phenomenon in mudstone-dominated areas, the riverine flux of dissolved cations derived from silicate weathering (and their use to precipitate new carbonate minerals) does not strictly represent an atmospheric CO<sub>2</sub> sink, but in fact reflects a net CO<sub>2</sub> release from OC<sub>petro</sub> oxidation. In respect to river-chemistry-based constraints on chemical weathering, it was also emphasized that OC<sub>petro</sub> should be considered as a source of acidity, in addition to sulfide minerals, during oxidative weathering – especially in steep terrains where high rock-derived CO<sub>2</sub> emissions occur (Chapter 2 and Chapter 4).

## 5.2 Future research directions

This work presented fundamental research on sedimentary rock weathering in highly erosive settings and may support future research in the following directions, which generally aim at a more detailed understanding of the weathering processes and how they operate in different landscapes on Earth:

### 5.2.1 The role of microorganisms during oxidative weathering of sedimentary rocks in highly erosive terrains

As summarized in Section 5.1.2, microorganisms that are present in sedimentary rocks are likely to be involved in their weathering in highly erosive terrains. This raises the question on how important this involvement is in respect to the weathering rates. To explore this question, several approaches could be adopted. For example, a microbial acceleration of oxidative weathering reactions for OC<sub>petro</sub> and pyrite minerals could be quantified in laboratory incubation experiments in combination with inoculation of microorganisms and abiotic controls. Alternatively, measurements of *in situ* CO<sub>2</sub> release with weathering chambers (Section 5.1.1) may be combined with repeated sampling of the living microbial community over several seasons, for example, with intact biomarkers such as phospholipid-derived fatty acids (Akondi et al., 2017; Petsch et al., 2001; Seifert et al., 2013), or analyses of the genome, transcriptome and proteome targeting the DNA, RNA and proteins, respectively (Berlendis et al., 2014; Knight

et al., 2018; Stasiuk et al., 2017; Włodarczyk et al., 2018). These analytical approaches would allow studying changes in size, structure and function of the microbial community and how these are related to changes in CO<sub>2</sub> emission.

If microorganisms are important for an efficient weathering of sedimentary carbon, the size of rock-derived CO<sub>2</sub> release may be regulated indirectly by controls on the microbial life. One such control may be related to the origin of microbial life in sedimentary rocks undergoing weathering. If there the recent community consists of microorganisms that originate from the surrounding biosphere (e.g., soils), high oxidative weathering rates may rely on efficient colonialization of the rock environment by allochthonous microorganisms. However, if the recent community consists of descendants of microorganisms that were deposited with the sedimentary rocks during their formation and that survived during burial and subsequent orogenic uplift (Wilkins and Fredrickson, 2015), oxidative weathering rates may be independent from the microbial connectivity to surrounding environments. The latter scenario would favour perpetuation of microbially driven weathering in highly erosive settings, where near-surface communities could be regularly eroded, whereas a dependence on the surrounding biosphere could represent an important constraint in areas experiencing rapid uplift over vast areas. An analogous control may be related to nutrients: do microorganisms thriving in sedimentary rocks rely on nutrient supply from surrounding environments, or is the sedimentary rock undergoing weathering itself a sufficient source of nutrients (Brantley et al., 2011)?

While addressing these research topics, it may also be possible to investigate further the coupling of the oxidation of OC<sub>petro</sub> and of sulfides coupled to carbonate dissolution that was found in the Draix-Bléone observatory (Section 5.1.3). To demonstrate this link, it seems vital to map the biological space (i.e., that occupied by living microorganisms) (Blagodatskaya et al., 2017; Nannipieri et al., 2017): where and how is it constituted in the porous, mixed matrix of various mineral types and OC<sub>petro</sub> from a holistic view across multiple scales of space and time (Brantley et al., 2007; Eglinton, 2015; Kleber et al., 2021).

In more detail, following the identification of the environmental impact of changes in rock temperature and precipitation on weathering rates in highly erosive terrains (Section 5.1.2), it is unclear: i) how microbial communities in sedimentary rocks respond to warming on different timescales in respect to changes in growth, metabolic activity, (geo-)respiration and community structure; ii) whether extreme droughts lead to a decline in microbial activity and CO<sub>2</sub> fluxes from weathering (Chapter 2); and iii) how extreme temperatures impact the microbial communities and CO<sub>2</sub> release. Regarding the latter research question, it should be noted that, so far, field-based measurements did not show evidence for a decline in weathering rates at high temperatures (Chapter 2 and Chapter 4) (Soulet et al., 2021).

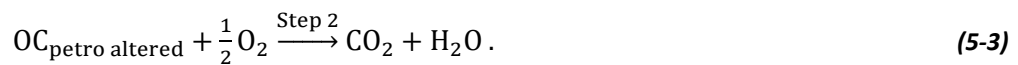
However, the rock temperatures sampled by the weathering chambers were mostly below 35 °C, whereas rock surface temperatures exceeded 55 °C in the Draix-Bléone observatory, and it may be that microorganisms cope by migrating into deeper rock layers when rock surface temperatures would favour denaturation of enzymes (Schipper et al., 2014).

### 5.2.2 Alteration of $OC_{\text{petro}}$ during oxidative weathering and the geological $O_2$ cycle

Previous research has shown that  $OC_{\text{petro}}$  can be significantly altered in respect to its composition and structure during oxidative weathering (Chang and Berner, 1999; Longbottom and Hockaday, 2019; Marynowski et al., 2011a; Petsch, 2014), and this process can be controlled by microorganisms (Hemingway et al., 2018; Petsch et al., 2001; Stasiuk et al., 2017). The (bio-)chemical alteration suggests that oxidative weathering of  $OC_{\text{petro}}$  (simplified here as  $CH_2O$ ), which is classically described by one reaction (Berner, 1999; Keller and Bacon, 1998; Petsch, 2014):



may be alternatively described by a stepwise oxidation with the formation of an intermediate ( $OC_{\text{petro altered}}$ ) (Chang and Berner, 1999), for example by:



So far, it is unclear how the environmental controls on  $CO_2$  emission during sedimentary rock weathering (Section 5.1.2 and Section 5.1.3) can be explained in a model of stepwise oxidation of  $OC_{\text{petro}}$  and subsequent  $CO_2$  release.

In general, small differences in the sensitivity to environmental changes of the different reaction steps (Equation 5-2 vs. Equation 5-3) may have large implications for the geological  $O_2$  cycle. That is because any reaction limitation that involves a higher performance of the first step (Equation 5-2) compared to the second step (Equation 5-3) results in the accumulation of (bio-)chemically altered, partially oxidized  $OC_{\text{petro}}$ . This, in turn, represents the build-up of a sedimentary  $O_2$  stock, which would act to lower the atmospheric  $O_2$  level while the atmospheric  $CO_2$  concentration is less impacted. For example, this may be part of an explanation why atmospheric  $O_2$  concentrations declined over the past 800,000 years while atmospheric  $CO_2$  concentration were steady (Stolper et al., 2016; Yan et al., 2021). It should be noted that an opposite version of the reaction limitation involving faster rates of the second part seems unlikely because it would hinder the observation of  $OC_{\text{petro altered}}$  in natural environments.

In respect to the temperature sensitivity of  $OC_{\text{petro}}$  oxidation, it was observed that  $CO_2$  release and  $O_2$  consumption responded roughly to similar degrees to temperature changes in

the Draix-Bléone observatory, but the temperature sensitivity of the O<sub>2</sub> fluxes could not be assessed precisely (Chapter 3). As such, based on this research, a scenario cannot be ruled out that the first step is faster than the second step at a given temperature. However, previous research has shown that OC<sub>petro altered</sub> possesses lower thermal activation energies than unweathered OC<sub>petro</sub> (Hemingway et al., 2018), which may indicate a low likelihood of this scenario.

There may also be important limitations on weathering rate imposed by the O<sub>2</sub> availability in the rock pore space (Chang and Berner, 1999). If the first part of the stepwise oxidation of OC<sub>petro</sub> is feasible at lower O<sub>2</sub> levels compared to the second step, this would result in the formation of pools of OC<sub>petro altered</sub> under low oxygen conditions. This could mean that wider, more gradually structured oxidative weathering fronts, for example, in terrains with moderate to low erosive rates (Section 5.2.3), may see greater degrees of alteration of OC<sub>petro</sub> compared to shallow weathering zones that are well-connected to the oxygen-rich atmosphere (Chapter 3).

Future research may address these topics with installations of weathering chambers or deeper boreholes in a wide range of settings. An aim to study the local exchange of O<sub>2</sub> and CO<sub>2</sub> in direct combination with measurements of aqueous DIC export from the weathering zone would allow an overall budget of the carbon release from oxidative weathering to be drawn. The corresponding study sites would need to be characterized in respect to the physical properties of the weathering zone and to the composition and structure of OC<sub>petro</sub> and OC<sub>petro altered</sub>, which may vary across the weathering fronts. While doing so, such research could quantify the impact of varying O<sub>2</sub> levels on the weathering rate that is essential for evaluating a negative feedback of atmospheric O<sub>2</sub> on OC<sub>petro</sub> weathering on geological timescales (Bolton et al., 2006; Chang and Berner, 1999).

In more detail, this research may also address the variability of OC<sub>petro</sub> alteration processes and how this may be associated with differences in the overall oxidation rate (e.g., resulting in differing CO<sub>2</sub> fluxes from similar parent material weathering in different terrains or climates). Furthermore, while doing so, it could also be studied in detail whether preferential oxidation of certain fractions of OC<sub>petro</sub> occurs (Petsch, 2014) and whether these, in turn, are associated with different reaction rates.

### 5.2.3 Sedimentary rock weathering in terrains with moderate to low erosion rates

The identification of highly erosive settings as hotspots of CO<sub>2</sub> release from oxidative weathering of OC<sub>petro</sub> and sulfide minerals (Section 5.1.1 and Section 5.1.3) may motivate future research to address the constraints on oxidative weathering in terrains with lower erosion rates that exhibit lower weathering fluxes (Bufe et al., 2021; Calmels et al., 2007; Hilton et al., 2014; Hilton and West, 2020; Keller and Bacon, 1998; Longbottom and Hockaday, 2019).

Based on the research presented here, the link of local erosion rate and oxidative weathering fluxes can be followed in a conceptual framework considering: i) the supply of OC<sub>petro</sub> and sulfide minerals; ii) the availability of O<sub>2</sub>; and iii) the speed at which the oxidation reactions proceed. The observation of OC<sub>petro</sub> and sulfide minerals in rocks outcropping in the highly erosive terrains in the Draix-Bléone observatory and in the Waiapu catchment indicates that the rate of the weathering reaction itself is limiting the CO<sub>2</sub> release since sufficient amounts of all reactants, including O<sub>2</sub>, are present there to facilitate the oxidation. Below the near-surface weathering zone, the transport of O<sub>2</sub> to depth (that is mostly driven by diffusion through the rock pore space, Chapter 3) limits the oxidation reaction. Given the very short lifetimes of OC<sub>petro</sub> and sulfide minerals in the oxygenated weathering zone (Chapter 4), two scenarios can be drawn. If the studied sedimentary rocks have higher porosities (i.e., supporting O<sub>2</sub> supply to depth), or if they experience less physical erosion (i.e., increasing the residence time of reactants), a complete oxidation of OC<sub>petro</sub> and sulfide minerals would occur towards the surface. This depletion would represent a bottleneck for the chemical weathering processes by the supply of OC<sub>petro</sub> and sulfide minerals to the oxygenated weathering zone. A global dominance of such a supply-limitation may explain the relation of erosion rates and oxidative weathering fluxes that is apparent across a wide range of erosion rates (Calmels et al., 2007; Hilton et al., 2014; Hilton and West, 2020).

However, in more detail, a wide range of physical, chemical and biological factors is likely impacting the local CO<sub>2</sub> efflux from oxidative weathering in terrains with moderate to low erosion rates (Section 5.1.2 and Section 5.1.3). For example, lower erosion rates that result in the accumulation of soil may reduce the connectivity of the underlying rocks to the surface and impact the water flow across the weathering zone so that export of CO<sub>2</sub> in the dissolved load is promoted and O<sub>2</sub> supply to depth is limited (Lebedeva and Brantley, 2020; Tremosa et al., 2020; Tune et al., 2020). Furthermore, uptake of O<sub>2</sub> in the soil horizon (e.g., by roots or microbial respiration of soil organic matter) may hinder the oxidative weathering of underlying sedimentary rocks. In contrast, organic substrates derived from roots or soil organic matter can

stimulate microbial activity (i.e., induce priming) that may result in increased oxidation of  $OC_{\text{petro}}$  and sulfide minerals (Kuzyakov, 2010; Seifert et al., 2011). In addition, the role of microorganisms (Section 5.2.1) may be impacted by the structure of the rock matrix, with fracturing promoting microbial presence (Bochet et al., 2020; Hasenmueller et al., 2017), and narrow pore spaces limiting microbial involvement in the weathering reaction at depth (Gu et al., 2020a). In turn, the rock structure may be governed by the tectonic history of the underlying parent material, with microfracturing promoting diffusive processes (Gu et al., 2020b).

From these examples follows that future research may need to utilize a broad range of tools developed by critical zone science (Chapter 1) to understand in detail what is controlling oxidative weathering locally in terrains with moderate or low erosion rates that occur over the vast majority of Earth's continental surface (Larsen et al., 2014). The resulting findings may reveal, amongst others, how erosion rate is related to: i) the link of organic and inorganic carbon weathering (Chapter 4); and ii) the overall carbon budget of sedimentary rock weathering considering the oxidation of  $OC_{\text{petro}}$  and sulfide minerals together with the dissolution of silicate minerals (Bufe et al., 2021; Hilton and West, 2020).

#### 5.2.4 Spatial and temporal upscaling of *in situ* constraints on chemical weathering processes

The understanding of how chemical weathering of sedimentary rocks operates locally in a given environment (based on *in situ* research as presented here) provides an opportunity for future research to upscale weathering processes spatially and temporally. For this, reaction rates and their environmental controls may be combined with two- or three-dimensional maps, including information on the composition of the bedrock, morphology, soil- and vegetation cover, and the extent and structure of the weathering zone, for example, derived from geophysical measurements (Bechet et al., 2016; Callahan et al., 2020; Holbrook et al., 2019; Mallet et al., 2020; Maquaire et al., 2002; Novitsky et al., 2018). This information may be used in numerical models to quantify weathering fluxes on the outcrop- to catchment-scale (Bao et al., 2017; Bolton et al., 2006; Carriere et al., 2020; Roelandt et al., 2010; Shaughnessy et al., 2021).

Results from upscaling *in situ* measurements to the catchment-scale may be compared with oxidative weathering fluxes derived from riverine tracers representing a catchment-wide integrated signal (Bufe et al., 2021; Calmels et al., 2007; Hilton et al., 2014; Horan et al., 2017, 2019; Märki et al., 2021; Ogrič, 2021; Zhang et al., 2020). In addition to the size of the weathering fluxes, it has been recently shown that environmental controls such as temperature can be traced on intra-annual timescales in dissolved sulfate fluxes (Crawford et al., 2019; Ogrič, 2021).

In alpine catchments in Colorado, USA, it was found that monthly, flow-normalized sulfate fluxes from pyrite oxidation are related to the cumulative air temperature over one month (Crawford et al., 2019). And in the Draix-Bléone observatory, riverine concentrations of sulfate and rhenium can be best explained by temperature-driven weathering of pyrite and  $OC_{\text{petro}}$ , respectively, considering average air temperatures on timescales between 7 days to 30 days, when sampling at low river flow to ensure similar hydrological conditions between the samples (Ogrič, 2021). In the future, knowledge of how weathering products move through a catchment may enable a direct link of riverine tracers with *in situ* measurements that report an instantaneous response of weathering reactions to temperature changes (Section 5.1.2). For doing so, considering the integrated residence times of pore and stream waters, and the precipitation of secondary minerals seems especially important (Erlanger et al., 2021).

Furthermore, upscaling of  $CO_2$  fluxes derived from *in situ* measurements may be of interest in respect to the impact on the carbon isotope composition of the receiving local atmosphere. High  $CO_2$  fluxes from oxidative weathering of sedimentary carbon (e.g., in steep mountainous areas) may have the potential to notably lower the radiocarbon content of local atmospheric  $CO_2$  and shift its stable isotope composition depending on the source (i.e.,  $OC_{\text{petro}}$  or carbonate minerals). For example, this may impact estimates of local fossil-fuel-derived  $CO_2$  emissions that rely on mapping the radiocarbon and stable carbon isotope composition of atmospheric  $CO_2$  (Graven et al., 2018; Graven and Gruber, 2011; Levin et al., 2013; Wang et al., 2018).

Finally, a successful translation of oxidative weathering fluxes and their controls from the outcrop- to the catchment-scale is the basis for further upscaling to the continental- to global-scale. This, in turn, is fundamental to unravelling Earth's geochemical and climatic history (Bernier and Bernier, 2012; Caves Rugenstein et al., 2019; Maffre et al., 2021; Mills et al., 2021).

## References

- Akondi, R.N., Trexler, R.V., Pfiffner, S.M., Mouser, P.J., Sharma, S., 2017. Modified Lipid Extraction Methods for Deep Subsurface Shale. *Frontiers in Microbiology* 8, 1408. <https://doi.org/10.3389/fmicb.2017.01408>
- Alt, J.C., Teagle, D.A.H., 1999. The uptake of carbon during alteration of ocean crust. *Geochimica et Cosmochimica Acta* 63, 1527–1535. [https://doi.org/10.1016/S0016-7037\(99\)00123-4](https://doi.org/10.1016/S0016-7037(99)00123-4)
- Amundson, R., Richter, D.D., Humphreys, G.S., Jobbagy, E.G., Gaillardet, J., 2007. Coupling between Biota and Earth Materials in the Critical Zone. *Elements* 3, 327–332. <https://doi.org/10.2113/gselements.3.5.327>
- Anderson, S.P., von Blanckenburg, F., White, A.F., 2007. Physical and Chemical Controls on the Critical Zone. *Elements* 3, 315–319. <https://doi.org/10.2113/gselements.3.5.315>
- Angert, A., Yakir, D., Rodeghiero, M., Preisler, Y., Davidson, E.A., Weiner, T., 2015. Using O<sub>2</sub> to study the relationships between soil CO<sub>2</sub> efflux and soil respiration. *Biogeosciences* 12, 2089–2099. <https://doi.org/10.5194/bg-12-2089-2015>
- Antoine, P., Giraud, A., Meunier, M., van Asch, T., 1995. Geological and geotechnical properties of the “Terres Noires” in southeastern France: Weathering, erosion, solid transport and instability. *Engineering Geology* 40, 223–234. [https://doi.org/10.1016/0013-7952\(95\)00053-4](https://doi.org/10.1016/0013-7952(95)00053-4)
- Ariagno, C., Le Bouteiller, C., van der Beek, P., Klotz, S., 2022. Sediment export in marly badland catchments modulated by frost-cracking intensity, Draix–Bléone Critical Zone Observatory, SE France. *Earth Surface Dynamics* 10, 81–96. <https://doi.org/10.5194/esurf-10-81-2022>
- Arrhenius, S., 1896. On the influence of carbonic acid in the air upon the temperature of the ground. *The London, Edinburgh, and Dublin Philosophical Magazine and Journal of Science* 41, 237–276. <https://doi.org/10.1080/14786449608620846>
- Bao, Z., Haberer, C.M., Maier, U., Amos, R.T., Blowes, D.W., Grathwohl, P., 2017. Modeling controls on the chemical weathering of marine mudrocks from the Middle Jurassic in Southern Germany. *Chemical Geology* 459, 1–12. <https://doi.org/10.1016/j.chemgeo.2017.03.021>
- Bardgett, R.D., Richter, A., Bol, R., Garnett, M.H., Bäuml, R., Xu, X., Lopez-Capel, E., Manning, D.A.C., Hobbs, P.J., Hartley, I.R., Wanek, W., 2007. Heterotrophic microbial communities use ancient carbon following glacial retreat. *Biology Letters* 3, 487–490. <https://doi.org/10.1098/rsbl.2007.0242>
- Battin, T.J., Luysaert, S., Kaplan, L.A., Aufdenkampe, A.K., Richter, A., Tranvik, L.J., 2009. The boundless carbon cycle. *Nature Geoscience* 2, 598–600. <https://doi.org/10.1038/ngeo618>

- Beaupré, S.R., Mahmoudi, N., Pearson, A., 2016. IsoCaRB: A novel bioreactor system to characterize the lability and natural carbon isotopic ( $^{14}\text{C}$ ,  $^{13}\text{C}$ ) signatures of microbially respired organic matter. *Limnology and Oceanography: Methods* 14, 668–681. <https://doi.org/10.1002/lom3.10121>
- Bechet, J., Duc, J., Jaboyedoff, M., Loye, A., Mathys, N., 2015. Erosion processes in black marl soils at the millimetre scale: preliminary insights from an analogous model. *Hydrology and Earth System Sciences* 19, 1849–1855. <https://doi.org/10.5194/hess-19-1849-2015>
- Bechet, J., Duc, J., Loye, A., Jaboyedoff, M., Mathys, N., Malet, J.-P., Klotz, S., Le Bouteiller, C., Rudaz, B., Travelletti, J., 2016. Detection of seasonal cycles of erosion processes in a black marl gully from a time series of high-resolution digital elevation models (DEMs). *Earth Surface Dynamics* 4, 781–798. <https://doi.org/10.5194/esurf-4-781-2016>
- Belcher, C.M., McElwain, J.C., 2008. Limits for Combustion in Low  $\text{O}_2$  Redefine Paleatmospheric Predictions for the Mesozoic. *Science* 321, 1197–1200. <https://doi.org/10.1126/science.1160978>
- Bergman, N.M., Lenton, T.M., Watson, A.J., 2004. COPSE: A new model of biogeochemical cycling over Phanerozoic time. *American Journal of Science* 304, 397–437. <https://doi.org/10.2475/ajs.304.5.397>
- Berlendis, S., Beyssac, O., Derenne, S., Benzerara, K., Anquetil, C., Guillaumet, M., Estève, I., Capelle, B., 2014. Comparative mineralogy, organic geochemistry and microbial diversity of the Autun black shale and Graissessac coal (France). *International Journal of Coal Geology* 132, 147–157. <https://doi.org/10.1016/j.coal.2014.07.005>
- Berner, E.K., Berner, R.A., 2012. *Global environment: Water, Air, and Geochemical cycles*, 2nd ed. Princeton University Press, New Jersey, USA.
- Berner, R.A., 2009. Phanerozoic atmospheric oxygen: New results using the GEOCARBSULF model. *American Journal of Science* 309, 603–606. <https://doi.org/10.2475/07.2009.03>
- Berner, R.A., 2004. *The Phanerozoic Carbon Cycle*. Oxford University Press, New York, USA.
- Berner, R.A., 1999. A New Look at the Long-term Carbon Cycle. *GSA Today* 9, 1–6.
- Berner, R.A., 1982. Burial of organic carbon and pyrite sulfur in the modern ocean; its geochemical and environmental significance. *American Journal of Science* 282, 451–473. <https://doi.org/10.2475/ajs.282.4.451>
- Berner, R.A., Caldeira, K., 1997. The need for mass balance and feedback in the geochemical carbon cycle. *Geology* 25, 955–956. [https://doi.org/10.1130/0091-7613\(1997\)025<0955:TNFMBA>2.3.CO;2](https://doi.org/10.1130/0091-7613(1997)025<0955:TNFMBA>2.3.CO;2)

- Betts, H.D., Trustrum, N.A., De Rose, R.C., 2003. Geomorphic changes in a complex gully system measured from sequential digital elevation models, and implications for management. *Earth Surface Processes and Landforms* 28, 1043–1058. <https://doi.org/10.1002/esp.500>
- Beyssac, O., Simoes, M., Avouac, J.P., Farley, K.A., Chen, Y.-G., Chan, Y.-C., Goffé, B., 2007. Late Cenozoic metamorphic evolution and exhumation of Taiwan. *Tectonics* 26, TC6001. <https://doi.org/10.1029/2006TC002064>
- Bickle, M.J., Tipper, E., Galy, A., Chapman, H., Harris, N., 2015. On discrimination between carbonate and silicate inputs to Himalayan rivers. *American Journal of Science* 315, 120–166. <https://doi.org/10.2475/02.2015.02>
- Blagodatskaya, E., Dungait, J.A.J., Schmidt, O., 2017. Commentary on the impact of Nannipieri et al. (2003). *European Journal of Soil Science* 68, 6–11. [https://doi.org/10.1111/ejss.3\\_12398](https://doi.org/10.1111/ejss.3_12398)
- Blair, N., Leu, A., Muñoz, E., Olsen, J., Kwong, E., Des Marais, D., 1985. Carbon isotopic fractionation in heterotrophic microbial metabolism. *Applied and Environmental Microbiology* 50, 996–1001. <https://doi.org/10.1128/aem.50.4.996-1001.1985>
- Blair, N.E., Aller, R.C., 2012. The Fate of Terrestrial Organic Carbon in the Marine Environment. *Annual Review of Marine Science* 4, 401–423. <https://doi.org/10.1146/annurev-marine-120709-142717>
- Blattmann, T.M., Liu, Z., Zhang, Y., Zhao, Y., Haghypour, N., Montluçon, D.B., Plötze, M., Eglinton, T.I., 2019a. Mineralogical control on the fate of continentally derived organic matter in the ocean. *Science* 366, 742–745. <https://doi.org/10.1126/science.aax5345>
- Blattmann, T.M., Wang, S.-L., Lupker, M., Märki, L., Haghypour, N., Wacker, L., Chung, L.-H., Bernasconi, S.M., Plötze, M., Eglinton, T.I., 2019b. Sulphuric acid-mediated weathering on Taiwan buffers geological atmospheric carbon sinks. *Scientific Reports* 9, 2945. <https://doi.org/10.1038/s41598-019-39272-5>
- Bochet, O., Bethencourt, L., Dufresne, A., Farasin, J., Pédrot, M., Labasque, T., Chatton, E., Lavenant, N., Petton, C., Abbott, B.W., Aquilina, L., Le Borgne, T., 2020. Iron-oxidizer hotspots formed by intermittent oxic–anoxic fluid mixing in fractured rocks. *Nature Geoscience* 13, 149–155. <https://doi.org/10.1038/s41561-019-0509-1>
- Bolton, E.W., Berner, R.A., Petsch, S.T., 2006. The Weathering of Sedimentary Organic Matter as a Control on Atmospheric O<sub>2</sub>: II. Theoretical Modeling. *American Journal of Science* 306, 575–615. <https://doi.org/10.2475/08.2006.01>
- Bond-Lamberty, B., Thomson, A., 2010. A global database of soil respiration data. *Biogeosciences* 7, 1915–1926. <https://doi.org/10.5194/bg-7-1915-2010>

- Bosatta, E., Ågren, G.I., 1999. Soil organic matter quality interpreted thermodynamically. *Soil Biology and Biochemistry* 31, 1889–1891. [https://doi.org/10.1016/S0038-0717\(99\)00105-4](https://doi.org/10.1016/S0038-0717(99)00105-4)
- Bouchez, J., Beyssac, O., Galy, V., Gaillardet, J., France-Lanord, C., Maurice, L., Moreira-Turcq, P., 2010. Oxidation of petrogenic organic carbon in the Amazon floodplain as a source of atmospheric CO<sub>2</sub>. *Geology* 38, 255–258. <https://doi.org/10.1130/G30608.1>
- Brand, U., Davis, A.M., Shaver, K.K., Blamey, N.J.F., Heizler, M., Lécuyer, C., 2021. Atmospheric oxygen of the Paleozoic. *Earth-Science Reviews* 216, 103560. <https://doi.org/10.1016/j.earscirev.2021.103560>
- Brantley, S.L., Goldhaber, M.B., Ragnarsdottir, K.V., 2007. Crossing Disciplines and Scales to Understand the Critical Zone. *Elements* 3, 307–314. <https://doi.org/10.2113/gselements.3.5.307>
- Brantley, S.L., Holleran, M.E., Jin, L., Bazilevskaya, E., 2013. Probing deep weathering in the Shale Hills Critical Zone Observatory, Pennsylvania (USA): the hypothesis of nested chemical reaction fronts in the subsurface. *Earth Surface Processes and Landforms* 38, 1280–1298. <https://doi.org/10.1002/esp.3415>
- Brantley, S.L., McDowell, W.H., Dietrich, W.E., White, T.S., Kumar, P., Anderson, S.P., Chorover, J., Lohse, K.A., Bales, R.C., Richter, D.D., Grant, G., Gaillardet, J., 2017. Designing a network of critical zone observatories to explore the living skin of the terrestrial Earth. *Earth Surface Dynamics* 5, 841–860. <https://doi.org/10.5194/esurf-5-841-2017>
- Brantley, S.L., Megonigal, J.P., Scatena, F.N., Balogh-Brunstad, Z., Barnes, R.T., Bruns, M.A., Van Cappellen, P., Dontsova, K., Hartnett, H.E., Hartshorn, A.S., Heimsath, A., Herndon, E., Jin, L., Keller, C.K., Leake, J.R., McDowell, W.H., Meinzer, F.C., Mozdzer, T.J., Petsch, S., Pett-Ridge, J., Pregitzer, K.S., Raymond, P.A., Riebe, C.S., Shumaker, K., Sutton-Grier, A., Walter, R., Yoo, K., 2011. Twelve testable hypotheses on the geobiology of weathering. *Geobiology* 9, 140–165. <https://doi.org/10.1111/j.1472-4669.2010.00264.x>
- Bufe, A., Hovius, N., Emberson, R., Caves Rügenstein, J.K., Galy, A., Hassenruck-Gudipati, H.J., Chang, J.-M., 2021. Co-variation of silicate, carbonate and sulfide weathering drives CO<sub>2</sub> release with erosion. *Nature Geoscience* 14, 211–216. <https://doi.org/10.1038/s41561-021-00714-3>
- Burke, A., Present, T.M., Paris, G., Rae, E.C.M., Sandilands, B.H., Gaillardet, J., Peucker-Ehrenbrink, B., Fischer, W.W., McClelland, J.W., Spencer, R.G.M., Voss, B.M., Adkins, J.F., 2018. Sulfur isotopes in rivers: Insights into global weathering budgets, pyrite oxidation, and the modern sulfur cycle. *Earth and Planetary Science Letters* 496, 168–177. <https://doi.org/10.1016/j.epsl.2018.05.022>

- Callahan, R.P., Riebe, C.S., Pasquet, S., Ferrier, K.L., Grana, D., Sklar, L.S., Taylor, N.J., Flinchum, B.A., Hayes, J.L., Carr, B.J., Hartsough, P.C., O'Geen, A.T., Holbrook, W.S., 2020. Subsurface Weathering Revealed in Hillslope-Integrated Porosity Distributions. *Geophysical Research Letters* 47, e2020GL088322. <https://doi.org/10.1029/2020GL088322>
- Calmels, D., Gaillardet, J., Brenot, A., France-Lanord, C., 2007. Sustained sulfide oxidation by physical erosion processes in the Mackenzie River basin: Climatic perspectives. *Geology* 35, 1003–1006. <https://doi.org/10.1130/G24132A.1>
- Calmels, D., Gaillardet, J., François, L., 2014. Sensitivity of carbonate weathering to soil CO<sub>2</sub> production by biological activity along a temperate climate transect. *Chemical Geology* 390, 74–86. <https://doi.org/10.1016/j.chemgeo.2014.10.010>
- Carriere, A., Le Bouteiller, C., Tucker, G.E., Klotz, S., Naaim, M., 2020. Impact of vegetation on erosion: Insights from the calibration and test of a landscape evolution model in alpine badland catchments. *Earth Surface Processes and Landforms* 45, 1085–1099. <https://doi.org/10.1002/esp.4741>
- Caves Rugenstein, J.K., Ibarra, D.E., von Blanckenburg, F., 2019. Neogene cooling driven by land surface reactivity rather than increased weathering fluxes. *Nature* 571, 99–102. <https://doi.org/10.1038/s41586-019-1332-y>
- Cerling, T.E., Barnette, J.E., Chesson, L.A., Douglas-Hamilton, I., Gobush, K.S., Uno, K.T., Wasser, S.K., Xu, X., 2016. Radiocarbon dating of seized ivory confirms rapid decline in African elephant populations and provides insight into illegal trade. *Proceedings of the National Academy of Sciences* 113, 13330–13335. <https://doi.org/10.1073/pnas.1614938113>
- Chamberlin, T.C., 1899. An Attempt to Frame a Working Hypothesis of the Cause of Glacial Periods on an Atmospheric Basis. *The Journal of Geology* 7, 545–584. <https://doi.org/10.1086/608524>
- Chang, S., Berner, R.A., 1999. Coal weathering and the geochemical carbon cycle. *Geochimica et Cosmochimica Acta* 63, 3301–3310. [https://doi.org/10.1016/S0016-7037\(99\)00252-5](https://doi.org/10.1016/S0016-7037(99)00252-5)
- Chappell, P.R., 2016. *The Climate and Weather of the Gisborne District, New Zealand*, NIWA Science and Technology Series 70.
- Chorover, J., Kretzschmar, R., Garcia-Pichel, F., Sparks, D.L., 2007. Soil Biogeochemical Processes within the Critical Zone. *Elements* 3, 321–326. <https://doi.org/10.2113/gselements.3.5.321>
- Clark, K.E., Hilton, R.G., West, A.J., Robles Caceres, A., Gröcke, D.R., Marthews, T.R., Ferguson, R.I., Asner, G.P., New, M., Malhi, Y., 2017. Erosion of organic carbon from the Andes and its effects on ecosystem carbon dioxide balance. *Journal of Geophysical Research: Biogeosciences* 122, 449–469. <https://doi.org/10.1002/2016JG003615>

- Clayton, J.L., Swetland, P.J., 1978. Subaerial weathering of sedimentary organic matter. *Geochimica et Cosmochimica Acta* 42, 305–312. [https://doi.org/10.1016/0016-7037\(78\)90183-7](https://doi.org/10.1016/0016-7037(78)90183-7)
- Copard, Y., Amiotte-Suchet, P., Di-Giovanni, C., 2007. Storage and release of fossil organic carbon related to weathering of sedimentary rocks. *Earth and Planetary Science Letters* 258, 345–357. <https://doi.org/10.1016/j.epsl.2007.03.048>
- Copard, Y., Di-Giovanni, C., Martaud, T., Albéric, P., Olivier, J.-E., 2006. Using Rock-Eval 6 pyrolysis for tracking fossil organic carbon in modern environments: implications for the roles of erosion and weathering. *Earth Surface Processes and Landforms* 31, 135–153. <https://doi.org/10.1002/esp.1319>
- Cras, A., Marc, V., Travi, Y., 2007. Hydrological behaviour of sub-Mediterranean alpine headwater streams in a badlands environment. *Journal of Hydrology* 339, 130–144. <https://doi.org/10.1016/j.jhydrol.2007.03.004>
- Crawford, J.T., Hinckley, E.-L.S., Litaor, M.I., Brahney, J., Neff, J.C., 2019. Evidence for accelerated weathering and sulfate export in high alpine environments. *Environmental Research Letters* 14, 124092. <https://doi.org/10.1088/1748-9326/ab5d9c>
- Dalai, T.K., Singh, S.K., Trivedi, J.R., Krishnaswami, S., 2002. Dissolved rhenium in the Yamuna river system and the Ganga in the Himalaya: role of black shale weathering on the budgets of Re, Os, and U in rivers and CO<sub>2</sub> in the atmosphere. *Geochimica et Cosmochimica Acta* 66, 29–43. [https://doi.org/10.1016/S0016-7037\(01\)00747-5](https://doi.org/10.1016/S0016-7037(01)00747-5)
- Das, A., Chung, C.-H., You, C.-F., 2012. Disproportionately high rates of sulfide oxidation from mountainous river basins of Taiwan orogeny: Sulfur isotope evidence. *Geophysical Research Letters* 39, L12404. <https://doi.org/10.1029/2012GL051549>
- Dasgupta, R., Hirschmann, M.M., 2010. The deep carbon cycle and melting in Earth's interior. *Earth and Planetary Science Letters* 298, 1–13. <https://doi.org/10.1016/j.epsl.2010.06.039>
- Davidson, E.A., Trumbore, S.E., 1995. Gas diffusivity and production of CO<sub>2</sub> in deep soils of the eastern Amazon. *Tellus* 47B, 550–565. <https://doi.org/10.3402/tellusb.v47i5.16071>
- Derry, L.A., Chadwick, O.A., 2007. Contributions from Earth's Atmosphere to Soil. *Elements* 3, 333–338. <https://doi.org/10.2113/gselements.3.5.333>
- Draix-Bléone Observatory, 2015. Observatoire hydrosédimentaire de montagne Draix-Bléone [Data set]. Irstea. <https://doi.org/10.17180/obs.draix>
- Drever, J.I., 1994. The effect of land plants on weathering rates of silicate minerals. *Geochimica et Cosmochimica Acta* 58, 2325–2332. [https://doi.org/10.1016/0016-7037\(94\)90013-2](https://doi.org/10.1016/0016-7037(94)90013-2)
- Ebelmen, J.J., 1845. Sur les produits de la décomposition des espèces minérales de la famille des silicates. *Annales des Mines* 7, 3–66.

- Eglinton, T.I., 2015. Grand challenges in biogeoscience. *Frontiers in Earth Science* 3, 39. <https://doi.org/10.3389/feart.2015.00039>
- Ehrlich, H.L., Newman, D.K., Kappler, A., 2015. *Ehrlich's Geomicrobiology*, 6th ed. CRC Press, Boca Raton, USA. <https://doi.org/10.1201/b19121>
- Emberson, R., Galy, A., Hovius, N., 2018. Weathering of Reactive Mineral Phases in Landslides Acts as a Source of Carbon Dioxide in Mountain Belts. *Journal of Geophysical Research: Earth Surface* 123, 2695–2713. <https://doi.org/10.1029/2018JF004672>
- Erba, E., 2004. Calcareous nannofossils and Mesozoic oceanic anoxic events. *Marine Micropaleontology* 52, 85–106. <https://doi.org/10.1016/j.marmicro.2004.04.007>
- Erlanger, E.D., Caves Rugenstein, J.K., Bufe, A., Picotti, V., Willett, S.D., 2021. Controls on Physical and Chemical Denudation in a Mixed Carbonate-Siliciclastic Orogen. *Journal of Geophysical Research: Earth Surface* 126, e2021JF006064. <https://doi.org/10.1029/2021JF006064>
- Esteves, M., Descroix, L., Mathys, N., Marc Lapetite, J., 2005. Soil hydraulic properties in a marly gully catchment (Draix, France). *Catena* 63, 282–298. <https://doi.org/10.1016/j.catena.2005.06.006>
- Etiopie, G., Klusman, R.W., 2010. Microseepage in drylands: Flux and implications in the global atmospheric source/sink budget of methane. *Global and Planetary Change* 72, 265–274. <https://doi.org/10.1016/j.gloplacha.2010.01.002>
- Etiopie, G., Klusman, R.W., 2002. Geologic emissions of methane to the atmosphere. *Chemosphere* 49, 777–789. [https://doi.org/10.1016/S0045-6535\(02\)00380-6](https://doi.org/10.1016/S0045-6535(02)00380-6)
- Feng, G., Wu, L., Letey, J., 2002. Evaluating aeration criteria by simultaneous measurement of oxygen diffusion rate and soil-water regime. *Soil Science* 167, 495–503. <https://doi.org/10.1097/00010694-200208000-00001>
- Fischer, C., Gaupp, R., 2005. Change of black shale organic material surface area during oxidative weathering: Implications for rock-water surface evolution. *Geochimica et Cosmochimica Acta* 69, 1213–1224. <https://doi.org/10.1016/j.gca.2004.09.021>
- Fischer, R.A., Cottrell, E., Hauri, E., Lee, K.K.M., Le Voyer, M., 2020. The carbon content of Earth and its core. *Proceedings of the National Academy of Sciences* 117, 8743–8749. <https://doi.org/10.1073/pnas.1919930117>
- France-Lanord, C., Derry, L.A., 1997. Organic carbon burial forcing of the carbon cycle from Himalayan erosion. *Nature* 390, 65–67. <https://doi.org/10.1038/36324>
- Francis, D.A., Christie, A.B., Brown, L.J., 1991. Sheet QM 303, Raukumara: geological resource map of New Zealand, 1:250 000 [Map]. New Zealand Geological Survey Report M180.

- Franks, P.J., Royer, D.L., Beerling, D.J., Van de Water, P.K., Cantrill, D.J., Barbour, M.M., Berry, J.A., 2014. New constraints on atmospheric CO<sub>2</sub> concentration for the Phanerozoic. *Geophysical Research Letters* 41, 4685–4694. <https://doi.org/10.1002/2014GL060457>
- Gaillardet, J., Braud, I., Hankard, F., Anquetin, S., Bour, O., N. Dorfliger, J.R., et. al., 2018. OZCAR: The French Network of Critical Zone Observatories. *Vadose Zone Journal* 17, 180067. <https://doi.org/10.2136/vzj2018.04.0067>
- Gaillardet, J., Calmels, D., Romero-Mujalli, G., Zakharova, E., Hartmann, J., 2019. Global climate control on carbonate weathering intensity. *Chemical Geology* 527, 118762. <https://doi.org/10.1016/j.chemgeo.2018.05.009>
- Gaillardet, J., Dupré, B., Louvat, P., Allègre, C.J., 1999. Global silicate weathering and CO<sub>2</sub> consumption rates deduced from the chemistry of large rivers. *Chemical Geology* 159, 3–30. [https://doi.org/10.1016/S0009-2541\(99\)00031-5](https://doi.org/10.1016/S0009-2541(99)00031-5)
- Galvez, M.E., Fischer, W.W., Jaccard, S.L., Eglinton, T.I., 2020. Materials and pathways of the organic carbon cycle through time. *Nature Geoscience* 13, 535–546. <https://doi.org/10.1038/s41561-020-0563-8>
- Galy, A., France-Lanord, C., 1999. Weathering processes in the Ganges–Brahmaputra basin and the riverine alkalinity budget. *Chemical Geology* 159, 31–60. [https://doi.org/10.1016/S0009-2541\(99\)00033-9](https://doi.org/10.1016/S0009-2541(99)00033-9)
- Galy, V., Beysac, O., France-Lanord, C., Eglinton, T., 2008. Recycling of Graphite During Himalayan Erosion: A Geological Stabilization of Carbon in the Crust. *Science* 322, 943–945. <https://doi.org/10.1126/science.1161408>
- Galy, V., Peucker-Ehrenbrink, B., Eglinton, T., 2015. Global carbon export from the terrestrial biosphere controlled by erosion. *Nature* 521, 204–207. <https://doi.org/10.1038/nature14400>
- Garel, E., Marc, V., Ruy, S., Cognard-Plancq, A.-L., Klotz, S., Emblanch, C., Simler, R., 2012. Large scale rainfall simulation to investigate infiltration processes in a small landslide under dry initial conditions: the Draix hillslope experiment. *Hydrological Processes* 26, 2171–2186. <https://doi.org/10.1002/hyp.9273>
- Garnett, M.H., Murray, C., 2013. Processing of CO<sub>2</sub> Samples Collected Using Zeolite Molecular Sieve for <sup>14</sup>C Analysis at the NERC Radiocarbon Facility (East Kilbride, UK). *Radiocarbon* 55, 410–415. <https://doi.org/10.1017/S0033822200057532>
- Garnett, M.H., Newton, J.-A., Ascough, P.L., 2019. Advances in the Radiocarbon Analysis of Carbon dioxide at the NERC Radiocarbon Facility (East Kilbride) using Molecular sieve Cartridges. *Radiocarbon* 61, 1855–1865. <https://doi.org/10.1017/RDC.2019.86>

- Giggenbach, W.F., Sano, Y., Wakita, H., 1993. Isotopic composition of helium, and CO<sub>2</sub> and CH<sub>4</sub> contents in gases produced along the New Zealand part of a convergent plate boundary. *Geochimica et Cosmochimica Acta* 57, 3427–3455. [https://doi.org/10.1016/0016-7037\(93\)90549-C](https://doi.org/10.1016/0016-7037(93)90549-C)
- Giggenbach, W.F., Stewart, M.K., Sano, Y., Goguel, R.L., Lyon, G.L., 1995. Isotopic and chemical composition of waters and gases from the East Coast Accretionary Prism, New Zealand. *International Atomic Energy Agency Conference Proceedings* 788, 209–231.
- Gomez, B., Brackley, H.L., Hicks, D.M., Neff, H., Rogers, K.M., 2004. Organic carbon in floodplain alluvium: Signature of historic variations in erosion processes associated with deforestation, Waipaoa River basin, New Zealand. *Journal of Geophysical Research* 109, F04011. <https://doi.org/10.1029/2004JF000154>
- Graven, H., Fischer, M.L., Lueker, T., Jeong, S., Guilderson, T.P., Keeling, R.F., Bambha, R., Brophy, K., Callahan, W., Cui, X., Frankenberg, C., Gurney, K.R., LaFranchi, B.W., Lehman, S.J., Michelsen, H., Miller, J.B., Newman, S., Paplawsky, W., Parazoo, N.C., Sloop, C., Walker, S.J., 2018. Assessing fossil fuel CO<sub>2</sub> emissions in California using atmospheric observations and models. *Environmental Research Letters* 13, 065007. <https://doi.org/10.1088/1748-9326/aabd43>
- Graven, H.D., Gruber, N., 2011. Continental-scale enrichment of atmospheric <sup>14</sup>CO<sub>2</sub> from the nuclear power industry: potential impact on the estimation of fossil fuel-derived CO<sub>2</sub>. *Atmospheric Chemistry and Physics* 11, 12339–12349. <https://doi.org/10.5194/acp-11-12339-2011>
- Graz, Y., Di-Giovanni, C., Copard, Y., Elie, M., Faure, P., Laggoun Defarge, F., Lévêque, J., Michels, R., Olivier, J.E., 2011. Occurrence of fossil organic matter in modern environments: Optical, geochemical and isotopic evidence. *Applied Geochemistry* 26, 1302–1314. <https://doi.org/10.1016/j.apgeochem.2011.05.004>
- Graz, Y., Di-Giovanni, C., Copard, Y., Mathys, N., Cras, A., Marc, V., 2012. Annual fossil organic carbon delivery due to mechanical and chemical weathering of marly badlands areas. *Earth Surface Processes and Landforms* 37, 1263–1271. <https://doi.org/10.1002/esp.3232>
- Gröcke, D.R., Price, G.D., Ruffell, A.H., Mutterlose, J., Baraboshkin, E., 2003. Isotopic evidence for Late Jurassic–Early Cretaceous climate change. *Palaeogeography, Palaeoclimatology, Palaeoecology* 202, 97–118. [https://doi.org/10.1016/S0031-0182\(03\)00631-X](https://doi.org/10.1016/S0031-0182(03)00631-X)
- Grosjean, E., Adam, P., Connan, J., Albrecht, P., 2004. Effects of weathering on nickel and vanadyl porphyrins of a Lower Toarcian shale of the Paris basin. *Geochimica et Cosmochimica Acta* 68, 789–804. [https://doi.org/10.1016/S0016-7037\(03\)00496-4](https://doi.org/10.1016/S0016-7037(03)00496-4)

- Gu, X., Heaney, P.J., Reis, F.D.A.A., Brantley, S.L., 2020a. Deep abiotic weathering of pyrite. *Science* 370, eabb8092. <https://doi.org/10.1126/science.abb8092>
- Gu, X., Rempe, D.M., Dietrich, W.E., West, A.J., Lin, T.-C., Jin, L., Brantley, S.L., 2020b. Chemical reactions, porosity, and microfracturing in shale during weathering: The effect of erosion rate. *Geochimica et Cosmochimica Acta* 269, 63–100. <https://doi.org/10.1016/j.gca.2019.09.044>
- Guo, L., Lin, H., 2016. Critical Zone Research and Observatories: Current Status and Future Perspectives. *Vadose Zone Journal* 15, vzj2016.06.0050. <https://doi.org/10.2136/vzj2016.06.0050>
- Halevy, I., Peters, S.E., Fischer, W.W., 2012. Sulfate Burial Constraints on the Phanerozoic Sulfur Cycle. *Science* 337, 331–334. <https://doi.org/10.1126/science.1220224>
- Hardie, S.M.L., Garnett, M.H., Fallick, A.E., Rowland, A.P., Ostle, N.J., 2005. Carbon Dioxide Capture Using a Zeolite Molecular Sieve Sampling System for Isotopic Studies (<sup>13</sup>C and <sup>14</sup>C) of Respiration. *Radiocarbon* 47, 441–451. <https://doi.org/10.1017/S0033822200035220>
- Hartmann, J., Moosdorf, N., 2012. The new global lithological map database GLiM: A representation of rock properties at the Earth surface. *Geochemistry, Geophysics, Geosystems* 13, Q12004. <https://doi.org/10.1029/2012GC004370>
- Hasenmueller, E.A., Gu, X., Weitzman, J.N., Adams, T.S., Stinchcomb, G.E., Eissenstat, D.M., Drohan, P.J., Brantley, S.L., Kaye, J.P., 2017. Weathering of rock to regolith: The activity of deep roots in bedrock fractures. *Geoderma* 300, 11–31. <https://doi.org/10.1016/j.geoderma.2017.03.020>
- Hasenmueller, E.A., Jin, L., Stinchcomb, G.E., Lin, H., Brantley, S.L., Kaye, J.P., 2015. Topographic controls on the depth distribution of soil CO<sub>2</sub> in a small temperate watershed. *Applied Geochemistry* 63, 58–69. <https://doi.org/10.1016/j.apgeochem.2015.07.005>
- Hashimoto, S., Komatsu, H., 2006. Relationships between soil CO<sub>2</sub> concentration and CO<sub>2</sub> production, temperature, water content, and gas diffusivity: implications for field studies through sensitivity analyses. *Journal of Forest Research* 11, 41–50. <https://doi.org/10.1007/s10310-005-0185-4>
- Hayes, J.M., Waldbauer, J.R., 2006. The carbon cycle and associated redox processes through time. *Philosophical Transactions of the Royal Society* 361B, 931–950. <https://doi.org/10.1098/rstb.2006.1840>
- Hedges, J.I., Keil, R.G., 1995. Sedimentary organic matter preservation: an assessment and speculative synthesis. *Marine Chemistry* 49, 81–115. [https://doi.org/10.1016/0304-4203\(95\)00008-F](https://doi.org/10.1016/0304-4203(95)00008-F)

- Heimsath, A.M., DiBiase, R.A., Whipple, K.X., 2012. Soil production limits and the transition to bedrock-dominated landscapes. *Nature Geoscience* 5, 210–214. <https://doi.org/10.1038/ngeo1380>
- Hemingway, J.D., Hilton, R.G., Hovius, N., Eglinton, T.I., Haghypour, N., Wacker, L., Chen, M.-C., Galy, V.V., 2018. Microbial oxidation of lithospheric organic carbon in rapidly eroding tropical mountain soils. *Science* 360, 209–212. <https://doi.org/10.1126/science.aao6463>
- Hemingway, J.D., Rothman, D.H., Grant, K.E., Rosengard, S.Z., Eglinton, T.I., Derry, L.A., Galy, V.V., 2019. Mineral protection regulates long-term global preservation of natural organic carbon. *Nature* 570, 228–231. <https://doi.org/10.1038/s41586-019-1280-6>
- Hemingway, J.D., Rothman, D.H., Rosengard, S.Z., Galy, V.V., 2017. Technical note: An inverse method to relate organic carbon reactivity to isotope composition from serial oxidation. *Biogeosciences* 14, 5099–5114. <https://doi.org/10.5194/bg-14-5099-2017>
- Hicks, D.M., Gomez, B., Trustrum, N.A., 2004. Event Suspended Sediment Characteristics and the Generation of Hyperpycnal Plumes at River Mouths: East Coast Continental Margin, North Island, New Zealand. *The Journal of Geology* 112, 471–485. <https://doi.org/10.1086/421075>
- Hicks, D.M., Gomez, B., Trustrum, N.A., 2000. Erosion thresholds and suspended sediment yields, Waipaoa River Basin, New Zealand. *Water Resources Research* 36, 1129–1142. <https://doi.org/10.1029/1999WR900340>
- Hicks Pries, C., Angert, A., Castanha, C., Hilman, B., Torn, M.S., 2020. Using respiration quotients to track changing sources of soil respiration seasonally and with experimental warming. *Biogeosciences* 17, 3045–3055. <https://doi.org/10.5194/bg-17-3045-2020>
- Hilton, R.G., 2017. Climate regulates the erosional carbon export from the terrestrial biosphere. *Geomorphology* 277, 118–132. <https://doi.org/10.1016/j.geomorph.2016.03.028>
- Hilton, R.G., Gaillardet, J., Calmels, D., Birck, J.-L., 2014. Geological respiration of a mountain belt revealed by the trace element rhenium. *Earth and Planetary Science Letters* 403, 27–36. <https://doi.org/10.1016/j.epsl.2014.06.021>
- Hilton, R.G., Galy, A., Hovius, N., Horng, M.-J., Chen, H., 2011. Efficient transport of fossil organic carbon to the ocean by steep mountain rivers: An orogenic carbon sequestration mechanism. *Geology* 39, 71–74. <https://doi.org/10.1130/G31352.1>
- Hilton, R.G., Galy, A., Hovius, N., Horng, M.-J., Chen, H., 2010. The isotopic composition of particulate organic carbon in mountain rivers of Taiwan. *Geochimica et Cosmochimica Acta* 74, 3164–3181. <https://doi.org/10.1016/j.gca.2010.03.004>
- Hilton, R.G., Turowski, J.M., Winnick, M., Dellinger, M., Schleppe, P., Williams, K.H., Lawrence, C.R., Maher, K., West, M., Hayton, A., 2021. Concentration-Discharge Relationships of

- Dissolved Rhenium in Alpine Catchments Reveal Its Use as a Tracer of Oxidative Weathering. *Water Resources Research* 57, e2021WR029844. <https://doi.org/10.1029/2021WR029844>
- Hilton, R.G., West, A.J., 2020. Mountains, erosion and the carbon cycle. *Nature Reviews Earth & Environment* 1, 284–299. <https://doi.org/10.1038/s43017-020-0058-6>
- Holbrook, W.S., Marcon, V., Bacon, A.R., Brantley, S.L., Carr, B.J., Flinchum, B.A., Richter, D.D., Riebe, C.S., 2019. Links between physical and chemical weathering inferred from a 65-m-deep borehole through Earth’s critical zone. *Scientific Reports* 9, 4495. <https://doi.org/10.1038/s41598-019-40819-9>
- Holland, H.D., 1978. *The chemistry of the atmosphere and oceans*. Wiley, New York, USA.
- Horan, K., Hilton, R.G., Dellinger, M., Tipper, E., Galy, V., Calmels, D., Selby, D., Gaillardet, J., Ottley, C.J., Parsons, D.R., Burton, K.W., 2019. Carbon dioxide emissions by rock organic carbon oxidation and the net geochemical carbon budget of the Mackenzie River Basin. *American Journal of Science* 319, 473–499. <https://doi.org/10.2475/06.2019.02>
- Horan, K., Hilton, R.G., Selby, D., Ottley, C.J., Gröcke, D.R., Hicks, M., Burton, K.W., 2017. Mountain glaciation drives rapid oxidation of rock-bound organic carbon. *Science Advances* 3, e1701107. <https://doi.org/10.1126/sciadv.1701107>
- Hua, Q., Barbetti, M., Rakowski, A.Z., 2013. Atmospheric Radiocarbon for the Period 1950–2010. *Radiocarbon* 55, 2059–2072. [https://doi.org/10.2458/azu\\_js\\_rc.v55i2.16177](https://doi.org/10.2458/azu_js_rc.v55i2.16177)
- Husson, J.M., Peters, S.E., 2017. Atmospheric oxygenation driven by unsteady growth of the continental sedimentary reservoir. *Earth and Planetary Science Letters* 460, 68–75. <https://doi.org/10.1016/j.epsl.2016.12.012>
- IPCC, 2021. *Climate Change 2021: The Physical Science Basis. Contribution of Working Group I to the Sixth Assessment Report of the Intergovernmental Panel on Climate Change*. Cambridge University Press, Cambridge, UK. In press.
- Isson, T.T., Planavsky, N.J., Coogan, L.A., Stewart, E.M., Ague, J.J., Bolton, E.W., Zhang, S., McKenzie, N.R., Kump, L.R., 2020. Evolution of the Global Carbon Cycle and Climate Regulation on Earth. *Global Biogeochemical Cycles* 34, e2018GB006061. <https://doi.org/10.1029/2018GB006061>
- Jaffe, L.A., Peucker-Ehrenbrink, B., Petsch, S.T., 2002. Mobility of rhenium, platinum group elements and organic carbon during black shale weathering. *Earth and Planetary Science Letters* 198, 339–353. [https://doi.org/10.1016/S0012-821X\(02\)00526-5](https://doi.org/10.1016/S0012-821X(02)00526-5)
- Janjou, D., 2004. Descriptif des cartes géologiques à 1/50 000 format “vecteurs” [Map]. Bureau de recherches géologiques et minières, France RP-53571.

- Jin, L., Ogrinc, N., Yesavage, T., Hasenmueller, E.A., Ma, L., Sullivan, P.L., Kaye, J., Duffy, C., Brantley, S.L., 2014. The CO<sub>2</sub> consumption potential during gray shale weathering: Insights from the evolution of carbon isotopes in the Susquehanna Shale Hills critical zone observatory. *Geochimica et Cosmochimica Acta* 142, 260–280. <https://doi.org/10.1016/j.gca.2014.07.006>
- Kalks, F., Noren, G., Mueller, C.W., Helfrich, M., Rethemeyer, J., Don, A., 2021. Geogenic organic carbon in terrestrial sediments and its contribution to total soil carbon. *SOIL* 347–362. <https://doi.org/10.5194/soil-7-347-2021>
- Kelemen, P.B., Matter, J., Streit, E.E., Rudge, J.F., Curry, W.B., Blusztajn, J., 2011. Rates and Mechanisms of Mineral Carbonation in Peridotite: Natural Processes and Recipes for Enhanced, in situ CO<sub>2</sub> Capture and Storage. *Annual Review of Earth and Planetary Sciences* 39, 545–576. <https://doi.org/10.1146/annurev-earth-092010-152509>
- Keller, C.K., Bacon, D.H., 1998. Soil respiration and georespiration distinguished by transport analyses of vadose CO<sub>2</sub>, <sup>13</sup>CO<sub>2</sub>, and <sup>14</sup>CO<sub>2</sub>. *Global Biogeochemical Cycles* 12, 361–372. <https://doi.org/10.1029/98GB00742>
- Kemeny, P.C., Lopez, G.I., Dalleska, N.F., Torres, M., Burke, A., Bhatt, M.P., West, A.J., Hartmann, J., Adkins, J.F., 2021. Sulfate sulfur isotopes and major ion chemistry reveal that pyrite oxidation counteracts CO<sub>2</sub> drawdown from silicate weathering in the Langtang-Trisuli-Narayani River system, Nepal Himalaya. *Geochimica et Cosmochimica Acta* 294, 43–69. <https://doi.org/10.1016/j.gca.2020.11.009>
- Kenny, J.A., 1984. Petrography of Cretaceous and Tertiary sedimentary rocks of the Ihungia catchment, Raukumara Peninsula, North Island, New Zealand. *New Zealand Journal of Geology and Geophysics* 27, 291–298.
- Killops, S., Killops, V., 2005. *Introduction to Organic Geochemistry*, 2nd ed. Blackwell Science Publishing, Malden, USA.
- Kleber, M., Bourg, I.C., Coward, E.K., Hansel, C.M., Myneni, S.C.B., Nunan, N., 2021. Dynamic interactions at the mineral–organic matter interface. *Nature Reviews Earth & Environment* 2, 402–421. <https://doi.org/10.1038/s43017-021-00162-y>
- Knight, R., Vrbanac, A., Taylor, B.C., Aksenov, A., Callewaert, C., Debelius, J., Gonzalez, A., Kosciolk, T., McCall, L.-I., McDonald, D., Melnik, A. v., Morton, J.T., Navas, J., Quinn, R.A., Sanders, J.G., Swafford, A.D., Thompson, L.R., Tripathi, A., Xu, Z.Z., Zaneveld, J.R., Zhu, Q., Caporaso, J.G., Dorrestein, P.C., 2018. Best practices for analysing microbiomes. *Nature Reviews Microbiology* 16, 410–422. <https://doi.org/10.1038/s41579-018-0029-9>

- Krause, A.J., Mills, B.J.W., Zhang, S., Planavsky, N.J., Lenton, T.M., Poulton, S.W., 2018. Stepwise oxygenation of the Paleozoic atmosphere. *Nature Communications* 9, 4081. <https://doi.org/10.1038/s41467-018-06383-y>
- Kuzyakov, Y., 2010. Priming effects: Interactions between living and dead organic matter. *Soil Biology and Biochemistry* 42, 1363–1371. <https://doi.org/10.1016/j.soilbio.2010.04.003>
- Lacis, A.A., Schmidt, G.A., Rind, D., Ruedy, R.A., 2010. Atmospheric CO<sub>2</sub>: Principal Control Knob Governing Earth's Temperature. *Science* 330, 356–359. <https://doi.org/10.1126/science.1190653>
- Larsen, I.J., Montgomery, D.R., Greenberg, H.M., 2014. The contribution of mountains to global denudation. *Geology* 42, 527–530. <https://doi.org/10.1130/G35136.1>
- Le Bouteiller, C., Chambon, G., Naaim-Bouvet, F., Mathys, N., 2021. Hydraulics and rheology of natural hyperconcentrated flows from Draix-Bleone observatory, French Alps. *Journal of Hydraulic Research* 59, 181–195. <https://doi.org/10.1080/00221686.2020.1744750>
- Lebedeva, M.I., Brantley, S.L., 2020. Relating the depth of the water table to the depth of weathering. *Earth Surface Processes and Landforms* 45, 2167–2178. <https://doi.org/10.1002/esp.4873>
- Lefèvre, R., Barré, P., Moyano, F.E., Christensen, B.T., Bardoux, G., Eglin, T., Girardin, C., Houot, S., Kätterer, T., van Oort, F., Chenu, C., 2014. Higher temperature sensitivity for stable than for labile soil organic carbon - Evidence from incubations of long-term bare fallow soils. *Global Change Biology* 20, 633–640. <https://doi.org/10.1111/gcb.12402>
- Leifeld, J., von Lützow, M., 2014. Chemical and microbial activation energies of soil organic matter decomposition. *Biology and Fertility of Soils* 50, 147–153. <https://doi.org/10.1007/s00374-013-0822-6>
- Leithold, E.L., Blair, N.E., Perkey, D.W., 2006. Geomorphologic controls on the age of particulate organic carbon from small mountainous and upland rivers. *Global Biogeochemical Cycles* 20, GB3022. <https://doi.org/10.1029/2005GB002677>
- Leithold, E.L., Blair, N.E., Wegmann, K.W., 2016. Source-to-sink sedimentary systems and global carbon burial: A river runs through it. *Earth-Science Reviews* 153, 30–42. <https://doi.org/10.1016/j.earscirev.2015.10.011>
- Levin, I., Kromer, B., Hammer, S., 2013. Atmospheric  $\Delta^{14}\text{CO}_2$  trend in Western European background air from 2000 to 2012. *Tellus* 65B, 20092. <https://doi.org/10.3402/tellusb.v65i0.20092>
- Li, S.-L., Calmels, D., Han, G., Gaillardet, J., Liu, C.-Q., 2008. Sulfuric acid as an agent of carbonate weathering constrained by  $\delta^{13}\text{CDIC}$ : Examples from Southwest China. *Earth and Planetary Science Letters* 270, 189–199. <https://doi.org/10.1016/j.epsl.2008.02.039>

- Liang, L.L., Riveros-Iregui, D.A., Emanuel, R.E., McGlynn, B.L., 2014. A simple framework to estimate distributed soil temperature from discrete air temperature measurements in data-scarce regions. *Journal of Geophysical Research: Atmospheres* 119, 407–417. <https://doi.org/10.1002/2013JD020597>
- Litchfield, N., Berryman, K., 2006. Relations between postglacial fluvial incision rates and uplift rates in the North Island, New Zealand. *Journal of Geophysical Research* 111, F02007. <https://doi.org/10.1029/2005JF000374>
- Lofi, J., Pezard, P., Loggia, D., Garel, E., Gautier, S., Merry, C., Bondabou, K., 2012. Geological discontinuities, main flow path and chemical alteration in a marly hill prone to slope instability: Assessment from petrophysical measurements and borehole image analysis. *Hydrological Processes* 26, 2071–2084. <https://doi.org/10.1002/hyp.7997>
- Longbottom, T.L., Hockaday, W.C., 2019. Molecular and isotopic composition of modern soils derived from kerogen-rich bedrock and implications for the global C cycle. *Biogeochemistry* 143, 239–255. <https://doi.org/10.1007/s10533-019-00559-4>
- Lowry, D.C., Francis, D.A., Bennett, D.J., 1998. Biogenic Gas: A New Play in the East Coast Basin of New Zealand. *New Zealand Petroleum Conference* 207–221.
- Lu, N., Godt, J., 2013. *Hillslope Hydrology and Stability*. Cambridge University Press, Cambridge, UK. <https://doi.org/10.1017/CBO9781139108164>
- Lyon, G.L., Giggenbach, W.F., 1992. The stable isotope composition of some East Coast natural gases. *New Zealand Petroleum Conference* 310–319.
- Lyons, W.B., Carey, A.E., Hicks, D.M., Nezat, C.A., 2005. Chemical weathering in high-sediment-yielding watersheds, New Zealand. *Journal of Geophysical Research* 110, F01008. <https://doi.org/10.1029/2003JF000088>
- Maffre, P., Swanson-Hysell, N.L., Godd eris, Y., 2021. Limited Carbon Cycle Response to Increased Sulfide Weathering Due to Oxygen Feedback. *Geophysical Research Letters* 48, e2021GL094589. <https://doi.org/10.1029/2021GL094589>
- Maher, K., Chamberlain, C.P., 2014. Hydrologic Regulation of Chemical Weathering and the Geologic Carbon Cycle. *Science* 343, 1502–1504. <https://doi.org/10.1126/science.1250770>
- Maier, M., Schack-Kirchner, H., 2014. Using the gradient method to determine soil gas flux: A review. *Agricultural and Forest Meteorology* 192–193, 78–95. <https://doi.org/10.1016/j.agrformet.2014.03.006>
- Mallet, F., Carri ere, S.D., Chalikakis, K., Marc, V., 2018. Assessing soil water content spatio-temporal variability at the hillslope scale in a headwater catchment using a multi variable interpolation model based on EMI surveys (Draix, South Alps, France). *Environmental Earth Sciences* 77, 507. <https://doi.org/10.1007/s12665-018-7687-9>

- Mallet, F., Marc, V., Douvinet, J., Rossello, P., Joly, D., Ruy, S., 2020. Assessing soil water content variation in a small mountainous catchment over different time scales and land covers using geographical variables. *Journal of Hydrology* 591, 125593. <https://doi.org/10.1016/j.jhydrol.2020.125593>
- Maquaire, O., Ritzenthaler, A., Fabre, D., Ambroise, B., Thiery, Y., Truchet, E., Malet, J.-P., Monnet, J., 2002. Caractérisation des profils de formations superficielles par pénétrométrie dynamique à énergie variable : application aux marnes noires de Draix (Alpes-de-Haute-Provence, France). *Comptes Rendus Geoscience* 334, 835–841. [https://doi.org/10.1016/S1631-0713\(02\)01788-1](https://doi.org/10.1016/S1631-0713(02)01788-1)
- Marden, M., Arnold, G., Seymour, A., Hambling, R., 2012. History and distribution of steepland gullies in response to land use change, East Coast Region, North Island, New Zealand. *Geomorphology* 153–154, 81–90. <https://doi.org/10.1016/j.geomorph.2012.02.011>
- Märki, L., Lupker, M., France-Lanord, C., Lavé, J., Gallen, S., Gajurel, A.P., Haghipour, N., Leuenberger-West, F., Eglinton, T., 2021. An unshakable carbon budget for the Himalaya. *Nature Geoscience* 14, 745–750. <https://doi.org/10.1038/s41561-021-00815-z>
- Marynowski, L., Kurkiewicz, S., Rakociński, M., Simoneit, B.R.T., 2011a. Effects of weathering on organic matter: I. Changes in molecular composition of extractable organic compounds caused by paleoweathering of a Lower Carboniferous (Tournaisian) marine black shale. *Chemical Geology* 285, 144–156. <https://doi.org/10.1016/j.chemgeo.2011.04.001>
- Marynowski, L., Szełęg, E., Jędrysek, M.O., Simoneit, B.R.T., 2011b. Effects of weathering on organic matter. Part II: Fossil wood weathering and implications for organic geochemical and petrographic studies. *Organic Geochemistry* 42, 1076–1088. <https://doi.org/10.1016/j.orggeochem.2011.06.017>
- Mason, D.C., Garcia-Pintado, J., Cloke, H.L., Dance, S.L., 2016. Evidence of a topographic signal in surface soil moisture derived from ENVISAT ASAR wide swath data. *International Journal of Applied Earth Observation and Geoinformation* 45, 178–186. <https://doi.org/10.1016/j.jag.2015.02.004>
- Massman, W.J., 1998. A review of the molecular diffusivities of H<sub>2</sub>O, CO<sub>2</sub>, CH<sub>4</sub>, CO, O<sub>3</sub>, SO<sub>2</sub>, NH<sub>3</sub>, N<sub>2</sub>O, NO, and NO<sub>2</sub> in air, O<sub>2</sub> and N<sub>2</sub> near STP. *Atmospheric Environment* 32, 1111–1127. [https://doi.org/10.1016/S1352-2310\(97\)00391-9](https://doi.org/10.1016/S1352-2310(97)00391-9)
- Mathys, N., Brochot, S., Meunier, M., Richard, D., 2003. Erosion quantification in the small marly experimental catchments of Draix (Alpes de Haute Provence, France). Calibration of the ETC rainfall–runoff–erosion model. *Catena* 50, 527–548. [https://doi.org/10.1016/S0341-8162\(02\)00122-4](https://doi.org/10.1016/S0341-8162(02)00122-4)

- Mathys, N., Klotz, S., 2008. DRAIX: A field laboratory for research on hydrology and erosion in mountain areas, in: Locat, D.D., Perret, D., Turmel, D. (Eds.), Proceedings of the 4th Canadian Conference on Geohazards: From Causes to Management. Presse de l'Université Laval, Québec, Canada.
- Matlakowska, R., Sklodowska, A., 2011. Biodegradation of Kupferschiefer black shale organic matter (Fore-Sudetic Monocline, Poland) by indigenous microorganisms. *Chemosphere* 83, 1255–1261. <https://doi.org/10.1016/j.chemosphere.2011.03.003>
- Mazengarb, C., Speden, I.G., 2000. Geological map of the Raukumara area [Map], 6th ed. Institute of Geological & Nuclear Sciences, Lower Hutt, New Zealand.
- Milliman, J.D., Syvitski, J.P.M., 1992. Geomorphic/Tectonic Control of Sediment Discharge to the Ocean: The Importance of Small Mountainous Rivers. *The Journal of Geology* 100, 525–544. <https://doi.org/10.1086/629606>
- Millington, R.J., 1959. Gas Diffusion in Porous Media. *Science* 130, 100–102. <https://doi.org/10.1126/science.130.3367.100-a>
- Mills, B.J.W., Donnadieu, Y., Goddérís, Y., 2021. Spatial continuous integration of Phanerozoic global biogeochemistry and climate. *Gondwana Research* 100, 73–86. <https://doi.org/10.1016/j.gr.2021.02.011>
- Milodowski, D.T., Mudd, S.M., Mitchard, E.T.A., 2015. Erosion rates as a potential bottom-up control of forest structural characteristics in the Sierra Nevada Mountains. *Ecology* 96, 31–38. <https://doi.org/10.1890/14-0649.1>
- Mook, W.G., Bommerson, J.C., Staverman, W.H., 1974. Carbon isotope fractionation between dissolved bicarbonate and gaseous carbon dioxide. *Earth and Planetary Science Letters* 22, 169–176. [https://doi.org/10.1016/0012-821X\(74\)90078-8](https://doi.org/10.1016/0012-821X(74)90078-8)
- Moon, S., Chamberlain, C.P., Hilley, G.E., 2014. New estimates of silicate weathering rates and their uncertainties in global rivers. *Geochimica et Cosmochimica Acta* 134, 257–274. <https://doi.org/10.1016/j.gca.2014.02.033>
- Nannipieri, P., Ascher, J., Ceccherini, M.T., Landi, L., Pietramellara, G., Renella, G., 2017. Microbial diversity and soil functions. *European Journal of Soil Science* 54, 655–670. [https://doi.org/10.1111/ejss.4\\_12398](https://doi.org/10.1111/ejss.4_12398)
- Nelson, C.S., Smith, A.M., 1996. Stable oxygen and carbon isotope compositional fields for skeletal and diagenetic components in New Zealand Cenozoic nontropical carbonate sediments and limestones: A synthesis and review. *New Zealand Journal of Geology and Geophysics* 39, 93–107. <https://doi.org/10.1080/00288306.1996.9514697>

- Neu, V., Ward, N.D., Krusche, A.V., Neill, C., 2016. Dissolved Organic and Inorganic Carbon Flow Paths in an Amazonian Transitional Forest. *Front Mar Sci* 3, 114. <https://doi.org/10.3389/fmars.2016.00114>
- Nicholson, R.V., Gillham, R.W., Reardon, E.J., 1988. Pyrite oxidation in carbonate-buffered solution: 1. Experimental kinetics. *Geochimica et Cosmochimica Acta* 52, 1077–1085. [https://doi.org/10.1016/0016-7037\(88\)90262-1](https://doi.org/10.1016/0016-7037(88)90262-1)
- Novitsky, C.G., Holbrook, W.S., Carr, B.J., Pasquet, S., Okaya, D., Flinchum, B.A., 2018. Mapping Inherited Fractures in the Critical Zone Using Seismic Anisotropy From Circular Surveys. *Geophysical Research Letters* 45, 3126–3135. <https://doi.org/10.1002/2017GL075976>
- Oertel, C., Matschullat, J., Zurba, K., Zimmermann, F., Erasmi, S., 2016. Greenhouse gas emissions from soils — A review. *Geochemistry* 76, 327–352. <https://doi.org/10.1016/j.chemer.2016.04.002>
- Ogrič, M., 2021. Chemical weathering of sedimentary rocks as a source of carbon dioxide to the atmosphere. Doctoral thesis, Durham University. Durham, UK.
- Oostwoud Wijdenes, D.J., Ergenzinger, P., 1998. Erosion and sediment transport on steep marly hillslopes, Draix, Haute-Provence, France: an experimental field study. *Catena* 33, 179–200. [https://doi.org/10.1016/S0341-8162\(98\)00076-9](https://doi.org/10.1016/S0341-8162(98)00076-9)
- Pagani, M., Zachos, J.C., Freeman, K.H., Tipple, B., Bohaty, S., 2005. Marked Decline in Atmospheric Carbon Dioxide Concentrations During the Paleogene. *Science* 309, 600–603. <https://doi.org/10.1126/science.1110063>
- Parkner, T., Page, M.J., Marutani, T., Trustrum, N.A., 2006. Development and controlling factors of gullies and gully complexes, East Coast, New Zealand. *Earth Surface Processes and Landforms* 31, 187–199. <https://doi.org/10.1002/esp.1321>
- Pearson, M.J., Nelson, C.S., 2005. Organic geochemistry and stable isotope composition of New Zealand carbonate concretions and calcite fracture fills. *New Zealand Journal of Geology and Geophysics* 48, 395–414. <https://doi.org/10.1080/00288306.2005.9515122>
- Peng, S., Hu, Q., Hamamoto, S., 2012. Diffusivity of rocks: Gas diffusion measurements and correlation to porosity and pore size distribution. *Water Resources Research* 48, W02507. <https://doi.org/10.1029/2011WR011098>
- Penman, H.L., 1940. Gas and vapour movements in the soil: I. The diffusion of vapours through porous solids. *The Journal of Agricultural Science* 30, 437–462. <https://doi.org/10.1017/S0021859600048164>
- Percak-Dennett, E., He, S., Converse, B., Konishi, H., Xu, H., Corcoran, A., Noguera, D., Chan, C., Bhattacharyya, A., Borch, T., Boyd, E., Roden, E.E., 2017. Microbial acceleration of aerobic

- pyrite oxidation at circumneutral pH. *Geobiology* 15, 690–703.  
<https://doi.org/10.1111/gbi.12241>
- Petsch, S.T., 2014. Weathering of Organic Carbon, in: *Treatise on Geochemistry*. Elsevier, Amsterdam, Netherlands, pp. 217–238. <https://doi.org/10.1016/B978-0-08-095975-7.01013-5>
- Petsch, S.T., Berner, R.A., Eglinton, T.I., 2000. A field study of the chemical weathering of ancient sedimentary organic matter. *Organic Geochemistry* 31, 475–487.  
[https://doi.org/10.1016/S0146-6380\(00\)00014-0](https://doi.org/10.1016/S0146-6380(00)00014-0)
- Petsch, S.T., Edwards, K.J., Eglinton, T.I., 2003. Abundance, distribution and  $\delta^{13}\text{C}$  analysis of microbial phospholipid-derived fatty acids in a black shale weathering profile. *Organic Geochemistry* 34, 731–743. [https://doi.org/10.1016/S0146-6380\(03\)00040-8](https://doi.org/10.1016/S0146-6380(03)00040-8)
- Petsch, S.T., Eglinton, T.I., Edwards, K.J., 2001.  $^{14}\text{C}$ -Dead Living Biomass: Evidence for Microbial Assimilation of Ancient Organic Carbon During Shale Weathering. *Science* 292, 1127–1131.  
<https://doi.org/10.1126/science.1058332>
- Pirk, N., Mastepanov, M., Parmentier, F.-J.W., Lund, M., Crill, P., Christensen, T.R., 2016. Calculations of automatic chamber flux measurements of methane and carbon dioxide using short time series of concentrations. *Biogeosciences* 13, 903–912.  
<https://doi.org/10.5194/bg-13-903-2016>
- Plank, T., Manning, C.E., 2019. Subducting carbon. *Nature* 574, 343–352.  
<https://doi.org/10.1038/s41586-019-1643-z>
- Rae, J.W.B., Zhang, Y.G., Liu, X., Foster, G.L., Stoll, H.M., Whiteford, R.D.M., 2021. Atmospheric  $\text{CO}_2$  over the Past 66 Million Years from Marine Archives. *Annual Review of Earth and Planetary Sciences* 49, 609–641. <https://doi.org/10.1146/annurev-earth-082420-063026>
- Raich, J.W., Schlesinger, W.H., 1992. The global carbon dioxide flux in soil respiration and its relationship to vegetation and climate. *Tellus* 44B, 81–99. <https://doi.org/10.1034/j.1600-0889.1992.t01-1-00001.x>
- Raymond, P.A., Hartmann, J., Lauerwald, R., Sobek, S., McDonald, C., Hoover, M., Butman, D., Striegl, R., Mayorga, E., Humborg, C., Kortelainen, P., Dürr, H., Meybeck, M., Ciais, P., Guth, P., 2013. Global carbon dioxide emissions from inland waters. *Nature* 503, 355–359.  
<https://doi.org/10.1038/nature12760>
- Regnier, P., Resplandy, L., Najjar, R.G., Ciais, P., 2022. The land-to-ocean loops of the global carbon cycle. *Nature* 603, 401–410. <https://doi.org/10.1038/s41586-021-04339-9>
- Reimer, P.J., Brown, T.A., Reimer, R.W., 2004. Discussion: Reporting and Calibration of Post-Bomb  $^{14}\text{C}$  Data. *Radiocarbon* 46, 1299–1304.  
<https://doi.org/10.1017/S0033822200033154>

- Repasch, M., Scheingross, J.S., Hovius, N., Lupker, M., Wittmann, H., Haghypour, N., Gröcke, D.R., Orfeo, O., Eglinton, T.I., Sachse, D., 2021. Fluvial organic carbon cycling regulated by sediment transit time and mineral protection. *Nature Geoscience* 14, 842–848. <https://doi.org/10.1038/s41561-021-00845-7>
- Reyes, A.G., Christenson, B.W., Faure, K., 2010. Sources of solutes and heat in low-enthalpy mineral waters and their relation to tectonic setting, New Zealand. *Journal of Volcanology and Geothermal Research* 192, 117–141. <https://doi.org/10.1016/j.jvolgeores.2010.02.015>
- Roelandt, C., Godd ris, Y., Bonnet, M.-P., Sondag, F., 2010. Coupled modeling of biospheric and chemical weathering processes at the continental scale. *Global Biogeochemical Cycles* 24, GB2004. <https://doi.org/10.1029/2008GB003420>
- Rohling, E.J., Sluijs, A., Dijkstra, H.A., K hler, P., van de Wal, R.S.W., von der Heydt, A.S., et al., 2012. Making sense of palaeoclimate sensitivity. *Nature* 491, 683–691. <https://doi.org/10.1038/nature11574>
- Romero-Mujalli, G., Hartmann, J., B rker, J., Gaillardet, J., Calmels, D., 2019. Ecosystem controlled soil-rock pCO<sub>2</sub> and carbonate weathering – Constraints by temperature and soil water content. *Chemical Geology* 527, 118634. <https://doi.org/10.1016/j.chemgeo.2018.01.030>
- Rov ra, G., Robert, Y., 2006. Conditions climatiques hivernales et processus d’ rosion p riglaciaires dans les bad-lands marneux de Draix (800 m, Alpes du Sud, France). *G ographie physique et Quaternaire* 59, 31–48. <https://doi.org/10.7202/013735ar>
- Šantr ckov, H., Bird, M.I., Lloyd, J., 2000. Microbial processes and carbon-isotope fractionation in tropical and temperate grassland soils. *Functional Ecology* 14, 108–114. <https://doi.org/10.1046/j.1365-2435.2000.00402.x>
- Scadden, P., Dooley, D., Boyes, A., 2016. Petroleum Basin Explorer [Data set], 3.3.3. ed. Institute of Geological & Nuclear Sciences, Lower Hutt, New Zealand.
- Scheingross, J.S., Hovius, N., Dellinger, M., Hilton, R.G., Repasch, M., Sachse, D., Gr cke, D.R., Vieth-Hillebrand, A., Turowski, J.M., 2019. Preservation of organic carbon during active fluvial transport and particle abrasion. *Geology* 47, 958–962. <https://doi.org/10.1130/G46442.1>
- Scheingross, J.S., Repasch, M.N., Hovius, N., Sachse, D., Lupker, M., Fuchs, M., Halevy, I., Gr cke, D.R., Golombek, N.Y., Haghypour, N., Eglinton, T.I., Orfeo, O., Schleicher, A.M., 2021. The fate of fluvially-deposited organic carbon during transient floodplain storage. *Earth and Planetary Science Letters* 561, 116822. <https://doi.org/10.1016/j.epsl.2021.116822>

- Schillawski, S., Petsch, S., 2008. Release of biodegradable dissolved organic matter from ancient sedimentary rocks. *Global Biogeochemical Cycles* 22, GB3002. <https://doi.org/10.1029/2007GB002980>
- Schipper, L.A., Hobbs, J.K., Rutledge, S., Arcus, V.L., 2014. Thermodynamic theory explains the temperature optima of soil microbial processes and high Q<sub>10</sub> values at low temperatures. *Global Change Biology* 20, 3578–3586. <https://doi.org/10.1111/gcb.12596>
- Schmidt, M.W.I., Torn, M.S., Abiven, S., Dittmar, T., Guggenberger, G., Janssens, I.A., Kleber, M., Kögel-Knabner, I., Lehmann, J., Manning, D.A.C., Nannipieri, P., Rasse, D.P., Weiner, S., Trumbore, S.E., 2011. Persistence of soil organic matter as an ecosystem property. *Nature* 478, 49–56. <https://doi.org/10.1038/nature10386>
- Schwab, V.F., Nowak, M.E., Elder, C.D., Trumbore, S.E., Xu, X., Gleixner, G., Lehmann, R., Pohnert, G., Muhr, J., Küsel, K., Totsche, K.U., 2019. 14C-Free Carbon Is a Major Contributor to Cellular Biomass in Geochemically Distinct Groundwater of Shallow Sedimentary Bedrock Aquifers. *Water Resources Research* 55, 2104–2121. <https://doi.org/10.1029/2017WR022067>
- Scott, A.C., Glasspool, I.J., 2006. The diversification of Paleozoic fire systems and fluctuations in atmospheric oxygen concentration. *Proceedings of the National Academy of Sciences* 103, 10861–10865. <https://doi.org/10.1073/pnas.0604090103>
- Seifert, A.-G., Trumbore, S., Xu, X., Zhang, D., Gleixner, G., 2013. Variable effects of plant colonization on black slate uptake into microbial PLFAs. *Geochimica et Cosmochimica Acta* 106, 391–403. <https://doi.org/10.1016/j.gca.2012.12.011>
- Seifert, A.-G., Trumbore, S., Xu, X., Zhang, D., Kothe, E., Gleixner, G., 2011. Variable effects of labile carbon on the carbon use of different microbial groups in black slate degradation. *Geochimica et Cosmochimica Acta* 75, 2557–2570. <https://doi.org/10.1016/j.gca.2011.02.037>
- Shaughnessy, A.R., Gu, X., Wen, T., Brantley, S.L., 2021. Machine learning deciphers CO<sub>2</sub> sequestration and subsurface flowpaths from stream chemistry. *Hydrology and Earth System Sciences* 25, 3397–3409. <https://doi.org/10.5194/hess-25-3397-2021>
- Shulmeister, J., 2017. *Landscape and Quaternary Environmental Change in New Zealand*. Atlantis Press, Paris, France. <https://doi.org/10.2991/978-94-6239-237-3>
- Smith, R.W., Bianchi, T.S., Allison, M., Savage, C., Galy, V., 2015. High rates of organic carbon burial in fjord sediments globally. *Nature Geoscience* 8, 450–453. <https://doi.org/10.1038/ngeo2421>

- Soucémariadin, L.N., Cécillon, L., Guenet, B., Chenu, C., Baudin, F., Nicolas, M., Girardin, C., Barré, P., 2018. Environmental factors controlling soil organic carbon stability in French forest soils. *Plant and Soil* 426, 267–286. <https://doi.org/10.1007/s11104-018-3613-x>
- Soulet, G., Hilton, R.G., Garnett, M.H., Dellinger, M., Croissant, T., Ogrič, M., Klotz, S., 2018. Technical note: In situ measurement of flux and isotopic composition of CO<sub>2</sub> released during oxidative weathering of sedimentary rocks. *Biogeosciences* 15, 4087–4102. <https://doi.org/10.5194/bg-15-4087-2018>
- Soulet, G., Hilton, R.G., Garnett, M.H., Roylands, T., Klotz, S., Croissant, T., Dellinger, M., Le Bouteiller, C., 2021. Temperature control on CO<sub>2</sub> emissions from the weathering of sedimentary rocks. *Nature Geoscience* 14, 665–671. <https://doi.org/10.1038/s41561-021-00805-1>
- Sparkes, R.B., Hovius, N., Galy, A., Liu, J.T., 2020. Survival of graphitized petrogenic organic carbon through multiple erosional cycles. *Earth and Planetary Science Letters* 531, 115992. <https://doi.org/10.1016/j.epsl.2019.115992>
- Speden, I.G., 1976. Geology of Mt Taitai, Tapuaeroa valley, Raukumara Peninsula. *New Zealand Journal of Geology and Geophysics* 19, 71–119.
- Spence, J., Telmer, K., 2005. The role of sulfur in chemical weathering and atmospheric CO<sub>2</sub> fluxes: Evidence from major ions,  $\delta^{13}\text{CDIC}$ , and  $\delta^{34}\text{SSO}_4$  in rivers of the Canadian Cordillera. *Geochimica et Cosmochimica Acta* 69, 5441–5458. <https://doi.org/10.1016/j.gca.2005.07.011>
- Stasiuk, R., Włodarczyk, A., Karcz, P., Janas, M., Skłodowska, A., Matlakowska, R., 2017. Bacterial weathering of fossil organic matter and organic carbon mobilization from subterrestrial Kupferschiefer black shale: long-term laboratory studies. *Environmental Microbiology Reports* 9, 459–466. <https://doi.org/10.1111/1758-2229.12559>
- Stolper, D.A., Bender, M.L., Dreyfus, G.B., Yan, Y., Higgins, J.A., 2016. A Pleistocene ice core record of atmospheric O<sub>2</sub> concentrations. *Science* 353, 1427–1430. <https://doi.org/10.1126/science.aaf5445>
- Stuiver, M., Polach, H.A., 1977. Discussion Reporting of <sup>14</sup>C Data. *Radiocarbon* 19, 355–363. <https://doi.org/10.1017/S0033822200003672>
- Sullivan, P.L., Hynek, S.A., Gu, X., Singha, K., White, T., West, N., Kim, H., Clarke, B., Kirby, E., Duffy, C., Brantley, S.L., 2016. Oxidative dissolution under the channel leads geomorphological evolution at the Shale Hills catchment. *American Journal of Science* 316, 981–1026. <https://doi.org/10.2475/10.2016.02>
- Sun, X., Turchyn, A.V., 2014. Significant contribution of authigenic carbonate to marine carbon burial. *Nature Geoscience* 7, 201–204. <https://doi.org/10.1038/ngeo2070>

- Sundquist, E.T., Visser, K., 2003. The Geologic History of the Carbon Cycle, in: *Treatise on Geochemistry*. Elsevier, Amsterdam, Netherlands, pp. 425–472. <https://doi.org/10.1016/B0-08-043751-6/08133-0>
- Tamamura, S., Ueno, A., Aramaki, N., Matsumoto, H., Uchida, K., Igarashi, T., Kaneko, K., 2015. Effects of oxidative weathering on the composition of organic matter in coal and sedimentary rock. *Organic Geochemistry* 81, 8–19. <https://doi.org/10.1016/j.orggeochem.2015.01.006>
- Thompson, C.E., 2009. Tracking Organic Matter from Source to Sink in the Waiapu River Watershed, New Zealand: A Geochemical Perspective. Doctoral thesis, NC State University. Raleigh, USA.
- Tokunaga, T.K., Kim, Y., Conrad, M.E., Bill, M., Hobson, C., Williams, K.H., Dong, W., Wan, J., Robbins, M.J., Long, P.E., Faybishenko, B., Christensen, J.N., Hubbard, S.S., 2016. Deep Vadose Zone Respiration Contributions to Carbon Dioxide Fluxes from a Semiarid Floodplain. *Vadose Zone Journal* 15, vzj2016.02.0014. <https://doi.org/10.2136/vzj2016.02.0014>
- Torres, M.A., West, A.J., Clark, K.E., Paris, G., Bouchez, J., Ponton, C., Feakins, S.J., Galy, V., Adkins, J.F., 2016. The acid and alkalinity budgets of weathering in the Andes–Amazon system: Insights into the erosional control of global biogeochemical cycles. *Earth and Planetary Science Letters* 450, 381–391. <https://doi.org/10.1016/j.epsl.2016.06.012>
- Torres, M.A., West, A.J., Li, G., 2014. Sulphide oxidation and carbonate dissolution as a source of CO<sub>2</sub> over geological timescales. *Nature* 507, 346–349. <https://doi.org/10.1038/nature13030>
- Torres, M.E., Hong, W.-L., Solomon, E.A., Milliken, K., Kim, J.-H., Sample, J.C., Teichert, B.M.A., Wallmann, K., 2020. Silicate weathering in anoxic marine sediment as a requirement for authigenic carbonate burial. *Earth-Science Reviews* 200, 102960. <https://doi.org/10.1016/j.earscirev.2019.102960>
- Travelletti, J., Sailhac, P., Malet, J.-P., Grandjean, G., Ponton, J., 2012. Hydrological response of weathered clay-shale slopes: water infiltration monitoring with time-lapse electrical resistivity tomography. *Hydrological Processes* 26, 2106–2119. <https://doi.org/10.1002/hyp.7983>
- Tremosa, J., Debure, M., Narayanasamy, S., Redon, P.-O., Jacques, D., Claret, F., Robinet, J.-C., 2020. Shale weathering: A lysimeter and modelling study for flow, transport, gas diffusion and reactivity assessment in the critical zone. *Journal of Hydrology* 587, 124925. <https://doi.org/10.1016/j.jhydrol.2020.124925>

- Tune, A.K., Druhan, J.L., Wang, J., Bennett, P.C., Rempe, D.M., 2020. Carbon Dioxide Production in Bedrock Beneath Soils Substantially Contributes to Forest Carbon Cycling. *Journal of Geophysical Research: Biogeosciences* 125, e2020JG005795. <https://doi.org/10.1029/2020JG005795>
- Turnbull, J.C., Mikaloff Fletcher, S.E., Ansell, I., Brailsford, G.W., Moss, R.C., Norris, M.W., Steinkamp, K., 2017. Sixty years of radiocarbon dioxide measurements at Wellington, New Zealand: 1954–2014. *Atmospheric Chemistry and Physics* 17, 14771–14784. <https://doi.org/10.5194/acp-17-14771-2017>
- Tuttle, M.L.W., Breit, G.N., 2009. Weathering of the New Albany Shale, Kentucky, USA: I. Weathering zones defined by mineralogy and major-element composition. *Applied Geochemistry* 24, 1549–1564. <https://doi.org/10.1016/j.apgeochem.2009.04.021>
- Vandenbroucke, M., Largeau, C., 2007. Kerogen origin, evolution and structure. *Organic Geochemistry* 38, 719–833. <https://doi.org/10.1016/j.orggeochem.2007.01.001>
- Voroney, R.P., Heck, R.J., 2015. The Soil Habitat, in: Paul, E.A. (Ed.), *Soil Microbiology, Ecology and Biochemistry*. Academic Press, London, UK, pp. 15–39. <https://doi.org/10.1016/C2011-0-05497-2>
- Waksman, S.A., Starkey, R.L., 1931. *The soil and the microbe*. J. Wiley & Sons, Inc., New York, USA. <https://doi.org/10.5962/bhl.title.7227>
- Walker, J.C.G., Hays, P.B., Kasting, J.F., 1981. A negative feedback mechanism for the long-term stabilization of Earth's surface temperature. *Journal of Geophysical Research* 86, 9776. <https://doi.org/10.1029/JC086iC10p09776>
- Wallmann, K., Aloisi, G., Haeckel, M., Tishchenko, P., Pavlova, G., Greinert, J., Kutterolf, S., Eisenhauer, A., 2008. Silicate weathering in anoxic marine sediments. *Geochimica et Cosmochimica Acta* 72, 2895–2918. <https://doi.org/10.1016/j.gca.2008.03.026>
- Wan, J., Tokunaga, T.K., Brown, W., Newman, A.W., Dong, W., Bill, M., Beutler, C.A., Henderson, A.N., Harvey-Costello, N., Conrad, M.E., Bouskill, N.J., Hubbard, S.S., Williams, K.H., 2021. Bedrock weathering contributes to subsurface reactive nitrogen and nitrous oxide emissions. *Nature Geoscience* 14, 217–224. <https://doi.org/10.1038/s41561-021-00717-0>
- Wang, Y., Broquet, G., Ciais, P., Chevallier, F., Vogel, F., Wu, L., Yin, Y., Wang, R., Tao, S., 2018. Potential of European <sup>14</sup>CO<sub>2</sub> observation network to estimate the fossil fuel CO<sub>2</sub> emissions via atmospheric inversions. *Atmospheric Chemistry and Physics* 18, 4229–4250. <https://doi.org/10.5194/acp-18-4229-2018>
- Weisbrod, N., Dragila, M.I., Nachshon, U., Pillersdorf, M., 2009. Falling through the cracks: The role of fractures in Earth-atmosphere gas exchange. *Geophysical Research Letters* 36, L02401. <https://doi.org/10.1029/2008GL036096>

- Weissert, H., Lini, A., Föllmi, K.B., Kuhn, O., 1998. Correlation of Early Cretaceous carbon isotope stratigraphy and platform drowning events: a possible link? *Palaeogeography, Palaeoclimatology, Palaeoecology* 137, 189–203. [https://doi.org/10.1016/S0031-0182\(97\)00109-0](https://doi.org/10.1016/S0031-0182(97)00109-0)
- Werth, M., Kuzyakov, Y., 2010.  $^{13}\text{C}$  fractionation at the root–microorganisms–soil interface: A review and outlook for partitioning studies. *Soil Biology and Biochemistry* 42, 1372–1384. <https://doi.org/10.1016/j.soilbio.2010.04.009>
- West, A.J., Galy, A., Bickle, M., 2005. Tectonic and climatic controls on silicate weathering. *Earth and Planetary Science Letters* 235, 211–228. <https://doi.org/10.1016/j.epsl.2005.03.020>
- Weston, R. J., Czochanska, Z., Sheppard, C. M., Woolhouse, A. D., & Cook, R. A., 1988. Organic geochemistry of the sedimentary basins of New Zealand. Part III. A biomarker correlation of three petroleum seeps and some rock bitumens from the East Coast of the North Island. *Journal of the Royal Society of New Zealand*, 18, 225–243. <https://doi.org/10.1080/03036758.1978.10429394>
- White, A.F., Brantley, S.L., 2003. The effect of time on the weathering of silicate minerals: why do weathering rates differ in the laboratory and field? *Chemical Geology* 202, 479–506. <https://doi.org/10.1016/j.chemgeo.2003.03.001>
- Whiticar, M.J., 1999. Carbon and hydrogen isotope systematics of bacterial formation and oxidation of methane. *Chemical Geology* 161, 291–314. [https://doi.org/10.1016/S0009-2541\(99\)00092-3](https://doi.org/10.1016/S0009-2541(99)00092-3)
- Wildman, R.A., 2004. The weathering of sedimentary organic matter as a control on atmospheric  $\text{O}_2$ : I. Analysis of a black shale. *American Journal of Science* 304, 234–249. <https://doi.org/10.2475/ajs.304.3.234>
- Wilkins, M., Fredrickson, J.K., 2015. Terrestrial subsurface ecosystem, in: Ehrlich, H.L., Newman, D.K., Kappler, A. (Eds.), *Ehrlich's Geomicrobiology*. CRC Press, Boca Raton, USA. <https://doi.org/10.1201/b19121>
- Włodarczyk, A., Lirski, M., Fogtman, A., Koblowska, M., Bidziński, G., Matlakowska, R., 2018. The Oxidative Metabolism of Fossil Hydrocarbons and Sulfide Minerals by the Lithobiontic Microbial Community Inhabiting Deep Subterrestrial Kupferschiefer Black Shale. *Frontiers in Microbiology* 9, 972. <https://doi.org/10.3389/fmicb.2018.00972>
- Yan, Y., Brook, E.J., Kurbatov, A. v., Severinghaus, J.P., Higgins, J.A., 2021. Ice core evidence for atmospheric oxygen decline since the Mid-Pleistocene transition. *Science Advances* 7, eabj9341. <https://doi.org/10.1126/sciadv.abj9341>

Zhang, D., Zhao, Z., Li, X., Zhang, L., Chen, A., 2020. Assessing the oxidative weathering of pyrite and its role in controlling atmospheric CO<sub>2</sub> release in the eastern Qinghai-Tibet Plateau. *Chemical Geology* 543, 119605. <https://doi.org/10.1016/j.chemgeo.2020.119605>